Conversion of CO_2 into valuable fuels and chemicals using non-thermal plasma

by

Yuxuan Zeng

The University of Liverpool

Thesis submitted for the degree

of

Doctor of Philosophy

Department of Electrical Engineering and Electronics

Liverpool, March 2017

Declaration

Yuxuan Zeng hereby declares that this thesis is his own work. All the reproduced and cited contents have been acknowledged in the references. Neither this thesis nor any part of it have been submitted to any other university or institution for the application of another degree or qualification.

Liverpool, March, 2017

Signature:

Abstract

This project studies the conversion of CO_2 into fuels and chemicals in a dielectric barrier discharge (DBD) reactor. CO_2, H_2 and CH_4 have been used as reactants, and special attention has been paid on understanding the plasma-catalytic synergy when a catalyst is placed in a plasma discharge. CO_2 and CH_4 are major greenhouse gases, responsible for the global greenhouse effect and climate change. The overall aim of this project is to initiate CO_2 hydrogenation and biogas reforming at ambient temperature and atmospheric pressure by using plasma-catalysis. In this project, non-thermal plasma has been generated in a DBD reactor with and without a packed-bed of catalyst, enabling the CO_2 conversion to be investigated under three conditions: Plasma alone, thermal catalysis and plasma-catalysis. Transitional metal catalysts such as Cu, Co, Mn, and Ni supported on Al_2O_3 and SiO_2 have been screened, and their performance in the CO_2 hydrogenation and biogas reforming have been compared under the three conditions. The synergy between non-thermal plasma and catalysts has been clearly identified. The effects of a catalyst's properties and operational parameters on the reactions have also been studied. The project starts by the investigation of CO_2 hydrogenation with H_2. Results showed that reverse water-gas shift reaction and CO_2 methanation were dominant in the plasma CO_2 hydrogenation process. Compared to plasma CO_2 hydrogenation without a catalyst, the combination of plasma with Cu/Al_2O_3, Mn/Al_2O_3 and $Cu\text{-}Mn/Al_2O_3$ catalysts enhanced the conversion of CO_2 by 6.7% to 36%. The Mn/Al_2O_3 catalyst showed the best catalytic activity, as it increased the CO yield by 114% and the energy efficiency of CO production by 116%. The Ni/Al_2O_3 was even better than the Mn/Al_2O_3 catalyst, while its presence in the DBD reactor has clearly demonstrated a plasma-catalytic synergy at low temperatures. In addition, the introduction of argon in the reaction has enhanced the conversion of CO_2, the yield of CO and CH_4 and the energy efficiency of the plasma process. The formation of metastable argon (Ar*) in the plasma has created new reaction-routes which made a significant contribution to the enhanced CO_2 conversion and CH_4 yield. Biogas

reforming has also been initiated at ambient temperatures by non-thermal plasma. The combination of plasma with the Co/Al_2O_3, Cu/Al_2O_3, Mn/Al_2O_3 and Ni/Al_2O_3 catalysts significantly enhanced CH_4 conversion and showed a plasma-catalytic synergy for CH_4 conversion and overall energy efficiency of the process. The best CH_4 conversion of 19.6% and syngas production have been achieved over the Ni/Al_2O_3 catalyst at a discharge power of 7.5 W and a gas flow rate of 50 ml min^{-1}. Moreover, the addition of K-promoter into the catalyst has further improved the performance of the Ni/Al_2O_3 catalyst.

A conclusion of the findings of this project and outlook for further work is presented in Chapter seven, where it is concluded that non-thermal plasma has initiated the CO_2 hydrogenation and biogas reforming at lower temperatures, comparing with thermal catalytic processes. The combination of plasma and catalyst has further improved the performance of the hydrogenation processes, in terms of conversion, yield, and energy efficiency, while significant synergy between DBD plasma and catalysts has been observed. By upgrading the catalyst and adjusting the operational parameters (*e.g.* molar ratio of feed gas, preparation method of catalyst, composition of catalyst, and promoters), the plasma-catalytic CO_2 hydrogenation and biogas reforming processes can be further optimised.

Acknowledgement

I would like to gratefully thank my primary supervisor Dr. Xin Tu for his guidance and support throughout the entire course of this project. Dr. Xin Tu has exhibited his enthusiasm and prudence throughout the project, which is impressive and inspiring.

My PhD fellowship is co-funded by the Doctoral Training Programme (DTP) at the University of Liverpool and the Chinese Scholarship Council (CSC). Great thanks to them for providing this opportunity for me.

I would like to thank Dr. Li Wang for her help with the preparation and characterisation of catalysts, interpreting the catalytic results, and advices on the manuscripts.

I would like to thank Bryony Ashford, Dr. Jidong Jin, Alan Edwards, Thomas Hardiment, Patrick McCarthy, Peter Ryan, and Gareth Blacoe for their useful comments on my manuscripts.

I would like to thank Dr. Vladimir Demidyuk for his help with the design, building and test of the heating device. Thanks to Shaojun Xu, Dr. Chunfei Wu and Dr. Mohamad Nahil for their help with characterisation of catalysts.

Thanks also go to Dr. James Walsh and Dr. Lin Jiang for supporting this project.

I would also like to thank the members of the research group, Dr. Xinbo Zhu, Dr. Hao Zhang, Fengsen Zhu, Dr. Danhua Mei, Chao Xu, Shiyun Liu, Yichen Ma, Jia Sun, and Yuxing Tian for their valuable assistance in the lab.

Finally but least, I want to thank Alan Roby, John Lynch, and Mark Norman in the workshop. Special thanks to Xuming Zhang, Jill Anson, Phil, and my beloved family.

List of publications

In the course of this project, the following works have been published on journals:

[1] **Yuxuan Zeng** and Xin Tu. "Plasma-catalytic hydrogenation of CO_2 for the cogeneration of CO and CH_4 in a dielectric barrier discharge reactor: Effect of argon addition.", *Journal of Physics D: Applied Physics*, 50.18 (2017): 184004.

[2] **Yuxuan Zeng** and Xin Tu. "Plasma-catalytic CO_2 hydrogenation at low temperatures.", *IEEE Transactions on Plasma Science*, 44. 4 (2016): 405-411.

[3] **Yuxuan Zeng**, Xinbo Zhu, Danhua Mei, Bryony Ashford, and Xin Tu. "Plasma-catalytic dry reforming of methane over γ-Al_2O_3 supported metal catalysts.", *Catalysis Today*, 256 (2015): 80-87.

[4] He Jiang, Jiafeng Zhou, Yi Huang, **Yuxuan Zeng**, Jim Humphries, Qian Xu, Chaoyun Song, Lei Xing, Zhouxiang Fei, and Jan Nalborczyk. "Design of a Marx Generator for HEMP filter evaluation taking account of parasitic effect of components.", In *Electromagnetic Compatibility-EMC EUROPE, 2016 International Symposium on*, pp. 839-843. IEEE, 2016.

[5] Xinbo Zhu, Xiang Gao, Rui Qin, **Yuxuan Zeng**, Ruiyang Qu, Chenghang Zheng, and Xin Tu. "Plasma-catalytic removal of formaldehyde over Cu–Ce catalysts in a dielectric barrier discharge reactor.", *Applied Catalysis B: Environmental*, 170 (2015): 293-300.

[6] Ramses Snoeckx, **Yuxuan Zeng**, Xin Tu, and Annemie Bogaerts. "Plasma-based dry reforming: improving the conversion and energy efficiency in a dielectric barrier discharge.", *RSC Advances*, 5. 38 (2015): 29799-29808.

One oral presentation, one invited talk and several posters have also been presented on conferences.

Table of contents

List of figures

List of tables

Chapter 1. Introduction

1.1. Greenhouse effect and greenhouse gases

The earth absorbs energy from solar radiation and reflects infrared to the atmosphere. The greenhouse effect is due to atmospheric greenhouse-gases (GHGs) trapping the thermal radiation from the earth, and reflecting it back to the earth (Figure 1.1). This process maintains the temperature of the earth's surface, and literately keeps the Earth's energy balance. Increasing the concentrations of GHGs results in an increase in the levels of reflected thermal radiations, leading to higher atmospheric temperatures, *i.e.* global warming [1-6].

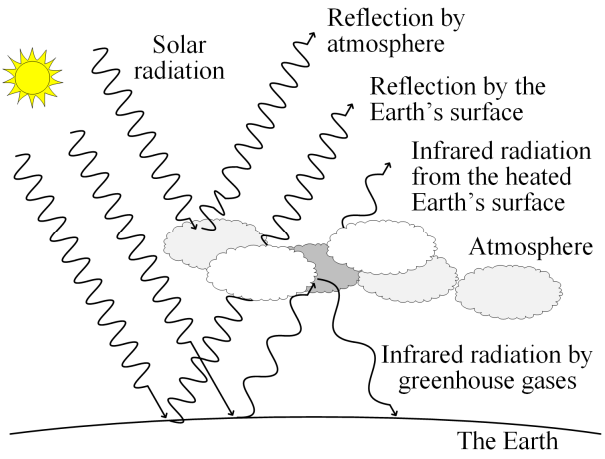

Figure 1.1 Schematic of greenhouse effect.

The major GHGs which are related to human activities are carbon dioxide (CO_2), methane (CH_4), nitrous oxide (N_2O), ozone (O_3), chlorofluorocarbons (HFCs, CFCs, HCFCs), perfluorocarbons (PFCs) and sulphur hexafluoride (SF_6). The main sources of these gases include fossil fuel combustion, road transportation, chemical production, oil and gas fields, refineries and landfill sites. The lifetime of GHGs in the atmosphere

ranges from decades to centuries. As a consequence, the earth would continue to warm up for a long time even if man-kind immediately stops all the GHG emissions.

The amplitude of global warming caused by a GHG is quantified by the Global Warming Potential (GWP) over a fixed period of time. It is the ratio that compares the warming effect of the specific gas with the same amount of CO_2. The GWP of CO_2 is 1.0, while that of other GHGs ranges from 7 to 32600, depending on their lifetimes (*e.g.* SF_6 has a value of 32600 in 500-year-time). Temperature statistics show that the surface temperature of the earth increased about 0.8 °C in the 20th century on the 1900 base [7]. If no action is taken, the temperature is estimated to increase by 3.1 °C–4.6 °C by 2100, and eventually increase by 3.5 °C -7 °C. The increase in the concentration of GHGs will have dramatic effects such as ocean acidification and algae tide. While global warming will bring significant changes to weather systems. Consequently, global climate change will result in increasing frequency of flood, drought or tsunami. This abnormal climate might kill crops and livestock, cause forest fire, and eventually famine.

1.2. Carbon capture and utilization

According to the 1997 Kyoto Protocol, CO_2 is recognised as the most significant GHG contributing to global climate change. The combustion of fossil fuel in industry and energy sectors is the major source of CO_2 emission. There is a growing and urgent demand for the development of novel technologies which can significantly reduce global CO_2 emissions while generating sustainable energy for modern society [2, 5]. According to the Department of Energy & Climate Change (DECC), CO_2 has always been the dominant greenhouse gas (GHG) emitted in the UK, especially prominent in the energy supply sector [8]. UK emissions of GHG were 514.4 million tonnes carbon dioxide equivalent (MtCO2e) in 2014, the energy supply sector being responsible for 31% of these emissions. CO_2 accounted for about 82% of the UK's GHGs emissions (GWP) in 2014, while CH_4 accounts for about 10%.

CO_2 reduction strategies can be categorised as CO_2 capture, CO_2 storage, CO_2 utilisation, and replacing fossil fuels with renewable energy for CO_2 neutral process. These strategies are usually integrated for engineering concerns and commercial applications. CO_2 capture and storage (CCS), CO_2 capture and utilisation (CCU) are two technological approaches being actively pursued.

1.3. Related legislation

1.3.1. Kyoto Protocol

The 1997 Kyoto Protocol recognises the significant effect of increased concentration of atmospheric CO_2 on global climate change. It is an international agreement among United Nations members to reduce their CO_2 emissions. Although the legally binding duration of this protocol expired in 2012, member states are continuing the research and development of CO_2 reduction technologies.

1.3.2. Energy Act 2004

The UK's Energy Act 2004 makes provision for the decommissioning of installations and sites related to nuclear activities, and for the cleaning up of radioactive waste. Crucially, in regard to the incentive for this project, it makes provision for the development, regulation and encouragement of the use of renewable energy sources. In addition, it covers the regulation of the gas and electricity industries [9].

1.3.3. Climate Change Act 2008

The UK has established a long-term domestic target for the reduction of greenhouse gas emissions, which is legally-binding to the Climate Change Act 2008 [10]. The target is to reduce UK's greenhouse gas emissions by 80% from 1900 levels by 2050, with an interim target of 34% reduction by 2020. A Committee on Climate Change has been set up, and a system of carbon budgeting has been devised according to the Climate Change Act 2008. The UK also has annual GHG reduction targets under the EU Effort Sharing Decision (ESD) for the period 2013–2020, aiming to reduce the GHG emissions by 16% from 2005 levels by the year of 2020.

1.3.4. Paris Agreement

The Paris Agreement regulates GHGs emissions, mitigation, adaptation and finance [11]. It's an agreement within the United Nations Framework Convention on Climate Change (UNFCCC) and was firstly negotiated by member-countries in 2015. The agreement went into effect on 4 November 2016. The aims of the agreement are "holding the increase in the global average temperature to well below 2 ^{o}C above pre-industrial levels and to pursue efforts to limit the temperature increase to 1.5 ^{o}C above

pre-industrial levels; Increasing the ability to adapt to the adverse impacts of climate change and foster climate resilience and low GHGs emissions development, in a manner that does not threaten food production; Making finance flows consistent with a pathway towards low GHGs emissions and climate-resilient development.

The consensus therefore, is that CO_2 reduction is vital for the UK, and the development of CO_2 reduction technologies will be necessary for the short and medium term. In fact in 2015, the UK Government announced it was axing its £ 1 billion competition to develop "carbon capture and storage (CCS)" technology for power stations. This might be a sign that the conversion and utilization of CO_2 (CCU) would be a more attractive approach than CCS.

1.4. Synthesis gas and its applications

1.4.1. Synthesis gas

Synthesis gas, which is also called syngas, is a mixture of H_2 and CO, and can be produced from many sources. There is a wide range of applications for syngas. The H_2 and CO can be separated and used individually for different processes. For instance, the H_2 is mainly used for the production of ammonia, while the CO is used for the synthesis of acetic acid, phosgene and formic acid. Either separated gases or the mixture of syngas can be used for the reduction of iron ore in steel industry, to produce direct-reduced iron (DRI) or sponge iron. Moreover, syngas can be combusted in gas turbines, internal combustion engines and boilers. Most of these applications are in power plants that have installed integrated gasification combined cycle (IGCC) systems. IGCC yields syngas from the gasification of coal, coke, heavy oil and biomass. However, purification is needed to remove H_2S, NH_3, metals and particulates before the syngas can be combusted in a gas turbine. Notably, when the syngas is from biomass, this process is considered renewable and CO_2 neutral. IGCC using biomass is a potential alternative technology for power plants in place of the combustion of fossil fuels. Finally and more importantly, syngas can be directly used as a mixture feedstock for the Fischer-Tropsch process. This process is extremely valuable and will be introduced in the following section.

1.4.2. Gas-to-liquid process

Gas-to-liquid (GTL) is a collection of processes that convert syngas into liquid chemicals and fuels. These techniques include the Fischer-Tropsch (FT) process, the direct synthesis of methanol from syngas, the production of dimethyl ether (DME), and hydroformylation (also known as oxo process, being an industrial process for the production of aldehydes from alkenes). For the synthesis of different products, syngas with different H_2/CO molar ratios is required. The H_2/CO ratio in the syngas is adjusted by water-gas shift reaction (WGS), which consumes H_2O and CO to produce H_2 and CO_2, and is usually integrated into a natural gas/methane reformer. A very interesting application of the GTL process is the utilisation of natural gas from offshore oil fields. Due to the abundance of natural gas and high cost of transporting gas from remote inland locations, the natural gas is generally considered a by-product and flared in this case. In contrast, the GTL process would make profit from the by-product and reduce the emission of CH_4.

1.4.3. Fischer-Tropsch process

The GTL process is usually operated over various metal catalysts, at elevated temperatures, and with very low aromatic or sulphur impurity. The Fischer-Tropsch (FT) process is a good example of a GTL process that converts syngas into higher hydrocarbons and alcohols. It was invented by Franz Fischer and Hans Tropsch in 1925. Examples of common products of FT process include liquefied petroleum gas (LPG), naphtha, synthetic gasoline and diesel. The FT process is usually carried out over iron, cobalt and ruthenium based catalysts, over a temperature range of 150 ºC–300 ºC and a pressure ranges from one to several tens of atmospheres. Higher temperatures accelerate reactions and improve conversions, but also unfortunately favour methane formation. The production of methane is against the original purpose of the FT process, which is primarily to produce liquid hydrocarbons and fuels. Therefore the reaction is set at temperatures lower than 300 ºC. The H_2/CO molar ratio in the feedstock is usually <2, but changes according to the catalyst and target product. The main reactions involved in the FT process can be summarised as:

$$(2n+1)\ H_2 + n\ CO \rightarrow C_nH_{2n+2} + n\ H_2O \qquad (1)$$

$$2n\ H_2 + n\ CO \rightarrow C_nH_{2n} + n\ H_2O \qquad (2)$$

$$CO + H_2O \rightarrow CO_2 + H_2 \quad (3)$$

$$2n\ H_2 + n\ CO \rightarrow C_nH_{2n+2}O + (n-1)\ H_2O \quad (4)$$

$$2\ CO \rightarrow C + CO_2 \quad (5)$$

Conventional refinery processes such as fractional distillation are used to separate the products into naphtha, gasoline, diesel, kerosene and waxes. The FT process nowadays is a well-established industry based on experience and knowledge gained in associated disciplines such as production process techniques, the synthesis of catalysts and the design of reactors. The production of syngas from renewable sources (*e.g.* biomass) can be included into this evolving industry in the future for the reduction of atmospheric CO_2.

1.5. Plasma

Since CO_2 is highly stable, the activation of CO_2 molecules requires a high energy input. For example, the thermodynamic equilibrium calculation for the decomposition of pure CO_2 shows that CO_2 begins to decompose into CO and O_2 near 2000 K with a very low conversion (<1%). A higher temperature (3000-3500 K) is required to achieve a reasonable conversion of CO_2 (30–60%). In addition, separation of CO and O_2 in the direct CO_2 decomposition process is also a challenge. Great efforts have been devoted to the investigation of CO_2 hydrogenation into CO and/or CH_4 using thermal catalytic [12-16], photocatalytic [17, 18] or electrochemical [19, 20] processes. However, significant fundamental works are still required to further enhance the overall energy efficiency and product selectivity of the process through the design and development of new reactor concepts and novel catalytic materials with higher activity and stability. Non-thermal plasma (NTP) and plasma-catalysis provide a promising alternative to the conventional catalytic approach for CO_2 conversion and utilisation at atmospheric pressure and low temperatures. The term “plasma” was firstly proposed by Langmuir in the 1920s. Plasma is the state of matter being either fully or partially ionised, consisting of positive ions and electrons. Plasma has an equal number of positive and negative charges, therefore being electrically neutral (quasi-neutral). Ionisation is usually caused by strong electric field, heating, electro-magnetic radiation, adiabatic compression of gas, or energetic nucleus/neutron beams. Plasma is natural and abundant in the universe in many forms such as stars, solar corona, solar wind and

nebula. Plasma also appears on the Earth in the form of lightning, aurora, fire and nuclear fusion plasma. The ionosphere is a region of Earth's upper atmosphere that is ionised by solar and cosmic radiations. Aurora usually appears near the poles and hundreds kilometres above the earth's surface, created by the collision between energised particles in solar wind and the gas molecules in the atmosphere. Lightning usually begins with charges accumulating in the clouds and a large potential difference building up between the clouds and the earth, eventually it ends with a discharge.

Table 1.1 Technological application of plasma.

Application	Example
Lighting	Excilamp, fluorescent lamp and neon light.
Display panel	Large area flat-screen television.
Laser	CO_2 laser, UV laser, cutting and boring.
Surface modification	Etching, waterproof treatment and corona treatment.
Thin film deposition	Coating and plasma vapour deposition.
Material synthesis	Fine particle preparation, electret synthesis and sulphur production from H_2S cracking.
Decontamination	Ozone production, volatile organic compounds (VOCs) removal, electrostatic precipitation (ESP), incineration and crystallisation.
Bio-medical treatment	Dental care, sterilisation and cell treatment.
Propelling	Actuator, floater and ion engine.
Other	Food preservation, fusion reactor, printing, melting and welding.

Ever since the first industrial application of artificial plasma: production of ozone using silent discharge by Siemens in the 1850s, the theory, generation, modulation and application of plasma has been studied. Table 1.1 summarises the wide range of technological applications of man-made plasma in the gas phase. However, fundamental understanding of the mechanism and behaviour of plasma is still needed in many areas.

Most of the technological plasmas are created by electric discharge in gases, essentially involving the Townsend Avalanche process. Essentially, free electrons in gases are subjected to acceleration by applying a strong electric field, the free electrons subsequently collide with and ionise gas molecules. When applied voltage exceeds the breakdown voltage, additional free electrons are released in this ionisation process and

it starts a chain reaction. As a result of increased number of free electrons, the gas region becomes electrically conductive and electric discharge occurs. The initiation and evolution of gaseous discharge is highly dependent on the pressure and the type of working gas. Figure 1.2 shows the onset of gaseous discharge at different voltages and low pressures.

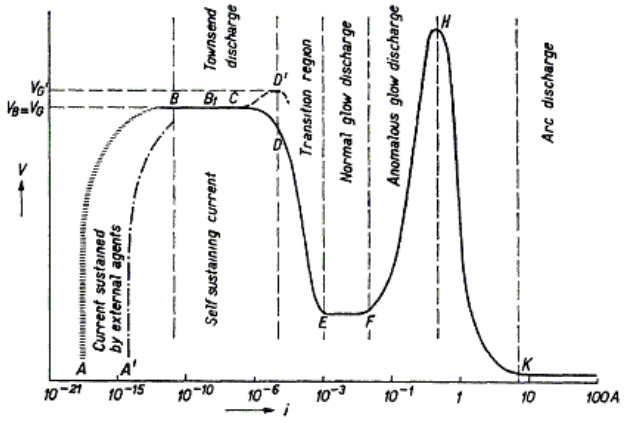

Figure 1.2 "Schematic characteristic of a gas discharge between flat parallel plates." Figure taken from [21]. The segment A'B in the figure is ascribed to the current with photo-emission from the cathode. Segment CD' shows the positive characteristic of Townsend discharge, as the breakdown potential V_B is lower than the starting potential of the glow discharge V_G. Segment CD shows the negative characteristic of Townsend discharge, where $V_B = V_G$.

The characteristics of plasma are determined by the operating pressure, properties of the source molecules, type of discharge, patterns of applied voltage and working temperature. The breakdown voltage (U_b) is the minimum voltage required to initiate a discharge. It is highly dependent on the product of gas pressure (p) and distance between the electrodes (d). The relationship between U_b and pd is explained by Paschen's Law,

$$U_b = \frac{Bpd}{\ln(Apd) - \ln(\ln(1/\gamma))} \qquad (6)$$

where A and B are constants that are characterised by the gas type, γ is the probability for secondary electron emission. As shown by the Paschen's Law, only few plasma devices work at high pressure due to the restriction of mean free path. For

instance, the mean free path of electrons reduces from 7 μm to 70 nm when the working pressure increases from 10 mbar to 1 bar. This substantially limits the energy that electrons can acquire in an electric field and so restricts the formation of plasma. Consequently, technological plasmas are usually operated at atmospheric pressure or in the vacuum. Barrier discharge (BD) and corona plasmas are usually used at atmospheric pressure. Thermal, DC discharge, radio frequency (RF) and microwave plasmas are widely used under all pressure regimes.

1.5.1. Thermal plasma

Technological plasmas are usually categorised into two types as thermal (also called as near-equilibrium, hot-) plasma and non-thermal (non-equilibrium, cold-) plasma. In thermal plasma, the bulk gas is thoroughly heated, electrons are energised by the thermal radiation and gas molecules are almost totally ionised at this temperature. The temperature of the ions, electrons and neutral species are very close, and the gas temperature can be high as 10^4 K. The energy density of thermal plasma usually ranges from 10^2 to 10^4 W cm^{-3}. Thermal plasma is used in various industrial applications such as arc welding, plasma cutting and drilling, incineration, waste treatment, arc furnaces and fine particle synthesis.

1.5.2. Non-thermal plasma

In non-thermal plasma (NTP) the temperature of the electrons is much higher than that of the ions and the neutral species. Electrons are accelerated or energised instead of gas molecules, usually by the strong electric field. The electron temperature of non-thermal plasma can reach 10^4 to 10^5 K (1 – 10 eV) while the temperature of the bulk gas remains close to the ambient temperature. Under these conditions the gas is weakly ionised, the ratio of charged particles to neutral species (degree of ionisation) generally ranges from 10^{-14} to 10^{-7}. Part of the gas molecules are excited vibrationally or rotationally to different "energy states", which can serve as energy carrier for the chemical reactions in plasma.

Since most of the injected energy is used to energise electrons, non-thermal plasma has higher energy efficiency in ionising particles and inducing reactions. Electron induced processes such as molecular excitation, ionization and dissociation produce various active species in the non-thermal plasma, including energized electrons, ions,

excited atoms and radicals; these are called the primary processes in plasma and usually react in a time period of 10^{-8} s. The active species can kinetically initiate and propagate chemical reactions at low temperatures, comparing against conventional thermal catalysis. Aerosols are also formed in ion- involved reactions in plasma, and this process usually happens on a time scale of 10^{-3} s. Due to a relatively low working temperature, non-thermal plasma can be used for all the applications summarised in Table 1.1 except crystallisation and fusion. Remarkably, in volatile organic contaminants (VOCs) removal, non-thermal plasma processes are more energy-efficient than conventional technologies, such as condensation or catalytic combustion. It is due to less energy wasted in cooling or heating the bulk gas molecules. NTP is also used for chemical reactions in the laboratory, for instance methane reforming for the production of hydrogen, and CO_2 conversion into CO and CH_4 [22-25].

1.5.2.1. Dielectric barrier discharge

Non-thermal plasma can be divided to several categories. Dividing by the discharge characteristic, there are corona, streamer, glow and arc plasma. Depending on the configuration of the reactor, there are corona, dielectric barrier discharge (DBD), jet and gliding arc plasma. Depending on the power applied, there are direct current (DC), alternating current (AC) and pulse plasma. Moreover, there are various reactors with packing materials, including packed bed, granular bed plasma reactor and so on.

DBD plasma has been commercially used for ozone production, surface modification, gaseous pollution control and water purification at atmospheric pressure [26]. It is also used for the reduction of particulate emissions from diesel engine exhausts [27]. The configuration of DBD includes planar, cylindrical (coaxial) and surface discharge, as illustrated in reference [26]. Generally, DBD plasma is created in the gas gap between two parallel planar electrodes or two coaxial cylindrical electrodes, with one or both of the electrodes covered by dielectric layer(s). Examples of the materials for dielectric layer and packing include glass, quartz, cerium oxide, aluminium oxide and barium titanium oxide. The dielectric constant (ε) is the relative permittivity of a dielectric material. It describes the ability of a material to store electric energy in an electric field. For instance, the dielectric constant of vacuum ε_0 is 1, the dielectric constant of atmosphere ε_{air} is 1.00059, and ε_{glass} is 5 –10. Dielectric constants of dielectric layer and packing materials affect the discharging characteristics therefore

are very important for DBD plasma. The electrodes of DBD reactors are powered by AC or pulsed excitations. When the electric field applied across the gap is strong enough, electron avalanche occurs in the gas and the gas breaks down. Sometimes, tiny and bright discharge channels, known as streamers, occur with electron avalanche. This is a type of transient electrical discharge which is also called filamentary discharge or micro-discharge. The dielectric layer prevents the formation of a spark between electrodes, while numerous streamers randomly distribute in the discharge gap and form a "restricted" plasma, as plasma is constrained in the micro- channels. In other cases, instead of streamers, the discharge uniformly spreads and fills the entire gap, creating a "diffusive" plasma. The characteristic of the DBD plasma is affected by the electrical conductivity of the dielectric material and the width of the discharge gap. Higher conductivity of the dielectric material and smaller discharge gap will lower the electric field in the gap and limit current flow through the reactor, therefore suppress the formation of streamers. The discharge gap usually ranges from 0.1 to 100 mm. The voltage-current characteristic of low temperature DBD shows a pattern similar to Figure 1.2, where the evolution of discharge mode from non-self-sustaining discharge, via Townsend discharge, to glow discharge can be clearly identified [28]. Catalysts can easily be integrated into a DBD system in different ways to generate a plasma-catalyst synergy and to further enhance the efficiency of the plasma process. This makes DBD a suitable plasma source for plasma-catalytic reactions for gas conversion and fuel production with the potential for process scale-up.

In this project, a revised version of packed-bed DBD reactor is used. And it is discussed in detail in Chapter two.

1.5.2.2. Packed-bed DBD reactor

The packed-bed DBD reactor is a variation design of the typical DBD reactor. In this design the gas gap between the electrode and the dielectric layer is partially or fully filled with packing material of high dielectric constant, in the form of powder, pellets, beads and wool. When a high voltage is applied across the gap, the packing material is polarised and results in an intensified electric field in the void within the packing. Micro-discharges occur at the contact points of pellets or beads, while both of surface discharge and dielectric barrier discharge take place [29]. Plasma is created around and among the packing materials.

A packed-bed arrangement can change the electric field distribution between electrodes and improve the uniformity of the discharge. Plasma can be generated across the electrodes with relatively large distance. Comparing with DBD without packing materials but using the same electrode configuration, the packed-bed lowers the burning voltage of the reactor [30]. Packed-bed DBD reactor is widely used to investigate the reaction performance of catalyst in plasma, and the interactions between non-thermal plasma and catalysts.

1.6. Plasma combined with catalyst, and plasma-catalysis

The hybrid process that combines plasma and catalysts has drawn growing interest in recent years [2, 31-35]. Comparing processes using plasma alone or thermal catalysis, plasma-catalysis improves the conversion and energy efficiency. Compared with conventional thermal-catalysis, the advantage of plasma-catalysis can be summarised as operates at low reaction temperature, has rapid start-up and shutdown, and eliminates the extra cost for heating.

The combination of non-thermal plasma and catalyst can be classified into two arrangements, known as two-stage and one-stage, depending on the position of catalyst [36]. The two-stage configuration has the catalyst being located downstream the plasma, also known as post-plasma catalysis. In this case, only long-lived species such as O_3 and NO_x produced in the plasma will travel to the catalyst and interact with reactants on the catalyst's surface. The lifetime of other reactive species in the plasma, for example the vibrationally excited molecules, is 1 to 100 ns under ambient condition, therefore being too short to interact with catalysts. As for the one-stage configuration, the catalyst is placed in the plasma volume, and the plasma is directly generated on/in the catalyst bed. The plasma is in contact with the catalyst. It is also called plasma–driven catalysis. In this case, the interactions between plasma and catalyst are very complex because the physio-chemical characteristics of plasma and catalyst are simultaneously changed by the presence of each other [33, 37]. This complex interaction is summarised in Figure 1.3. The one stage configuration is adopted as the experimental setup for this project and is further discussed in Chapter two.

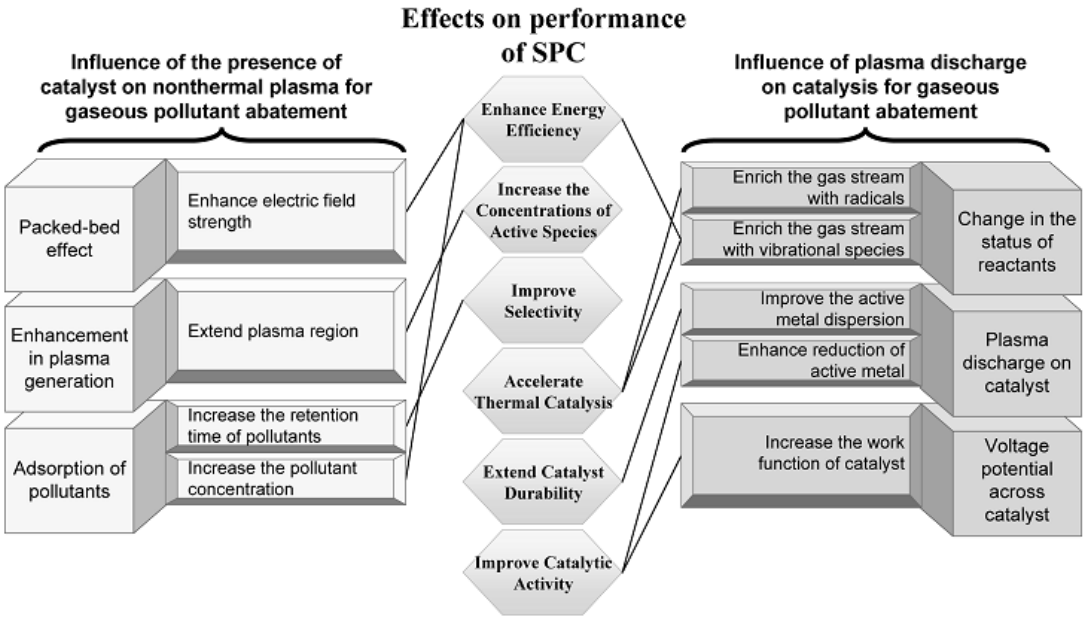

Figure 1.3 The interaction and synergy between plasma and catalyst. (Figure taken from [36])

When catalyst is directly placed in the plasma, surface discharge and short-lived radicals such as excited atoms and molecules, radicals, energised electrons and UV radiation are also involved in the reactions on the surface of the catalyst. The internal energies of these active species (1 to 10 eV) are usually higher than the activation energies of the reactant molecules. For comparison in thermal catalysis, when the gas species are adsorbed onto the catalyst surface, they are usually in the ground state. In the plasma, the internal energy of vibrationally excited species usually ranges from 0.1 to 1 eV, which is too low to initiate chemical reactions. However, a vibrational state can assist the adsorption of gas species into the catalysts' surface. The internal energy of rotationally excited species is 0.01 – 0.1 eV and is not usually involved in plasma catalytic reactions. Apparently, plasma activates catalysts and initiates reaction at low temperature, avoiding the need to heat the catalyst. While conventional thermal catalytic reaction would not normally occur at the same low temperature. The energy efficiency of the whole process is improved as a result. Additionally, plasma modifies the surface of the catalysts thus changing their catalytic properties. Plasma assists the reduction of supported metal species and improves the dispersion of metal particles. Electric charges accumulate on the surface of the catalyst during discharge, changing the polarity and hydrophobicity of the catalyst, affecting catalytic performance.

At the same time, due to the dielectric property of the catalyst, the distribution of electric field in the discharge gap is changed, and the electric field strength in the gas is enhanced. Consequently, this promotes the ionisation of working gas and might increase the mean electron energy. Intensified discharge occurs at the contact points between the catalyst pellets/beads. The increased number and energy of ions and free electrons improve electron impact reactions. Due to the dielectric property of the catalysts' surface, the plasma extends along the surface, increases the plasma area and volume. This subsequently increases the production of active species, and increases the chance for reactant molecules colliding with the active species, which improves the conversion of reactants. When gas molecules are adsorbed on the surface of the catalysts, the reactants are concentrated, and the retention time of reactants in the plasma increases, these factors further increase the conversion. Moreover, a properly selected catalyst brings alternative reaction pathways, improves the selectivity towards desired products and reduces the formation of by-products.

A synergistic effect between plasma and catalyst is also observed for some reactions where the performance of plasma-catalytic process is better than the sum of the individual steps (plasma alone or thermal catalysis) [31, 37-39]. However, the synergy of plasma-catalysis might only occur under fine-tuned conditions [24].

1.7. Conversion of CO_2 with H_2

As discussed, CO_2 is a major greenhouse gas and in order to mitigate global warming the CO_2 emission related to human activities needs to be brought under control. The direct use of CO_2 for the production of value-added fuels and chemicals after the CO_2 capture process, or even without capture, has been considered as a promising process to tackle the current global energy and environmental challenges [40]. Clearly, this process can also be considered as a key approach for chemical energy storage [41]. Due to the inert property of CO_2 molecules, thermal catalytic, plasma-driven and plasma-catalytic CO_2 hydrogenation have been investigated. Recently reported studies are summarised in Table 1.2.

Table 1.2 Summary of works on CO_2 hydrogenation.

H_2/CO_2 molar ratio	Flow rate (ml min^{-1})	Process	Reaction conditions	Catalyst	CO_2 conversion (%)	CH_4 selectivity (%)	CO selectivity (%)	Ref
1:1	50	Thermal	80% He, 260 °C	$Pd/La_2O_3/Al_2O_3$	8	23	76	[44]
4:1	250	DBD	260 °C, 17 W	Ni/Al_2O_3	85	97	2	[45]
4:1	20	RF impulse	2.4 Torr, 20 W	-	20	20	80	[46]
4:1	50	Thermal	350 °C	$Ni\text{-}CeO_2/Al_2O_3$	85	100	–	[47]
3.5:1	30	Thermal	350 °C	$Ce\text{-}Ni/Al_2O_3$	80	100	–	[48]
4:1	10	Thermal	400 °C	$Rh/K/Al_2O_3$	30	–	100	[49]
4:1	0.2	Thermal	400 °C	Ni/ZrO_2/clay	57	97	2	[50]
4:1	110	Thermal	9% N_2, 350 °C	$Ni\text{-}Co/SiO_2$	84	–	–	[51]
4:1	166.7	Thermal	350 °C	$Ru/CeO_2/Al_2O_3$	90	99.5	–	[52]
5:1	871.7	Thermal	500 °C	Ni/Al_2O_3	71	86	14	[53]
4:1	78.7	Thermal	250 °C	80% He, Ru/Al_2O_3	81	98	1	[54]
1:1	34.6	DBD	35 W	Mn/Al_2O_3	10.2	7.5	91	[24]

1.7.1. CO_2 Methanation

In the methanation reaction, CO_2 reacts with hydrogen to produce methane and water. This reaction was first discovered by Sabatier and Senderens in 1920. The CO produced during methanation is recognised as an important intermediate in the reaction pathways. Ni based catalysts are widely used in methanation process since the reaction highly endothermic.

$$CO_2 + 4\ H_2 \rightarrow CH_4 + 2\ H_2O,\ \Delta H° = -253.6\ kJ\ mol^{-1} \quad (7)$$

$$CO + 3\ H_2 \rightarrow CH_4 + H_2O,\ \Delta H° = -249.8\ kJ\ mol^{-1} \quad (8)$$

1.7.2. Reverse water-gas shift reaction

The reverse water-gas shift (RWGS) reaction converts CO_2 and H_2 to produce CO and H_2O. The reverse-reaction of this reaction is the water-gas shift reaction (WGS). Both reactions are used in industry to adjust the CO concentration in the output of steam reforming process, and to adjust the H_2/CO ratio in the feed gas of Fischer-Tropsch synthesis. CO is an important chemical feedstock for Fischer-Tropsch synthesis (FTS) to produce higher hydrocarbons such as liquefied petroleum gas (LPG), naphtha, gasoline and diesel; or for the synthesis of valorised products such as acetic acid, phosgene and formic acid [32, 42, 43].

$$CO_2 + H_2 \leftrightarrow CO + H_2O,\ \Delta H° = -3.8\ kJ\ mol^{-1} \quad (9)$$

1.7.3. CO_2 hydrogenation into higher hydrocarbons

The production of hydrocarbons from CO_2 hydrogenation is considered a modification of the Fischer–Tropsch synthesis, as it substitutes the CO in syngas with CO_2. The corresponding hydrogenation processes can be divided into two categories: methanol-mediated and non-methanol-mediated reactions. The former approach mainly produces light alkanes due to the catalytic hydrogenation of alkenes occurring in the hydrogenation processes. The latter approach is a two-step process involving RWGS and FTS reactions [35].

1.7.4. CO_2 hydrogenation into methanol

Methanol (methyl alcohol) can be naturally produced by the anaerobic metabolism of bacteria. It is called "wood alcohol" because it was once produced by the destructive distillation of wood. In modern industry, methanol can be directly produced from a catalytic process of CO_2 hydrogenation or CO hydrogenation. The manufactured methanol has been widely used as a solvent and feedstock for the chemical industry.

$$CO_2 + 3\ H_2 \rightarrow CH_3OH + H_2O, \qquad \Delta H° = -131.8\ kJ\ mol^{-1} \qquad (10)$$

$$CO + 2\ H_2 \rightarrow CH_3OH, \qquad \Delta H° = -128.0\ kJ\ mol^{-1} \qquad (11)$$

1.7.5. Plasma assisted CO_2 hydrogenation

Non-thermal plasma offers an attractive alternative to the thermal catalytic route for CO_2 conversion and utilization at low temperatures and atmospheric pressure [34, 37, 55-58]. In non-thermal plasma, highly energetic electrons collide with gas molecules to produce chemically reactive species including free radicals, excited atoms, ions and molecules [59]. Both high energy electrons and reactive species contribute to the initiation and propagation of a variety of physical and chemical reactions in low temperature plasma processes [60]. In non-thermal plasmas, the temperature of electrons and heavy particles (free radicals, atoms, molecules and ions) are significantly different. The overall gas kinetic temperature in plasma can be as low as room temperature, whilst the electrons are highly energetic and have a typical electron temperature of 1-10 eV, which can break most chemical bonds present in inert molecules (*e.g.* CO_2). The non-equilibrium characteristic of NTP could overcome the kinetic barriers in chemical reactions and enable highly endothermic reactions (*e.g.* RWGS, dry reforming of methane) to occur at a relatively low temperature. High reaction rate and fast attainment of steady state in a plasma system allow rapid start-up and shutdown of plasma processes compared to thermal processes, which significantly reduces the overall energy cost.

The combination of non-thermal plasma and catalysis, known as plasma-catalysis, thus can be regarded as an attractive and promising solution to convert CO_2 into higher value chemicals at low temperatures and atmospheric pressure [34, 38]. Plasma-catalysis has great potential to generate a synergistic effect, which can reduce the activation energy of the reaction, enhance the conversion of reactants and improve

selectivity and yield towards the desired products [33, 37]. These characteristics contribute in different ways to increasing the energy efficiency of the plasma process, as well as the reactivity and stability of the catalyst. Comparing with conventional thermal catalytic processes, plasma catalysis usually operates under less harsh conditions, thus extend the lifetime of the catalysts. In the past few years, significant efforts have been dedicated to understanding the plasma-assisted conversion of CO_2 into CO [24, 35, 61-65].

To achieve a CO_2-neutral CO_2 hydrogenation process, it is important that hydrogen used in the CO_2 hydrogenation should be sourced using renewable energy (*e.g.* from water electrolysis using solar power or wind power, or from bioenergy [66, 67]) as well as being cost-effective. In addition, it is key to lower the operating temperature of the CO_2 hydrogenation to minimise the energy consumption of the process [68]. However, due to the high chemical stability of CO_2, the CO_2 hydrogenation process is highly endothermic, which favours high reaction temperatures, making it difficult to achieve high CO_2 conversion at low temperatures. For example, it requires over 1000 K to achieve a CO_2 conversion of 50% in the RWGS reaction (H_2/CO_2 molar ratio = 1:1) at atmospheric pressure [69]. A wide range of catalysts have been designed and developed for lowering the kinetic barrier and operating temperature of this reaction. Cheng *et al.* investigated the reaction mechanisms of CO formation in the RWGS reaction over a Cu/γ-Al_2O_3 catalyst at 500 °C [70]. Tanaka *et al.* have reported that Cu-Mn oxide catalysts with different additives are active in the RWGS reaction [71]. Liu *et al.* have developed a computational model to compare the thermodynamic catalytic activities of transit metal complexes in the RWGS reaction. They found that Mn-based catalysts were the most promising catalysts in the RWGS reaction [72]. Plasma-catalysis has been regarded as an attractive and promising solution to convert CO_2 and renewable H_2 into higher value chemicals at low temperatures and atmospheric pressure.

However, very limited work has focused on plasma CO_2 hydrogenation for the production of CO and/or CH_4 at low temperatures, the comparison between plasma-driven hydrogenation against thermal catalytic process, or the performance of the same catalyst (for instance, silica or alumina supported Ni- or Co- catalysts) in both thermal-catalytic and plasma-catalytic hydrogenation processes. Jwa *et al.* have investigated the hydrogenation of CO_2 and CO over a Ni/Al_2O_3 catalyst in a dielectric barrier discharge (DBD) plasma at 200 °C–300 °C [45]. Sekine *et al.* have reported the effect of electric field on the RWGS reaction over a Pt/La-ZrO_2 catalyst at 130 ml min^{-1} total feed flow

rate and 600 ^{o}C [69]. Notably, Ni and Co have been extensively used as transitional metal catalysts for the conversion of CO_2, especially for the dry reforming of methane, due to their low cost and comparable catalytic activity to the noble catalysts [73]. SiO_2 and Al_2O_3 are also widely used as supports for catalysts in the CO_2 conversion reactions due to their economic prices, robust mechanical strength and decent thermal stability [74, 75].

Interestingly, in either direct CO_2 splitting or dry reforming processes based on NTP technology, the presence of dilution gas (*e.g.* He and Ar) has shown the positive effect of enhancing the conversion of reactants [12, 76]. However, this process is only advantageous when the injected dilution gas can be recycled to form a chemical looping process due to the cost of these gases. It is also interesting to investigate how the presence of these gases affects the characteristics of the plasma and consequently changes the reaction performance. N_2 has been also used as dilution gas, but cyanide may be produced in the plasma. Yet again, very limited work has been focused on the investigation of how the dilution gases (*e.g.* Ar) affect the plasma-catalytic chemical reactions, especially CO_2 hydrogenation for the synthesis of fuels and chemicals such as the cogeneration of CO and CH_4.

1.8. Conversion of CO_2 with CH_4

Methane is the simplest but most abundant hydrocarbon in the atmosphere. It is one of the major GHGs with a GWP of 21, and is emitted from various sources including natural fermentation of biomass in paddy fields and swamps, flaring in oil fields and refineries, venting in mines and landfill sites and from certain processes like waste water treatment and sludge treatment.

Methane is extensively consumed in the energy sector, in the form of natural gas, shale gas, biogas and landfill gas. It is also used to produce synthetic chemicals such as methanol, ammonia and liquid fuels. In this case, methane is firstly converted into synthesis gas (syngas) via established industrial processes (for example steam methane reforming). The produced syngas is then used as feedstock for Fischer-Tropsch synthesis which is also a well-established industrial process. However, methane is a very stable molecule, the C-H bond has an average bond enthalpy of 413 kJ mol^{-1}. High reaction temperatures are usually necessary for the effective conversion of CH_4.

1.8.1. Natural gas and biogas

Natural gas is formed from plants that were buried beneath the earth over millions of years ago and mostly consists of methane. It is one of the most common fossil fuels, abundantly distributed around the world, especially in Mid-East countries and Russia. However due to the high GWP of methane, growing concerns are attracted for sustainable utilisation of methane.

Britain discovered natural gas in the North Sea in 1965. Soon after the national fuel network was upgraded for distributing natural gas to homes and this was completed in 1976. Since then, natural gas has been used for cooking and central heating systems, and for gas-fired power plants in UK.

Biogas mainly consists of methane and carbon dioxide, and originally it was produced from the anaerobic decomposition of organic wastes. The composition of biogas varies according to the biomass source. It generally consists of 50 -75% methane, 25 -50% carbon dioxide, 0 -10% nitrogen, 0 -1% hydrogen, 0 -1% hydrogen sulphide and small amount of oxygen, water vapour, siloxanes, ammonia and halogenated compounds [77].

Biogas is a renewable resource because nearly all the natural organic matter can be used as feedstock for biogas production. This is very attractive due to the simultaneously reduction of waste and production of valorised product (methane). The produced methane can be collected and transported to factories. Constituents that can be used for making biogas include sludge from wastewater treatment, cattle manure from big farms and remains of food ingredients used in food processing industries. These wastes mostly consist of organic compounds and water. Traditional disposal processes, for example landfill, occupy large land areas and incurs considerable financial cost. Anaerobic digestion tanks are being tested for the treatment of these wastes, this technique is considered viable, bio-safe, eco-friendly and economic. Interestingly, landfill is also a normal technology for the disposal of municipal waste and solid waste. Large amounts of biogas are produced in landfill sites across the UK, but it is difficult to exploit. The biogas is either vented or flared because of unstable gas pressure and complex gas composition. In 2013, up to 101 kilo-tonnes of methane was flared at operational sites [78]. Interestingly, the renewable characteristic of plants and algae, in-land energy crop farms, and off-shore algae farms are being evaluated as a possible solution for large-scale biogas production. However they require a large area

of land or ocean surface and might consequently compete with traditional food production such as food crops and fisheries.

A very straight forward application for biogas is combustion as a fuel. Although the combustion of biogas is actually the combustion of CH_4, and this process emits CO_2, it is still favourable for CO_2 emission-control because the carbon content in biogas is originated from the photosynthesis of plants, in which process the plants absorbed CO_2 from atmosphere. It is the same amount of carbon that returns to the atmosphere through the combustion of plant-derived CH_4, and no additional CO_2 is released into the atmosphere. This results in a CO_2-neutral life-cycle and would help to slow the pace of global warming. However, the high CO_2 content in the biogas decreases the quality and heating value of the fuel gas; N_2 and H_2S might be contained in the biogas thus resulting in the need for pre-treatment. In some circumstances, upgradation of biogas to increase the CH_4 concentration and removal of toxic compounds are necessary before the biogas can be properly combusted. The high cost of this pre-treatment is a big challenge for the commercial application of biogas. Therefore the conversion of CO_2 and CH_4 into more valuable products has been considered as an alternate process to mitigate the current environmental and energy issues [73, 79, 80].

1.8.2. Methane reforming

There are established industrial processes for methane reforming including steam reforming (SMR), partial oxidation (POM), mixed reforming and dry reforming (DRM). The reforming processes involving CO_2 are related to this project. Due to the highly endothermic nature of the reactions, high temperatures and catalysts are usually required for the operation of these processes. High energy consumption increases the cost of methane reforming processes and therefore many researches are focussed on developing alternative technologies; including methane reforming at a lower temperature while maintaining good methane conversion.

1.8.2.1. Autothermal reforming

Autothermal reforming (ATR) is a common process for the production of syngas, in which CH_4 reacts with an O_2/CO_2 mixture or an O_2/H_2O mixture gas. It can be regarded as a combination of POM, SMR and DRM. The total reaction is mildly exothermic due to the reaction between oxygen and methane. The CH_4/H_2O and

CH_4/CO_2 molar ratios in the feed gas are adjusted according to the target H_2/CO molar ratio in the resulting syngas. For example when ATR uses CO_2 (no H_2O), the H_2/CO ratio is 1. When ATR uses steam (no CO_2), the H_2/CO ratio is 2.5,

$$2\ CH_4 + O_2 + CO_2 \rightarrow 3\ H_2 + 3\ CO + H_2O, \quad \Delta H° = -32.513\ kJ\ mol^{-1} \qquad (12)$$

$$4\ CH_4 + O_2 + 2\ H_2O \rightarrow 10\ H_2 + 4\ CO, \quad \Delta H° = 425.8\ kJ\ mol^{-1} \qquad (13)$$

This is advantageous because syngas with adjustable H_2/CO can be used for the further synthesis of different products. For instance, the syngas with a H_2/CO ratio of 1 is suitable for the synthesis of DME, while the syngas with a H_2/CO ratio of 2.5 is suitable for FT synthesis of gasoline.

1.8.2.2. Tri-reforming

Tri-reforming is similar to auto-thermal reforming and it is a three-step reaction process designed for the treatment of flue gas from power plants [81]. The flue gas from natural gas–fired power plants typically consists of 8% –10% CO_2, 18% –20% H_2O, 2% –3% O_2 and 67% –72% N_2. For comparison, that from coal-fired boilers typically consists of 12% –14% CO_2, 8% –10% H_2O, 3% –5% O_2 and 72% –77% N_2. With the addition of natural gas, a combination of dry reforming, steam reforming and oxidation of methane would occur simultaneously, as listed below.

$$CH_4 + CO_2 \rightarrow 2\ H_2 + 2\ CO, \quad \Delta H° = 245.9\ kJ\ mol^{-1} \qquad (14)$$

$$CH_4 + H_2O \rightarrow 3\ H_2 + CO, \quad \Delta H° = 204.7\ kJ\ mol^{-1} \qquad (15)$$

$$2\ CH_4 + O_2 \rightarrow 4\ H_2 + 2\ CO, \quad \Delta H° = -73.7\ kJ\ mol^{-1} \qquad (16)$$

$$CH_4 + 2O_2 \rightarrow 2\ H_2O + CO_2, \quad \Delta H° = -892.9\ kJ\ mol^{-1} \qquad (17)$$

1.8.2.3. Dry reforming of methane

Dry reforming of methane (DRM) is an attractive process because it consumes two major GHGs (CO_2 and CH_4) to produce syngas [82, 83]. DRM process generates syngas with a relative low H_2/CO ratio close to unity, which is suitable for the synthesis of value-added oxygenates. Low-grade natural gas and biogas consists >55% CH_4 and <45% CO_2, and therefore are suitable feedstock for DRM process. Landfill gas and

flared shale gas can be also used as feedstock, which maximises the energy utilisation and minimises the negative environmental impact. The produced syngas can be directly used as a clean energy source, or is highly suitable for the FT synthesis of fuels and value added chemicals such as hydrocarbons, ammonia, or oxidised compounds [84, 85]. However DRM is highly endothermic and the reaction requires very high reaction temperatures (>600 ºC) to maintain reasonable conversions of reactants and yields of syngas. The high energy consumption makes the DRM process for CO_2 reduction economically unfeasible.

$$CH_4 + CO_2 \rightarrow 2\ CO + 2\ H_2, \quad \Delta H° = 245.9\ kJ\ mol^{-1} \qquad (18)$$

Catalysts are usually necessary for the DRM process. Over the past decades, great efforts have been devoted to investigate the reforming of biogas using thermal catalytic [86, 87], photo-catalytic [88] and electro-chemical methods [89-91]. Significant works have been done to the design and development of novel catalysts to enhance the conversion of CH_4 and CO_2, and improve the energy efficiency [80, 92, 93]. Noble metals such as Ru, Rh, Pd, Ir and Pt exhibit good catalytic performance. However, the cost of using expensive noble metal catalysts may be prohibitive. Consequently, transition metals such as Fe, Co, Ni, Mn and Cu are investigated, Ni is extensively used as a substitute for noble metals in DRM catalysts, because of their relatively low prices. An oxide with large surface area, good mechanical strength and good thermal stability, such as SiO_2, Al_2O_3, MgO, CeO_2, ZrO_2 and La_2O_3 are used as catalyst supports. Although the support is usually inert for chemical reactions, the basicity of the support is important for the activation and conversion of CO_2 during DRM [94, 95]. The effect of basicity of support on the conversion of CH_4 is not yet clear. In addition, bimetallic catalysts and promoted catalysts are investigated to increase the reactivity and lifetime of catalysts. A challenge for catalytic DRM is the formation of carbon deposition on the catalyst surface, causing rapid deactivation of catalysts, especially for non-noble metal catalysts [37, 96]. Novel processes such as plasma-driven or plasma-catalytic DRM are studied to improve the reaction performance, in terms of conversion of reactants, selectivity of favoured products, energy efficiency and carbon resistance. Table 1.3 and Table 1.4 summarise the recently reported works on the dry reforming of methane.

Table 1.3 Summary of works on the thermal DRM process. (Sort by year)

CH_4/CO_2 molar ratio	Flow rate (ml min^{-1})	Process	Reaction conditions	Catalyst	Conversion of CH_4 (%)	Conversion of CO_2 (%)	Selectivity of H_2 (%)	Selectivity of CO (%)	Energy efficiency (mmol kJ^{-1})	Fuel production efficiency (%)	Ref
1:1	–	Thermal	33.3% N_2, 700 °C	Ni/Al_2O_3	81	81	–	–	–	–	[137]
1:1	91.7	Thermal	33.3% N_2, 750 °C	$Ni\text{-}Co/AlMgO_x$	84	87	–	–	–	–	[138]
1:1	15000	Thermal	47.4% N_2, 700 °C	$Ni/TiO_2/Al_2O_3$	–	–	85	100	–	–	[139]
2:3	36667	Thermal	77.3% N_2, 9.6 kW	Ni/Al_2O_3	88.3	76.1	72.5	89.1	–	–	[140]
1:1	40	Thermal	50% Ar, 800 °C	Ni/Al_2O_3	84	89	–	–	–	–	[120]
1:1	–	Thermal	700 °C	$Co\text{-}Ce/ZrO_2$	50.8	64.1	46.5	99	–	–	[126]
1:1	–	Thermal	550 °C	$Ni\text{-}K/CeO_2$	3.5	23	–	–	–	–	[141]
1:1	–	Thermal	60% He, 700 °C	$Ni\text{-}Pt/Al_2O_3$	69	76	–	–	–	–	[142]
3:2	–	Thermal	850 °C	Reformax 250	73	85	28.8	2	–	–	[143]
1:3.5	–	Thermal	850 °C	Ni/MgO	99	64	49.7	56.4	–	–	[144]

Table 1.4 Summary of reported works on the plasma-assisted dry reforming of methane.

CH_4/CO_2 molar ratio	Flow rate (ml min^{-1})	Process	Reaction conditions	Catalyst	Conversion of CH_4 (%)	Conversion of CO_2 (%)	Selectivity of H_2 (%)	Selectivity of CO (%)	Energy efficiency (mmol kJ^{-1})	Fuel production efficiency (%)	Ref
1:1	100	RF	90% Ar, 20 Torr, 50 W	–	–	48	45	35	–	–	[145]
2:1	150	DBD	500 W, 150 °C	Zeolite	51.6	41.7	20.2	31.7	0.108	0.37	[146]
1:1	200	DBD	500 W, 150 °C	Zeolite NaY	66.6	39.9	19.3	21.4	0.158	0.32	[147]
1:1	200	DBD	500 W, 150 °C	Zeolite HY	62	37	34.4	41.8	0.147	0.60	[119]
2:1	60	DBD	100 W	–	64	43	49.5	32.2	0.254	0.55	[113]
1:2.3	13.3	Packed DBD	22.5 W	PZT ceramic	33	–	–	–	0.087	5.4	[148]
1:1	50	Corona	4% O_2	Pt/KL[a]	37	21	–	–	–	–	[149]
1:2	60	Corona	30 W	Ni/Al_2O_3	59.2	50.9	73.2	91.5	0.799	2.2	[150]
1:1	12700	GA	544 W, 177 °C	–	41	30	38.9	47.3	6.166	0.81	[151]
2:3	16660	Jet	50% N_2, 770 W	Ni/Al_2O_3	51	36	90	91	3.381	1.9	[152]
3:2	22.5	DBD	16 W, 500 °C	$LaNiO_3$	19	15	35	26	0.182	0.44	[112]
1:1	60	Glow	23 W	–	61	50	77	65	1.077	1.3	[153]
2:3	2200	Glow	69.85 W	–	61	49.9	89.3	72.6	12.73	1.7	[116]
1:1	60	DBD	50% Ar, 75 W	$Ni-Cu/Al_2O_3$	69	75	56	75	0.214	1.3	[114]
2:1	16.67	DBD	18 W, 240 °C	Ag/Al_2O_3	52	29	55.2	72.9	0.305	0.89	[118]
14:1	80	DBD	81.3% He, 53 W, 400 °C	La_2O_3/Al_2O_3	21.4	56.1	19.5	24.8	0.050	0.35	[122]

CH_4/CO_2 molar ratio	Flow rate (ml min^{-1})	Process	Reaction conditions	Catalyst	Conversion of CH_4 (%)	Conversion of CO_2 (%)	Selectivity of H_2 (%)	Selectivity of CO (%)	Energy efficiency (mmol kJ^{-1})	Fuel production efficiency (%)	Ref
3:2	150	Spark	–	–	72	63	81	68	–	–	[105]
1:1	50	DBD	35 W	Quartz wool	27	11	23	28	0.202	0.38	[123]
3:2	1400	RGA	28.6% O_2	–	83	35	49	92	–	–	[154]
3:2	1360	RGA	26.5% O_2	–	69	28	52	92	–	–	[101]
1:1	150	RGA	50 W	–	74	63	79	81	1.529	1.5	[155]
1:1	6000	RGA	175 W	–	48	54	100	100	13.01	2.1	[156]
1:1	4000	GA	190 W	NiO/Al_2O_3	15	18	52	48	2.585	1.1	[157]
1:1	600	DBD	–	Zeolite	49	52	55	50	–	–	[158]
10:7	1360	Spark-shade	26.1% O_2	–	77	35	55	94	–	–	[159]
3:2	50	DBD	160 W	$LaNiO_3/SiO_2$	67	63	75	78	0.152	1.2	[160]
3:2	50	Spark	20 W	–	72	62	58	56	1.265	0.95	[161]
2:1	–	DBD	70 W	Ni/Al_2O_3	60	77	–	17	–	–	[162]
1:1	162000	Microwave	38.3% H_2O, 4.5 kW	–	7	–	–	–	–	–	[163]
1.29	16000	GA	720 W	NiO/Al_2O_3	48.6	56.5	36	51.6	8.606	0.92	[164]
3:2	15000	RGA	32.1% O_2, 279 W	–	76	23	56	92	14.88	1.0	[100]
1:1	–	Pulse	8.5 kJ/L	–	45	36	62	61	–	–	[23]
3:2	4000	RGA	26.5% O_2, 59.5 W, 779 °C	$Ni/CeO_2/Al_2O_3$	82	19	81	99	20.88	1.2	[99]

a: KL is a type of molecular sieve.

DRM (or biogas reforming) has been investigated at ambient temperatures [97-103] or elevated temperatures [104-108], with or without a catalyst. The studies were also using different plasma systems including dielectric barrier discharge (DBD) [109-114], gliding arc [104], corona discharge [115] and glow discharge [116]. However, the energy efficiency of the plasma process and selectivity towards target products (*e.g.* syngas) are not satisfied in the absence of a catalyst. In addition to the production of syngas, noticeable amounts of C_2-C_4 and oxygenates are often produced [117-119]. For plasma-catalytic dry reforming process, those catalysts that have successfully demonstrated their activities in thermal catalytic dry reforming are generally used as a starting point to be combined with plasmas, including Ni/Al_2O_3 [37, 96, 111, 114, 120], Co/Al_2O_3 [31, 86, 98, 121], Cu/Al_2O_3 [114], $Ni–Cu/Al_2O_3$ [114], Pd/Al_2O_3 [118], Ag/Al_2O_3 [118], La_2O_3/Al_2O_3 [122] and zeolite [119, 123]. Interestingly, the Ni/Al_2O_3 catalyst has been widely used for the conventional thermal catalytic biogas reforming process, and metal species such as K, Na, Ca, Mg, Y, La and Ce are extensively used as a modifier to promote the catalysts [3, 4, 94, 95, 124-130]. K, Mg and Ce promoters, for example, have been reported to significantly reduce coke deposition on the surface of spent catalysts, and consequently improve the stability of the catalytic performance in thermal catalytic reforming processes [94, 95, 124-126, 131]. However, the properties and reforming performance of the promoted catalyst under plasma-catalytic conditions are not yet clear; while the effect of promoters on the plasma-catalytic biogas reforming at low temperatures is seldom investigated and reported.

Up until now, the exploration of low cost and active catalysts is still not fully satisfied for the plasma-catalytic reforming reaction. This is partly due to the lack of the necessary knowledge of catalyst design for the control of relevant catalytic properties in plasma-catalysis systems. There are very limited works that evaluate the difference between metal catalysts, while the plasma-catalytic dry reforming over different Al_2O_3 supported non-noble metal catalysts (*i.e.* Ni, Co, Cu and Mn) has not been investigated and reported before. In addition, evaluating the effect of different metal phases on the performance of plasma-catalytic dry reforming process in terms of the conversion of reactants, the selectivity and yield of target products, as well as the energy efficiency of the plasma process, would provide a better understanding of the synergistic effects resulted from the combination of plasma with catalysts [31, 37, 132]. Moreover, the effect of temperature on plasma-catalytic DRM has seldom been reported, despite the fact that thermal catalytic reforming processes have previously

demonstrated significant temperature-dependence of catalytic performance. There are also limited works comparing catalyst preparation methods for plasma-catalytic reforming, such as the synthesis (impregnation, co-deposition, sol-gel, *etc.*), calcination (thermal or plasma-driven) and reduction of catalysts, although the effect of preparation method has been widely investigated in thermal catalytic process [133, 134].

1.8.3. Carbon deposition

As mentioned previously, supported Ni/Al_2O_3 catalyst has been reported to exhibit excellent catalytic activity in DRM. Compared with noble metals, the transitional metal Ni is more cost–effective and more easily available, while alumina support is widely used for its good mechanical strength and low cost. However Ni/Al_2O_3 quickly deactivates during reforming due to coke deposition and metal sintering [95, 135, 136]. Carbon deposition is a great challenge for catalytic reforming of methane, including steam reforming (SMR) and DRM. As the carbon gradually forms and accumulates on the surface of the catalyst during reforming processes, the metallic active sites of the catalyst are eventually covered by the carbon and the catalyst is no longer active during reactions. The production of carbon is attributed to direct methane decomposition and the Boudouard reaction (disproportionation of carbon monoxide), as shown by the following equations:

$$CH_4 \rightarrow C + 2\,H_2, \qquad \Delta H° = 73.8 \text{ kJ mol}^{-1} \qquad (19)$$

$$2\,CO \rightarrow C + CO_2, \qquad \Delta H° = -172.1 \text{ kJ mol}^{-1} \qquad (20)$$

Industrial SMR and DRM processes are usually operated at elevated temperature and pressure, as this enhances the reaction rate, increases the gas conversion capacity and reduces the size of reactor. However, high temperature and pressure also favours carbon production and deposition. The acidic characteristic of Al_2O_3 supports enhance carbon generation and deposition, whilst γ–Al_2O_3 withstands phase change at high temperatures. All of these factors contribute to the deactivation of the catalyst [165].

In industrial SMR processes, excess steam is added into the reactor partially because water reduces carbon production, although it increases the H_2/CO molar ratio in the product. As for DRM process, the CH_4/CO_2 molar ratio is also decreased to reduce the carbon deposition, at the expense of smaller H_2/CO molar ratio. The carbon

deposition in DRM is more pronounced than that in SMR or partial oxidation of methane (POM), due to the low O/C atomic ratio in the feed gas. The Calcor process, for instance, introduces excess CO_2 for the DRM reaction over a Ni based catalyst to produce CO rich syngas while minimising carbon production. This can be also used for producing high purity CO.

To mitigate carbon deposition, it is also important to upgrade catalysts for reduced carbon deposition and improved carbon resistance. Many solutions have been examined to improve the thermal stability and coke resistance of the Ni/Al_2O_3 catalyst, including adjusting the physio–chemical structure of the catalysts [166, 167], optimising preparation methods [137, 168, 169], synthesis of bi–metal catalysts [94, 170, 171], adding promoters into the catalysts [95, 126, 172, 173], using plasma-catalysis [98, 118, 174], studying and exploiting the synergistic effect between active species or between plasma and heating [37, 175], and changing the composition of feed gas by adding N_2 [109], O_2 [176], or noble gases [129, 176, 177]. It can be concluded that the activity and stability of the catalyst can be adjusted by the addition of promoters, mainly using alkaline or alkaline earth metals and two rare earth elements (Ce and La). These strengthen the textile structure and thermal stability of the support, improving the dispersion of metal species and catalytic activity of the catalyst, and so diminishing sintering and accumulation of deposited carbon [124, 125]. Ballarini *et al.* reported that the acidity of the alumina support was suppressed by adding Na and K dopant, facilitating the dissociation of CO_2 and reducing carbon deposition on the surface. K–doped catalyst showed a higher conversion of CO_2 and selectivity for CH_4. Under the same conditions, Mg helped stabilise the form, maintain the surface area of γ–Al_2O_3, and aid the dispersion of Pt particles [176]. Sengupta *et al.* modified Al_2O_3 supported Ni and Ni–Co catalysts with CaO or MgO, and reported the resulting effects on the reducibility, amount of H_2 and CO_2 adsorbed, and the property of metal crystallite. Strong interactions between MgO and Ni, Co species changed the redox status of the catalyst and showed an adverse effect on the conversion and H_2/CO molar ratio [94]. Debek *et al.* claimed that the addition of Ce into catalyst increased the reducibility of nickel species and the CO_2 adsorption capacity, consequently improving the conversion of the reagents [129]. Interestingly, the loading of promoter has a significant effect on the performance of catalytic biogas reforming [125, 131, 172, 173]. However, limited works on plasma-catalytic DRM over promoted catalysts have been reported.

Another special solution for mitigating coke deposition is the sulphur-passivated reforming (SPARG). The SPARG process mildly poisons and deactivates the catalyst by addition of H_2S into the feed gas. With carefully calculated amount of addition, the sulphur that adsorbed on the active metal sites blocks the nucleation of carbon on the surface of the catalyst, while the catalyst remains active for the effective conversion of methane. This process is mainly used in SMR and petrol industry.

1.9. Thermodynamic equilibrium of CO_2 conversions

The equilibrium composition in this section was calculated using HSC chemistry software. Figure 1.4 shows the thermodynamic equilibrium of CO_2 hydrogenation over a temperature range of 27 °C – 1600 °C. The equilibrium conversion of CO_2 is dependent on the H_2/CO_2 molar ratio in the feed gas. When the H_2/CO_2 molar ratio is 4, the equilibrium conversion of CO_2 at 0 °C is 100%. The equilibrium product at low temperatures consists mostly of CH_4 and water. At a temperature lower than 300 °C, almost all the CO_2 would be converted to CH_4 under equilibrium. However as the temperature increases, the equilibrium molar ratio of CH_4 in the product decreases rapidly, while that of CO increases. At a temperature higher than 700 °C, nearly all the CO_2 would be converted to CO under equilibrium status, suggesting that the selectivity of product in the CO_2 hydrogenation process is dependent on the temperature.

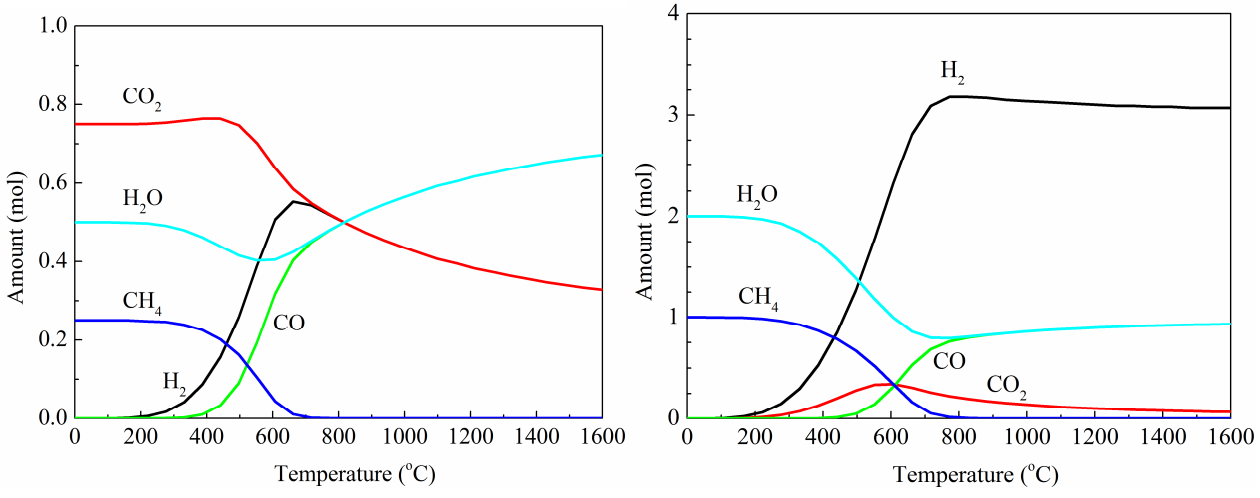

Figure 1.4 Thermodynamic equilibrium of CO_2 hydrogenation with H_2. (a) H_2/CO_2 molar ratio is 1: 1; (b) H_2/CO_2 molar ratio is 4: 1.

Figure 1.5 shows the thermodynamic equilibrium of CO_2 reforming with CH_4 with a CH_4/CO_2 molar ratio of 1: 1 and 3: 2. The CO_2 and CH_4 reactants are effectively converted only at elevated temperatures (*e.g.* >600 °C). At a temperature higher than 1000 °C, CO_2 would be completely converted. Syngas is the dominant product of reforming process, regardless of temperature and CH_4/CO_2 ratio.

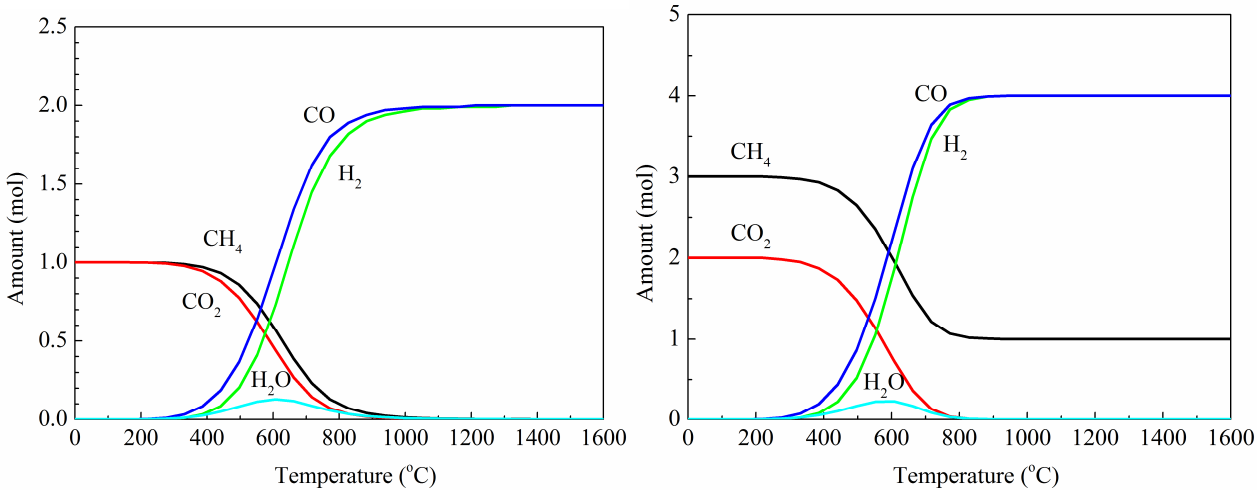

Figure 1.5 Thermodynamic equilibrium of CH_4 reforming with CO_2. (a) With a CH_4/CO_2 molar ratio of 1: 1; (b) CH_4/CO_2 molar ratio is 3: 2.

1.10. Methodology and novelty of this project

Figure 1.6 briefs the research methodology of this project. Since H_2 and CH_4 are the most common hydrogen-sources for CO_2 conversion and utilisation, this project covers two major research topics: plasma-catalytic CO_2 hydrogenation and plasma-catalytic biogas reforming. Each research starts with screening of catalyst. By choosing the catalysts that are effective in thermal catalysis, this stage investigates and compares the performance of these catalysts under plasma-catalytic conditions. After the best catalysts were determined through the screening. Systematic studies on CO_2 hydrogenation and biogas reforming were carried out using the best catalysts. In consideration of the state-of-the-art of plasma-assisted CO_2 hydrogenation and biogas reforming with or without using catalyst, the effect of Argon addition, temperature and plasma/heating power on CO_2 hydrogenation were evaluated; while the effect of promoters, temperature, preparation method and loading of promoter on biogas reforming were examined. The plasma-catalytic synergy was quantified and evaluated.

Finally, an optimised solution for plasma-catalytic CO_2 hydrogenation and biogas reforming under ambient conditions was summarised.

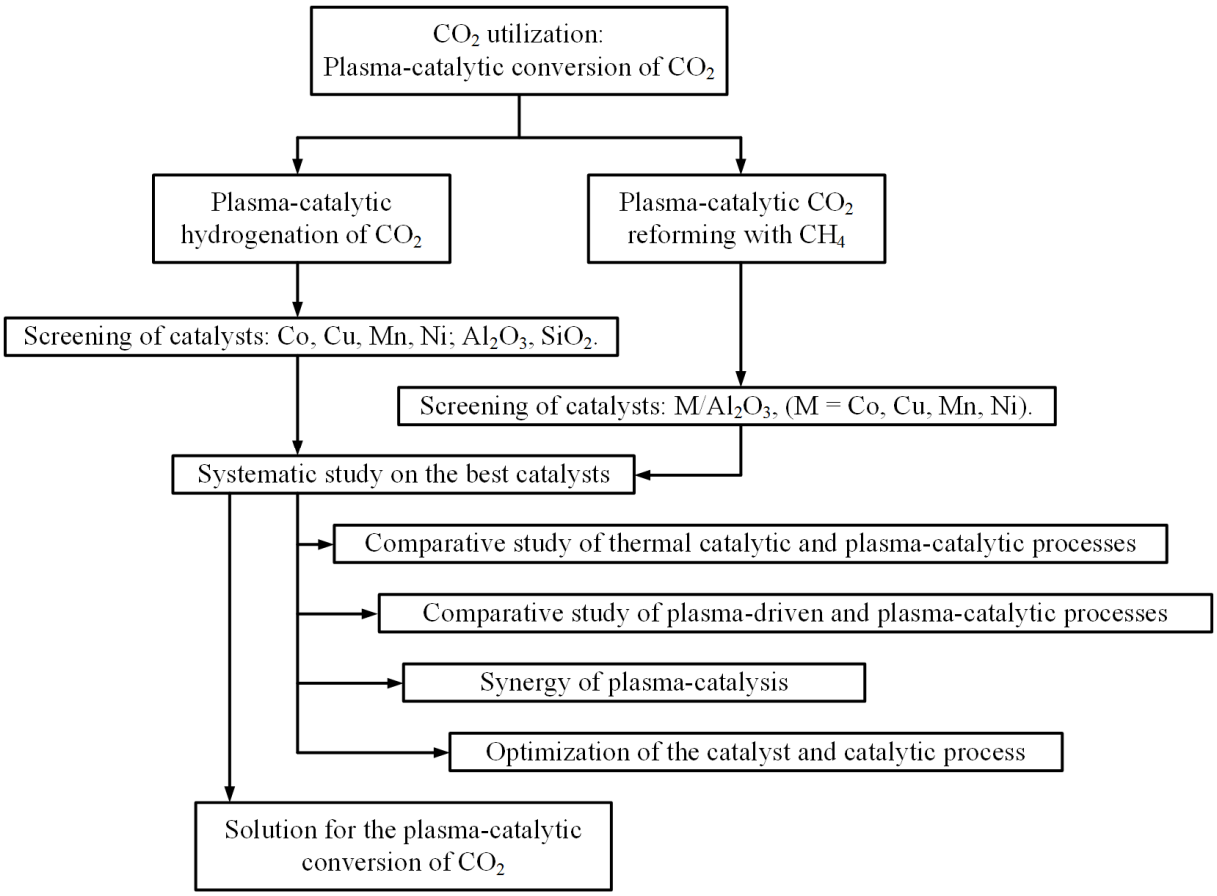

Figure 1.6 Methodology of the project.

The novelty of this project can be summarised:

CO_2 hydrogenation and biogas reforming have been successfully initiated under ambient conditions.

The plasma-catalytic synergy has been quantified.

As for CO_2 hydrogenation, novel catalysts such as Mn/Al_2O_3, $Cu\text{-}Mn/Al_2O_3$, Ni/SiO_2 and Co/SiO_2 have been investigated and compared.

The individual contribution of heating and plasma power on CO_2 hydrogenation has been studied.

As for plasma-catalytic biogas reforming, new catalysts such as Mn/Al_2O_3, Cu/Al_2O_3, $Ni\text{-}X/Al_2O_3$ (X = K, Mg and Ce) have been compared with Ni/Al_2O_3.

The carbon deposition during plasma-catalytic biogas reforming using promoted catalysts has been investigated.

Chapter 2. Experimental setup

2.1. Dielectric barrier discharge reactor

In this project, the plasma-catalytic conversion of CO_2 has been carried out in a coaxial packed-bed DBD reactor. In the reactor, the gap between dielectric layer and inner electrode was filled with packing materials such as a granular catalyst, quartz wool or γ–Al_2O_3 beads. Comparing with DBD reactors without packing, plasma can be initiated under relatively low applied-voltages and over a larger discharge gap due to the distorted and enhanced electric field in the gap. Discharges at stable power and at atmospheric pressure were consequently obtained.

2.1.1. Experimental setup for hydrogenation of CO_2

Figure 2.1 shows the configuration of the packed DBD reactor. The catalyst was packed and sandwiched by quartz wool or γ–Al_2O_3 beads in the centre of the reactor.

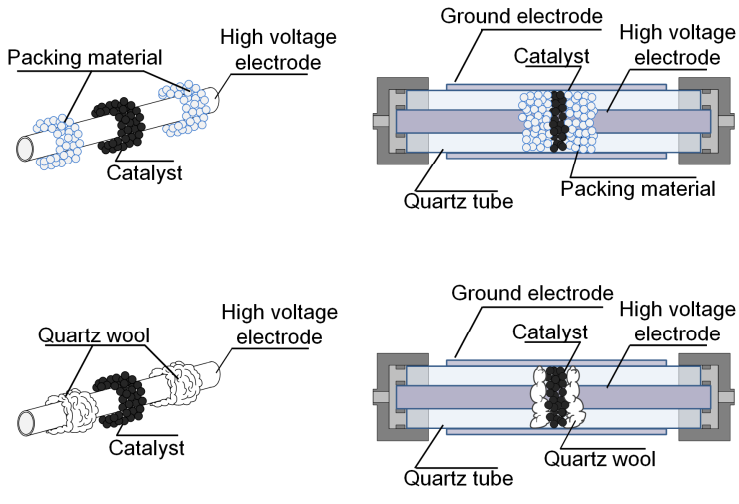

Figure 2.1 Schematic of catalyst and packing materials in the DBD reactor.

Figure 2.2 shows an example experimental setup for plasma-catalytic CO_2 hydrogenation. For the DBD reactor in Chapter 3, the wall thickness of the quartz tube

was 1 mm. The diameter of the inner electrode was 14 mm and the gap between dielectric layer and inner electrode was 2.5 mm. A stainless steel mesh (ground electrode) was wrapped around the outside of a quartz tube with an outer diameter of 21 mm. A stainless steel rod was placed in the centre of the quartz tube and used as a high-voltage electrode. The discharge length was 100 mm. The outer mesh electrode was grounded *via* an external capacitor C_{ext}. The DBD reactor was connected to a high voltage AC power supply with a maximum peak voltage of 10 kV and a frequency of 8.7 kHz. The frequency was chosen according to the resonance frequency of the plasma system. By changing the setting of the power supply, and replacing the quartz tube and inner electrode, a variation of this DBD reactor has been used in Chapter 4. In the first section of Chapter 4, the wall thickness of quartz tube was 2.5 mm. The diameter of the inner electrode was 13 mm and the gap between dielectric layer and inner electrode was 1.5 mm. The frequency of power supply was 9.2 kHz. Again, the frequency was chosen according to the resonance frequency of the plasma system. In the section 2 and section 3 of Chapter 4, the dimension of the DBD reactor was exactly the same as that in section 1, while the frequency of power supply was 22 kHz. A summary of experimental setups in this project can be found in the following section (Table 2.1).

The applied voltage was measured by a high-voltage probe (Testec, HVP-15HF), whereas the current was recorded by a current monitor (Bergoz CT-E0.5). The voltage across the external capacitor C_{ext} (0.47 μF) was also measured. All the electrical signals were sampled by a four-channel digital oscilloscope (Tektronix MDO3024). The *Q*-*U* Lissajous method was used to calculate the discharge power (*P*) of the plasma reactor [64, 96]. A homemade online power measurement system was used to monitor and control the discharge power in real time.

The DBD reactor was placed in a tube furnace, which enabled the CO_2 hydrogenation reaction to be investigated under three different conditions: plasma alone, thermal catalysis and plasma-catalysis. Under plasma alone conditions, no catalyst or packing material (Al_2O_3 bead or quartz wool) was placed in the reactor and the reaction was only driven by the plasma. In thermal catalytic reaction, the catalyst and packing material were packed into the middle of the reactor and heated in the tube furnace without plasma. In the plasma-catalytic process, the catalyst and packing material were placed in the DBD plasma with interactions between the plasma and catalyst. When the temperature was adjusted, the input power for DBD plasma was kept the same.

The gas composition was analysed by a two-channel gas chromatograph (Shimadzu GC-2014) equipped with a flame ionisation detector (FID) and a thermal conductivity detector (TCD). For each measurement, three samples of gas products were taken and analysed when the reaction reached a steady state. The steady state was judged by the reproducibility of the measurements.

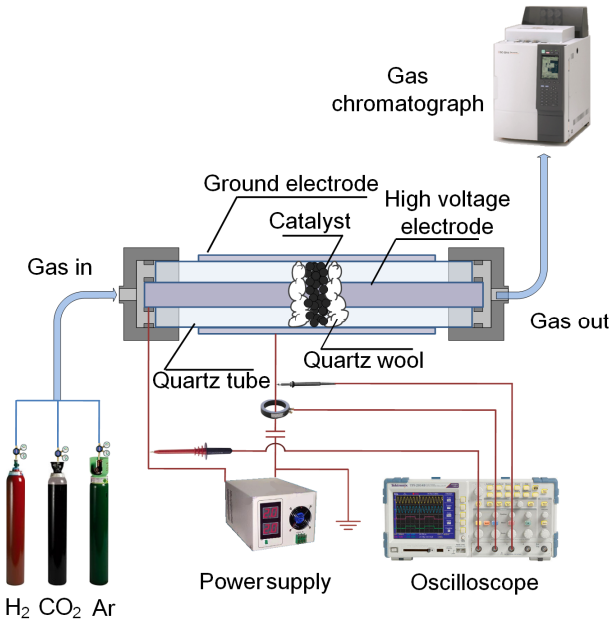

Figure 2.2 Schematic diagram of experimental setup for CO_2 hydrogenation at elevated temperatures.

2.1.2. Experimental setup for dry reforming of methane

Figure 2.3 shows the two types of DBD reactors used for the plasma-catalytic DRM. The reactor shown in Figure 2.3(a) was used in the first section of Chapter 5. In this case, a stainless steel mesh (ground electrode) was wrapped around the outside of a quartz tube. The tube has an outer diameter of 22 mm and wall thickness of 1.5 mm, while a stainless steel rod with an outer diameter of 14 mm was placed in the centre of the quartz tube and used as a high voltage electrode. The length of the discharge region was 90 mm with a discharge gap of 2.5 mm. The DBD reactor was supplied by a high voltage AC power supply with a peak-to-peak voltage of 10 kV and a frequency of 50 Hz. For comparison, the reactor used in Chapter 6, and the section 2 of Chapter 5 was very similar to that illustrated in Figure 2.2, except that the frequency of power supply was 22 kHz, and the feed gas was CH_4 and CO_2 (Figure 2.3(b)).

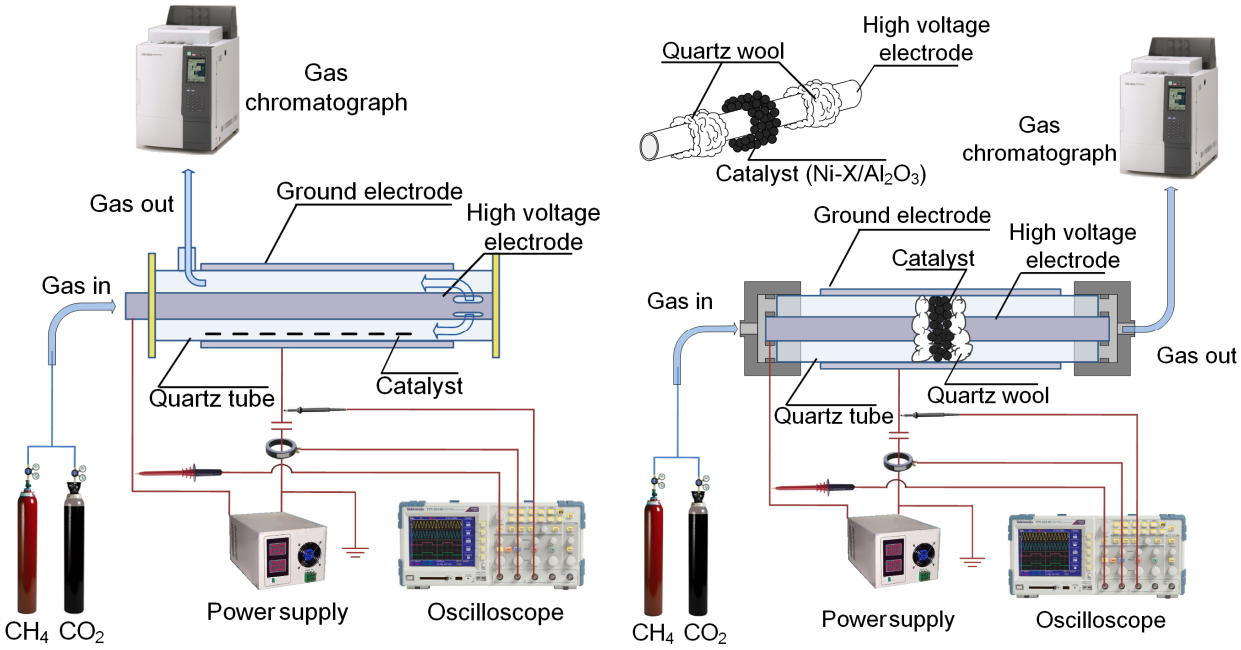

Figure 2.3 Schematic diagram of experimental setup for (a) dry reforming of methane, and (b) biogas reforming.

Table 2.1 summarises the experimental setups for individual works in this project.

Table 2.1 A summary of experimental configurations in this project.

Chapter	Section	Packed bed	Reaction
3	1	Catalyst + γ–Al_2O_3	CO_2 hydrogenation
4	1	Catalyst + γ–Al_2O_3	CO_2 hydrogenation
4	2, 3	Catalyst + quartz wool	CO_2 hydrogenation
5	1	Catalyst pellet	Dry reforming
5	2	Catalyst + quartz wool	Dry reforming
6	1, 2, 3	Catalyst + quartz wool	Dry reforming

2.2. Measurements and characterisations

2.2.1. Power measurement

The energy consumption of the plasma-catalytic reactor was determined by measuring the input power and discharge power of system. Specifically, the input

power was the electric power injected into the system, including the power consumed by the transformer, power supply, plasma reactor, and external heating device (if installed). It reflects the operational cost of the whole system, assesses feasibility for potential commercial applications. In this project, the input power was measured by a power meter set up between the mains and the system. The discharge power was the electric power exclusively consumed by the plasma. It can be further used to calculate the energy efficiencies of the system. In this project, the discharge power was obtained by using Lissajous figure.

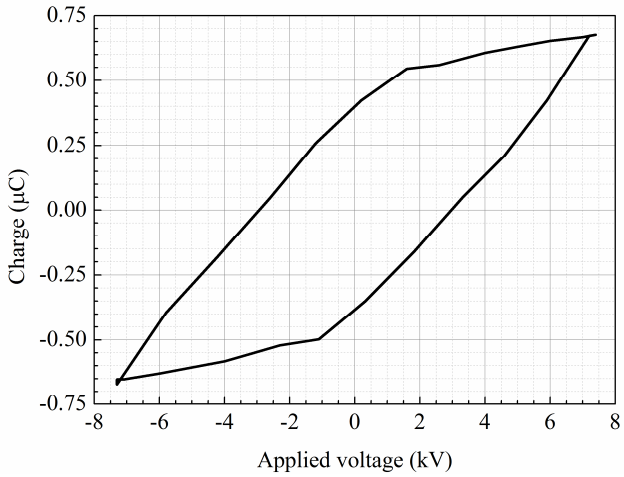

Figure 2.4 Example of Lissajous figure obtained in the plasma-catalytic hydrogenation of CO_2. (Taken from Chapter 4).

Although the Lissajous method was first proposed by Manley in 1943, it is still worth using today [178]. Besides discharge power, the Lissajous figure provides information of discharge mode, capacitance of plasma system during power cycle and transferred charge. The Lissajous method requires measurement of the applied voltage on the reactor, and the total charge transferred through the reactor. The latter is done by connecting a capacitor in series to the reactor and recording the voltage signal across this capacitor. After recording a full cycle of the applied voltage, a Q–U Lissajous figure can be obtained by plotting the charge against the voltage. The area that encircled by the figure equals to the discharge power.

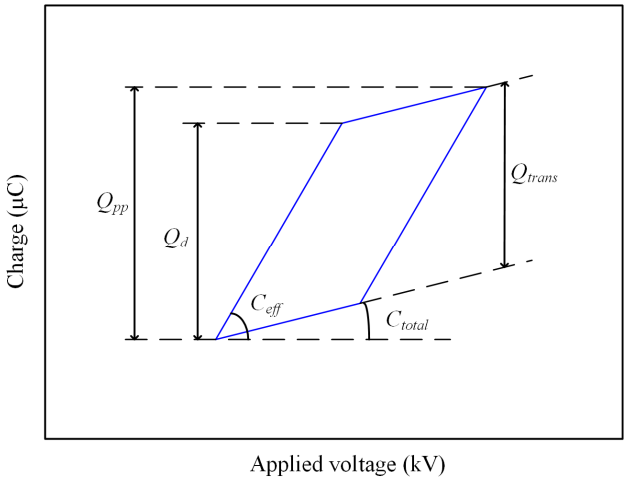

Figure 2.5 Analysis of the Lissajous figure.

2.2.2. Gas Chromatography

Gas chromatography (GC) is a well-established method to analyse the composition of gas samples. The analysis is consisted of the separation and detection of gaseous species. The separation of gas components in the sample is carried out in the column of GC. After being injected into the injection port, a gas sample is carried into the GC column by carrier gas (N_2, He, or Ar). Sample molecules interact (adsorption and desorption) with the stationary phase which is coated on the inner surface or packed in the volume of the column. Depending on their characteristics, the species in the gas sample adsorb/desorb at different rate, and their retention times in the column become subsequently different. Therefore, gaseous species can be separated and identified according to their retention time. The affinity of gaseous species to the stationary phases strongly depends on the specification of the column such as the polarity and composition of stationary phase, the thickness of the stationary phase, the diameter and length of the column. The retention time of gases are also determined by operational parameters, including the type of carrier gas, the flow rate and pressure of carrier gas, and the temperature of the column. As a consequence, calibration is always necessary. And the calibration and measurements must be carried out under the same set of conditions for any application. The detection of separated sample species is carried out by passing the gas through various detectors. The detectors usually measure a single characteristic of the species such as number of carbon atoms or thermal conductivity of the species. The intensity of signals are calculated for the concentrations of the species.

A GC is commonly equipped with capillary columns, a TCD and/or an FID. The detectors will be introduced in the following sections. Sometimes, packed columns are also used in a GC. In this project, the GC was equipped with two columns of different types. Both columns were using Ar as carrier gas and were connected to TCD and FID.

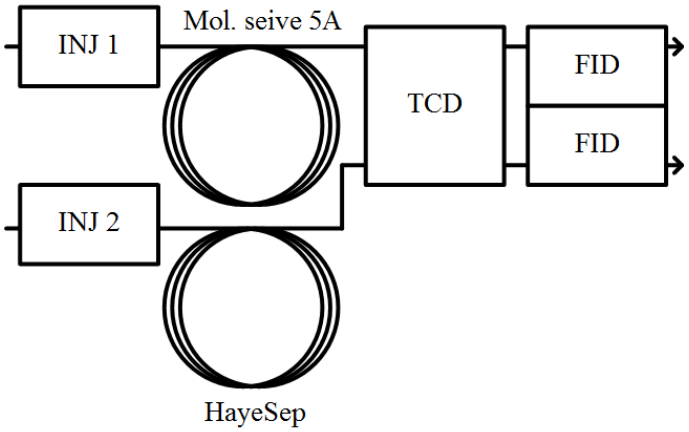

Figure 2.6 The flow configuration of GC in this project.

2.2.2.1. Flame ionisation detector

FID is a standalone device that extensively used to measure the concentration of organic compounds in the sample flow. Inside of the FID in a GC, any organic compound in the carrier gas is brought to and combusted in a hydrogen flame. A cluster of ions that is proportional to the concentration of the organic matter is generated during the combustion. These ions are captured by an electric field and collected on the surface of an electrode, subsequently creating a signal. The FID is very sensitive for hydrocarbons and the amplitude of response is proportional to the number of carbon atoms in their molecules. However, FID is unable to detect H_2, CO, and CO_2.

2.2.2.2. Thermal conductivity detector

The TCD is also called Katharometer, which monitors changes in the thermal conductivity of gas flowing through the sample column by comparing the signal from sample column with that from the reference column. The comparison relies on the sensitivity of a Wheatstone bridge responding to the change of resistance, while in a TCD that change of resistance results from the change of thermal conductivity of gas in sample column. Both the sample column and reference column contain a constantly heating filament in contact with the gas flow. The Wheatstone bridge is balanced when

both columns are filled with the same carrier gas. As soon as the thermal conductivity of gas flowing through the sample column changes (which is a result of different gas composition), the rate of loss of heat from the filament becomes different, then the temperature of the filament changes. This consequently alters the resistance of the filament and breaks the balance of the bridge circuit so that a signal is generated. However, the response of the filament to the concentration of gaseous species is usually non-linear, the calibration for each type of gas is required for actual applications.

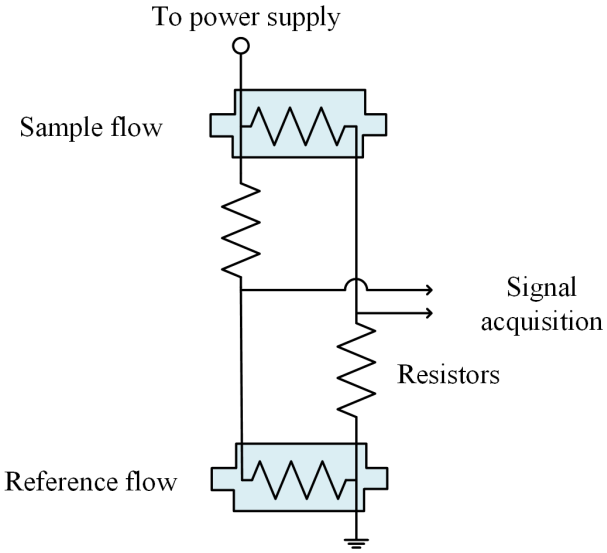

Figure 2.7 Schematic of a thermal conductivity detector.

2.2.3. X-ray diffraction

X-ray diffraction (XRD) is an analytical technique for identifying the phase and crystalline structures of a material. The measurement is based on the interference between monochromatic X-ray and the finely ground granules of an unknown sample. The constructive interference and characterised reflection would occur when the incident radiation and the lattice properties of the sample satisfy Bragg's Law, then the reflection is measured. By scanning the X-ray through an incident angle from 10° –80°, all the possible diffraction corresponding to the constructive reflection can be measured, due to the random orientation of crystalline surfaces of the sample grains. Scherrer's equation is usually used to calculate the mean crystalline size of the sample:

$$d = \frac{0.89\lambda}{(\beta - \beta_0)\cos\theta} \qquad (1)$$

where d is the average volume diameter of the crystallite, λ is the wavelength of the incident X–ray, θ is the incidence angle of the X–ray with respect to the level surface, β is the width at half peak height in radians, and β_0 is the instrumental line broadening.

2.2.4. Transmission electron microscopy

Transmission electron microscopy (TEM) enables the observation and examination of fine detail on sample material at atomic level. In contrast to the conventional optical microscopy, whose resolution is limited by the diffraction of light radiation, TEM uses a beam of electrons to transmit through an ultra-thin film of sample material. By measuring the electrons interacted with the material, an image of the sample can be reconstructed. Although TEM is a well-established and widely accepted technique, there are still several concerns when using this method. For instance, extensive preparation is required to guarantee the sample film is thin enough and electron transparent. However the throughput of the sample films is usually low, while the field of view is also limited. Moreover, the sample is possibly damaged by the electron beam during measurement.

2.2.5. Thermogravimetric analysis

Thermogravimetric analysis (TGA) is a thermal analytic method measuring the weight- change of samples at increasing temperatures. The weight-change, in most of the cases is weight-loss, relates to the progress of physical and chemical processes in response to the increasing temperature and/or elapsed heating-time. The physical processes include absorption, adsorption, desorption, and vaporisation, while the chemical processes include chemisorption-desorption, oxidation, reduction, decomposition, and gasification. It can also be used to determine the carbon deposition on the spent catalysts. During the measurement, the sample is gradually heated to a temperature up to 2000 °C while its weight is continuously monitored. The effluent gas is analysed by coupled infrared spectrometer or mass spectrometer (MS). A limitation for the TGA is that it is difficult to distinguish the individual processes and their contribution to the weight-change during the heating when such change results from several simultaneous-processes, for instance the decomposition of a metal nitrate salt

accompanied by the oxidation of metal species and desorption of gases in the sample grain.

2.2.6. Temperature-programmed reduction

Temperature-programmed reduction (TPR) is usually used for the characterization of solid catalysts to investigate their reduction temperature and reducibility. The analysis is carried out with a U-shape tube, which is filled with sample catalyst, purged by inert gas, and placed in a temperature-programmed furnace. Hydrogen is added into the feed flow when the air in the tube is driven out, the furnace is subsequently turned on. The temperature of the sample is measured by a thermocouple, and the composition of the effluent gas is analysed by a GC coupled with TCD or MS. The hydrogen consumption corresponding to the reduction of the sample at a certain temperature is therefore measured and recorded.

2.2.7. N_2 adsorption-desorption analysis

This method is always used to determine the surface properties of solid materials, in terms of specific surface area, pore size, pore volume, and adsorption capacity. The method is based on the multi-layer adsorption of N_2 and capillary condensation on the surface of the solid sample, which is well-described by the Brunauer-Emmett-Teller (BET) theory. The calculation of results is based on measuring the amount of N_2 adsorbed at different partial pressure of N_2. It can also be used to determine the shape of pores on the surface of the sample material.

2.3. Definition of parameters

All the following parameters were averaged values that were calculated from the GC signals of three parallel samples. For the plasma-catalytic CO_2 hydrogenation, the conversion (X) of CO_2 is defined as:

$$X_{CO2}\ (\%) = \frac{\mathrm{CO_2\ converted\ (mol)}}{\mathrm{CO_2\ input\ (mol)}} \times 100 \qquad (2)$$

The selectivity (S) and yield (Y) of the main products are calculated as:

$$S_{CO}\ (\%) = \frac{\text{CO produced (mol)}}{\text{CO}_2\text{ converted (mol)}} \times 100 \quad (3)$$

$$S_{CH4}\ (\%) = \frac{\text{CH}_4\text{ produced (mol)}}{\text{CO}_2\text{ converted (mol)}} \times 100 \quad (4)$$

$$Y_{CO}\ (\%) = \frac{\text{CO produced (mol)}}{\text{CO}_2\text{ input (mol)}} \times 100 \quad (5)$$

$$Y_{CH4}\ (\%) = \frac{\text{CH}_4\text{ produced (mol)}}{\text{CO}_2\text{ input (mol)}} \times 100 \quad (6)$$

The H_2/CO_2 molar ratio and carbon balance (B) are determined as follows:

$$\frac{\text{H}_2}{\text{CO}_2} = \frac{\text{H}_2\text{ input (mol)}}{\text{CO}_2\text{ input (mol)}} \quad (7)$$

$$B_{carbon}\ (\%) = \frac{[\text{CH}_4]_{\text{out}} + [\text{CO}_2]_{\text{out}} + [\text{CO}]_{\text{out}}}{[\text{CO}_2]_{\text{in}}} \times 100 \quad (8)$$

The total energy efficiency for the production of CO and CH_4, and the fuel production efficiency (FPE) of the process are determined as follows:

$$E\ (\text{mmol}\ kJ^{-1}) = \frac{\text{CH}_4\text{ produced (mol}\ s^{-1}) + \text{CO produced (mol}\ s^{-1})}{\text{Power (W)}} \quad (9)$$

$$FPE\ (\%) = \frac{\text{LHV}_{\text{CO}}\ (\text{J mol}^{-1}) \times \text{CO output (mol s}^{-1}) + \text{LHV}_{\text{CH4}}\ (\text{J mol}^{-1}) \times \text{CH}_4\text{ output (mol s}^{-1})}{\text{LHV}_{\text{H2}}\ (\text{J mol}^{-1}) \times \text{H}_2\text{ input (mol s}^{-1}) + \text{power (W)}} \times 10 \quad (10)$$

where power is the sum of plasma power and heating power. LHV is the lower heating value of fuels. The synergistic capability of plasma catalysis in percentage (SC) is calculated as [179]:

$$SC_{\zeta}\ (\%) = \frac{\zeta_{p+c} - \zeta_p - \zeta_c}{\zeta_p + \zeta_c} \times 100 \quad (11)$$

where ζ can be the conversion of CO_2, the yield of CO, the selectivity and yield of CH_4, or the fuel production efficiency. The subscripts $p+c$, p, and c represent the results from plasma-catalysis, plasma alone, and thermal catalysis (catalyst only), respectively.

For the biogas reforming, the conversion (X) of CH_4 and CO_2 are defined as:

$$X_{CH4}\ (\%) = \frac{\text{CH}_4\text{ converted (mol)}}{\text{CH}_4\text{ input (mol)}} \times 100 \quad (12)$$

$$X_{CO2}\ (\%) = \frac{CO_2 \text{ converted (mol)}}{CO_2 \text{ input (mol)}} \times 100 \quad (13)$$

The selectivity (S) and yield (Y) of the main products are calculated as:

$$S_{CO}\ (\%) = \frac{\text{CO produced (mol)}}{CO_2 \text{ converted (mol)} + CH_4 \text{ converted (mol)}} \times 100 \quad (14)$$

$$S_{H2}\ (\%) = \frac{H_2 \text{ produced (mol)}}{2 \times CH_4 \text{ converted (mol)}} \times 100 \quad (15)$$

$$S_{CxHy}\ (\%) = \frac{x \times C_xH_y \text{ produced (mol)}}{CO_2 \text{ converted (mol)} + CH_4 \text{ converted (mol)}} \times 100 \quad (16)$$

$$Y_{CO}\ (\%) = \frac{\text{CO produced (mol)}}{CO_2 \text{ input (mol)} + CH_4 \text{ input (mol)}} \times 100 \quad (17)$$

$$Y_{H2}\ (\%) = \frac{H_2 \text{ produced (mol)}}{2 \times CH_4 \text{ input (mol)}} \times 100 \quad (18)$$

$$Y_{CxHy}\ (\%) = \frac{x \times C_xH_y \text{ produced (mol)}}{CO_2 \text{ input (mol)} + CH_4 \text{ input (mol)}} \times 100 \quad (19)$$

The H_2/CO molar ratio in the product is determined as:

$$\frac{H_2}{CO} = \frac{H_2 \text{ produced (mol)}}{\text{CO produced (mol)}} \quad (20)$$

The carbon balance of the process is defined as:

$$B_{\text{carbon}}\ (\%) = \frac{[CH_4]_{out} + [CO_2]_{out} + [CO]_{out} + 2 \times [C_2]_{out}}{[CH_4]_{out} + [CO]_{in}} \times 100 \quad (21)$$

The energy efficiency for the conversion of CH_4 or CO_2, and the overall energy efficiency of the plasma dry reforming in terms of gas conversion are defined as

$$E_{CH4}\ (\text{mmol kJ}^{-1}) = \frac{CH_4 \text{ converted (mol s}^{-1})}{\text{Power (W)}} \quad (22)$$

$$E_{CO2}\ (\text{mmol kJ}^{-1}) = \frac{CO_2 \text{ converted (mol s}^{-1})}{\text{Power (W)}} \quad (23)$$

$$E\ (\text{mmol kJ}^{-1}) = \frac{CH_4 \text{ converted (mol s}^{-1}) + CO_2 \text{ converted (mol s}^{-1})}{\text{Power (W)}} \quad (24)$$

The fuel production efficiency (*FPE*) of biogas reforming [180] is defined as

$$FPE\ (\%) = \frac{LHV_{CO}(J\ mol^{-1}) \times CO\ output\ (mol\ s^{-1}) + LHV_{H2}(J\ mol^{-1}) \times H_2\ output\ (mol\ s^{-1})}{LHV_{CH4}(J\ mol^{-1}) \times CH_4\ input\ (mol\ s^{-1}) + discharge\ power\ (W)} \times 100 \quad (25)$$

The definition of synergy capacity (*SC*) of the plasma-catalytic methane reforming process is the same as that of plasma-catalytic CO_2 hydrogenation.

Chapter 3. Plasma-catalytic CO_2 hydrogenation at low temperatures

In this chapter, the plasma-catalytic CO_2 hydrogenation has been investigated in a coaxial packed-bed DBD reactor at low temperatures and atmospheric pressure. The influence of H_2/CO_2 molar ratio and different catalysts (Cu/γ-Al_2O_3, Mn/γ-Al_2O_3 and Cu-Mn/γ-Al_2O_3) on the reaction performance of the plasma-catalytic CO_2 hydrogenation has been evaluated in terms of the conversion of CO_2, the selectivity and yield of CO and CH_4, and the energy efficiency for CO and CH_4 production.

3.1. Experimental setup

3.1.1. Plasma reactor and catalyst

A detailed explanation of the setup can be found in Chapter 2. In this chapter, the discharge power of the plasma process was fixed at 35 W. The temperature in the catalyst bed was less than 150 °C, measured by a fibre optical thermometer (Omega, FOB102). The reactants and products were analysed by a two-channel gas chromatograph (Shimadzu GC-2014) equipped with a flame ionisation detector and a thermal conductivity detector.

The 8 wt.% Cu/γ-Al_2O_3, 8 wt.% Mn/γ-Al_2O_3, and 4 wt.% Cu- 4wt.% Mn/γ-Al_2O_3 catalysts were prepared by wetness impregnation using nitrate salts (Alfa Aesar, 99.5%) as the metal precursors. Catalyst support (γ-Al_2O_3 beads, 1.5 mm in diameter) was added to the solution of nitrate salts. The mixture slurry was stirred at 80 °C for 4 hrs and then dried at 110 °C overnight, followed by calcination at 600 °C for 6 h. The supported catalyst beads (1.5 mm in diameter and 1 g in total) were packed into the reactor with 13.6 g $BaTiO_3$ beads (1 mm in diameter). In the packed-bed DBD reactor, plasma could form in both the catalyst bed and packing material area. Filamentary discharges could be generated in the small gap between the bead–bead wall and the

bead–quartz wall, while surface discharges could form on the surface of beads near the contact points between the beads [181]. Prior to the plasma-catalytic CO_2 hydrogenation, the catalysts were reduced in an argon-hydrogen discharge at a discharge power of 7.5 W (50 ml min^{-1}, 20 vol. % H_2) for 30 minutes in the same DBD reactor.

3.1.2. Definition of parameters

For the plasma-catalytic CO_2 hydrogenation, the conversion (C) of CO_2, the selectivity (S) and yields (Y) of the main products, the H_2/CO_2 ratio and carbon balance (B), and the energy efficiency (E) of the plasma CO_2 hydrogenation process for CO and CH_4 production are defined in Chapter 2.

3.2. Results and Discussion

3.2.1. Effect of H_2/CO_2 molar ratio

Figure 3.1 shows the effect of different H_2/CO_2 molar ratios on the reaction performance of the plasma-catalytic CO_2 hydrogenation over a Cu/γ-Al_2O_3 catalyst at a discharge power of 35 W. CO and H_2O are the major products, whereas a small amount of CH_4 and a trace amount of C_2H_6 and C_4H_{10} (3-10 ppm) are also detected in the effluent. The conversion of CO_2 increases almost linearly with the increase of the H_2/CO_2 molar ratio at a fixed flow rate (Figure 3.1(a)). For instance, the conversion of CO_2 is increased from 8% to 11% when the H_2/CO_2 molar ratio is changed from 1:1 to 2:1, and reaches the maximum of 22.5% when further increasing the H_2/CO_2 ratio from 2:1 to 4:1. This result suggests that increasing H_2 content in the reactant mixture significantly enhances the CO_2 conversion.

Figure 3.1(b) and (c) show that the H_2/CO_2 molar ratio affects the selectivity of CO and CH_4. As the H_2/CO_2 molar ratio varies from 1:1 to 4:1, the CO selectivity slightly increases and reaches 90%, whereas the CO yield is tripled. However, the selectivity of CH_4 achieves its maximum at the H_2/CO_2 ratio of 3:1. Further increasing the H_2 content decreases the CH_4 selectivity. These findings could be useful in the optimisation of the plasma-catalytic CO_2 hydrogenation processes, since the conversion of CO_2 and the production of CO and CH_4 could be controlled by adjusting the H_2/CO_2 molar ratio. The carbon balance of the plasma-catalytic process is very high (98.8%-

99.6%), which can be confirmed by the formation of very low concentration of C_2 and C_4 by-products in the process. No carbon deposition has been observed in the DBD reactor.

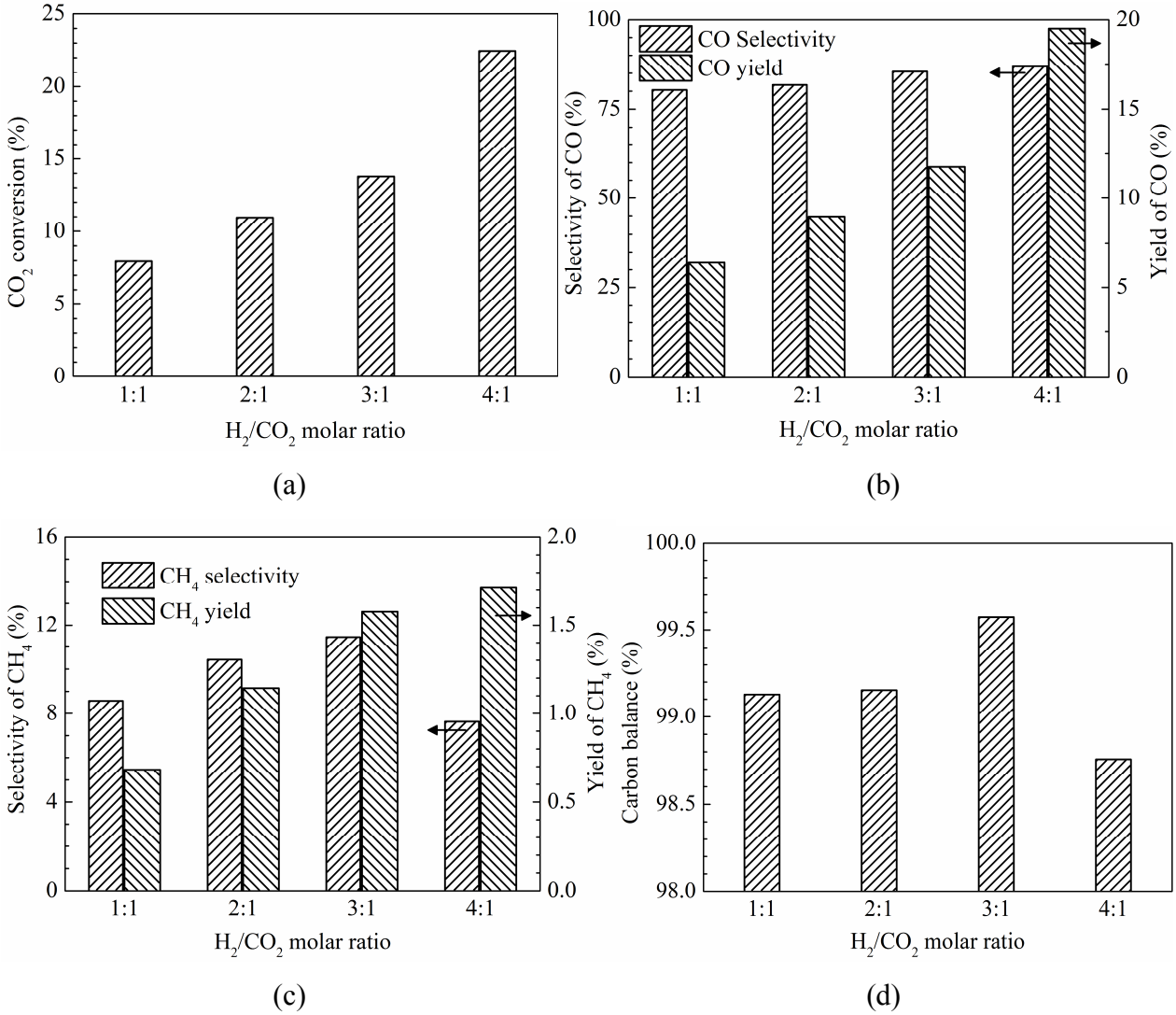

Figure 3.1 Effect of H_2/CO_2 molar ratio on plasma-catalytic CO_2 hydrogenation over a 8 wt.% Cu/γ-Al_2O_3 catalyst. (a) Conversion of CO_2. (b) Selectivity and yield of CO. (c) Selectivity and yield of methane. (d) Carbon balance (discharge power 35 W and total feed flow rate 34.6 ml min^{-1}).

Figure 3.2 shows the effect of the H_2/CO_2 molar ratio on the energy efficiency for CO and CH_4 production. Increasing the H_2/CO_2 molar ratio significantly enhances the energy efficiency for CO production. By changing the H_2/CO_2 ratio from 1:1 to 4:1, the energy efficiency of CO production is enhanced by a factor of 2.4, which can be ascribed to the enhanced conversion of CO_2 and CO yield when increasing the H_2

content in the mixture feed gas. Similarly, the maximum energy efficiency for methane production is achieved at the H_2/CO_2 ratio of 3:1.

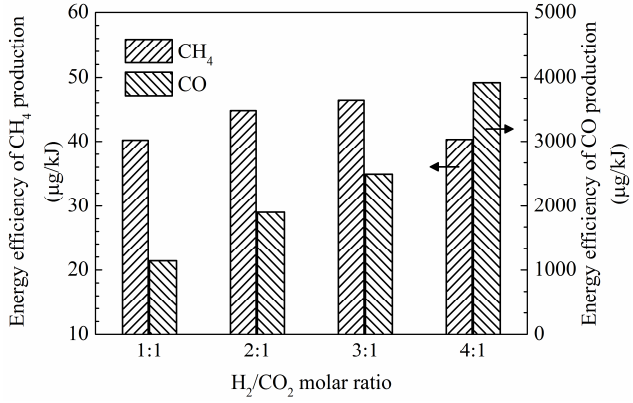

Figure 3.2 Effect of H_2/CO_2 molar ratio on the energy efficiency of CO and CH_4 production. (8 wt.% Cu/γ-Al_2O_3, discharge power 35 W, and total feed flow rate 34.6 ml min^{-1}).

3.2.2. Effect of Catalysts

Figure 3.3 shows the influence of different γ-Al_2O_3 supported metal catalysts on the performance of the plasma CO_2 hydrogenation at a H_2/CO_2 molar ratio of 1:1. Mn is usually added to supported metal catalysts as a modifier or promoter to enhance catalyst activity and has rarely been reported in thermal-catalytic CO_2 hydrogenation. In this chapter, the combination of DBD with the Mn/γ-Al_2O_3 catalysts significantly enhances the conversion of CO_2 by 36% in the plasma CO_2 hydrogenation compared with the plasma reaction without using a catalyst. Similar findings have been reported in the plasma-catalytic dry reforming reaction [98]. However, note the presence of the Cu/γ-Al_2O_3 catalyst in the DBD reactor only slightly improves the CO_2 conversion by 6.7%, whereas adding Mn into the Cu/γ-Al_2O_3 catalyst shows a better CO_2 conversion compared with the Cu/γ-Al_2O_3 catalyst, though the performance of this bimetallic catalyst (Cu-Mn/γ-Al_2O_3) in the plasma-catalytic CO_2 hydrogenation is still lower than when using the Mn/γ-Al_2O_3 catalyst. Cu-based catalysts are commonly used in the WGS reaction, as shown in (3) [182]. Using the Cu/γ-Al_2O_3 catalyst in the DBD reactor might promote the WGS reaction in the plasma-catalytic CO_2 hydrogenation process, leading to a higher concentration of CO_2 in the reactor and a lower apparent CO_2 conversion [98, 182]. For the Cu-Mn/γ-Al_2O_3 bimetallic catalyst, the addition of Mn into the Cu/γ-Al_2O_3 catalyst could partly cover the copper particles on the catalyst

surface, which might slow down the WGS reaction. In addition, the addition of Mn could promote the adsorption of CO_2 by forming reactive carbonate species on the catalyst surface [72]. The combined effects contributes to a better catalytic activity of the Cu-Mn/γ-Al_2O_3 bimetallic catalyst comparing with the Cu/γ-Al_2O_3 catalyst. In this chapter, the maximum CO_2 conversion of 10.2% is achieved in the plasma-catalytic reaction combined with the Mn/γ-Al_2O_3 catalyst at a H_2/CO_2 molar ratio of 1:1 and a discharge power of 35 W, as shown in Figure 3.3(a).

WGS reaction: $CO + H_2O \rightarrow CO_2 + H_2$ (3)

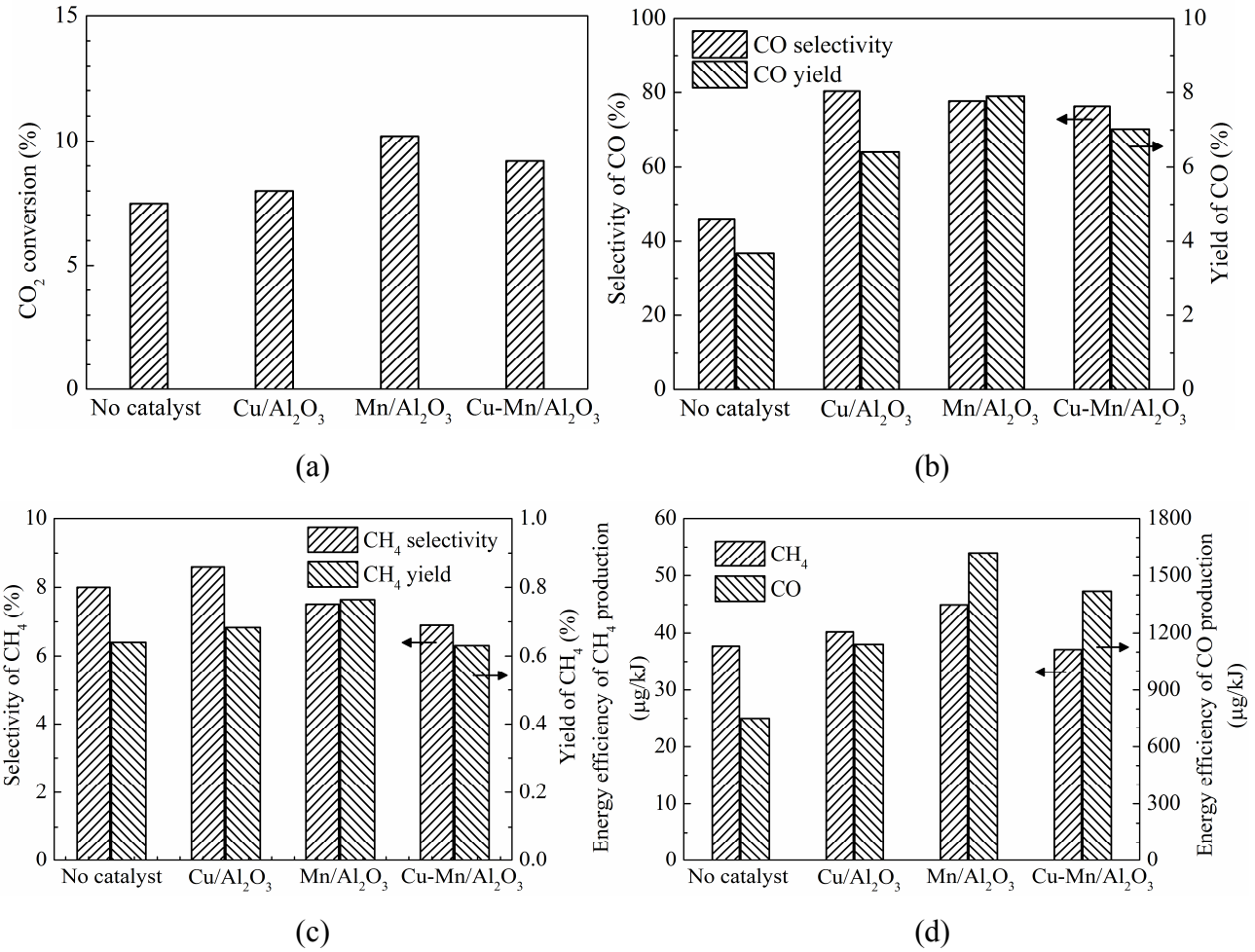

Figure 3.3 Effect of catalysts on plasma-catalytic CO_2 hydrogenation. (a) CO_2 conversion. (b) CO selectivity and yield. (c) CH_4 selectivity and yield. (d) Energy efficiency for CH_4 and CO production (Flow rate 34.6 ml min^{-1}, discharge power 35 W, and H_2/CO_2 molar ratio 1:1).

The selectivity and yield of major gas products (CO and CH_4) produced in the plasma-catalytic CO_2 hydrogenation process are shown in Figure 3.3. The combination of plasma with these catalysts increases the selectivity and yield of CO. Compared with the plasma reaction in the absence of a catalyst, the presence of the Mn/γ-Al_2O_3 catalyst in the plasma process significantly increases the yield of CO by 114%, followed by the Cu-Mn/γ-Al_2O_3 bimetallic catalyst (91%), whilst placing the Cu/γ-Al_2O_3 catalyst in the DBD reactor increases the CO yield by 73%. In contrast, these catalysts show completely different activities for CH_4 formation in the plasma-catalytic CO_2 hydrogenation. Only the Cu/γ-Al_2O_3 catalyst exhibits a higher CH_4 selectivity compared with the plasma reaction without a catalyst. The integration of the DBD and Mn/γ-Al_2O_3 catalyst decreases the selectivity of CH_4 by 6.3% (from 8% to 7.5%), while the use of the Cu-Mn/γ-Al_2O_3 catalyst in the plasma reactor decreases the selectivity of CH_4 by 13.3%. The combination of DBD with the Cu-Mn/γ-Al_2O_3 catalyst could suppress the formation of CH_4 in the RWGS reaction. These results suggest that different catalysts could be used to control the formation of desirable products.

The energy efficiency for CO and CH_4 production in the plasma reaction without a catalyst is 750 and 37.7 μg kJ^{-1}, respectively, as shown in Figure 3.3(d). The presence of all three catalysts in the DBD reactor improves the energy efficiency of CO production. Packing the Mn/γ-Al_2O_3 catalyst in the plasma is found to improve the energy efficiency of CO production by 116%, while using the Cu-Mn/γ-Al_2O_3 and Cu/γ-Al_2O_3 catalysts in the DBD reactor increases the energy efficiency of CO production by 52% and 89.3%, respectively. The maximum energy efficiency of CO production (1620 μg/kJ) is achieved at a discharge power of 35 W and a total flow rate of 34.6 ml min^{-1} when the Mn/γ-Al_2O_3 catalyst is placed in the DBD reactor. Similarly, the combination of plasma with the Mn/γ-Al_2O_3 catalyst shows the best performance in terms of the energy efficiency for CH_4 production. Note that the plasma-catalytic process does not always enhance the energy efficiency of the CO_2 hydrogenation. In this chapter, compared with the plasma process without catalyst, the presence of the Cu/γ-Al_2O_3 in the DBD reactor only slightly increases the energy efficiency of CH_4 production by 6.6%, whereas combining the Cu-Mn/γ-Al_2O_3 catalyst with plasma slightly decreases the energy efficiency for CH_4 production.

Table 3.1 compares the performance of CO_2 hydrogenation via thermal or plasma processes using different catalysts. All the listed values are cited or calculated from the literature. The performance of CO_2 hydrogenation is significantly affected by a wide

range of operating parameters, such as the H_2/CO_2 molar ratio, total reactant flow rate, reaction temperature, and catalyst composition. Different supported metal catalysts have been investigated for the CO_2 hydrogenation into CO or CH_4. The reaction temperature in the plasma processes is much lower than that in thermal catalytic reactions. For instance, in this chapter, the reaction temperature in the plasma-catalytic CO_2 hydrogenation process is less than 150 ^oC without using extra heating, whereas the operating temperatures in thermal-catalytic CO_2 hydrogenation are between 260 ^oC and 500 ^oC. The maximum CO selectivity and energy efficiency for CO production achieved in this chapter are comparable with those using either thermal or plasma processes. For example, Kano *et al.* investigated the CO_2 hydrogenation in a radio-frequency impulse plasma reactor without a catalyst and achieved a maximum CO selectivity of 80% [46]. However, it should be noted that their experiment was carried out using a much lower gas flow rate with a H_2/CO_2 molar ratio of 4:1 in a low-pressure plasma reactor. In this chapter, the performance of the plasma-catalytic CO_2 hydrogenation could be further optimized and enhanced by choosing suitable plasma sources with higher efficiency (*e.g.*, pulsed DBD) and more active catalysts.

3.3. Summary

The combination of plasma with the Cu/γ-Al_2O_3, Mn/γ-Al_2O_3, and Cu-Mn/γ-Al_2O_3 catalysts enables the CO_2 hydrogenation reactions to occur at low temperatures. The H_2/CO_2 molar ratio significantly affects the CO_2 conversion, the yield of CO and CH_4. Increasing the H_2 content in the reactant mixture significantly increases the CO_2 conversion. Compared with the plasma CO_2 hydrogenation in the absence of a catalyst, the combination of plasma with the catalysts enhances the conversion of CO_2 by 6.7%-36%, while the Mn/γ-Al_2O_3 catalyst shows the best catalytic activity for CO production, followed by the Cu-Mn/γ-Al_2O_3 and Cu/γ-Al_2O_3 catalysts. The presence of Mn/γ-Al_2O_3 catalyst in the DBD reactor significantly enhances the yield of CO by 114%, compared with the plasma reaction without a catalyst. In addition, packing the Mn/γ-Al_2O_3 catalyst into the plasma reactor is found to improve the energy efficiency of CO production by 116%, while using the Cu/γ-Al_2O_3 and Cu-Mn/γ-Al_2O_3 catalysts in the DBD reactor leads to an increase of 52% and 89.3%, respectively.

Table 3.1 CO_2 hydrogenation using different processes.

H_2/CO_2 molar ratio	Total flow rate (ml min^{-1})	Process	Reaction conditions	Catalyst	$C(CO_2)$ (%)	S(CO) (%)	Y(CO) (%)	$S(CH_4)$ (%)	$Y(CH_4)$ (%)	Ref
1 : 1	34.6	DBD	135 °C, 35 W	Mn/Al_2O_3	10.2	77.7	7.9	7.5	0.76	**This work**
1 : 1 (50% Ar)	100	Corona	150 °C, 5 W	$Pt\text{-}La/ZrO_2$	40	99	40	-	-	[69]
4 : 1	20	RF impulse	2.4 Torr, 20 W	-	20	80	16	20	4	[183]
4 : 1	250	DBD	260 °C, 17 W	Ni/Al_2O_3	85	-	-	97	82	[56]
1 : 1 (80% He)	25	Thermal	260 °C	$Pd/La_2O_3/Al_2O_3$	0.6	-	-	30	0.18	[44]
4 : 1	166.7	Thermal	350 °C	Cu/MSN [a]	3.3	21	69	79	2.6	[184]
1 : 1	240	Thermal	400 °C	NiO/CeO_2	5	100	5	-	-	[185]
4 : 1	10	Thermal	400 °C	$Rh/K/Al_2O_3$	30	100	30	0	0	[49]
4 : 1	0.2	Thermal	400 °C	Ni/ZrO_2/clay	57	-	-	97	55	[50]
4 : 1	50	Thermal	300 °C	$Ni\text{-}CeO_2/Al_2O_3$	70	0	0	99	70	[47]
3.5 : 1	30	Thermal	350 °C	$Ce\text{-}Ni/Al_2O_3$	80	0	0	100	80	[48]
1 : 1 (60% He)	1	Thermal	500 °C	SCZT [b]	~1	-	0.0063	-	-	[186]
2 : 1	15	Thermal & photocatalysis	400 °C	Au/TiO_2	~3	-	-	-	-	[187]

[a]MSN: Mesostructured Silica Nanoparticles.

[b]SCZT: $Sr_3CaZr_{0.5}Ta_{1.5}O_{8.75}$.

Chapter 4. Plasma-catalytic CO_2 hydrogenation at elevated temperatures

In the previous chapter, hydrogenation of CO_2 for the cogeneration of CO and CH_4 has been carried out in a coaxial dielectric barrier discharge (DBD) reactor with and without a catalyst at atmospheric pressure and low temperature. In this chapter, to understand the synergistic effect of plasma-catalysis, thermal catalytic hydrogenation of CO_2 has been performed at 150 ^oC for comparison. The effect of the composition of catalyst and the effect of Ar as a dilution gas on the CO_2 hydrogenation process under three different operating conditions (plasma only, plasma-catalysis and thermal catalysis) has been investigated in terms of the conversion of CO_2, the selectivity and yield of target products (CO and CH_4), and the fuel production efficiency of the process. The promotional effect of Ar on the electrical properties of the DBD, the synergistic effect of plasma-catalysis, and the individual contribution of plasma power and heating power on the hydrogenation are also discussed.

4.1. Plasma-catalytic CO_2 hydrogenation for the generation of CO and CH_4 in a dielectric barrier discharge reactor: Effect of argon addition

4.1.1. Experimental setup

The experimental setup of this section is explained in Chapter 2. The discharge power was fixed at 30 W. A reactant mixture of H_2 and CO_2 with a H_2/CO_2 molar ratio of 4:1 was used and the Ar concentration was varied to 0, 30%, 50% and 60%. The total gas flow rate was 69.2 ml min^{-1}. 15 wt.% Ni/Al_2O_3 catalyst was prepared by impregnation method using nitrate salt (Alfa Aesar, ACS reagents) as the metal precursor. Catalyst support (Al_2O_3 beads with a diameter of around 1.5 mm) was added to the solution of nitrate salt. The mixture slurry was continuously stirred for 1 hr and

impregnated for 3 hrs, then dried at 90 °C overnight, followed by calcination at 400 °C for 4 hrs. 0.4 g Ni catalyst was packed into the reactor and sandwiched by 2 g Al_2O_3 beads. Prior to the plasma-catalytic CO_2 hydrogenation, the catalyst was reduced in an argon-hydrogen discharge at a discharge power of 30 W (69.2 ml min^{-1}, 20 vol. % H_2) for 30 minutes in the same reactor.

The DBD reactor was placed in a tube furnace, as explained in Chapter 2. In this section however, only for the thermal-catalytic process was the reactor heated by the tube furnace, while no extra heating was provided to the plasma process with or without a catalyst. The gas composition was analysed by a two-channel gas chromatograph (Shimadzu GC-2014). CO and CH_4 were the major gas products in the plasma hydrogenation of CO_2. Trace amount of saturated hydrocarbons C_2H_6 (40-110 ppm), C_3H_8 (2-20 ppm) and C_4H_{10} (2-20 ppm) were also detected.

4.1.2. Definition of parameters

An equivalent circuit developed from our previous work is used to simplify and describe the DBD system in this work [96]. As shown in Figure 4.1, l_{total} is the length (100 mm) of the discharge area and l_{cat} is the actual length of the catalyst bed containing gas, while l_{bed} is the actual length (60 mm) of the packed bed, consisting of the Ni catalysts (black sphere), alumina beads (white sphere) and the gas in the bed. Ideally, considering the solid (packing material) and gas in the packed bed separately, two equivalent parameters $l_{packing}$ and $l_{gas,2}$ can be introduced. $l_{packing}$ represents the equivalent length of the packed materials (Ni/Al_2O_3 catalyst and Al_2O_3 beads) excluding gas, while $l_{gas,2}$ is the equivalent length of the gas in the packed bed. $l_{gas,1}$ is used to describe the equivalent length of the gas outside of the packing bed.

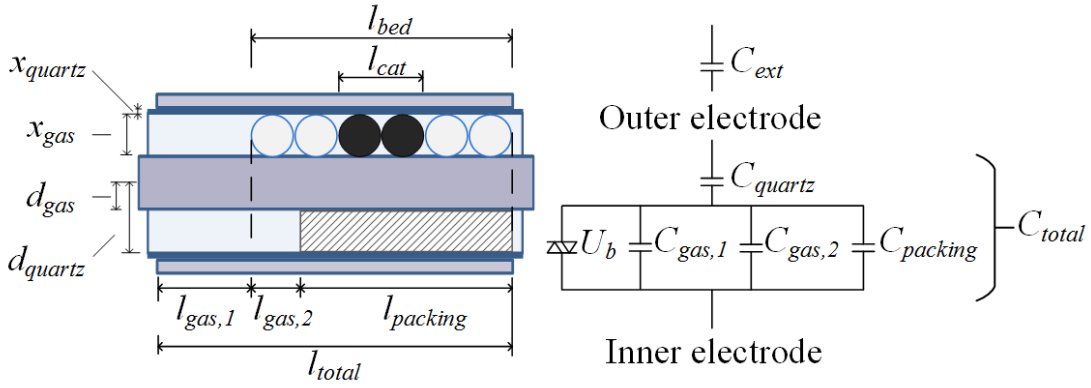

Figure 4.1 Equivalent circuit of the DBD-catalytic reactor.

The equivalent capacitance (before breakdown) of these parameters is denoted as $C_{packing}$, $C_{gas,2}$ and $C_{gas,1}$, respectively, as shown in Figure 4.1. The capacitance of the quartz barrier is denoted as C_{quartz}. U_b is the breakdown voltage of the gas in the reactor, while the bidirectional diode represents the breakdown and discharge in the reactor. Since the diameter of Al_2O_3 beads is the same as the discharge gap (1.5 mm), it can be assumed that there was only one layer of packing materials (Ni catalyst and Al_2O_3) in the gap when they were tightly packed. In this circumstance, this configuration can be considered as a two-dimensional analogue of the Kepler conjecture and the fraction β of the volume packed with the Ni catalyst and Al_2O_3 beads is about 0.9 [188]. The relationship of these parameters is summarised below.

$$l_{packing} = l_{bed} \times \beta \quad (1)$$

$$l_{gas,2} = l_{bed} - l_{packing} = l_{total} - l_{packing} - l_{gas,1} \quad (2)$$

The values of the capacitances fit the following equations.

$$\frac{1}{C_{total}} = \frac{1}{C_{quartz}} + \frac{1}{C_{gap}} = \frac{1}{C_{quartz}} + \frac{1}{(C_{gas,1}+C_{gas,2}+C_{packing})} \quad (3)$$

where C_{total} is the total capacitance of the reactor packed with catalysts and Al_2O_3, C_{gap} is the overall capacitance of the gap. Both parameters were calculated from the Lissajous figure [189]. $C_{gas,1}$, $C_{gas,2}$ and C_{quartz} were calculated from the following equation of cylindrical capacitors [190]:

$$C_i = \frac{2\pi\varepsilon_0\varepsilon_i l_i}{ln(d_i+x_i) - ln\, d_i} \quad (4)$$

where ε_0 is the dielectric constant of vacuum (8.85×10^{-12} F m^{-1}). ε_i, l_i, d_i and x_i are the relative dielectric constant, the (equivalent) length, the inner radius and thickness of the corresponding material (Figure 4.1), respectively. Here ε_{quartz} is 4.65 [191], while ε_{gas} is 1 because the relative dielectric constants of Ar, H_2 and CO_2 are close to unity [192-194]. The overall relative dielectric constant of the packing material (Ni/Al_2O_3 and Al_2O_3 beads) $\varepsilon_{packing}$ is unknown, because the Ni particles supported on Al_2O_3 have

changed its surface properties. However this parameter can be determined via $C_{packing}$ and Lissajous figure.

As explained in our previous work [96], the charge transferred through the reactor (Q_{pp}) can be measured by the capacitor C_{ext}, while the charge transferred during the discharge (Q_d) and the charge transferred from one electrode to the other (Q_{trans}) can be calculated via the Lissajous figure. The voltage applied on the reactor, the discharge gap, the quartz wall, two parts of gas in the gap namely $l_{gas,1}$ and $l_{gas,2}$, are presented as U, U_{gap} , U_{quartz}, $U_{gas,1}$ and $U_{gas,2}$, respectively. Thus:

$$U_{gap} = U_{gas,1} = U_{gas,2} \quad (5)$$

$$U_{gap} = U - U_{quartz} = U - \frac{C_{ext}U_{ext}}{C_{quartz}} \quad (6)$$

where U_{ext} is the voltage across the external capacitor.

For the plasma-catalytic CO_2 hydrogenation, the conversion (X) of CO_2, the selectivity (S) and yield (Y) of the main products CO and CH_4, the H_2/CO_2 molar ratio in the product, the carbon balance (B), the fuel production efficiency (FPE) of the process and the synergistic capability of plasma catalysis in percentage (SC) [179] are defined in Chapter 2.

4.1.3. Effect of Ar on CO_2 hydrogenation

Figure 4.2 shows the influence of argon content on the conversion of CO_2 at the same temperature of 150 ºC under different process conditions. Without using plasma, it is almost impossible to convert CO_2 or H_2 at such a low temperature in the thermal catalytic hydrogeneration of CO_2 (R3 and R4) [55, 195]. In the plasma process without a catalyst, the conversion of CO_2 significantly increases from 18.3% to 38.0% when increasing the Ar content from 0 to 60%. Similarly, in the plasma-catalytic hydrogeneration of CO_2, the CO_2 conversion is almost doubled (from 29.1% to 56.1%) when increasing the Ar content from 0 to 60%, while the carbon balance remains constant at 99%. Clearly, the presence of Ar in the plasma process has a positive effect on the conversion of CO_2.

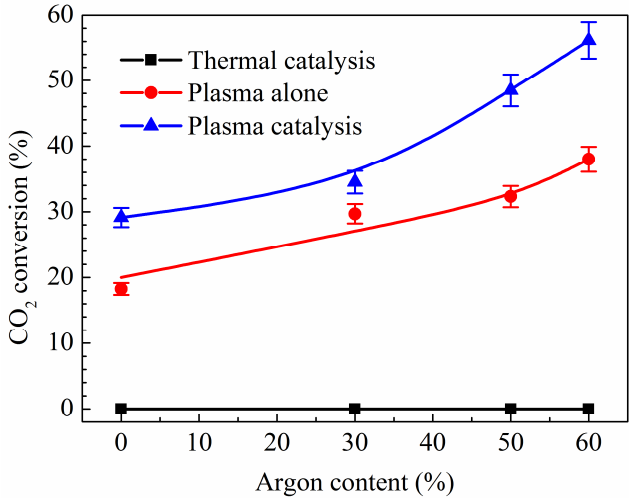

Figure 4.2 Effect of Ar content on CO_2 conversion using different process conditions at 150 °C. (H_2/CO_2 = 4: 1, total flow rate 69.2 ml min^{-1}, and discharge power of DBD 30 W).

The addition of Ar decreases the concentration of CO_2 and H_2 in working gas, although the specific input energy is kept the same. The addition of Ar in the mixture gas (CO_2 + H_2) increases the average first townsend ionisation coefficient of the feed gas, which makes the discharge form more easily. Ramakers *et al.* calculated the electron density, mean electron energy and rate constant relating to the dissociation of CO_2 in a DBD plasma [196]. They found that all these values increased when adding Ar in the CO_2 DBD. The ionisation of Argon requires a much higher electron energy (15.76 eV) than that for the excitation of Argon such as 11.55 eV for Ar ($4s^3P_2$) and 11.72 eV for Ar ($4s'^3P_0$) [197]. Thus, Ar is more likely to be excited to its metstable state (R5) rather than being ionised. The presence of metastable Ar species (Ar*) could create new reaction pathways for the dissociation of CO_2 and H_2 in the plasma-hydrogenation of CO_2, as shown in reaction R6 and R7 [197-199]. All these effects contribute to the enhanced conversion of H_2 and CO_2 when increasing the Ar content in the $Ar/CO_2/H_2$ DBD.

$$e^- + CO_2 \rightarrow CO + O + e^- \quad \text{(R3)}$$

$$e^- + H_2 \rightarrow H + H + e^- \quad \text{(R4)}$$

$$e^- + Ar \rightarrow e^- + Ar^* \quad \text{(R5)}$$

$$Ar^* + CO_2 \rightarrow CO + O + Ar \quad \text{(R6)}$$

$$Ar^* + H_2 \rightarrow H + H + Ar \quad \text{(R7)}$$

In addition, compared with the plasma reaction without a catalyst, the combination of the plasma with the Ni catalyst significantly enhances the conversion of CO_2 by 16%–60%. Increasing the Ar content in the feed also enhances the conversion of CO_2. The presence of Ar in the CO_2 DBD leads to a more uniform discharge, which might increase the contact area between the plasma and catalyst, and consequently enhances the plasma-catalyst interactions and plasma-assisted surface reactions. It is also worth noting that the CO_2 conversion in the plasma-catalytic hydrogenation of CO_2 is always higher than the sum of the CO_2 conversion in the plasma reaction without a catalyst and that of the thermal-catalytic reaction at the same temperature. These results clearly show a low temperature synergistic effect of plasma-catalysis, resulting from the interactions between the plasma and Ni/Al_2O_3 catalyst in the plasma-catalytic reaction. The selectivity and yield of CO and CH_4 under different conditions are shown in Figure 4.3. Neither CO nor CH_4 is detected in the thermal catalytic hydrogeneration of CO_2 at 150 ^oC, due to the very low conversion of CO_2 at such a low temperature. In the plasma reaction without a catalyst, increasing the Ar content from 0 to 60% significantly enhances the selectivity of CH_4 by 85%. By contrast, the selectivity of CO is almost constant when changing the Ar concentration in the CO_2 DBD. This phenomenon suggests that the presence of Ar* in the reaction might create new reaction routes for the formation of CH_4, resulting in the enhanced CH_4 selectivity and slightly decreased CO selectivity when increasing the Ar content.

To understand the reaction pathways for the formation of CH_4 in the plasma hydrogenation of CO_2, a zero-dimensional chemical kinetics model to simulate the plasma chemistry in the CO_2/H_2 DBD has been developed. In this model, the time evolution of the density of species is calculated based on the production and loss terms, as defined by the chemical reactions. The electron temperature is calculated with an energy balance equation, while the rate coefficients of the electron impact reactions are calculated in a Boltzmann equation model, as a function of the electron temperature and cross-section of target species [195]. The plasma chemistry used in the model is based on the plasma chemistry set established in the literature [200]. The reactions can be found in the appendix. Figure 4.4 shows the possible major reactions for the formation of CH_4 in the plasma process.

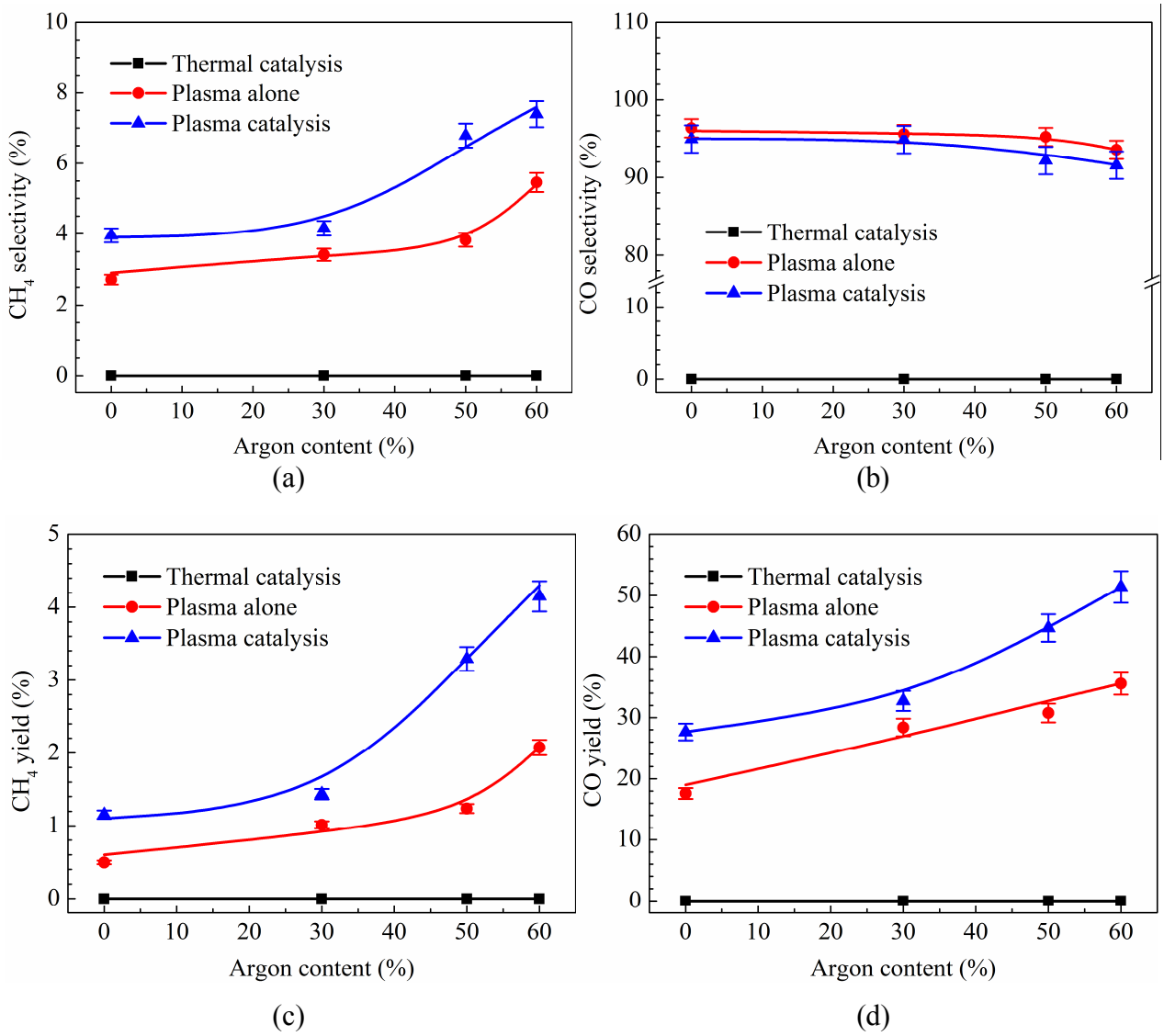

Figure 4.3 Effect of Ar content on: (a) CH_4 selectivity; (b) CO selectivity; (c) CH_4 yield and (d) CO yield in the hydrogenation of CO_2 at 150 ºC. (H_2/CO_2 = 4: 1, total flow rate 69.2 ml min^{-1}, and discharge power of plasma 30 W).

In the plasma hydrogenation of CO_2 without a catalyst, CH_4 is mainly formed from CO as described in reaction R8–R10 [201]. CH has been considered the most important precursor for the formation of CH_4. The plasma modelling shows that CH radicals are mainly generated through the reaction of carbon with H_2 (R11), while carbon could be produced from the dissociation of CO by electrons and Ar* (R13 and R14). The rate coefficient of reaction R12 to form CH_2 directly from carbon and H_2 is significantly lower than that of reaction R11 [202, 203]. The reaction of CO with H can produce HCO intermediate (R15) [204]. However, further hydrogenation of HCO can easily happen to produce H_2 and CO [205]. The rate coefficient of this reaction (R16) is similar

to that of reaction R15. The formation of CH from CHO is very difficult in the gas-phase reaction.

The selectivity of CH_4 is significantly lower than the CO selectivity as the dissociation of CO to form carbon is weak. In addition, no carbon deposition is observed in the DBD reactor as the formed carbon can react with H_2 to form CH_x species due to the high H_2/CO_2 ratio. The presence of Ar* could also contribute to the dissociation of CO to generate carbon (R14), which might explain the enhanced CH_4 formation with a higher Ar content in the reactants.

$$CH + H_2 \rightarrow CH_2 + H \quad \text{(R8)}$$

$$CH_2 + H_2 \rightarrow CH_3 + H \quad \text{(R9)}$$

$$CH_3 + H + M \rightarrow CH_4 + M \quad \text{(R10)}$$

$$C + H_2 \rightarrow CH + H \quad \text{(R11)}$$

$$C + H_2 \rightarrow CH_2 \quad \text{(R12)}$$

$$e^- + CO \rightarrow C + O + e^- \quad \text{(R13)}$$

$$Ar^* + CO \rightarrow C + O + Ar \quad \text{(R14)}$$

$$H + CO + M \rightarrow HCO + M \quad \text{(R15)}$$

$$HCO + H \rightarrow H_2 + CO \quad \text{(R16)}$$

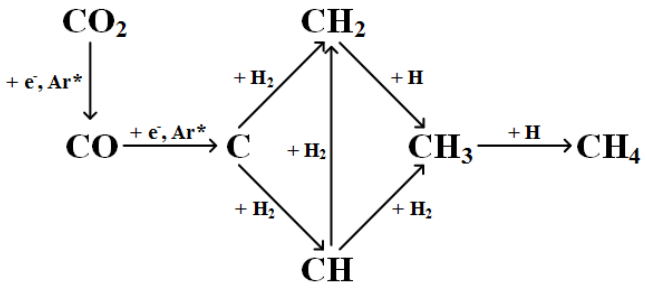

Figure 4.4 Major reaction pathways of CH_4 formation in the plasma-driven CO_2 hydrogenation.

Compared with the plasma hydrogenation of CO_2 without a catalyst, the coupling of DBD plasma with the Ni/Al_2O_3 catalyst further enhances the selectivity of CH_4 due to the creation of new reaction routes over the surface of the Ni/Al_2O_3 catalyst. A synergistic effect between the plasma and catalyst on the selectivity of CH_4 can be

clearly identified. The selectivity of CH_4 in the plasma-catalytic CO_2 hydrogenation (S_{p+c}) is always larger than the sum of the CH_4 selectivity in the plasma-alone and catalysis-alone processes ($S_{p+c} > S_p + S_c$). However, the presence of the Ni/Al_2O_3 catalyst in the plasma-hydrogenation of CO_2 has a weak effect on the selectivity of CO. The reaction mechanisms proposed for catalytic CO_2 methanation over a Ni catalyst involve the conversion of CO_2 to CO, and subsequent reactions following the same mechanism as CO methanation [35]. In the plasma-catalytic CO_2 hydrogenation, the adsorbed CO can originate from the dissociation of CO_2 in the gas phase (R3) [55] or the dissociation of adsorbed CO_2 on the catalyst surface (R17 and R18) [206, 207]. It has been proposed that CH_4 can be formed from the formation of the CHO intermediate (R19) and its hydrogenation (R20, R24 and R25) [208], or the formation of surface carbon in CO dissociation (R21 and R22) and its interaction with hydrogen (R23–R25) [35, 206].

$$CO + M \rightarrow CO_{ads} \quad \text{(R17)}$$

$$CO_{2,\,ads} \rightarrow CO_{ads} + O_{ads} \quad \text{(R18)}$$

$$CO_{ads} + H_{ads} \rightarrow CHO_{ads} \quad \text{(R19)}$$

$$CHO_{ads} \rightarrow CH_{ads} + O_{ads} \quad \text{(R20)}$$

$$CO_{ads} \rightarrow C_{ads} + O_{ads} \quad \text{(R21)}$$

$$2\,CO_{ads} \rightarrow C_{ads} + CO_{2,\,ads} \quad \text{(R22)}$$

$$C_{ads} + H_{ads} \rightarrow CH_{ads} \quad \text{(R23)}$$

$$CH_{ads} + H_{ads} \rightarrow CH_{2,\,ads} \quad \text{(R24)}$$

$$CH_{2,\,ads} + 2\,H_{ads} \rightarrow CH_4 \quad \text{(R25)}$$

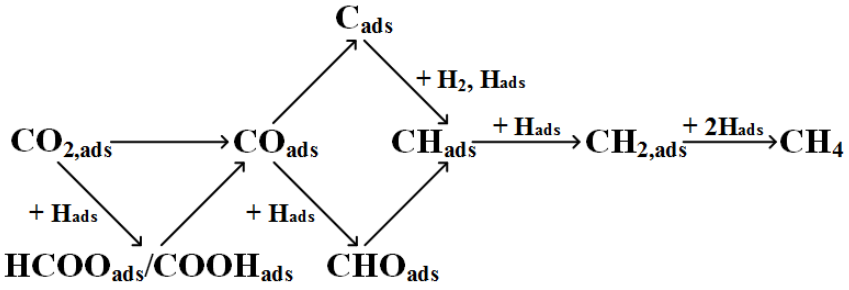

Figure 4.5 Possible major reactions for the formation of CH_4 on the Ni/Al_2O_3 catalyst.

The yield of CH_4 and CO increases with the Ar content in the plasma process with or without the Ni/Al_2O_3 catalyst. For instance, increasing the Ar content from 0 to 60% significantly enhances the CH_4 yield by 250% in the plasma-catalytic process, while the CO yield is only increased by 85.6%. Placing the Ni/Al_2O_3 catalyst in the DBD also enhances the yield of CH_4 and CO compared with the plasma reaction in the absence of the Ni catalyst. A significant synergistic effect between the plasma and the Ni catalyst on the yield of CH_4 and CO can be clearly identified in Figure 4.3.

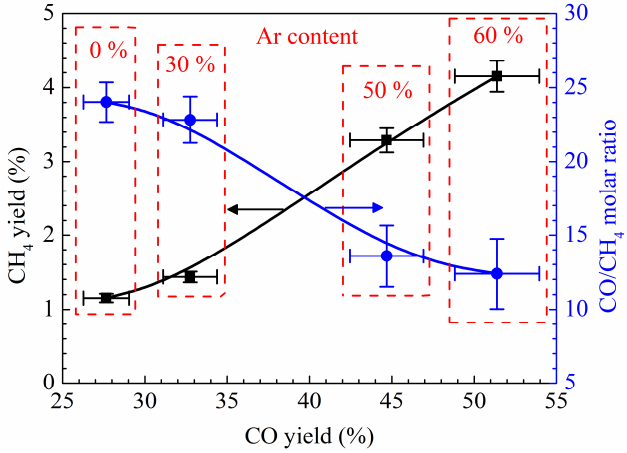

Figure 4.6 Effect of Ar content on the yield of gas products (CO/CH_4) and CO/CH_4 molar ratio in the plasma-catalytic CO_2 hydrogenation process. (H_2/CO_2 = 4: 1, total flow rate 69.2 ml min^{-1}, and discharge power of plasma 30 W).

Figure 4.6 shows the influence of changing the Ar content on the yield of CO and CH_4, and the CO/CH_4 molar ratio in the product during the plasma-catalytic CO_2 hydrogenation. The yield of CH_4 changes more quickly than that of CO when increasing the Ar content up to 60%. Thus, raising the Ar content from 0 to 60% significantly reduces the CO/CH_4 molar ratio from 24 to 12. It is known that using different catalysts can control the selectivity of target products and change the distribution of different products in a chemical reaction. This interesting phenomenon suggests that the molar ratio of CO/CH_4 in the plasma-catalytic hydrogenation of CO_2 can also be controlled by changing the Ar content.

Figure 4.7 compares the fuel production efficiency of CO_2 hydrogenation under different process conditions. Clearly, the combination of the DBD with the Ni catalyst shows a higher fuel production efficiency due to the plasma-catalytic synergy. In the

plasma-catalytic hydrogenation of CO_2, increasing the Ar content slightly enhances the fuel production efficiency of the process. By contrast, the fuel production efficiency of the plasma reaction without the Ni catalyst reaches a maximum at an Ar content of 30%, then decreases with further increasing of the Ar content. The different evolutions of the fuel production efficiency between the plasma-catalytic process and plasma process when changing the Ar content might be attributed to the following effects. The addition of Ar decreases the CO_2 and H_2 content in feed gas since the total flow rate is fixed. At a higher Ar content (*e.g.* > 30%), some of the input energy might go in to the ionisation of Ar rather than the conversion of CO_2. However, in the plasma-catalytic reaction, higher Ar content leads to a more uniform discharge, which significantly enhances the interactions between the plasma and Ni/Al_2O_3 catalyst and consequently the reaction performance of the plasma-catalytic hydrogenation of CO_2. This effect is predominant over the waste of input energy (due to higher Ar content) in the plasma-catalytic process.

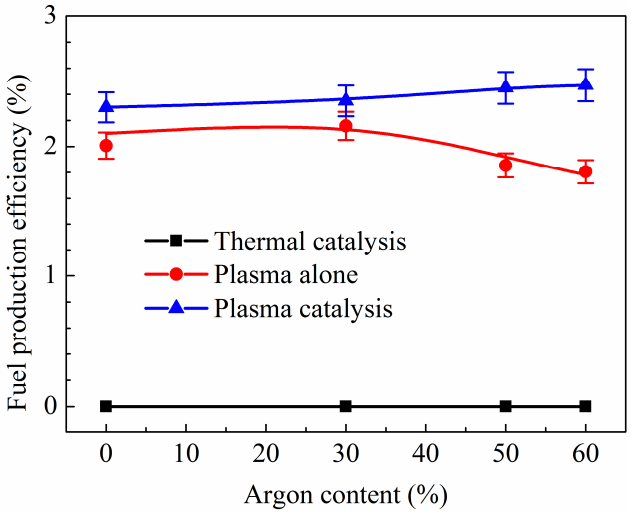

Figure 4.7 Effect of Ar content on the energy efficiency of CO_2 hydrogenation under different process conditions. (H_2/CO_2 = 4: 1, total flow rate 69.2 ml min^{-1}, discharge power of plasma 30 W, and temperature 150 °C).

4.1.4. Effect of Ar on the plasma-catalytic synergy

Synergistic capacity is used to quantify the reaction performance of the plasma-catalytic hydrogenation of CO_2, compared with that using plasma alone or catalyst alone at the same temperature (150 °C), as shown in Table 4.1. The plasma-catalytic synergy in terms of the conversion of CO_2, the selectivity and yield of CO and CH_4 and

the energy efficiency of the process can be clearly seen even without Ar (0%) in the feed gas. For instance, in the plasma-catalytic hydrogenation of CO_2 without Ar, the conversion of CO_2 is 59.6% larger than the sum of the CO_2 conversion using the plasma hydrogenation (without catalyst) and thermal catalysis (without plasma) at the same temperature. The most significant plasma-catalytic synergy is highlighted by the yield of CH_4, which has a synergistic capacity of 132% in the absence of Ar and reaches a peak value of 166% at an Ar content of 50%. The synergistic capacity of the plasma-catalytic process is significantly enhanced when increasing the Ar content from 30% to 60%. As discussed previously, the combination of plasma and Ni catalyst has a more significant effect on the enhanced reaction performance (conversion, selectivity, yield and energy efficiency) compared with the plasma reaction without the Ni catalyst at a higher Ar content (> 30%). Enhanced contact area between the plasma and catalyst and the resulting strong interactions between them when increasing the Ar content from 30% to 60% could be the main driving force for the significant synergistic capacity of the plasma-catalytic process, although increasing the Ar content wastes energy due to the excitation and ionisation of Ar atoms.

Table 4.1 Effect of Ar content on the synergistic capacity (*SC*) of the processes. (H_2/CO_2 = 4: 1, total flow rate 69.2 ml min^{-1}, discharge power of plasma 30 W, and temperature 150 °C).

Ar (%)	SC_C (%)	SC_Y (%)			SC_S (%)	SC_{FPE} (%)
		CH_4	CO	Total		
0	59.6	132	57.3	45.6	59.5	17.1
30	16.2	42	15.3	16.3	21.9	6.5
50	50.0	166	45.2	49.9	77.5	32.2
60	47.7	100	44.5	47.6	35.5	20.8

4.1.5. Effect of Ar on electrical properties of the DBD

Figure 4.8 shows the Lissajous figures of the plasma-catalytic CO_2 hydrogenation with different Ar contents at the same discharge power of 30 W. Although the size of the Lissajous figures change with the Ar content, the gradient of the edges of the parallelograms is maintained when changing the Ar content from 0 to 50%. Various

electrical properties of the DBD can be calculated through the Lissajous figure, including C_{total}, C_{eff} (measured from the gradient on the Lissajous figure), U_b, Q_{pp}, Q_d and Q_{trans}. Theoretically, the effective capacitance C_{eff} is equal to the capacitance of the dielectric material (*i.e.* C_{quartz}) when the discharge gap is "fully bridged" by the discharge. However, if the gap is not "fully bridged" and fails to transfer all of the charge accumulated on the dielectric material, partial discharging occurs and the value of C_{eff} could be smaller than C_{quartz} [30]. Table 4.2 shows that the Ar content has a very weak effect on the effective capacitance of the DBD reactor and the properties of charges. However, the calculated C_{eff} (around 139 pF) is lower than the C_{quartz} calculated by Equation 6 (154 pF), which suggests the occurrence of partial discharging. The energy-efficiency of the plasma reaction decreases when partial discharging occurs, due to the presence of charge residue on the dielectric layer. As the Ar content increases, the slightly increased effective capacitance of the reactor (C_{eff}) suggests that more power is injected into the plasma for chemical reactions rather than deposited and 'wasted' on the dielectric surface. This finding agrees with the enhanced CO_2 conversion and yield of CH_4 and CO when increasing the Ar content in the reactants.

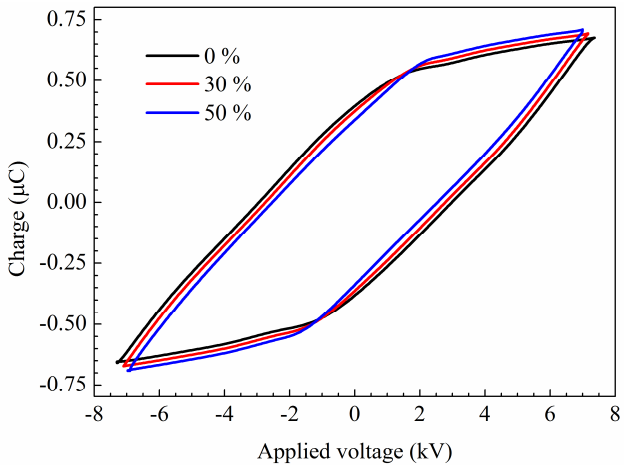

Figure 4.8 Effect of Ar content on Lissajous figures of the DBD in the plasma-catalytic CO_2 hydrogenation process. (H_2/CO_2 = 4: 1, total flow rate 69.2 ml min^{-1}, and discharge power of plasma 30 W).

The equivalent relative dielectric constant of the packing materials is different from the relative dielectric constant of pure NiO and Al_2O_3 (see Definition section). However it is difficult to measure the equivalent relative dielectric constant of the packing materials (including the Ni catalyst and pure alumina) $\varepsilon_{packing}$ in a DBD reactor,

especially when $\varepsilon_{packing}$ is simultaneously affected by the gas gap in packing, the composition of the catalyst, the loading and redox status of supported metal and the working status of plasma. However in this work, by solving the formula of C_{total}, C_{quartz} and C_{gap} in Equation 6, the equivalent $\varepsilon_{packing}$ can be estimated as 0.79. This value is much smaller than the relative dielectric constant of Al_2O_3 (9 to 10), implying that the deposition of Ni particles on the surface of Al_2O_3 beads significantly changes its dielectric constant.

As described previously, Q_{pp}, Q_d and Q_{trans} evaluate the charge transferred through the DBD reactor during one "discharge off" phase and one "plasma on" phase. A slight increase (~1.5%) is observed for all these parameters when changing the Ar content. The change is almost neglectable, although such phenomenon is reasonable, since the discharge power is kept at 30 W. Increasing the Ar content slightly decreases the applied voltage U_{pp} (Figure 4.9) and accordingly increases the discharge current; thus assisting the charge transfer. The increased discharge current is reflected by the increased Q_d, and the enhanced charge transfer can be evidenced by the enlarged Q_{trans}, as summarised in Table 4.2.

Table 4.2 Effect of Ar content on the capacitances of the reactor and charges in the plasma-catalytic CO_2 hydrogenation. (H_2/CO_2 = 4: 1, total flow rate 69.2 ml min^{-1}, and discharge power of plasma 30 W).

Ar content (%)	C_{eff} (pF)	C_{total} (pF)	Q_{pp} (μC)	Q_d (μC)	Q_{trans} (μC)
0	138.2	27.8	1.35	1.21	0.93
30	139.1	27.2	1.37	1.23	0.99
50	139.4	27.8	1.40	1.25	1.03

Figure 4.9 shows the effect of the Ar content on the peak-to-peak voltage and breakdown voltage of the DBD in the presence of the Ni catalyst. At a constant discharge power, increasing the Ar content from 0 to 50% slightly decreases the U_{pp} (from 14.7 to 14.1 kV), which suggests that the discharge current would increase with increasing Ar content at a fixed discharge power, and contribute to the enhanced CO_2 conversion at a higher H_2 content. The breakdown voltage U_b also decreased from 3.1 to 2.6 kV when increasing the Ar content from 0 to 50%. As mentioned previously, the addition of Ar increases the average first Townsend ionisation coefficient α of the feed

gas. Auriemma *et al.* calculated the Townsend coefficient of a gas mixture with various Ar/CO_2 molar ratios. They found that the coefficient of the gas mixture significantly increases with the Ar concentration [209]. In addition, as CO_2 is an electro-negative gas, the introduction of Ar lowers the chance of free electron attachment on CO_2 molecules, facilitating the acceleration of free electrons [196]. Moreover, the increasing amount of Ar decreases the average dielectric strength of the working gas [210]. As a consequence of all these factors, the feed gas between the electrodes would electrically breakdown at a lower voltage U_b, and the DBD plasma would also be sustained at a lower voltage U_{pp}.

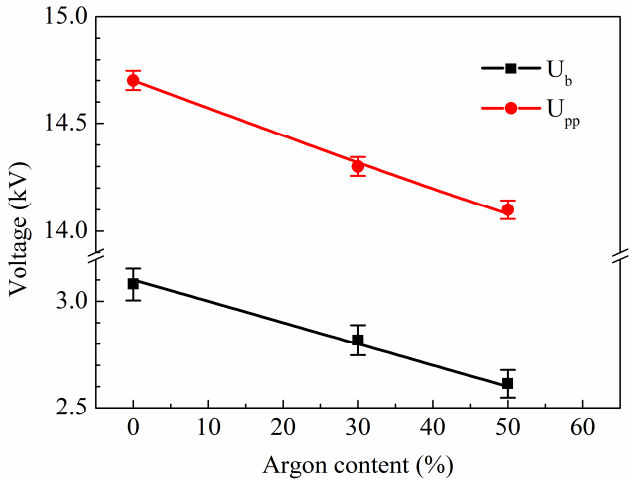

Figure 4.9 Effect of Ar content on breakdown and peak-to-peak voltages of the DBD in the plasma-catalytic hydrogenation. (H_2/CO_2 = 4: 1, total flow 69.2 ml min^{-1}, and discharge power of plasma 30 W).

4.2. CO_2 hydrogenation using a Ni/Al_2O_3 catalyst in a temperature controlled DBD reactor

In this section, hydrogenation of CO_2 to CO and CH_4 has been carried out in a coaxial DBD reactor with and without a Ni/Al_2O_3 catalyst at atmospheric pressure and elevated temperature to understand the temperature dependence of the plasma-catalytic hydrogenation process. Ar was used as dilution gas according to the results in the previous section. The effect of temperature on the CO_2 hydrogenation process under three different operating conditions (plasma only, plasma-catalysis and thermal catalysis) has been investigated in terms of the conversion of CO_2, the selectivity and

yield of CO and CH_4 products and the energy efficiency of the process. The individual contribution of DBD plasma and external heating to the performance of plasma-catalytic CO_2 hydrogenation is also discussed.

4.2.1. Experimental setup

The setup was very similar to that in the previous section. In the current case, the H_2: CO_2: Ar molar ratio in the feed gas was 4: 1: 5. The total feed flow rate was fixed at 69.2 ml min^{-1}.

30 wt.% Ni/Al_2O_3 catalyst was prepared by the impregnation method. $Ni(NO_3)_2$ (Alfa Aesar, ACS reagents) and Al_2O_3 were used as the metal precursors and support respectively. After calcination at 400 °C for 5 hrs, weighed support was added into the solution of precursors, well-mixed and impregnated for 3 hrs, then dried at 90 °C overnight, followed by calcination at 540 °C for 3 hrs. This calcination temperature was chosen to guarantee the catalyst being stable at high temperatures. 0.4 g of granular catalyst was packed and sandwiched into the reactor with quartz wool. Prior to the plasma-catalytic hydrogenation, the catalyst was reduced in an argon-hydrogen discharge at an input power of 40 W (50 ml min^{-1}, 20 vol. % H_2) for 40 minutes in the same DBD reactor.

The input power of the plasma was measured by a power meter connected between the power supply and mains. The input power was kept at 38 W when investigating the effect of temperature on CO_2 hydrogenation, and the temperature for all three conditions was controlled by adjusting the input power of external heating, monitored by a fibre optic thermometer (FOB102). When investigating the contribution of plasma power and heating power to CO_2 hydrogenation, the temperature was kept at 320 °C for all three conditions, and both of the input power of DBD plasma and external heating were adjusted.

Definitions of the conversion (X) of CO_2, the selectivity (S) and yield (Y) of the main products, the H_2/CO_2 molar ratio and carbon balance (B), the total energy efficiency (E) and fuel production efficiency (FPE) of the process can be found in Chapter 2.

4.2.2. XRD and N_2 adsorption–desorption analysis

Figure 4.10 shows the XRD patterns of the support and catalyst. Three major diffraction peaks located at 2θ = 37.6°, 45.9° and 67.0° can be observed on the figure, corresponding to the cubic structure of alumina crystallite (JCPDS 10–425) [37]. The diffraction peaks corresponding to NiO crystallite (JCPDS 1–75–197) can also be clearly seen on the XRD pattern of the Ni/Al_2O_3 catalyst [98].

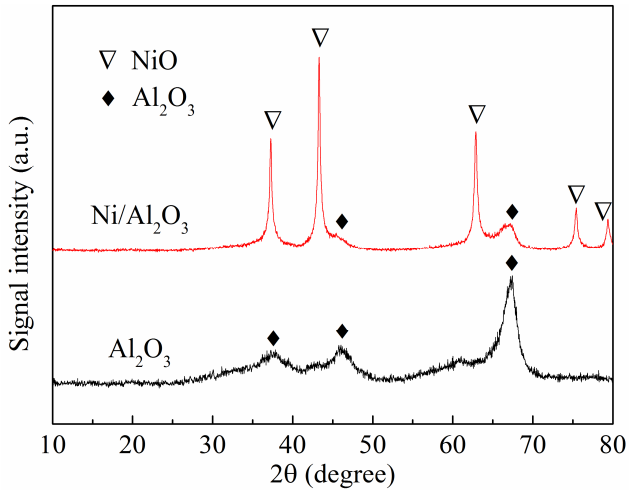

Figure 4.10 XRD patterns of the support and catalyst. (▽ NiO, ◆ Al_2O_3)

Table 4.3 shows the surface properties of the support and the catalyst. The BET specific surface area of the Al_2O_3 support was 174.6 $m^2\ g^{-1}$. For comparison, the specific surface area of Ni/Al_2O_3 catalyst decreased to 105.5 $m^2\ g^{-1}$, due to the coverage of the support's surface by NiO. This can be evidenced by the decreased total pore volume on the Ni/Al_2O_3 catalyst.

Table 4.3 Physicochemical characteristics of the fresh catalyst.

Catalyst	S_{BET} ($m^2\ g^{-1}$)	Total pore volume ($cm^3\ g^{-1}$)	Average pore size (nm)
Al_2O_3	174.6	0.44	4.9
Ni/Al_2O_3	105.5	0.28	4.9

4.2.3. TPR analysis of the Ni/Al_2O_3 catalyst

The reducibility is very important for the reactivity and performance of a catalyst in CO_2 hydrogenation with or without a plasma. The TPR result of Ni/Al_2O_3 catalyst

shows a broad feature with the first peak located at 440 ºC (Figure 4.11), recognised as the reduction of bulk NiO. The overlapping peak locates at 590 °C corresponds to the reduction of less active NiO. Compared to bulk NiO, the higher reduction temperature of less active NiO was due to its interaction with the Al_2O_3 support [120]. This portion of NiO is more difficult to be reduced due to their interaction with the support.

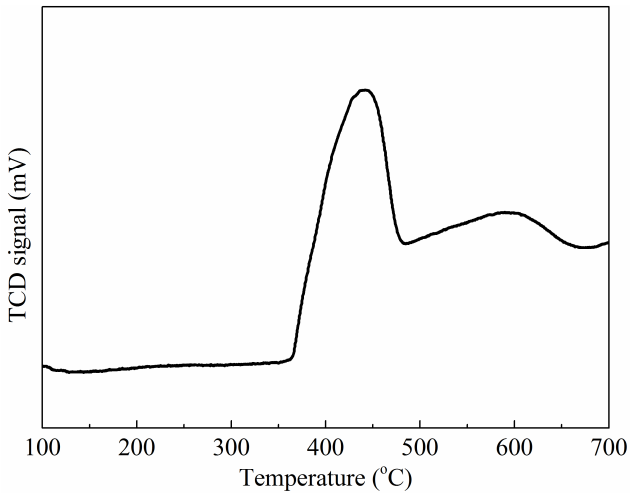

Figure 4.11 TPR profile of the Ni/Al_2O_3 catalyst.

4.2.4. Effect of temperature on the CO_2 hydrogenation

Figure 4.12 shows the effect of temperature on the CO_2 hydrogenation process. In the plasma hydrogenation without a catalyst, the conversion of CO_2 decreased from 25.2% to 19.6% when the temperature increased from 260 ºC to 500 ºC. Probably resulting from the change of discharge-mode in response to the increased temperature. Atmospheric-pressure DBD plasma can be operated in filamentary, patterned or completely diffuse mode, depending on the composition of feed gas, the surface properties of the dielectric layer and the operational conditions [211]. The temperature of the feed gas and reactor determines the discharge-mode, and consequently affecting the properties of corresponding plasma and plasma-driven reactions, such as the conversion of feed gas, the burning voltage and discharge power of plasma [212-214]. For the same reason, in this chapter, the discharge-mode of the plasma was expected to transform when the temperature increased. Subsequently the conversion of CO_2 decreased when the temperature increased.

In thermal catalytic hydrogenation, CO_2 was only effectively converted when the temperature was above 350 °C. The CO_2 conversion increased quickly when the temperature was higher than 320 °C and achieved its maximum (61.1%) at 380 °C. The CO_2 conversion started to decrease when the temperature further increased, ascribed to the limitation of thermodynamic equilibrium. However, the CO_2 conversion was still approaching the equilibrium value during the same process, suggesting that the reaction rate of catalytic hydrogenation was promoted at elevated temperatures. It can be concluded that the thermal-catalytic conversion of CO_2 in this work was highly dependent on temperature and the optimal temperature was above 350 °C.

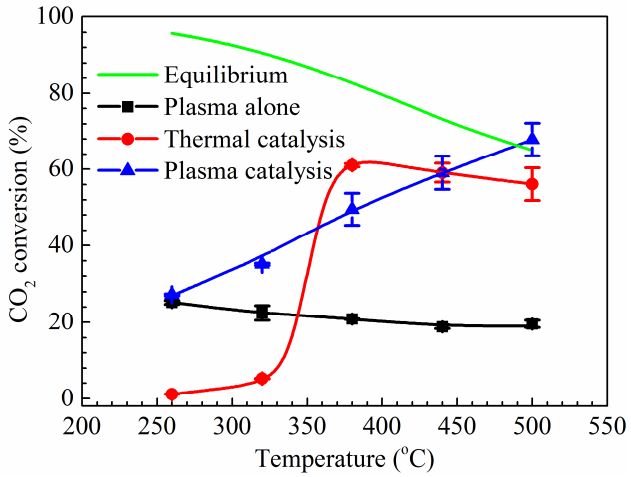

Figure 4.12 CO_2 conversion during the CO_2 hydrogenation. (H_2/CO_2 = 4:1, total flow rate 69.2 ml min^{-1}, and Ar content 50%)

In the plasma-catalytic CO_2 hydrogenation, the conversion of CO_2 was enhanced compared to the plasma-alone process, and increased from 27.2% to 67.9% when the temperature increased from 260 °C to 500 °C. Interestingly, when the temperature was lower than 320 °C, the CO_2 conversion of plasma-catalytic hydrogenation was larger than the sum of those obtained in plasma alone and thermal catalytic hydrogenation, clearly indicating the synergy between plasma and catalyst at this temperature. When the temperature was lower than 360 °C or higher than 440 °C, the plasma-catalytic hydrogenation achieved higher CO_2 conversion than thermal catalysis.

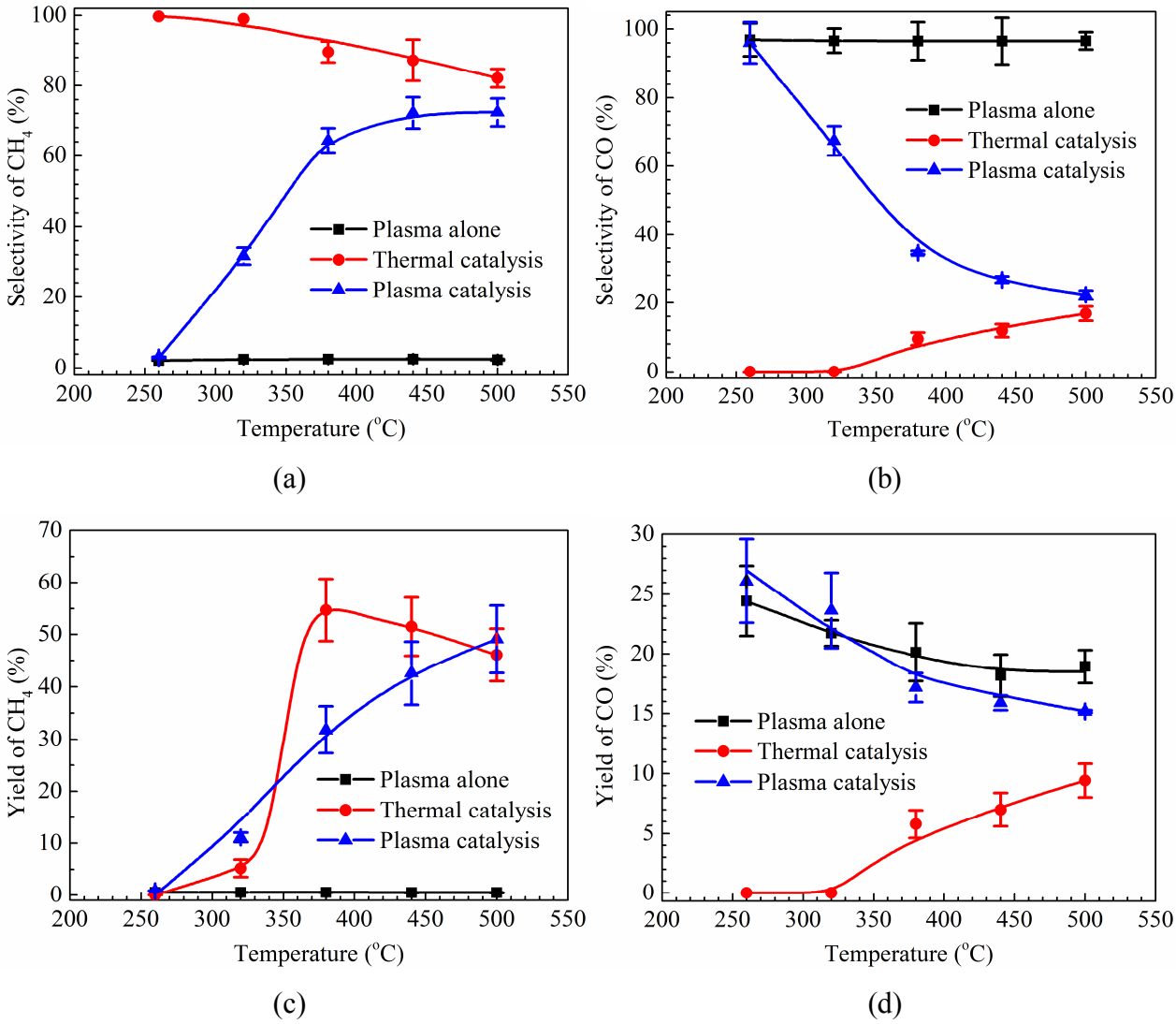

Figure 4.13 Effect of temperature on CO_2 hydrogenation: (a) Selectivity of CH_4; (b) Selectivity of CO; (c) Yield of CH_4; (d) Yield of CO. (H_2/CO_2 = 4:1, total flow rate 69.2 ml min^{-1}, and Ar content 50%)

Figure 4.13 shows the influence of temperature on the selectivity and yield of CH_4 and CO. When the CO_2 hydrogenation was performed without a catalyst, the selectivity of CO was always above 96%, regardless of temperature, suggesting that CO was the prominent product of this plasma-driven reaction. Notably, the yield of CO slightly decreased when the temperature increased, ascribing to the temperature dependence of CO_2 conversion. In the thermal catalytic hydrogenation process, the selectivity of CH_4 decreased from 99.9% to 82% when the temperature increased from 260 °C to 500 °C, due to the limitation of thermodynamic equilibrium. Although the selectivity of CH_4 was nearly 100% at temperatures below 260 °C, the actual yield of CH_4 was very low

due to the poor conversion of CO_2. For comparison, both of the selectivity and yield of CO were nearly 0% below 320 °C. The increased temperature showed a limited enhancement on the production of CO. Remarkably, the CH_4 selectivity of thermal catalytic hydrogenation was always higher than that of plasma-catalytic hydrogenation, suggesting that the Ni/Al_2O_3 catalyst particularly improved the methanation of CO_2, while the plasma process might be more suitable for the production of CO. In the plasma-catalytic CO_2 hydrogenation, the elevated temperature significantly increased selectivity and yield of CH_4, due to the temperature dependence of the Ni/Al_2O_3 catalyst. In other words, the catalytic CO_2 methanation as explained in Figure 4.5 was promoted at elevated temperatures.

Figure 4.14 shows the effect of temperature on the total energy efficiency for the production of CH_4 and CO and the fuel production efficiency of the CO_2 hydrogenation process. In the plasma-driven hydrogenation process without a catalyst, the efficiency decreased when the temperature increased, attributed to decreased CO_2 conversion. For comparison, the energy efficiency of thermal catalytic hydrogenation exhibited a temperature dependence. The total energy efficiency increased quickly with the temperature and achieved its maximum of 0.034 mmol kJ^{-1} at 340 °C, while the fuel production efficiency exhibited a very similar pattern and achieved its maximum of 2.5% at the same temperature of 340 °C. In a narrow temperature range between 370 °C and 440 °C, the thermal catalytic CO_2 hydrogenation achieved the best total energy efficiency and fuel production efficiency among all the three operational conditions. In the plasma-catalytic CO_2 hydrogenation, the total energy efficiency decreased from 0.034 to 0.027 mmol kJ^{-1} when the temperature increased from 260 °C to 500 °C, while the fuel production efficiency firstly increased from 1.0% and achieved its maximum of 2.0% at 440 °C, then slightly decreased to 1.7% at 500 °C. A summary of energy efficiency can be found in Table 4.6.

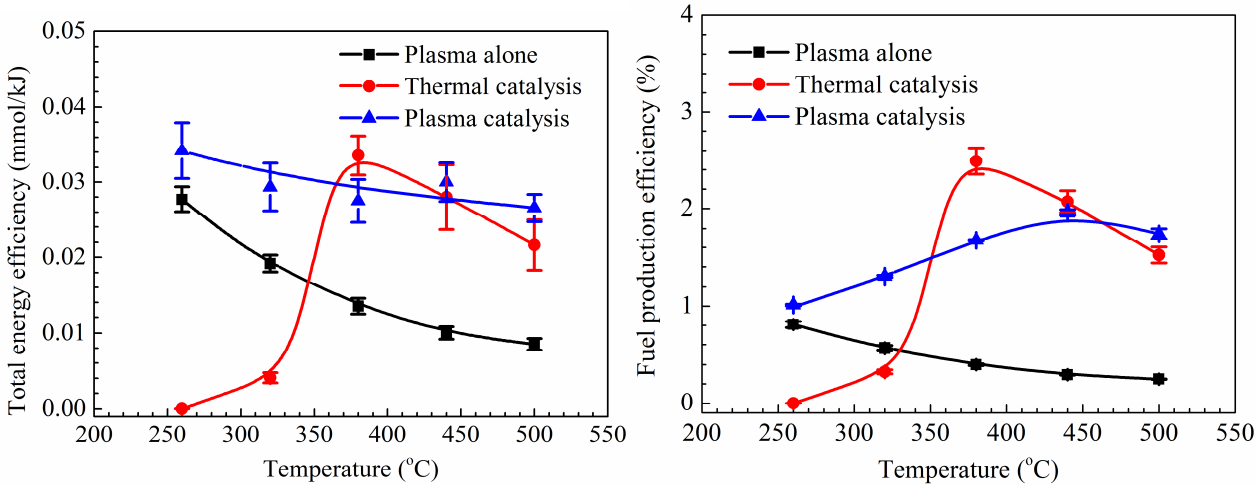

(a) (b)

Figure 4.14 (a) Total energy efficiency and (b) fuel production efficiency of the CO_2 hydrogenation. (H_2/CO_2 = 4:1, total flow rate 69.2 ml min^{-1}, and Ar content 50%)

4.2.5. Contribution of heating and plasma power on plasma-catalytic CO_2 hydrogenation

To obtain a more pronounced understanding of the process, a detailed insight into the individual effect of plasma power and heating power on hydrogenation is necessary. In this section, the input power of both the DBD plasma and tube furnace were adjusted while maintaining the temperature of the reactor at constant (320 °C). Accordingly, the value δ describes the ratio of plasma power over heating power, it was adjusted to 0, 0.14, 0.30, 0.62 and 1.09 respectively, as calculated by power and listed in Table 4.4. When the plasma/heating power ratio was 0, the hydrogenation was actually a thermal catalytic process. When the ratio was 1.09, the CO_2 hydrogenation was operated under plasma-catalytic condition and at 320 °C, being exactly the same as discussed in the previous section.

$$\delta = \frac{\text{Plasma power (W)}}{\text{Heating power (W)}} \qquad (14)$$

Table 4.4 Value δ and corresponding input powers for plasma and heating. (H_2/CO_2 = 4:1, total flow rate 69.2 ml min^{-1}, and Ar content 50%)

	Input power (W)	
δ	Plasma power	Heating power
0	0	75
0.14	9	64
0.30	17	56
0.62	28	45
1.09	38	35

Figure 4.15 shows the effect of value δ on the CO_2 conversion in plasma-catalytic CO_2 hydrogenation at 320 °C. Clearly, the CO_2 conversion became higher when the plasma power increased. When δ increased from 0 to 0.30, the conversion of CO_2 increased from 5.2% to 24.2%. It is reasonable because in addition to the heating effect, the DBD plasma produced a cluster of reactive species such as energetic electrons, ions, excited molecules and radicals, effectively dissociating the H_2 and CO_2 molecules at 320 °C. In addition, the interactions between plasma and catalyst activated the metallic active sites on the catalyst, enhanced the adsorptive surface reaction of gaseous species on the Ni/Al_2O_3 catalyst, and improved the conversion of reactants in the feed gas.

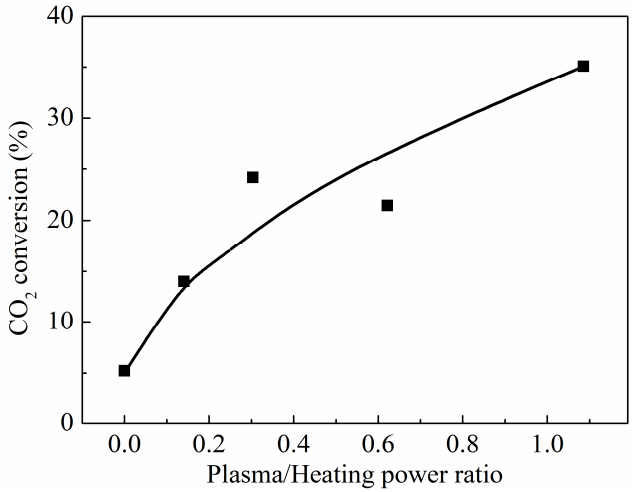

Figure 4.15 Conversion of CO_2 in the plasma-catalytic CO_2 hydrogenation. (H_2/CO_2 = 4:1, total flow rate 69.2 ml min^{-1}, and Ar content 50%)

Figure 4.16 shows the influence of value δ on the selectivity and yield of CH_4 and CO. When δ changed from 0 to 1.09, the selectivity of CO was improved from 0 to 67.4%, while the selectivity of CH_4 decreased from 99.0% to 31.6%. This result again

confirms that the DBD plasma enhanced the CO production while the Ni/Al_2O_3 catalyst improved the production of CH_4. The yield of CO also increased with the plasma/heating power ratio. For instance when δ increased from 0.14 to 1.09, the yield of CO increased from 5% to 23.6%, while the yield of CH_4 slightly increased from 9% to 11.1% as a combined result of enhanced CO_2 conversion and suppressed CH_4 selectivity.

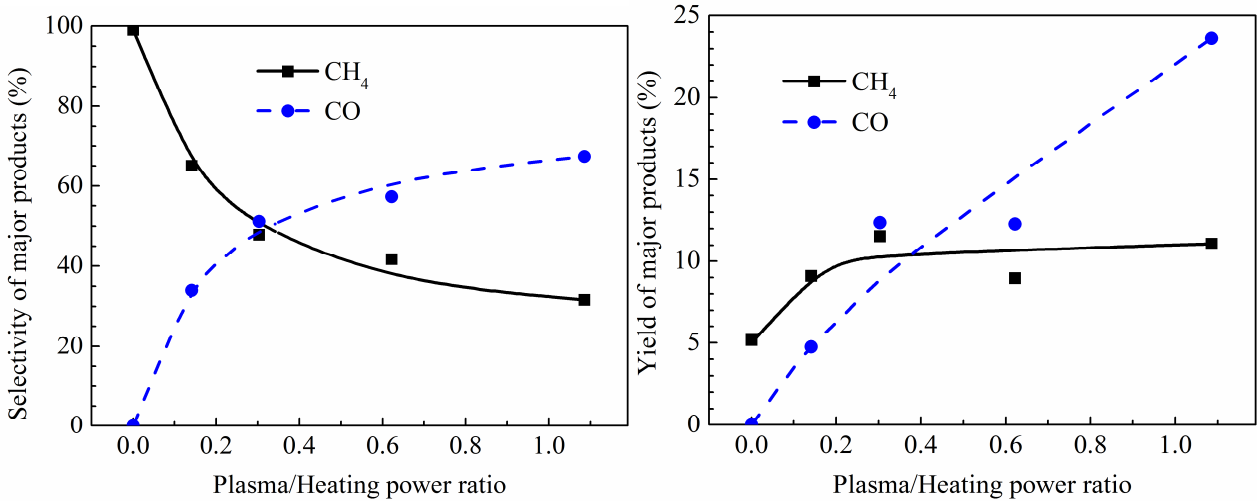

Figure 4.16 (a) Selectivity and (b) yield of CH_4 and CO during the hydrogenation. (H_2/CO_2 = 4:1, total flow rate 69.2 ml min^{-1}, and Ar content 50%)

Figure 4.17 compares the effect of value δ on the total energy efficiency and fuel production efficiency. The total energy efficiency significantly increased from 0.004 to 0.029 mmol kJ^{-1} as δ increased from 0 to 1.09. Since the total energy efficiency was calculated as the amount of product detected after consuming per unit of electrical power, the result implies that the plasma was more energy-efficient at converting CO_2 into CO and CH_4 at 320 °C. Similarly, the fuel production efficiency of the plasma-catalytic CO_2 hydrogenation process increased from 0.3% to 1.3% as δ increased from 0 to 1.09.

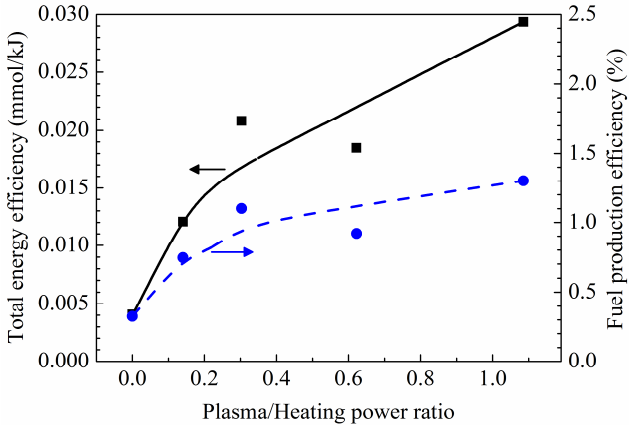

Figure 4.17 Total energy efficiency and fuel production efficiency during the CO_2 hydrogenation. (H_2/CO_2 = 4:1, total flow rate 69.2 ml min^{-1}, and Ar content 50%)

4.3. CO_2 hydrogenation over supported Co, Ni catalysts in a temperature controlled DBD reactor

In this section, plasma-catalytic CO_2 hydrogenation for the production of CO and CH_4 was carried out in a coaxial DBD reactor using Co/SiO_2, Co/Al_2O_3, Ni/SiO_2 and Ni/Al_2O_3 catalysts. As mentioned in the introduction, Ni and Co based transitional metal catalysts have been extensively used for the conversion of CO_2, such as dry reforming of methane and CO_2 hydrogenation, due to their low cost and comparable catalytic activity comparing with noble catalysts [73]. SiO_2 and Al_2O_3 are also widely used as supports for catalysts in CO_2 conversion reactions due to their economic prices, robust mechanical strength and decent thermal stability [74, 75].

4.3.1. Experimental setup

The experimental setup in this section was the same as explained in Chapter 2. The input power was 38 W, measured by a power meter connecting the power supply and mains. A H_2 and CO_2 mixture gas with a molar ratio of 4:1 was used as the reactants and 50% Ar (volume ratio) in the feed gas as dilution gas. The total feed flow rate was fixed at 69.2 ml min^{-1}.

The 30 wt.% Co/SiO_2, Co/Al_2O_3, Ni/SiO_2 and Ni/Al_2O_3 catalysts were prepared by impregnation method using nitrate salts (Alfa Aesar, ACS reagents) as the metal precursors and using fumed SiO_2 or Al_2O_3 powder as the support. Weighed support was calcinated at 400 ^oC for 5 hrs before being added to the solution of nitrate salts. The

mixture slurry was continuously stirred for 1 hr and impregnated for 3 hrs, then dried at 90 °C overnight, followed by calcination at 540 °C for 3 hrs. 0.4 g of granular catalyst was packed and sandwiched into the reactor with quartz wool. Prior to the plasma-catalytic hydrogenation, the catalyst was reduced in an argon-hydrogen discharge at an input power of 40 W (50 ml min^{-1}, 20 vol. % H_2) for 40 minutes in the same DBD reactor. The temperature of the DBD reactor was measured and controlled as explained in the previous section.

Definitions of the conversion (X) of CO_2, the selectivity (S) and yield (Y) of the main products, the H_2/CO_2 molar ratio and carbon balance (B), the total energy efficiency (E) and fuel production efficiency (FPE) of the process are explained in Chapter 2.

4.3.2. XRD analysis of catalysts

Figure 4.18 shows the XRD patterns of supports and fresh catalysts. Three major diffraction peaks can be observed at $2\theta = 37.6°$, 45.9° and 67.0°, corresponding to the cubic structure of alumina crystallite (JCPDS 10–425) [37]; while only one broad peak of amorphous SiO_2 can be found at $2\theta = 22°$ (JCPDS 29–0085). The reflection peaks of NiO (JCPDS 1–75–197) and Co_3O_4 (JCPDS 42–1467) can also be clearly seen on the XRD patterns of relevant catalysts [98]. The Scherrer equation was used to estimate the size of crystallites on the catalysts [215]. It was found that the Ni/Al_2O_3 catalyst had a smaller crystallite size than that of the Co/Al_2O_3 catalyst. Similarly, the Ni/SiO_2 catalyst had a smaller crystallite size than that of the Co/SiO_2 catalyst, as summarised in Table 4.5. The Ni/Al_2O_3 catalyst had the smallest crystallite size (29.7 nm) among all the catalysts. This result implies that the Ni catalysts might have stronger interaction with Al_2O_3 or SiO_2 support than the Co catalysts, resulting in smaller crystallite sizes. It is also possible that NiO was better dispersed on the surface of the catalyst, as compared with Co_3O_4.

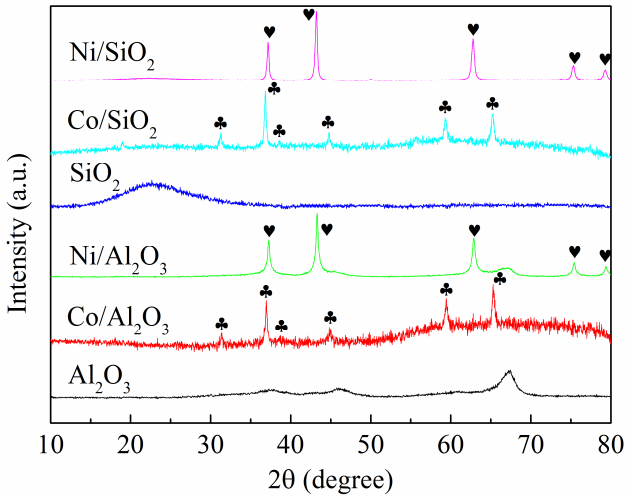

Figure 4.18 XRD patterns of the fresh samples of supports and catalysts. (♥ NiO, ♣ Co_3O_4)

4.3.3. N_2 adsorption–desorption analysis

Nitrogen adsorption–desorption isotherms were used to characterise the textural properties of the catalysts, as summarised in Table 4.5. The BET profiles of Al_2O_3 and SiO_2 supports are also listed for comparison. Clearly, the Al_2O_3 and SiO_2 supports showed higher adsorption capacity and larger BET specific surface area (S_{BET}) than those of the corresponding catalysts, due to the coverage of the supports' surface by the crystallite of active metal species. The Ni-based catalysts exhibited higher adsorption capacity and larger specific surface area than the Co-based catalysts. The specific surface area of the supports and catalysts follows the order of SiO_2 > Ni/SiO_2 > Co/SiO_2 > Al_2O_3 > Ni/Al_2O_3 > Co/Al_2O_3. Since the Co/Al_2O_3 and Co/SiO_2 catalysts showed larger crystallite sizes but smaller specific surface area than their Ni counterparts, probably some pores and tunnels on the surface of Co catalysts were blocked by the Co species.

Table 4.5 Physicochemical characteristics of the fresh catalysts.

Catalyst	S_{BET} (m^2 g^{-1})	Total pore volume (cm^3 g^{-1})	Crystallite size (nm)
Al_2O_3	174.6	0.44	–
Co/Al_2O_3	97.6	0.23	37.5
Ni/Al_2O_3	105.5	0.28	29.7
SiO_2	203.8	1.02	–
Co/SiO_2	128.5	0.85	45.1
Ni/SiO_2	133.4	0.94	30.7

4.3.4. TPR analysis of catalysts

Figure 4.19 shows the H_2-TPR profiles of the Co- and Ni- based catalysts. The Co/Al_2O_3 catalyst showed two overlapping peaks at 360 °C and 430 °C, a very typical feature of Co_3O_4 reduction [216]. The first peak results from the reduction of Co_3O_4 to Co^{2+} species, while the second peak is identified as the further reduction of Co^{2+} to Co^0 [217, 218]. On the TPR profile of the Ni/Al_2O_3 catalyst, the well-defined peak at 430 °C corresponds to the reduction of bulk NiO [120, 219]. The Co/SiO_2 catalyst exhibits a distinguishable TPR pattern from that of the Co/Al_2O_3 catalyst. The reduction of Co_3O_4 to Co^{2+} species started at a lower temperature and the corresponding peak located at 340 °C. The peaks locate at 430 °C are attributed to the reduction of several Co species to metallic Co particles [218]. The Co/Al_2O_3 catalyst had a wider range of reduction-temperature than the Co/SiO_2 catalyst, implying that the Co/Al_2O_3 catalyst was easier to be reduced. It agrees with the XRD results shown in Table 4.5, where the Co/SiO_2 catalyst has a larger crystallite size. The Ni/SiO_2 catalyst had a uni-peak feature similar to that of the Ni/Al_2O_3 catalyst. This is consistent with their similar crystallite sizes. Interestingly, the reduction peaks of the Co- based catalysts (Co/Al_2O_3 and Co/SiO_2) were broader than those of the Ni- based catalysts (Ni/Al_2O_3 and Ni/SiO_2), agreeing well again with the larger crystallite sizes of the Co- catalysts. Moreover, comparing with the Co- catalysts, the reduction of Ni- catalysts started at higher temperatures, implying that the interaction between Ni species and the supports might be stronger than Co species. However, the reduction of Co_3O_4 to metallic Co is a two-step process which happens in a wide temperature range. It is still difficult to judge whether Ni or Co is the better active species, or to assert whether silica or alumina is the better support, simply from their reducibility. The reducibility of the catalysts has a significant effect on the number of metallic surface sites, thus determining the performance of corresponding catalysts in catalytic reactions [220-222]. The catalyst with a higher dispersion of metal particles is usually harder to reduce, and vice versa. Therefore, the most suitable catalyst for plasma–catalytic CO_2 hydrogenation would ultimately depend on reaction conditions and must be examined via experiment.

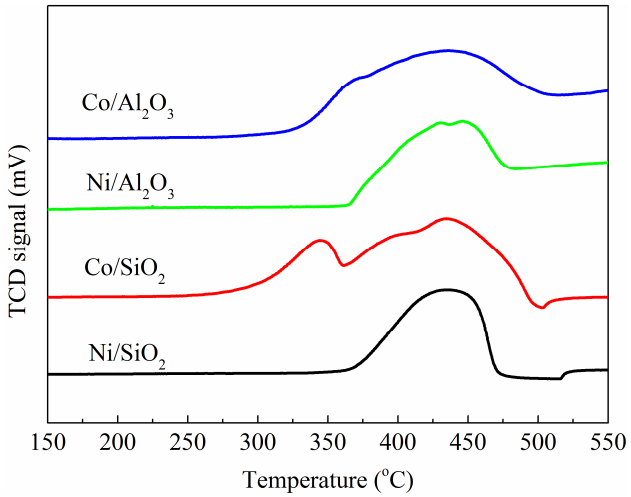

Figure 4.19 TPR profiles of the fresh catalysts.

4.3.5. Thermal catalytic CO_2 hydrogenation with/without plasma: Comparison of catalysts

Figure 4.20 shows the effect of catalyst on CO_2 conversion at 350 °C. A synergistic effect can be clearly identified from the results. All four catalysts improved the CO_2 conversion under thermal- and plasma- catalytic conditions. Plasma-catalysis achieved better CO_2 conversion than thermal catalysis. For instance, with the combination of plasma and catalyst, the CO_2 conversion over the Ni/SiO_2 catalyst increased from 47.6% to 61.5%, while that over the Ni/Al_2O_3 catalyst increased by 32%. Notably, the CO_2 conversion over Co/SiO_2 and Ni/SiO_2 catalysts were higher than that over the Co/Al_2O_3 and Ni/Al_2O_3 catalysts. This might result from the strong interaction between Ni-, Co-species and the Al_2O_3 support, as concluded from the TPR results previously. However, less significant differences were observed between the performances of Ni- and Co-catalysts on the same support.

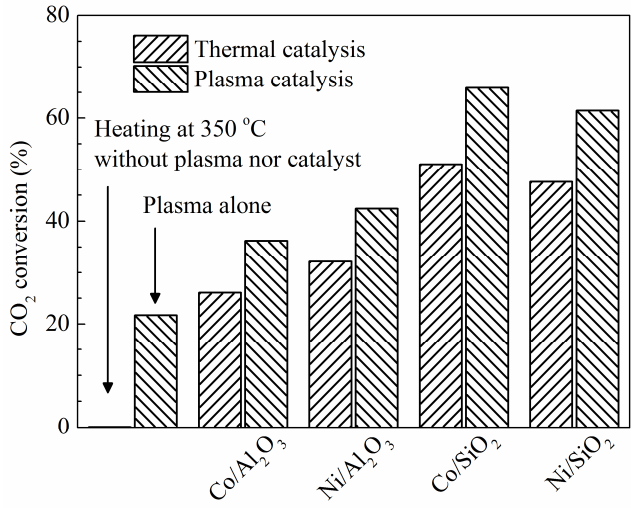

Figure 4.20 CO_2 conversion using different catalysts. (H_2/CO_2 = 4:1, total flow rate 69.2 ml min^{-1}, Ar content 50%, and reaction temperature 350 °C)

Figure 4.21 shows the effect of catalysts on the selectivity and yield of the major products, CH_4 and CO, in the catalytic CO_2 hydrogenation at 350 °C. Remarkably, high CH_4 selectivity (> 90%) was achieved over the Ni/Al_2O_3, Co/SiO_2 and Ni/SiO_2 catalysts in the thermal catalytic process at 350 °C, while a CH_4 selectivity of 59.0% was achieved over the Co/Al_2O_3 catalyst under the same condition. The presence of DBD plasma decreased the CH_4 selectivity over all the catalysts. For instance, the CH_4 selectivity over the Ni/Al_2O_3 catalyst significantly decreased from 94.3% to 48.6% when the non-thermal plasma (NTP) was introduced into the hydrogenation process, implying that NTP changed the reaction routes in the gas phase and on the surface of the catalyst. For instance, NTP could initiate the dry reforming of methane [98] and reversed water-gas shift [24] reactions at 350 °C. These reactions consume CH_4 and produce CO, consequently decreasing the overall selectivity of CH_4. As compared with thermal catalytic hydrogenation, the combination of NTP and catalyst significantly increased the CO selectivity. For instance, with the introduction of plasma, the CO selectivity over the Ni/Al_2O_3 and Ni/SiO_2 catalysts were increased by 10 fold and 4 fold, respectively, comparing with that in thermal catalytic processes. The highest CO selectivity of 96.6% was achieved in plasma- hydrogenation without a catalyst, while the Co/Al_2O_3 catalyst achieved the highest CO selectivity in thermal catalytic process, and the Ni/Al_2O_3 catalyst showed the highest CO selectivity in plasma-catalysis.

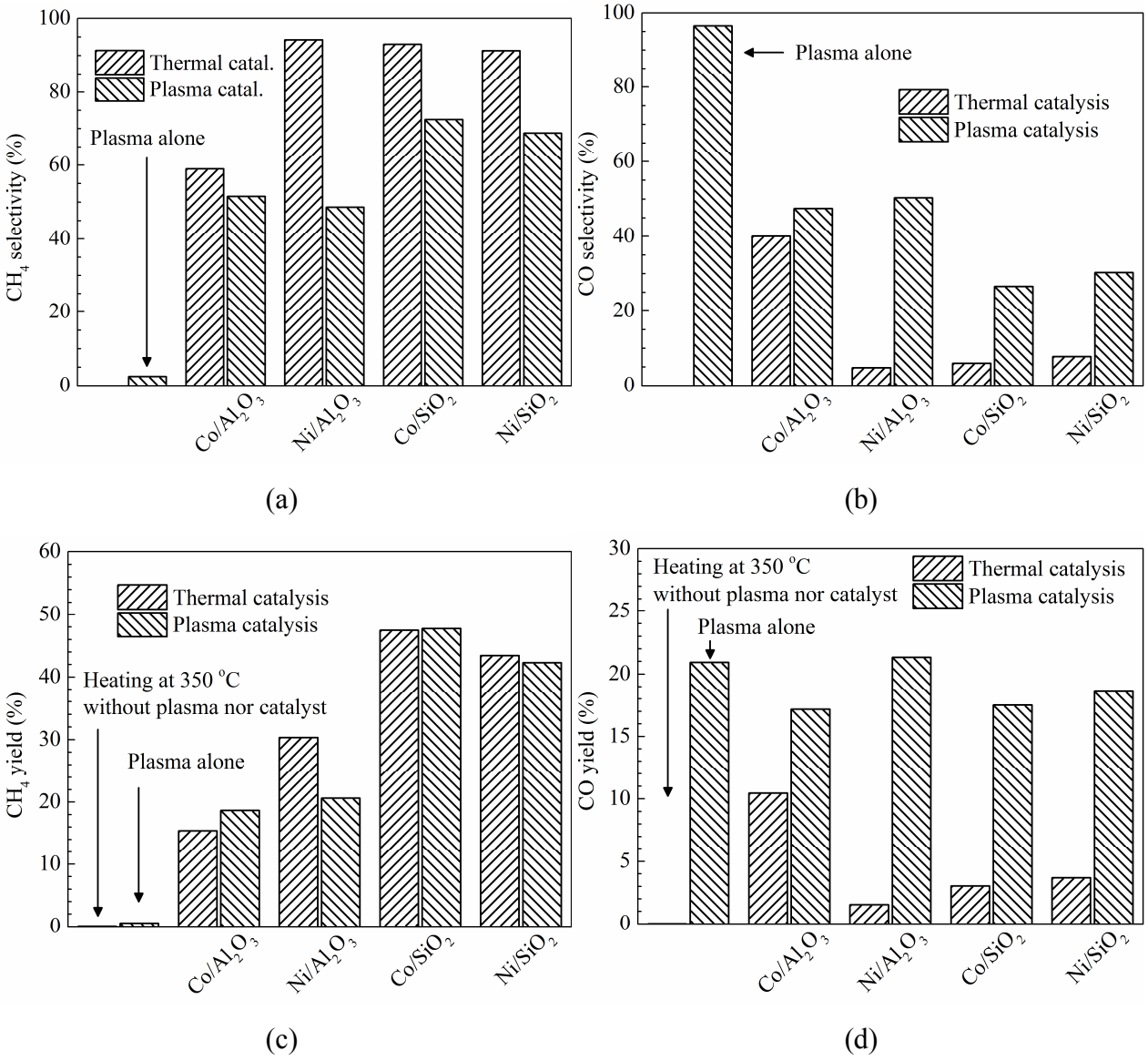

Figure 4.21 Effect of catalyst on CO_2 hydrogenation: (a) Selectivity of CH_4; (b) Selectivity of CO; (c) Yield of CH_4; (d) Yield of CO. (H_2/CO_2 = 4:1, total flow rate 69.2 ml min^{-1}, Ar content 50%, and reaction temperature 350 °C)

A significant synergistic effect between the plasma and catalyst was observed in terms of the CH_4 yield. The Co/SiO_2 and Ni/SiO_2 catalysts exhibited higher CH_4 yield than the Co/Al_2O_3 and Ni/Al_2O_3 catalysts, with or without using plasma, while the Co/Al_2O_3 catalyst had the lowest CH_4 yield. The Co/SiO_2 and Ni/SiO_2 catalysts achieved similar CH_4 yields of 48% and 43% respectively. For comparison, the composition of catalyst had a limited effect on the yield of CO in the plasma-hydrogenation process. The CO yield followed the order of Ni/Al_2O_3 (21.3%) > plasma alone (20.9%) > Ni/SiO_2 (18.6%) > Co/SiO_2 (17.5%) > Co/Al_2O_3 (17.2%). It is

plausible because in the plasma-alone process, the CO selectivity was very high but the CO_2 conversion was low; while in the catalytic process the CO_2 conversion was improved at the expense of decreasing CO selectivity. The CO yield under such conditions were subsequently close to each other.

Figure 4.22 presents the influence of the catalysts on the carbon balance of the CO_2 hydrogenation. The products in this work consisted of CO, CH_4, C_2H_6, C_3H_8 and C_4H_{10}. Unsaturated hydrocarbons were not detected, while solid carbon, C_5+ hydrocarbons and oxidised compounds were not monitored. The carbon balance of thermal catalytic hydrogenation over the Co/SiO_2 and Ni/SiO_2 catalysts were lower than those over the Co/Al_2O_3 and Ni/Al_2O_3 catalysts, while the CO_2 conversion over the SiO_2 supported catalysts were higher than the Al_2O_3 supported ones, suggesting that in this circumstance the yield of undetected species (*e.g.* carbon deposition) increased along with the CO_2 conversion. By contrast, the carbon balance of plasma- catalytic reactions over the Co/SiO_2 and Ni/SiO_2 catalysts were almost 100%, even though the CO_2 conversion was also enhanced under this condition. This result was ascribed to the combination of plasma and the Co/SiO_2, Ni/SiO_2 catalysts which promoted the overall selectivity towards gaseous products in the plasma-catalytic hydrogenation of CO_2 at 350 °C.

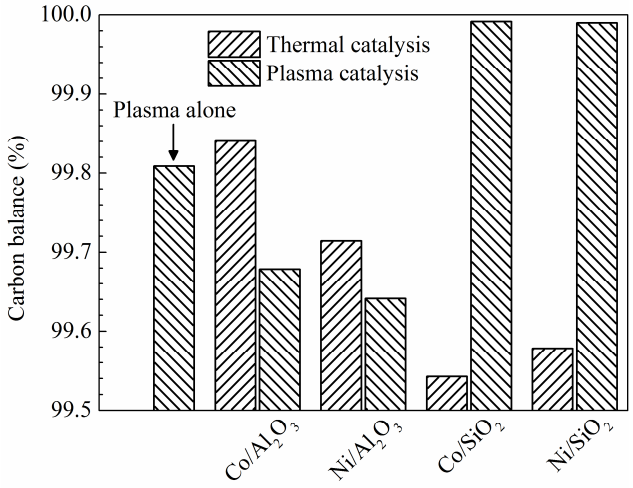

Figure 4.22 Carbon balance of CO_2 hydrogenations over different catalysts. (H_2/CO_2 = 4:1, total flow rate 69.2 ml min^{-1}, Ar content 50%, and reaction temperature 350 °C)

Figure 4.23 shows the fuel production efficiency for the production of CO and CH_4 in CO_2 hydrogenation process using different catalysts. The plasma-catalytic synergy was clearly identified from the results. Notably, the values of fuel production efficiency were small for two reasons: The stoichiometric ratio of fed H_2 and produced combustible gases (mainly CH_4 and CO) were large (4: 1 for CH_4 and 1: 1 for CO); while both of the plasma power and heating power were used to calculate the fuel production efficiency. As the results show, the Co/SiO_2 and Ni/SiO_2 catalysts exhibited better fuel production efficiency than the Co/Al_2O_3 and Ni/Al_2O_3 catalysts, regardless of the presence of plasma, due to their significant improvement on the CH_4 yield. The Co/SiO_2 catalyst achieved the highest fuel production efficiency in both of the thermal catalytic hydrogenation (3.0%) and plasma-catalytic process (3.5%). Surprisingly, very few works on the thermal catalytic CO_2 hydrogenation reported the energy consumption of heating, and there are very limited studies on the plasma-catalytic CO_2 hydrogenation. A summary of energy efficiency of CO_2 hydrogenation in this study can be found in the following section.

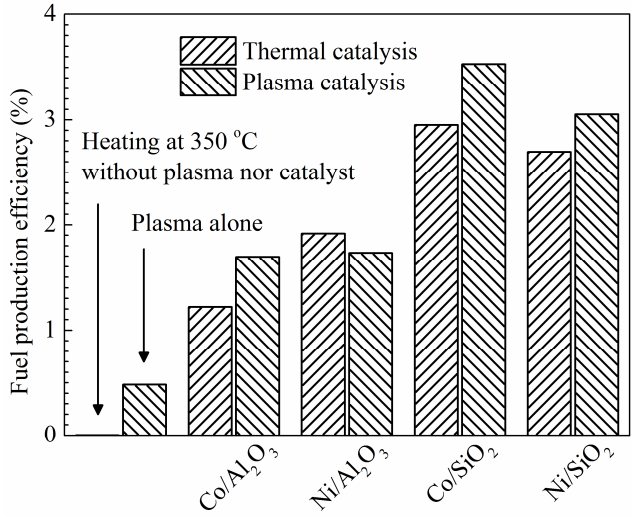

Figure 4.23 Fuel production efficiencies of CO_2 hydrogenations over different catalysts. (H_2/CO_2 = 4:1, total flow rate 69.2 ml min^{-1}, Ar content 50%, and reaction temperature 350 °C)

4.3.6. Effect of temperature on the plasma-catalytic CO_2 hydrogenation

In this section, plasma-catalytic CO_2 hydrogenation was carried out at an elevated temperature of 500 °C to compare the performance of different catalysts in response to the change of temperature. The input power for the DBD plasma was fixed at 38 W, while the heating power was adjusted to heat the reactor to 500 °C.

Figure 4.24 shows the effect of elevated temperature on the CO_2 conversion over the four catalysts in plasma-catalytic hydrogenation. When the temperature increased from 350 °C to 500 °C, there was only a slight change of CO_2 conversion over the Co/SiO_2 and Ni/SiO_2 catalysts, however, the CO_2 conversions over Co/Al_2O_3 and Ni/Al_2O_3 catalysts was significantly increased. For instance, the CO_2 conversion over the Co/Al_2O_3 catalyst increased from 36.2% to 65.2% (nearly doubled) as the temperature increased to 500 °C, while the Ni/Al_2O_3 catalyst achieved the highest CO_2 conversion of 67.8% at the same temperature.

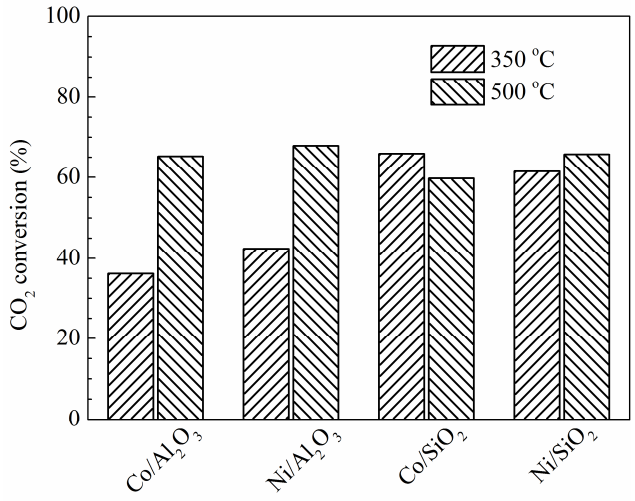

Figure 4.24 CO_2 conversions over different catalysts at the two temperatures. (H_2/CO_2 = 4:1, total flow rate 69.2 ml min^{-1}, Ar content 50%, and input power 38 W)

Notably all the catalysts achieved similar CO_2 conversion under this same condition, and the conversion followed the order of Ni/Al_2O_3 > Ni/SiO_2 > Co/Al_2O_3 > Co/SiO_2, suggesting that Ni-based and Al_2O_3 supported catalysts had better CO_2 conversion at 500 °C. Interestingly, the reduction temperature of the catalysts followed the same order of Ni/Al_2O_3 > Ni/SiO_2 > Co/Al_2O_3 > Co/SiO_2. The reduction of Co/Al_2O_3 and Co/SiO_2 catalysts was initiated at about 320 °C, while the reduction

temperature of the Ni/Al_2O_3 and Ni/SiO_2 catalysts was higher than 350 °C. Moreover, the reduction processes of all four catalysts were only completed once the temperature increased to 500 °C. The reductive feature of the catalysts agrees well with the evolution of CO_2 conversion over these catalysts at different temperatures, implying that the degree of reduction and the reducibility of the catalyst play key roles in the plasma-catalytic hydrogenation at elevated temperatures.

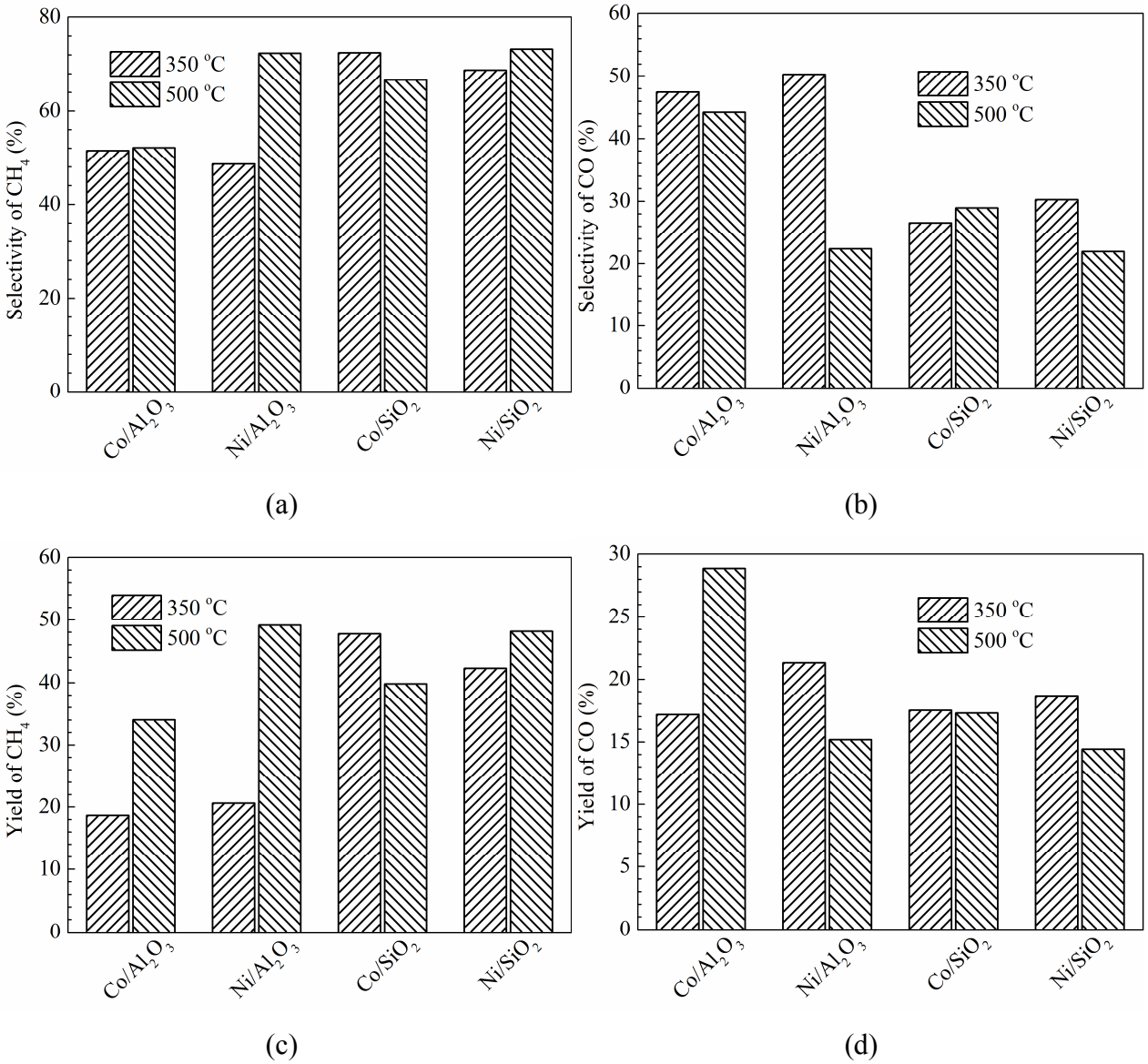

Figure 4.25 Effect of catalyst on CO_2 hydrogenation: (a) Selectivity of CH_4; (b) Selectivity of CO; (c) Yield of CH_4; (d) Yield of CO. (H_2/CO_2 = 4:1, total flow rate 69.2 ml min^{-1}, Ar content 50%, and input power 38 W)

Figure 4.25 shows the effect of increased temperature on the selectivity and yield of CH_4 and CO in the plasma-catalytic hydrogenation of CO_2. When the temperature increased from 350 ºC to 500 ºC, the selectivity of CH_4 obtained using the Ni/SiO_2, Co/Al_2O_3 and Ni/Al_2O_3 catalysts increased, and the CO selectivity over the mentioned catalysts decreased. Most notably, the CH_4 selectivity over the Ni/Al_2O_3 catalyst significantly increased from 48.6% to 72.4%, while the CO selectivity over the same catalyst significantly decreased from 50.3% to 22.4%. On one hand, it is explained that the plasma-catalytic CO_2 methanation over the Ni/Al_2O_3 catalyst was enhanced at 500 °C, due to the increasing reaction rate coefficient at elevated temperatures. On the other hand, the different evolution of CH_4 selectivity implies that the mechanism of plasma-catalytic CO_2 methanation at elevated temperatures is dependent on the composition of catalyst. The different behaviour of the Co/SiO_2 catalyst might be attributed to its highest reduction temperature. The yield of CH_4 over the Ni/SiO_2, Co/Al_2O_3 and Ni/Al_2O_3 catalysts increased at 500 ºC, due to their significant improvement on the CO_2 conversion and CH_4 selectivity. The Ni/Al_2O_3 catalyst had the highest CH_4 yield of 49.1%, and a relatively low CO yield of 15.2%.

Figure 4.26 shows the effect of increasing temperature on the fuel production efficiency of CO_2 hydrogenation into CO and CH_4 using plasma-catalysis. Again, the small values of the fuel production efficiency were not only due to the large stoichiometric ratio between fed H_2 and produced fuel gases, but also because the power used to calculate the fuel production efficiency included heating power and plasma power. At the temperature of 350 ºC, the Co/SiO_2 and Ni/SiO_2 catalysts achieved fuel production efficiency almost twice as high as those achieved over the Co/Al_2O_3 and Ni/Al_2O_3 catalysts, but greatly deteriorated when the temperature increased. It is explained that more heating power was required for the hydrogenation at 500 °C, although the production of CH_4 at such temperature was generally improved. The fuel production efficiency over the Co/SiO_2 catalyst decreased from 3.5% to 1.5% when the temperature increased from 350 °C to 500 °C. The fuel production efficiency of plasma-catalytic CO_2 hydrogenation at 500 °C followed the order of Ni/Al_2O_3 > Ni/SiO_2 > Co/SiO_2 > Co/Al_2O_3, suggesting that the Ni- based catalysts had higher energy efficiency for the hydrogenation process at this temperature. Table 4.6 summarises the energy efficiency of the CO_2 hydrogenation processes in this study. It can be concluded that plasma-catalysis is necessary for the energy-effective conversion of CO_2. In addition, to fully exploit the advantage of NTP, the temperature inside of the reactor

should be low. However, by contrast, elevated temperature is needed for increasing reaction rate and enhancing conversion of CO_2. Moreover, filling the plasma volume with packing materials would improve the energy efficiency of the process.

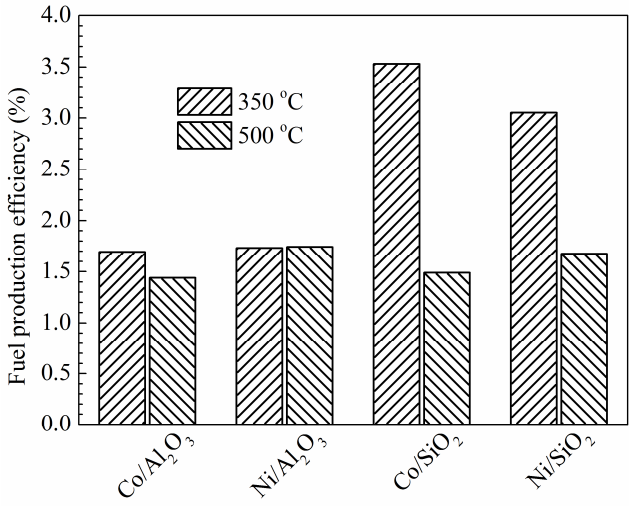

Figure 4.26 Fuel production efficiencies of CO_2 hydrogenations over different catalysts. (H_2/CO_2 = 4:1, total flow rate 69.2 ml min^{-1}, and Ar content 50%)

Table 4.6 Energy efficiency of CO_2 hydrogenation in this study. (H_2/CO_2 = 4:1, total flow rate 69.2 ml min^{-1}, Ar content 50%, power consumption is presented as temperature)

Catalyst	Temperature (°C)	CO_2 conversion (%)	*E* (mmol kJ^{-1})	*FPE* (%)
–	148	32.3	0.062	1.9
Ni/Al_2O_3+Al_2O_3	148	48.5	0.089	2.5
–	260	25.2	0.028	0.8
–	380	20.9	0.014	0.4
–	500	19.6	0.008	0.3
Ni/Al_2O_3	260	27.2	0.034	1.0
Ni/Al_2O_3	380	49.5	0.027	1.7
Ni/Al_2O_3	500	67.9	0.027	1.7
Co/SiO_2	500	59.7	0.024	1.5
Ni/SiO_2	500	65.7	0.025	1.7
Co/Al_2O_3	500	65.2	0.026	1.4
Ni/Al_2O_3	500	67.9	0.027	1.7

4.4. Summary

In this chapter, CO_2 hydrogenation for the production of CO and CH_4 was systematically investigated under a set of conditions. Significant plasma-catalytic synergy was observed throughout the investigations. Firstly, the experiment demonstrated that non-thermal plasma could effectively enable and drive the CO_2 hydrogenation at 150 ºC, a relatively low temperature, over a Ni/Al_2O_3 catalyst and with a H_2/CO_2 molar ratio of 4 in the feed gas. Inspired by this result, the CO_2 hydrogenation was then carried out under three conditions: plasma alone, thermal catalysis and plasma-catalysis. The effect of reaction conditions on the catalytic performance of a Ni/Al_2O_3 catalyst have been investigated, including the addition of Ar, the temperature inside of the reactor and the composition of catalyst. The plasma-catalytic synergy and individual contribution of plasma and heating on the conversion of CO_2 have been also discussed. The results suggest that the combination of DBD plasma and the Ni/Al_2O_3 catalyst improved the performance of hydrogenation in terms of CO_2 conversion, CH_4 yield and fuel production efficiency. Subsequently, in the final section of this chapter, two active metal species (Ni and Co) and two supports (Al_2O_3 and fumed SiO_2) for the synthesis of catalysts were examined at different temperature, revealing the different evolutions of catalytic performance under plasma-catalytic and thermal catalytic conditions.

The combination of the plasma and Ni/Al_2O_3 catalyst clearly generated a synergistic effect, as a result of the interactions between the plasma and catalyst, which enhanced the CO_2 conversion, the yield of CO and CH_4 and the energy efficiency of the process compared with the reaction using either plasma-alone or the thermal catalytic approach at the same temperature (150 ºC). In the plasma CO_2 hydrogenation with and without a catalyst, the addition of Ar in the feed gas enhanced the conversion of CO_2, the selectivity of CH_4 and the fuel production efficiency, while the selectivity of CO was almost independent of the Ar content. The addition of Ar in the feed gas (CO_2/H_2) shifted the discharge mode from "partial discharging" to "fully-bridged" discharge and enhanced the interactions between the DBD and Ni catalyst. The presence of Ar* opened new reaction routes which made a significant contribution to the enhanced reaction performance. The results show that the molar ratio of CO/CH_4 in the gas product could be adjusted by changing the Ar content in the feed gas. In addition, the presence of Ar in the feed gas changed the electrical properties of the plasma,

including decreasing the breakdown voltage and promoting charge transfer through the reactor. The equivalent relative dielectric constant of the packing material (overall dielectric constant of Ni/Al_2O_3 catalyst and Al_2O_3 beads) in the DBD reactor was 0.79, which suggests that loading NiO particles on the surface of alumina changed its electrical properties.

The investigation on the effect of temperature on the performance of CO_2 hydrogenation under three conditions has been carried out: plasma-alone, thermal catalysis and plasma-catalysis. The conversion of CO_2, selectivity and yield of CO and CH_4 and fuel production efficiency of the process have been considered. Results suggest that the Ni/Al_2O_3 catalyst showed a temperature dependence in the thermal catalytic hydrogenation and its performance was best at a temperature range between 320 ^oC and 380 ^oC. The combination of plasma and catalyst exhibited better performance at a wide temperature range. The plasma-catalytic hydrogenation process had higher CO_2 conversion and CO selectivity. Moreover, NTP and external heating showed different effects on the conversion of CO_2, the selectivity and yield of CO and CH_4 and the fuel production efficiency of the process. In order to exploit the advantage of plasma-catalysis, the operational parameters such as reaction temperature and plasma/heating power ratio should be carefully designed.

In plasma-catalytic CO_2 hydrogenation over different catalysts at 350 °C and 500 °C, the reducibility of the investigated catalysts followed the order of Co/SiO_2 > Ni/SiO_2 > Ni/Al_2O_3 > Co/Al_2O_3. The catalytic performance of the catalysts, in terms of CO_2 conversion and fuel production efficiency, exhibited a temperature dependence that agreed with their reducibility. All the catalysts improved the CO_2 conversion compared to the case using plasma alone, and the combination of plasma with catalyst further improved the CO_2 conversion. The Co/SiO_2 and Ni/SiO_2 catalysts achieved better CH_4 yield than the Al_2O_3 supported catalysts (Co/Al_2O_3 and Ni/Al_2O_3) at 350 °C, with or without plasma, and consequently achieving higher fuel production efficiency. However, when the temperature increased from 350 ^oC to 500 °C, the presence of Co/Al_2O_3 and Ni/Al_2O_3 catalysts significantly enhanced the CO_2 conversion, CO and CH_4 yield. The highest CO_2 conversion and highest CH_4 yield were achieved over the Ni/Al_2O_3 catalyst, while the highest CO yield was achieved over the Co/Al_2O_3 catalyst under the same condition. The result suggests that the Co/SiO_2 and Ni/SiO_2 catalysts are very suitable for the thermal catalytic CO_2 hydrogenation into CO and gaseous alkanes, while the Ni/Al_2O_3 catalyst would exhibit better performance in plasma-

catalytic hydrogenation at 500 °C, in terms of CO_2 conversion, CH_4 selectivity, CH_4 yield, and energy efficiency. The selection of proper catalyst for CO_2 hydrogenation is highly dependent on the reducibility of catalysts, the existence of plasma and the reaction temperature for the plasma process.

Chapter 5. Plasma-catalytic biogas reforming at low temperatures

Similar to H_2, CH_4 is also a common hydrogen source for CO_2 conversion. In this chapter, plasma-catalytic dry reforming over Al_2O_3 supported metal catalysts M/Al_2O_3 (M = Ni, Co, Cu and Mn) have been investigated in a coaxial DBD reactor at low temperatures, exhibiting the fundamental study on the individual effect of these factors on the plasma-catalytic dry reforming. In the first section, the influence of different experimental conditions (*e.g.* CO_2/CH_4 molar ratio and total reactant flow rate) and catalyst composition on the performance of the plasma-catalytic reforming process has been evaluated in terms of the conversion of feed gases, the selectivity and yield of major gas products, as well as the energy efficiency of the process. In the following section, the plasma-catalytic biogas reforming over a Ni/Al_2O_3 catalyst at low temperatures has been further studied, the effect of K, Mg and Ce promoters on the biogas reforming has also been examined.

5.1. Plasma-catalytic biogas reforming over Al_2O_3 supported metal catalysts

5.1.1. Experimental setup

In this section, the experimental system used is described in Chapter 2. CO_2 and CH_4 were used as feed gases with a variable total flow rate of 25-200 ml min^{-1} and a CO_2/CH_4 molar ratio from 1:9 to 9:1. The gas temperature in the discharge area near the catalyst bed was measured by using a fibre optical thermometer (Omega, FOB102) and the maximum value was less than 150 ^oC.

Weighed catalyst pellets (0.2 g) were directly placed in the discharge region and in contact with the plasma in the dry reforming reaction [37]. Prior to the plasma-catalytic dry reforming reaction, the Al_2O_3 supported catalysts were reduced in an

argon-hydrogen discharge at a discharge power of 7.5 W (50 ml min^{-1}, 20 vol. % H_2) for 30 mins in the same DBD reactor.

10 wt.% M/Al_2O_3 (M = Ni, Co, Cu and Mn) catalysts were prepared by wetness impregnation using nitrate salts (Alfa Aesar, 99.5%) as the metal precursor. Weighed support (Al_2O_3) was added to the solution of nitrate salts. The slurry was continuously stirred at 80 °C for 4 hrs and then dried at 110 °C overnight, followed by calcination at 500 °C for 5 h. All the catalysts were pelleted and sieved to 20 - 40 meshes prior to plasma reaction.

X-ray diffraction (XRD) patterns of the catalysts samples were recorded by an X-ray diffractometer (Rigaku, D/max-2200) using a Cu-Kα radiation source in the 2θ range from 10^o to 80^o. The Al_2O_3 crystallite size of the samples was calculated using Scherrer equation, as explained in Chapter 1. Transmission electron microscopy (TEM) analysis of the spent catalysts was performed using a Hitachi H-9500 microscope operating at an acceleration voltage of 300 kV. For the TEM measurement, the catalyst samples were prepared by ultrasonication in ethanol, evaporating a drop of the resultant suspension onto a carbon-coated copper grid.

In this chapter, H_2 and CO were identified as the main products in the plasma dry reforming reaction, while a small amount of ethane (C_2H_6) was produced. Acetylene, ethylene and propane were also detected, but their concentrations were very low and negligible compared to the major gas products.

For the plasma dry reforming reaction, the conversion (X) of CH_4 and CO_2, the selectivity (S) and yield (Y) of the products, the H_2/CO molar ratio in the product, the carbon balance (B_{carbon}), the energy efficiency for the conversion of CH_4 or/and CO_2 are defined in Chapter 2.

5.1.2. Plasma dry reforming reaction without catalyst

5.1.2.1. Effect of CO_2/CH_4 molar ratio

Figure 5.1 shows the effect of different CO_2/CH_4 molar ratios on the performance of the plasma dry reforming process in the absence of a catalyst. The conversion of CH_4 increased almost linearly with the increase of the CO_2/CH_4 molar ratio at a fixed total flow rate, which suggests that lower content of CH_4 in the reactant mixture led to the improvement of the CH_4 conversion.

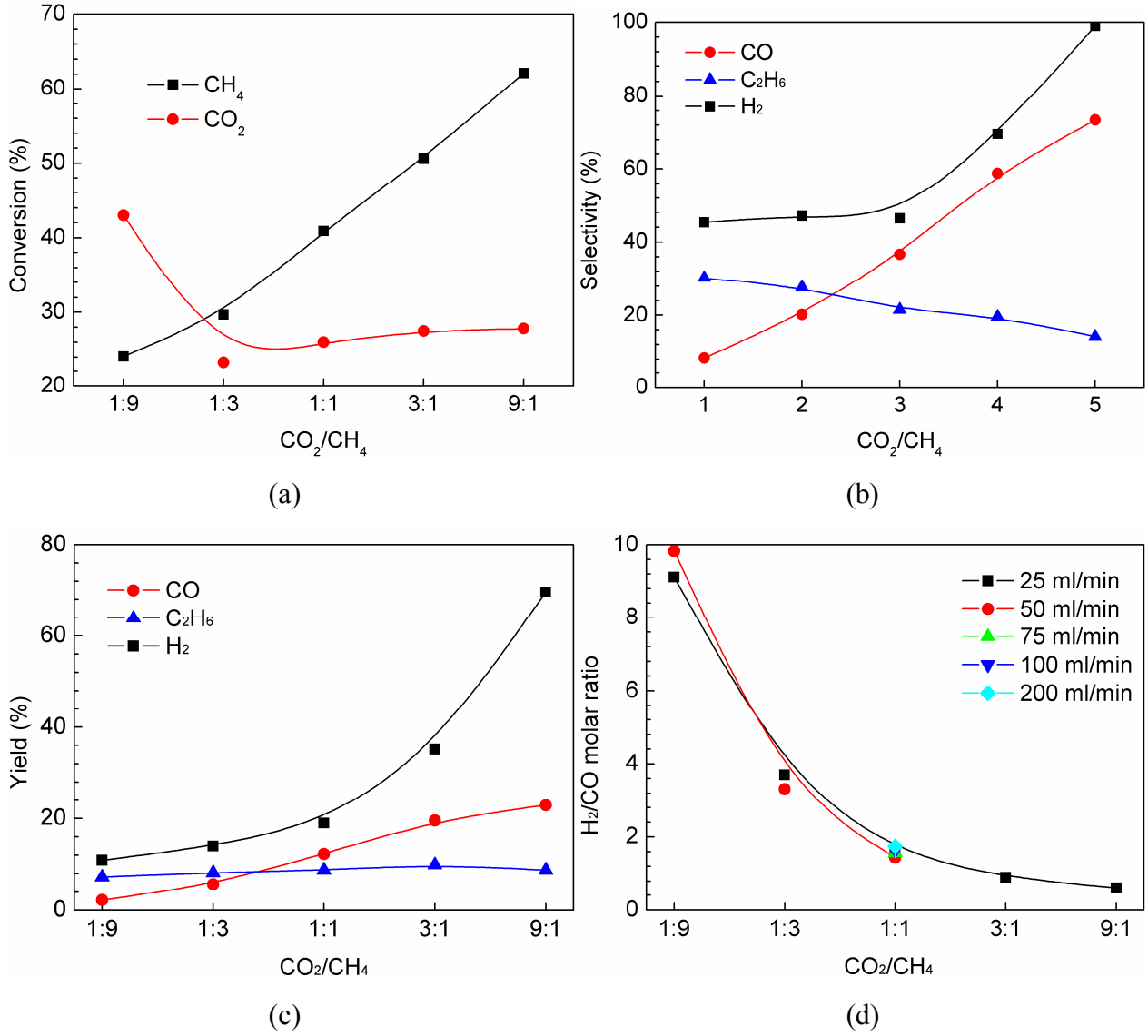

Figure 5.1 Effect of different CO_2/CH_4 molar ratios on the performance of plasma dry reforming reaction. (a) Conversion of reactants; (b) Selectivity of major products; (c) Yield of major products and (d) H_2/CO ratio (total feed flow 25 ml min^{-1} and discharge power 15 W)

In contrast, the conversion of CO_2 significantly decreased from 41.5% to 21.3% when the CO_2/CH_4 molar ratio changed from 1:9 to 1:3, and the conversion slightly increased as the CO_2/CH_4 ratio further increased from 1:3 to 9:1. Figure 5.1(b) shows that the CO_2/CH_4 molar ratio significantly affected the selectivity of H_2 and CO. As the CO_2/CH_4 molar ratio increased from 1:9 to 9:1, the H_2 selectivity was almost doubled and close to 100%, while the CO selectivity was enhanced by 8.8 times. However, the selectivity of C_2H_6 was decreased by 53% with the increase of the CO_2/CH_4 ratio between 1:9 and 9:1. In addition, increasing CO_2 content in the gas mixture significantly

increased the yield of H_2 and CO. It can be seen that the H_2 yield was increased by a factor of 6.4 (from 11% to 70%) as the CO_2/CH_4 ratio changed from 1:9 to 9:1. In contrast, the yield of C_2H_6 was almost independent on the CO_2/CH_4 ratio. These results suggest that excessive CO_2 in the reactant mixture not only enhanced the CH_4 conversion, the selectivity and yields of CO and H_2, but also suppressed the recombination of CH_x species to form higher hydrocarbons. Moreover, it was found that the H_2/CO molar ratio in the gas product was totally determined by the CO_2/CH_4 molar ratio, while the total feed gas flow rate had a negligible effect on the H_2/CO ratio at a fixed CO_2/CH_4 ratio of 1:1, as plotted in Figure 5.1(d). These results could be useful in the optimisation of plasma dry reforming process since the production of H_2 and CO can be controlled by adjusting the CO_2/CH_4 ratio.

5.1.2.2. Effect of total feed flow rate

Figure 5.2 shows the influence of total reactant flow rate on the plasma dry reforming of CH_4 and CO_2. The conversions of CH_4 and CO_2 decreased significantly with the increase of the total flow rate. Increasing the reactant flow rate substantially decreased the retention time of CO_2 and CH_4 in the plasma zone, which reduced the chance of CO_2 and CH_4 reacting with energetic electrons and reactive species present in the plasma, resulting in the decrease of the conversions of both reactants and the yields of major gas products (H_2, CO and C_2H_6). It was found that the C_2H_6 selectivity was doubled, changing from 22% to 43% with the increase of the gas flow rate, while the total flow rate showed an insignificant influence on the selectivity of H_2 and CO. In contrast, the gas flow rate significantly affected the yield of major reforming products (H_2, CO and C_2H_6), as shown in Figure 5.2(b). The H_2 yield was decreased from 19% to 3.8% as the total feed flow increased from 25 ml min^{-1} to 200 ml min^{-1}.

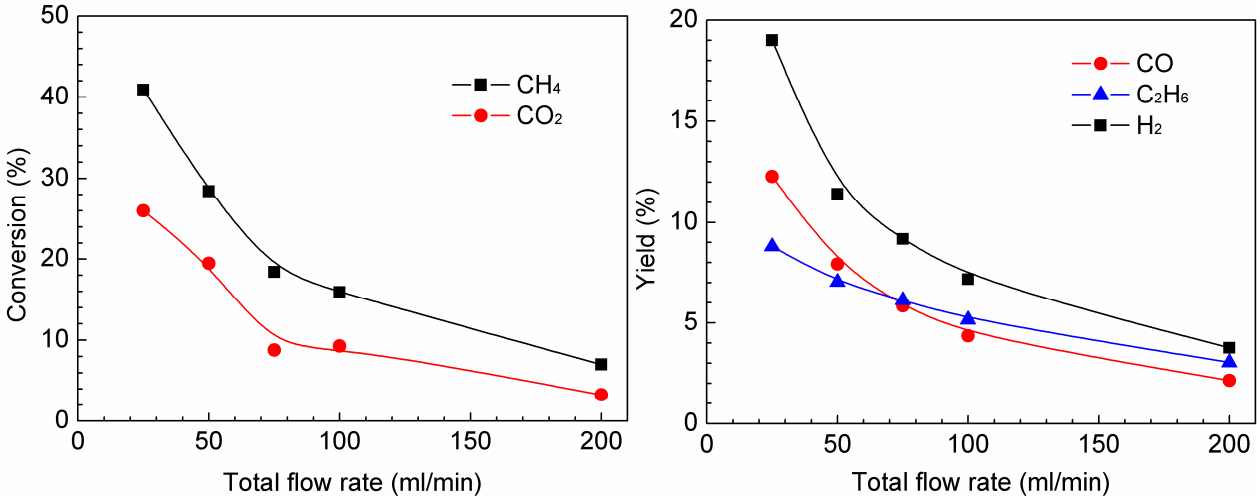

(a) (b)

Figure 5.2 Effect of different total feed flow rates on the performance of plasma dry reforming reaction. (a) Conversions of reactants; (b) Yield of major products (CO_2/CH_4 = 1: 1 and discharge power 15 W)

5.1.3. Plasma-catalytic dry reforming reaction

5.1.3.1. Catalyst characterisation

Figure 5.3 shows the XRD patterns of the fresh samples. The XRD pattern of the Al_2O_3 support shows three major diffraction peaks located at 2θ = 37.6°, 45.9° and 67.0°, corresponding to the cubic structure of Al_2O_3 crystalline (JCPDS 00-010-0425). These peaks can also be observed in the XRD patterns of the MO_x/Al_2O_3 catalysts. The Al_2O_3 crystalline size of these samples calculated by Scherrer equation is very similar, between 4.78 and 5.34 nm. The XRD pattern of the Cu/Al_2O_3 catalyst shows intense reflections corresponding to CuO (at 35.5° and 38.8°), while the peaks of MnO_2 (28.7°, 37.3°, 42.8° and 56.7°) are clearly visible in the spectrum of the Mn/Al_2O_3 sample. In addition, weak diffraction peaks of Co_3O_4 (JCPDS 00-042-1467) and NiO (JCPDS 01-075-0197) can also be found in the corresponding catalyst. The XRD patterns of these samples clearly indicate the formation of metal oxide crystallites after catalyst calcination. Previous works have shown that these metal oxide phases can be reduced in the low temperature Ar-H_2 plasma process [37, 223].

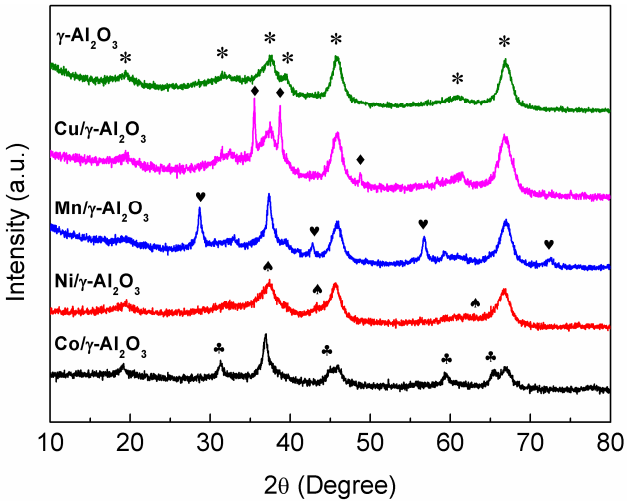

Figure 5.3 XRD patterns of the fresh catalysts. (♣ Co_3O_4, ♠ NiO, ♥ MnO_2, ♦ CuO, * Al_2O_3)

5.1.3.2. Effect of different catalysts

Figure 5.4 shows the effect of Al_2O_3 supported transition metal catalysts on the plasma dry reforming of CH_4 and CO_2. Compared to the plasma reforming reaction with no catalyst, the combination of the plasma with the Ni/Al_2O_3 and Mn/Al_2O_3 catalysts significantly enhanced the conversions of CH_4 by 42% and 30%, respectively. However, the presence of the Co/Al_2O_3 and Cu/Al_2O_3 in the DBD reactor only slightly improved CH_4 conversion by 12% and 6%, respectively. The maximum CH_4 conversion of 42% was achieved in the plasma-catalytic dry reforming over the Ni/Al_2O_3 catalyst at a discharge power of 7.5 W and a gas flow rate of 50 ml min^{-1}, which suggests that the activity of Ni was much higher than that of other metal phases (*i.e.* Cu, Co and Mn). It is worth noting that the presence of these catalysts in the DBD reactor did not enhance CO_2 conversion. This could be partly attributed to the enhanced water gas shift (WGS) side reaction at low temperatures.

$$CO + H_2O \rightarrow CO_2 + H_2 \quad (2)$$

$$H_2 + CO_2 \rightarrow CO + H_2O \quad (3)$$

In the plasma-catalytic dry forming of CH_4, produced CO may react with water to form H_2 and CO_2, thus lower the conversion of CO_2 [37]. This could be evidenced by the molar ratio of H_2/CO (>1) in the experiment. Compared to the Ni and Mn based catalysts, the Co/Al_2O_3 and Cu/Al_2O_3 catalysts showed the lowest CO_2 conversion but

had the highest H_2/CO ratio, as shown in Figure 5.4. Both are typical catalysts for the low temperature water gas shift reaction. The presence of these catalysts in the plasma reforming process promoted the water gas shift reaction and generated more H_2.

In this chapter, the temperature near the catalyst bed in the plasma reactor was below 150 °C. Since the plasma dry reforming reactions under different experimental conditions took place at temperatures much lower than the reaction temperature of thermal catalytic reforming reaction (*e.g.* > 600 °C), the theoretical conversions of CH_4 and CO_2 at thermodynamic equilibrium were < 5% at a low temperature of <300 °C [37, 224]. It can be expected that the dry reforming reaction at 150 °C had a very poor performance without plasma. These results show that the conversions of methane were significantly enhanced through the combination of the plasma with the Ni/Al_2O_3 or Mn/Al_2O_3 catalysts, which was much higher than the sum of the reforming reactions using plasma-alone and catalysis alone, indicating a synergy of plasma-catalysis for CH_4 conversion. However, placing the Co and Cu based catalysts in the DBD reactor did not show a synergistic effect of plasma-catalysis. Furthermore, there was no synergy of plasma-catalysis obtained for the conversion of CO_2.

From the stoichiometry of dry reforming of CH_4 and CO_2 (1), equal conversions of CH_4 and CO_2 would be expected. However, it is found that the CH_4 conversion was always higher than the CO_2 conversion in the plasma dry reforming reaction with or without a catalyst at the CH_4/CO_2 molar ratio of 1:1. This phenomenon was also reported in both experimental and simulated plasma dry reforming reactions [37, 174]. In addition, this behavior is different to thermal catalytic dry reforming of CH_4 at high temperatures (*e.g.* > 600 °C) in which the CO_2 conversion is generally higher than the conversion of CH_4 due to the occurrence of reverse water gas shift (RWGS) reaction. Previous thermodynamic equilibrium calculation also showed that the conversion of CO_2 was higher than that of CH_4 over a wide reaction temperature range [37].

Compared with the CO_2 conversion, the higher conversion of CH_4 in plasma- DRM can be explained that more reaction pathways exist for plasma-assisted CH_4 conversion especially in the gas phase reactions such as electron-impact dissociation of CH_4 to generate different radicals CH_x (x=1-3) (4-6), with subsequent recombination of radicals to generate hydrogen and hydrocarbons or further electron-impact dissociation of radicals (*e.g.* CH_x) [37].

$$CH_4 + e^- \rightarrow CH_3 + H + e^- \quad (4)$$

$$CH_4 + e^- \rightarrow CH_2 + H_2 + e^- \quad (5)$$

$$CH_4 + e^- \rightarrow CH + H + H_2 + e^- \quad (6)$$

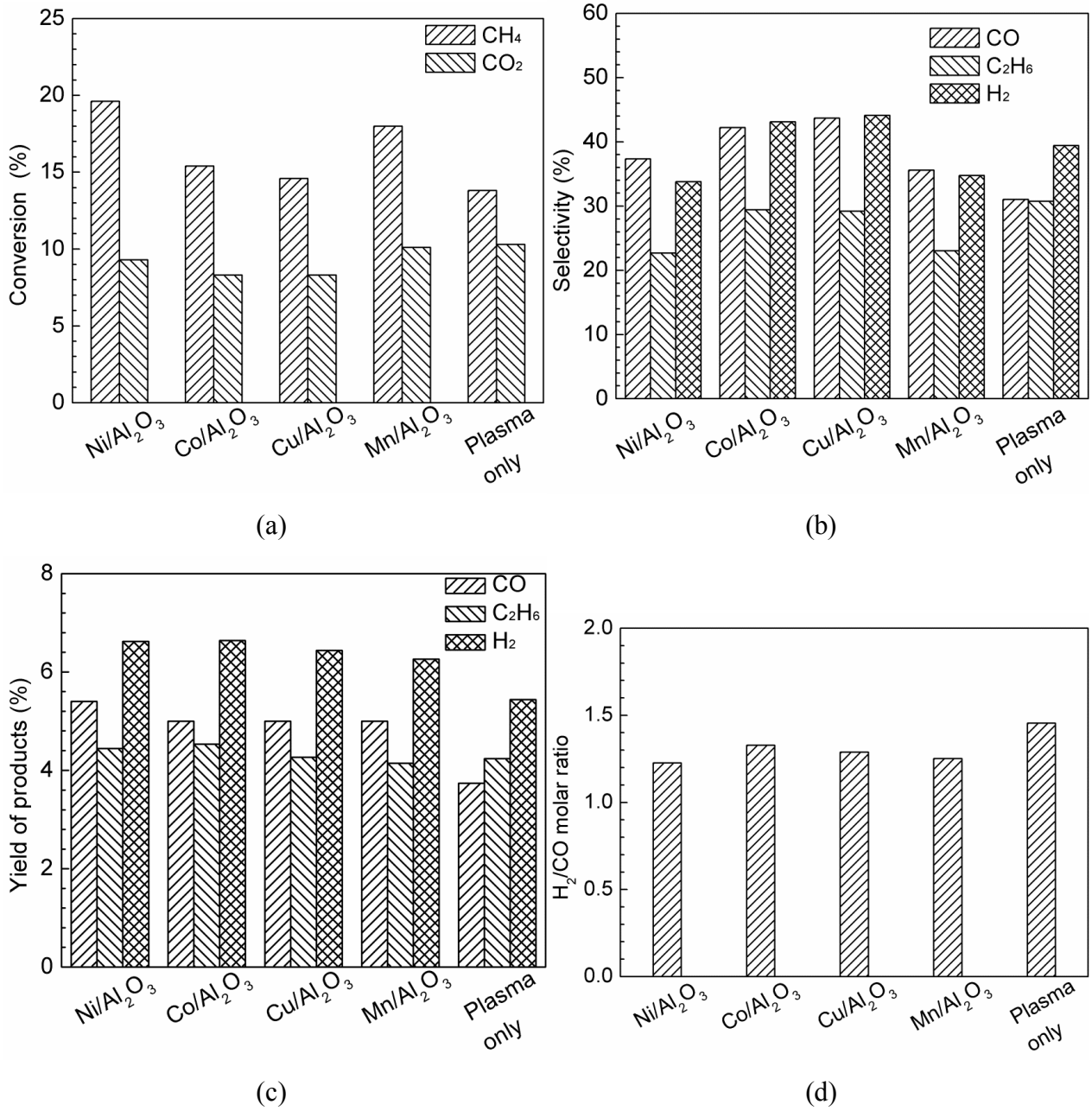

Figure 5.4 Effect of different catalysts on the performance of the plasma dry reforming reaction. (a) Conversion of reactants; (b) Selectivity of major products; (c) Yield of major products; (d) Energy efficiency for conversion (CO_2/CH_4 = 1: 1, total feed flow rate 50 ml min^{-1}, and discharge power 7.5 W)

In addition, recent simulations have revealed that the following reaction plays a predominant role in the production of CO_2 in the plasma dry reforming reaction [174], which leads to a lower CO_2 conversion.

$$CO_2^+ + CH_4 \rightarrow CH_4^+ + CO_2 \quad (7)$$

The selectivity of the major products produced in the plasma reforming process is presented in Figure 5.4(b). The addition of these catalysts in the DBD reactor decreased the selectivity of C_2H_6 but increased the CO selectivity. Both the Ni and Mn based catalysts showed better performance in suppressing the formation of C_2H_6, while the presence of Co and Cu catalysts in the plasma improved CO selectivity. The integration of plasma and a Ni/Al_2O_3 catalyst decreased the selectivity of C_2H_6 by around 30% (from 30.7% to 22.7%), while the Co/Al_2O_3 catalyst weakly affected the selectivity of C_2H_6 (from 30.7% to 29.4%). Only the Co and Cu catalysts showed a higher H_2 selectivity compared to the reaction without a catalyst, while the Ni and Mn based catalysts decreased the selectivity towards CO.

The combination of the DBD and M/Al_2O_3 catalysts enhanced the yields of CO and H_2. The Ni/Al_2O_3 catalyst showed the best catalytic activity, followed by the Co/Al_2O_3, Cu/Al_2O_3 and Mn/Al_2O_3. The presence of the Ni/Al_2O_3 catalyst in the plasma process significantly increased the yields of CO and H_2 by 42% and 20%, respectively compared to the plasma reaction in the absence of a catalyst, while the Co/Al_2O_3 catalyst increased the yields of CO and H_2 by 32% and 22%, respectively.

The carbon balance based on the major gas products for the plasma dry reforming reaction with and without a catalyst were between 93% and 96%. Compared to the plasma reaction in the absence of a catalyst (B_{carbon} = 93.8%), the combination of the plasma with the Cu/Al_2O_3 or Co/Al_2O_3 catalyst slightly increased the carbon balance (95%-96%). The Cu/Al_2O_3 catalyst showed the highest carbon balance of 96%, while the Ni and Mn catalysts had the lowest carbon balance of around 93%. The effect of the catalysts on the carbon balance agreed with the conversions of CH_4 and CO_2 using different catalysts in the plasma system. The surface morphography of the catalysts after reforming reaction has been investigated using TEM. The Ni/Al_2O_3 and Cu/Al_2O_3 were selected as the representatives since the Ni/Al_2O_3 catalyst showed the highest CH_4 conversion and lowest carbon balance, while the Cu/Al_2O_3 catalyst had the highest carbon balance and selectivity of H_2 and CO. It can be seen that most of the metal

particles were less than 20 nm and were homogeneously dispersed on the Al_2O_3 surface. Similar morphologies have been reported previously for Al_2O_3 supported Ni or Cu catalyst analysed by TEM [225]. No obvious carbon deposition could be found on the surface of both catalysts after running the reforming reaction for 3 hours. Neither carbon nanofibers nor carbon nanotubes were observed, although carbon filament deposition on the catalyst surface was often reported in many previous works [136, 226]. This also agreed with the obtained high carbon balance in the plasma reforming process.

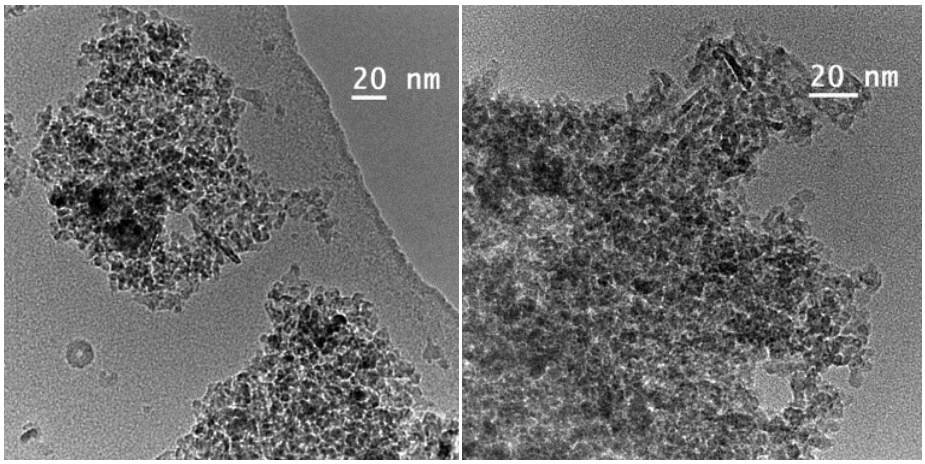

(a) (b)

Figure 5.5 TEM images of the used catalysts. (a) Ni/Al_2O_3; (b) Cu/Al_2O_3

These findings suggest that there is still room for manipulating the interactions between the plasma and catalysts in the plasma-catalytic dry methane reforming process to maximize the performance of the plasma process. By using deliberately designed catalysts and suitable reaction conditions, multiple targets including enhanced reactant conversions, balanced H_2/CO ratio and enhanced selectivity of products could be achieved simultaneously.

5.1.4. Energy efficiency of plasma process

Figure 5.6 shows that the energy efficiency of the plasma reforming reaction was 0.60 mmol kJ^{-1} without catalyst. Note that the combination of the plasma with catalysts cannot always enhance the energy efficiency of the plasma reforming process. In this section, introducing the Ni/Al_2O_3 and Mn/Al_2O_3 catalysts into the discharge gap was found to improve the overall energy efficiency of conversion by 20% and 17%, respectively, while packing the Cu and Co catalysts into the DBD reactor slightly

decreased the energy efficiency of the plasma process. The maximum energy efficiency for the conversion of CH_4 and CO_2 (0.72 mmol kJ^{-1}) was achieved at a discharge power of 7.5 W and a total flow rate of 50 ml min^{-1} when the Ni/Al_2O_3 catalyst was placed in the plasma.

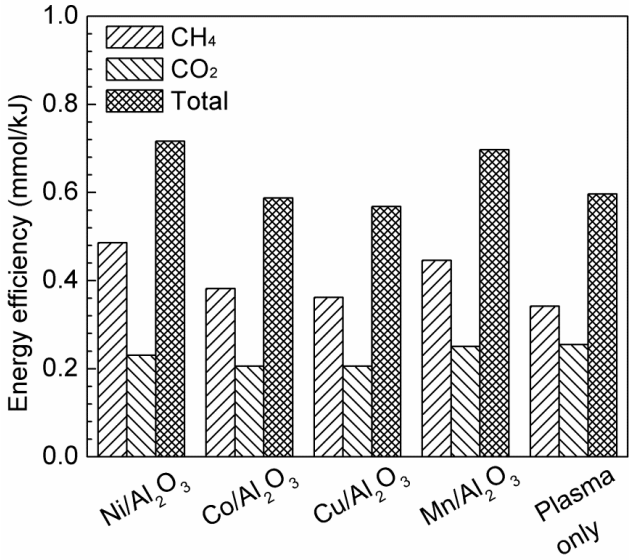

Figure 5.6 Energy efficiency of the plasma dry reforming process using different catalysts. (CO_2/CH_4 = 1: 1, total flow 50 ml min^{-1}, and discharge power 7.5 W)

Table 5.1 compares the energy efficiency of dry methane reforming using different atmospheric pressure plasma sources. A more informative comparison can be found in Chapter 1. The energy efficiency of the plasma-catalytic reforming process achieved in this chapter is much higher than that of plasma reforming using similar dielectric barrier discharges. This value is still relatively low compared to the plasma reforming process with either gliding arc or thermal plasma. However, it is worth noting that one of the advantages of DBD technology is its ability to be combined with other technologies such as heterogeneous catalysis, known as hybrid plasma-catalytic process, while catalysis technology will be difficult to be integrated into gliding arc or thermal plasma process since a significant amount of carbon can be produced in the plasma dry methane reforming process, causing quick catalysts deactivation due to coke deposition. By choosing highly active and stable catalysts, the energy efficiency of the plasma reforming process in a DBD reactor can be further enhanced since the conversions of CH_4 and CO_2 are still low and there is still room for further improvement. It is also noticed that the plasma dry reforming process can be maintained at a low power in

dielectric barrier discharges compared to other plasma technologies (*e.g.* gliding arc and thermal plasma), which may offer flexibility of the DBD systems for processes requiring low energy and low temperature. Our previous work has shown that packing ferroelectric materials (*e.g.* $BaTiO_3$ pellets) in the DBD reactor can significantly enhance the conversion of reactant and energy efficiency of the plasma process for gas conversion [64]. DRM reported by reference [227] achieved relatively high CH_4 conversion and CO_2 conversion at 3.33 W power. It could be attributed to the effect of dilution gas (Ar), there were 5%–10% CH_4 and CO_2 in the feed gas. For comparison in this work, the feed gas only consisted of CH_4 and CO_2.

Table 5.1 Energy efficiency of dry reforming process for conversion using different plasma sources.

Plasma	Power (W)	Feed flow (ml min^{-1})	Conversion (%)		E (mmol kJ^{-1})	Reference
			CH_4	CO_2		
DBD	97	50	18	12.5	0.033	[96]
DBD	35	50	27	11	0.202	[123]
DBD	50	50	56.4	30.2	0.32	[37]
DBD	3.33	40	36	22	0.55	[227]
DBD	7.5	50	19.6	9.3	0.72	**this work**
DC corona	45	60	80	70	0.74	[115]
Gliding arc	165	7500	13.1	8.4	3.1	[104]
Gliding arc	720	16000	48.6	56.5	8.6	[164]
Gliding arc	190	4000	15	18	2.6	[157]
Rotational GA	175	6000	48	54	13.0	[156]
Pulsed DC arc	165	100	99.5	97.6	0.9	[228]
RF plasma	36.2	200	65.9	57.8	2.4	[108]
Thermal	3400	16000	90	88	3.1	[229]

5.2. Effect of K, Mg and Ce promoters on plasma-catalytic biogas reforming

In this section, the catalytic biogas reforming over K, Mg and Ce promoted Ni/Al_2O_3 catalysts with and without a plasma has been investigated in a coaxial DBD reactor at atmospheric pressure and low temperature (160 ^oC). To understand the synergy of plasma-catalysis, plasma-driven biogas reforming has also been carried out

at the same temperature of 160 ºC for comparison. The properties and textural structure of the catalysts were characterised by XRD, BET and TPR techniques. The effect of promoters on the reforming process under plasma-catalytic conditions has been investigated in terms of the conversion of CO_2 and CH_4, the selectivity and yield of gas products, the H_2/CO molar ratio in the product and the energy efficiency of the reforming process. The carbon deposition on the spent catalyst after reforming process was also examined and discussed.

5.2.1. Experimental setup

A detailed explanation of the experimental setup can be found in Chapter 2. In this section, the discharge power was fixed at 16 W. A simulated biogas with a typical CH_4/CO_2 molar ratio of 3:2 was used as reactants and the flow rate was 50 ml min^{-1}. The 8 wt.% Ni/γ–Al_2O_3 and 8 wt.% Ni– 2 wt.% X/γ–Al_2O_3 (X = K, Mg and Ce) catalysts were prepared by impregnation method using nitrate salt (Alfa Aesar, ACS reagents) as the metal precursor. A calculated amount of support (granular Al_2O_3) was added to the solution of nitrate salt. The mixture was continuously stirred for 1 hr and impregnated for 3 hrs, then dried at 90 °C overnight, followed by calcination at 400 °C for 4 hrs. A total amount of 0.4 g Ni-based catalyst was packed into the reactor and sandwiched by quartz wool on both sides. Prior to the plasma-catalytic reforming, the Ni-based catalyst was reduced in an argon-hydrogen discharge at a discharge power of 16 W (50 ml min^{-1}, 20 vol. % H_2) for 30 minutes in the same DBD reactor. The catalysts, Ni/Al_2O_3, Ni–K/Al_2O_3, Ni–Mg/Al_2O_3 and Ni–Ce/Al_2O_3 are denoted as NiAl, NiKAl, NiMgAl and NiCeAl in the following discussions, respectively.

The DBD reactor was placed in a tube furnace, as explained in Chapter 2. The temperature inside of the reactor was 160 ± 5 ºC for all three conditions, measured by a fibre optical thermometer (Omega FOB102). However only for the thermal-catalytic process, the reactor was heated by the tube furnace, while no extra heating was provided to the plasma process with or without a catalyst.

N_2 adsorption–desorption analysis was performed at −196 °C to measure the pore size and specific surface area of the catalysts (Micrometrics ASAP 2020 instrument, USA). Prior to the measurement, the samples were outgassed at 350 °C for 3 hrs under vacuum to remove moisture and other adsorbed gases. The specific surface area of the samples were calculated using the Brunauer−Emmett−Teller (BET) method. XRD

patterns of the catalyst samples were measured by an X–ray diffractometer (Rigaku D–Max 2400, Cu–K_α radiation, Japan) in the 2θ scanning range between 10° and 80°. The reducibility of the catalysts was investigated by temperature–programmed reduction with hydrogen (H_2–TPR) using an automated chemisorption analyzer (Quantac chrome ChemBET 3000, USA). Before each measurement, the sample was firstly treated at 400 °C for 1 hr in a 20 ml min^{-1} He flow. After cooled to 150 °C, the sample was saturated with H_2 for 30 min and then purged with a He flow at 150 °C for 1 hr. The carbon deposition on the spent catalysts was determined by thermal gravimetric analysis (TGA) in an air atmosphere. The spent catalyst was heated from 30 °C to 800 °C at a heating rate of 10 °C min^{-1} in an air flow of 30 ml min^{-1}.

For the biogas reforming, the conversion (X) of CH_4 and CO_2, the selectivity (S) and yield (Y) of the products, the H_2/CO molar ratio in the product, the total energy efficiency for the conversion of CH_4 and CO_2 (E) [98], fuel production efficiency (FPE) of the biogas reforming [180] and synergy capacity (SC) of the plasma-catalysis [179] are defined in Chapter 2.

5.2.2. Textural properties of catalysts

Figure 5.7 shows the XRD patterns of the fresh catalysts. Three major diffraction peaks located at $2\theta = 37.6°$, 45.9° and 67.0° are corresponding to the cubic structure of alumina crystallite (JCPDS 10–425). Diffraction peaks of NiO crystallite (JCPDS 1–75–197) can also be clearly seen on the XRD patterns of all the catalysts. However, only weak reflections of MgO (JCPDS 1–1235) and CeO_2 (JCPDS 3–65–5923) crystallite were found in the results [230, 231]; while the diffraction peaks of cubic K_2O (JCPDS 23–493) were not observed at all [232], suggesting the well-dispersion of K species [233]. Scherrer equation was used to estimate the crystallite size of catalysts, as summarised in Table 5.2 [215]. The crystallite size of NiAl catalyst was 6.1 nm, but significantly increased to 9.6 nm with the addition of Mg. Similar phenomenon of increased crystalline size on promoted catalysts has also been reported in thermal catalytic reforming [95, 124]. Notably, few promoters (*e.g.* adding La into Co/ZrO_2) have been reported to improve the dispersion of active metal species on the surface of the catalyst. However, K, Mg and Ce promoters have been observed to agglomerate the active metal species and result in larger particle sizes [126]. Interestingly, larger particle sizes generally facilitate coke deposition [234-236]. In thermal catalytic processes, the

K, Mg and Ce promoters preferentially bind to "coking sites" and suppressing the formation of graphite, without significantly affecting the reforming performance [237].

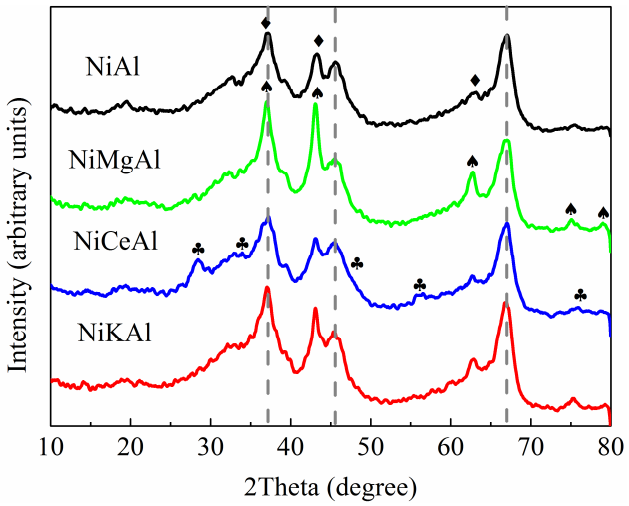

Figure 5.7 XRD patterns of the fresh catalysts. (♦ NiO, ♠ MgO, ♣ CeO_2, dash line γ–Al_2O_3)

Table 5.2 shows the textural properties of the catalysts. The BET specific surface area of the NiAl catalyst was 164.9 m^2 g^{-1}, while that of the promoted catalysts were slightly decreased and in the range between 152 and 158 m^2 g^{-1}. The BET area of the catalysts follow the order of NiAl > NiMgAl > NiCeAl > NiKAl.

Table 5.2 Textural characteristics of fresh catalysts.

Catalyst	Specific surface area (m^2 g^{-1})	Total pore volume (cm^3 g^{-1})	Average crystallite size (nm)
NiAl	164.9	0.286	6.1
NiMgAl	159.5	0.252	9.6
NiCeAl	157.9	0.293	6.9
NiKAl	152.4	0.290	7.8

5.2.3. Temperature-programmed reduction of the catalysts

The reducibility of supported metal catalysts is a critical factor affecting the catalytic performance. Figure 5.8 shows the H_2–TPR result of the fresh Ni-based catalysts. On the TPR profile of the NiAl catalyst, the first peak at 290 °C corresponds to the reduction of bulk NiO, while the overlapping peak at 410 °C is assigned to the

reduction of less active NiO. The less active NiO has higher reduction temperature due to its interaction with the support of the catalyst [120, 219]. The addition of K, Mg and Ce promoters exhibit different effects on the reducibility of the Ni-based catalyst. On the TPR result of the NiMgAl catalyst, the reduction temperature of bulk NiO greatly increased to 340 °C. The intensity of peaks corresponding to the reduction of NiO are diminished. It is likely due to the intensified interaction between NiO and Al_2O_3 by the Mg species [136, 238]. The reduction of bulk NiO on the NiCeAl catalyst occurred at 230 °C, clearly the lowest reduction temperature among the catalysts. However, the broad reduction peak of the Ce- promoted catalyst implies that the NiCeAl catalyst might show a limited catalytic performance at low temperatures (*e.g.* 160 °C). The NiKAl catalyst has a TPR profile very similar to the NiAl catalyst except that the reduction temperature of bulk NiO decreases to 260 °C. It can be concluded that the reducibility of the investigated catalysts follows the order of NiCeAl > NiKAl > NiAl > NiMgAl.

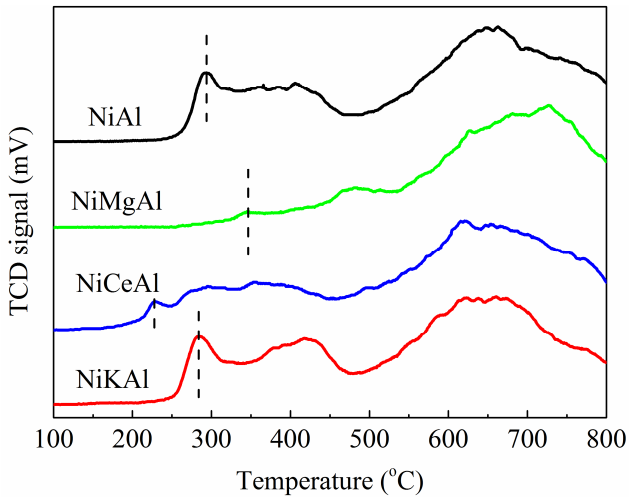

Figure 5.8 H_2–TPR profiles of fresh catalysts.

5.2.4. Biogas reforming over promoted catalysts

Figure 5.9 shows the conversion of CH_4 and CO_2 in the biogas reforming process at the same temperature of 160 °C under different conditions: plasma-alone, thermal catalysis and plasma-catalysis. A synergy between the DBD plasma and the NiKAl catalyst can be clearly identified. At such a low temperature, the reforming reaction is only initiated with the presence of plasma, regardless of the use of catalyst. Without

plasma, the conversion of CH_4 and CO_2 were negligible. For comparison, the conversion of CH_4 and CO_2 in the plasma-driven biogas reforming at 160 ^oC were 25.1% and 18.2%, respectively. The promotional effect of plasma suggests that at 160 ^oC, DBD plasma was the key driving force for the reforming of CH_4 and CO_2, ascribe that it can activate the catalyst, dissociate gas molecules and initiate reforming reaction. Figure 5.10(a) shows the effect of different catalysts on the conversion of CH_4 and CO_2 at the same temperature of 160 ^oC. The promoted catalysts enhanced the conversion of CH_4 in the feed gas, comparing with reforming over the NiAl catalyst, and the K- and Ce- promoted catalysts increased the conversion of CO_2. However, the Mg- promoted catalyst decreased the CO_2 conversion. In the plasma-catalytic biogas reforming over the promoted catalysts, the best conversion of CH_4 and CO_2 was achieved by the NiKAl catalyst, closely followed by the NiCeAl catalyst.

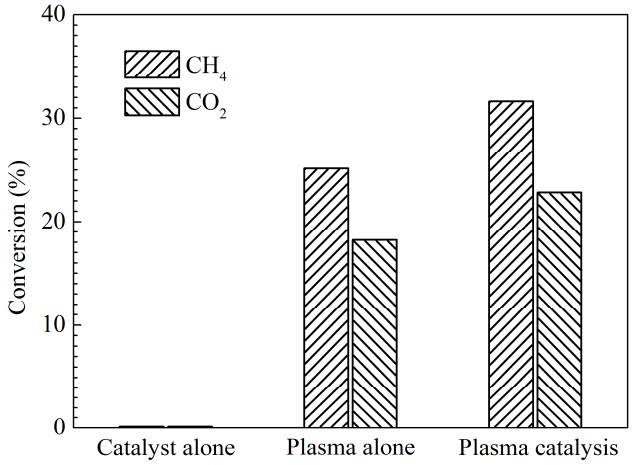

Figure 5.9 Conversions of CH_4 and CO_2 under different conditions. (CH_4/CO_2 molar ratio 1.5, flow rate 50 ml min^{-1}, discharge power 16 W, temperature 160 ^oC, and using NiKAl catalyst)

Interestingly, in the reported works on thermal catalytic dry reforming of methane at higher temperatures, where Ni/Al_2O_3 catalysts were prepared by wetness incipient methods, the K- and Ce- promoted catalysts decreased the conversion of both CH_4 and CO_2 [124, 125], while the Mg- promoted catalyst is reported to improve the conversion of CO_2, as compared with the results obtained over un-promoted catalysts [94, 95, 127]. For instance Nandini *et al.* carried out thermal catalytic biogas reforming over a 8.8 wt.% Ni/Al_2O_3 catalyst at 800 ^oC, with a feed gas ratio CH_4: CO_2: N_2 of 1: 1: 0.9, after the addition of 0.5 wt.% K content into the catalyst they found that the conversion of CH_4

decreased from 84.7% to 70.2%, while the CO_2 conversion decreased from 81.4% to 72.1% [124]. Alipour *et al.* reported the thermal catalytic dry reforming of methane over a 5 wt.% Ni/Al_2O_3 catalyst at 650 °C, with the addition of 3 wt.% Mg content into the catalyst, the conversion of CO_2 increased from 66% to 77% [95]. By contrast, Wang *et al.* prepared a $NiO\text{-}CeO_2\text{-}Al_2O_3$ catalyst by an improved one-pot evaporation-induced self-assembly (EISA) method, and investigated the thermal catalytic DRM using this Ni-Ce-Al catalyst at 700 °C [128, 239]. The authors found that when the Ce/Al molar ratio of the Ni-Ce-Al catalyst increased from 0 to 1:50, the conversion of CH_4 increased from 60% to 80%, and that of CO_2 increased from 59% to 73%, respectively [239]. It can be concluded that the conversion of CH_4 and CO_2 in the catalytic biogas reforming processes is highly dependent on the reaction condition such as the preparation method of catalyst. The effects of K, Mg and Ce promoters on the plasma-catalytic biogas reforming are also affected by the presence of DBD plasma.

The selectivity of H_2 and CO in the plasma biogas reforming with or without a catalyst are shown in Figure 5.10(b). The presence of catalyst clearly decreased CO selectivity. However, only the NiKAl catalyst effectively improved the H_2 selectivity; while other catalysts exhibited limited effect on the selectivity of H_2. More specifically, among all the investigated catalysts, the NiKAl catalyst achieved the highest H_2 selectivity (43.3%), while the NiMgAl catalyst exhibited the lowest CO selectivity (29.4%). This is actually consistent with the result of conversions as shown in Figure 5.10(a): The CH_4 conversion was preferentially enhanced by the combination of DBD plasma and catalyst. As a consequence, the amount of resulting products such as H_2 and C_2–C_4 alkanes was increased in the effluent gas. This can be evidenced by the enlarged H_2/CO molar ratio as shown in Figure 5.10(d). The use of NiAl and NiMgAl catalysts favoured the production of C_2–C_4 alkanes; while the presence of NiKAl catalyst promoted the production of H_2 (Figure 5.11). All these results decreased the apparent selectivity for CO but increased that for alkanes when using the NiAl and NiMgAl catalysts. Similarly, the apparent selectivity for H_2 when using the NiKAl catalyst was also increased. In our previous work, the H_2/CO molar ratio was also increased when using a Ni/Al_2O_3 catalyst [98]. It is remarkable that among the catalysts, the NiMgAl catalyst achieved the largest H_2/CO ratio of 2.2, while the NiKAl and NiCeAl catalysts had the smallest ratios of 1.9. Interestingly, the H_2/CO ratio obtained over different catalysts followed the exactly reversed order as the reducibility of these Ni-based catalysts, NiCeAl < NiKAl < NiAl < NiMgAl. This is plausible since the production of

CO is dependent on the conversion of CO_2, while the CO_2 conversion is dependent on the reducibility of the catalyst.

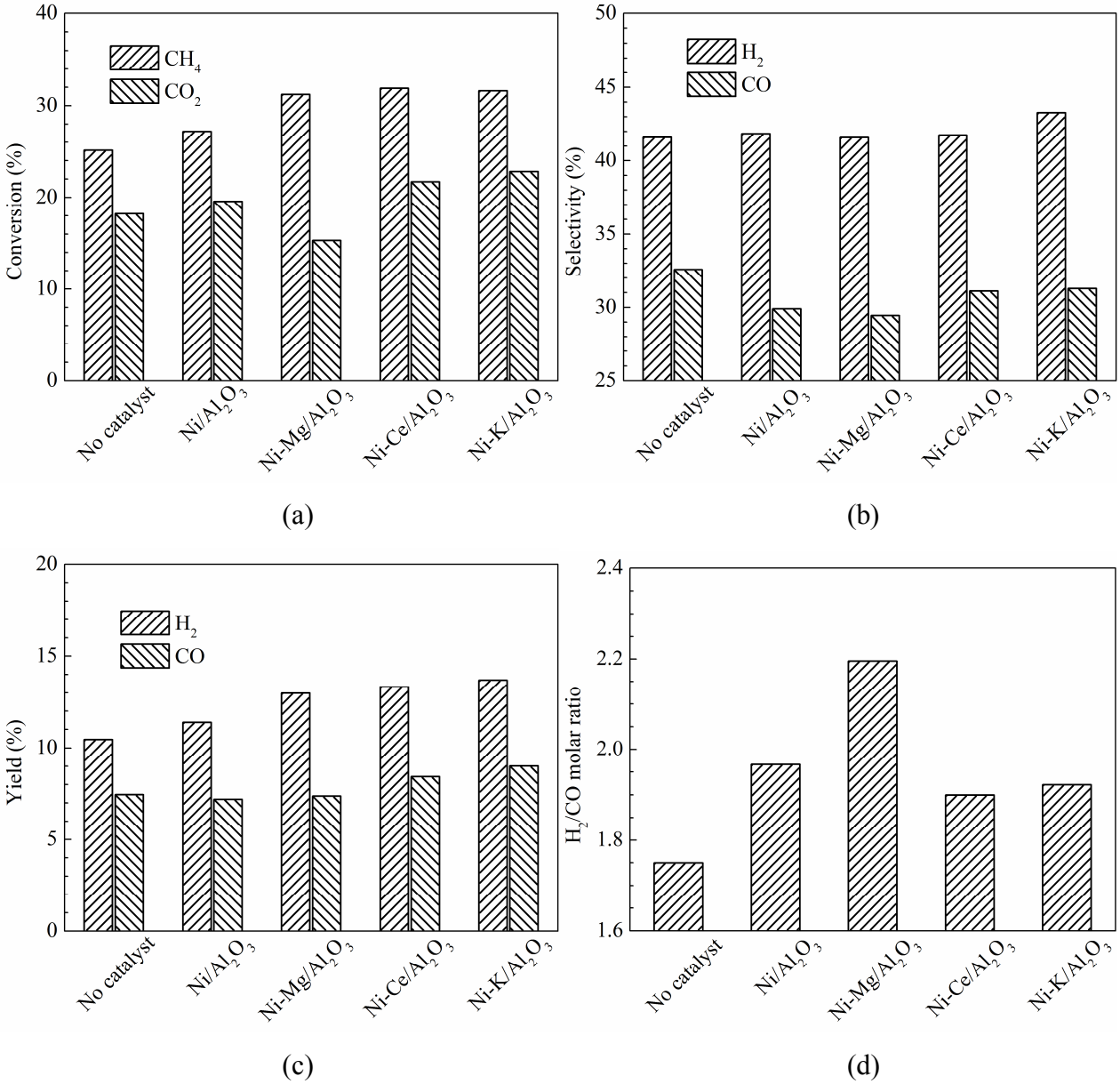

Figure 5.10 (a) Conversion of CH_4 and CO_2, (b) Selectivity and (c) Yields of H_2 and CO, and (d) H_2/CO molar ratio in the product after using different catalysts. (CH_4/CO_2 molar ratio 1.5, flow rate 50 ml min^{-1}, and discharge power 16 W)

The Mg- promoted catalyst was distinguishable from the K- and Ce- promoted catalysts, in terms of CO_2 conversion, CO selectivity and H_2/CO molar ratio in the product. This is probably ascribed to the relatively low reducibility of NiMgAl catalyst as confirmed by the TPR profile. The higher reduction temperature of NiMgAl catalyst

suggests the catalytic activity being greatly suppressed at low temperatures. Hence, the CO_2 decomposition on the surface of the catalyst was suppressed at 160 ^oC, subsequently decreasing the CO_2 conversion while enlarging the H_2/CO ratio in the product.

Saturated hydrocarbons including ethane, propane and butane, together with unsaturated ethylene and acetylene were detected during the biogas reforming over promoted catalysts, as shown in Figure 5.11. The amounts of alkanes in the effluent gas are two orders of magnitude larger than those of unsaturated ones. Therefore only the selectivity and yields of alkanes in the product are presented. The NiMgAl catalyst achieved the highest selectivity towards ethane and propane, while the NiKAl catalyst had the lowest. All the catalysts had similar selectivity of butane. It is noticeable that butane was produced only when a catalyst was used. Moreover, all the catalysts improved the yield of C_2 to C_4 alkanes and promoted catalysts showed better improvements. Compared to reforming using plasma alone, the combination of DBD plasma and NiKAl catalyst enhanced the yield of ethane by 16.5%; it also enhanced the yield of propane by 25.5%. These results are due to the significant enhancement of conversion using the catalysts.

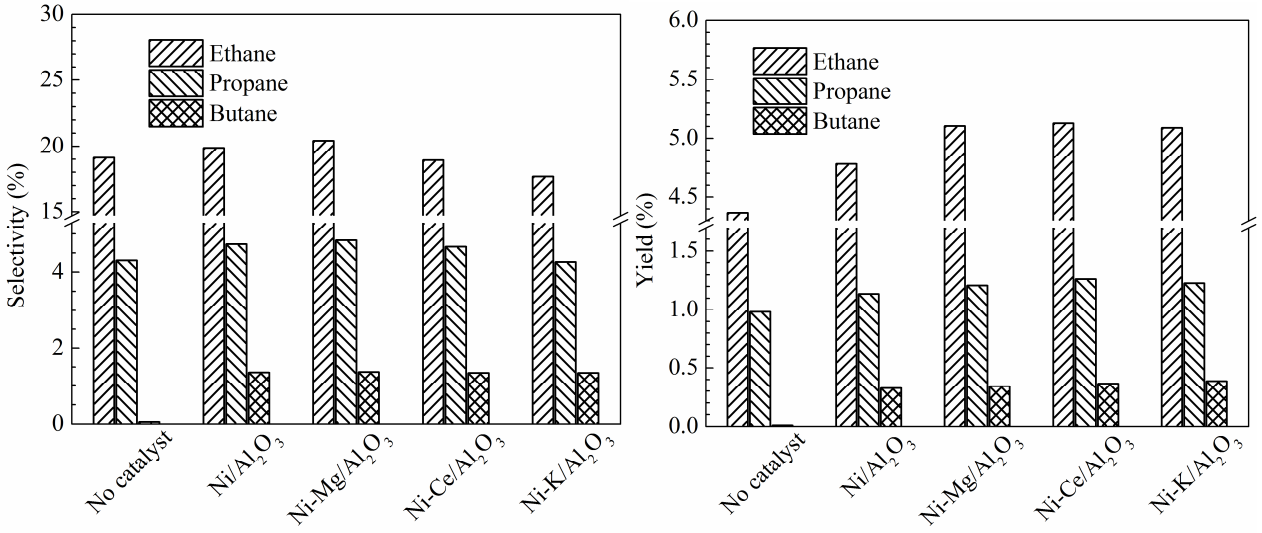

Figure 5.11 (a) Selectivity and (b) Yield of C_2 -C_4 alkanes over different catalysts. (CH_4/CO_2 molar ratio 1.5, flow rate 50 ml min^{-1}, and discharge power 16 W)

Figure 5.12 shows the influence of catalysts on the total energy efficiency and fuel production efficiency of plasma biogas reforming. Clearly, compared to the plasma reforming of biogas without a catalyst, the combination of the DBD with the Ni-catalysts enhanced the total energy efficiency and fuel production efficiency due to the generation of plasma-catalytic synergy. In plasma-catalytic biogas reforming, the use of K, Mg and Ce promoted Ni/Al_2O_3 catalysts showed higher energy efficiency compared with the NiAl catalyst. The highest energy efficiency (0.67 mmol/kJ) and fuel production efficiency (14.4%) were achieved when placing the NiKAl catalyst in the plasma biogas reforming process. Table 5.3 presents a summary of the energy efficiency obtained in plasma biogas reforming under similar conditions.

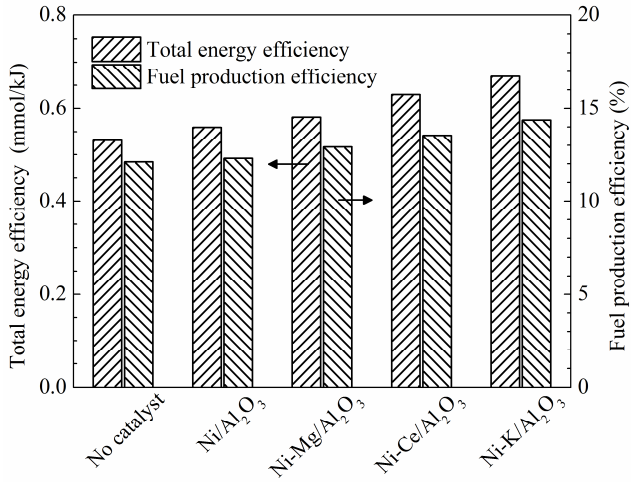

Figure 5.12 Total energy efficiency and fuel production efficiency of plasma reforming over different catalysts. (CH_4/CO_2 molar ratio 1.5, flow rate 50 ml min^{-1}, and discharge power 16 W)

Table 5.3 DBD plasma assisted dry reforming of methane.

Catalyst	Feed flow (ml min^{-1})	CH_4/CO_2	P (W)	Conversion (%)		Selectivity (%)		E (mmol kJ^{-1})	FPE (%)	Ref
				CH_4	CO_2	CO	H_2			
None	20	1:1	107	72.8	44.4	82.0	70.0	0.137	4.0	[240]
Ni/Al_2O_3	30	1:1	130	55.7	33.5	60.9	51.9	0.096	3.0	[241]
Ni/Al_2O_3	50	1:1	30	26.1	16.3	48.8	34.6	0.112	10.4	[97]
Ni/Al_2O_3	50	1:1	7.5	19.6	9.3	38.0	34.0	0.720	11.6	[98]
Ni/Al_2O_3	50	1:1	50	56.4	30.2	52.4	31.0	0.320	13.1	[37]
Ni/Al_2O_3	50	3:2	16	27.2	19.6	29.9	41.2	0.559	12.3	**This work**
$Ni\text{-}K/Al_2O_3$	50	3:2	16	31.6	22.8	31.3	43.3	0.669	14.4	**This work**

Synergistic capacity is used to quantify the reaction performance of plasma-catalytic biogas reforming, comparing against the individual processes using plasma-alone or catalyst-alone at the same temperature of 160 °C, as shown in Table 5.4. Significant synergy between the plasma and the Ni-based catalysts is highlighted by the conversion of CH_4, the yield of H_2 and propane, and the total energy efficiency. For instance the yield of H_2 had a synergistic capacity of 9% in the absence of a promoter and reached a maximum value of 31% over the NiKAl catalyst. The synergistic capacity of the plasma-catalytic process was significantly enhanced over the K- promoted catalyst. The suppression of CO_2 conversion over the NiMgAl catalyst was also clearly reflected by the negative synergistic capacity. As shown in Figure 5.10 and Figure 5.12, the addition of K, Mg and Ce promoters showed a more pronounced effect on the reaction performance (conversion, selectivity, yield and energy efficiency). The interaction between DBD plasma and promoted catalysts [33, 34], and the improving effect of Ar (in the feed gas) on the plasma-assisted reactions [196] could be the main driving force for the significant synergistic capacity of the plasma-catalytic biogas reforming.

Table 5.4 Synergy capacities (unit: %) of plasma catalytic biogas reforming. (CH_4/CO_2 molar ratio 1.5, flow rate 50 ml min^{-1}, discharge power 16 W, and reaction temperature 160 °C)

Catalyst	Q_{CH4}	Q_{CO2}	Q_{H2}	Q_{CO}	Q_{C2H6}	Q_{C3H8}	Q_E	Q_{FPE}
NiAl	8	7	9	-3	9	16	5	2
NiMgAl	24	-16	24	-1	17	23	9	7
NiCeAl	27	19	27	13	17	28	19	12
NiKAl	26	25	31	21	17	25	26	19

5.2.5. Effect of promoters on carbon deposition

The types of carbon deposition on spent catalysts can be divided into three categories, according to the oxidation temperature of these carbonaceous species. They are distinguished by the peaks on the TGA profiles: active carbonaceous species (C_α), less active carbonaceous species (C_β) and inactive carbonaceous species (C_γ) [242, 243]. In this section, the peak located at about 310 °C represents the active C_α species which

usually exist as a mixture of amorphous carbon, higher hydrocarbons and polymers. C_α species can be easily oxidised to form CO. The peak at about 520 ºC was assigned to the less active C_β species which existed in the mixed form of amorphous and filamentous carbon [95, 124, 125]. A negligible amount of C_γ species was observed on the spent catalysts. As shown in Figure 5.10, the combination of plasma and catalyst significantly enhanced the conversion of CH_4, and the K-, Ce- promoted catalysts also greatly increased the conversion of CO_2. As a consequence, the promoted catalysts increased the carbon production, which can be reflected by the weight losses corresponding to different carbon species as shown in Table 5.5. The amount of carbon deposition follows the order of NiCeAl > NiKAl ≈ NiMgAl > NiAl, agreeing with the results of CH_4 conversion as shown in Figure 5.10. This is plausible because the decomposition of CH_4 is an important source of carbon solid in the biogas reforming reactions. The amount of carbon deposition also agrees with the reducibility of the promoted catalysts (NiCeAl > NiKAl ≈ NiAl > NiMgAl). This is reasonable since the reducibility of catalysts reflect their reactivity. However, it is very interesting that for the thermal catalytic biogas reforming, the carbon deposition on the surface of the catalyst has been reported to be significantly reduced over the K-, Mg- and Ce-promoted catalysts, comparing with using the corresponding un-promoted catalysts [94, 95, 124-126, 131]. For instance, Sengupta *et al.* reported that by adding 5 wt.% MgO content into the 15 wt.% Ni/Al_2O_3 catalyst, the carbon deposition on the spent catalyst after dry reforming of methane at 600 ºC and for 3 hrs decreased from 24.5 wt.% to 14.4 wt.% [94]. Ozkara-Aydinoglu *et al.* reported that the carbon deposition on the spent Co/ZrO2 catalyst was decreased from 4% to 2.6% after the addition of Mg promoters [126]. The different behaviour of carbon production and deposition under thermal- and plasma- catalytic conditions suggests its dependence on the presence of non-thermal plasma, which again confirms the conclusion made on the conversion of CH_4 and CO_2. The combination of non-thermal plasma and promoted catalysts significantly enhanced the conversion of CH_4 and CO_2, improved the energy efficiency of the catalytic biogas reforming process, and consequently increased coke production; while the addition of K, Mg and Ce promoters kept the increased coke deposition in the form of reactive species. However, it worth noting that although the promoted catalysts increased the carbon deposition by 22%-26% compared to the NiAl catalyst, the increased carbon deposition on the catalysts is mainly in the form of C_α species. This reactive carbonaceous species contributed more than 70% of the increased amount of

carbon deposition. On one hand, the reactive species are easier to react with CO_2 or O species to form CO, consequently "regenerating" the catalyst. In other words, the promoted catalysts could have relatively long lifetime in the biogas reforming process. On the other hand, this result agrees well with the reported mechanism of K-promoter suppressing the formation of graphite during reforming [237]. Most importantly, the carbon deposition on the surface of the promoted catalyst in this work was still comparable or even less than the reported value (13%-40%) obtained in the thermal catalytic dry reforming of methane over promoted Ni/Al_2O_3 catalysts [94, 125], even though the CH_4/CO_2 molar ratio in this work is higher than that in a DRM process. This result suggests that the DBD plasma significantly reduced the carbon production in the plasma-catalytic biogas reforming reaction at 160 °C.

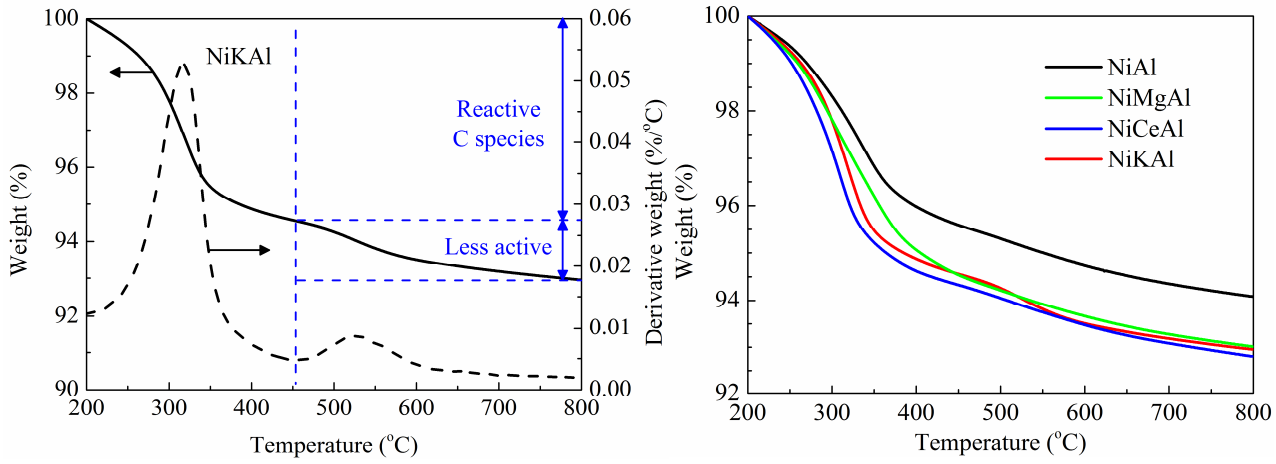

(a) (b)

Figure 5.13 TPO profiles of (a) spent NiKAl catalyst and (b) spent Ni based catalysts after biogas reforming.

Table 5.5 Amount of carbon deposited on the spent catalysts.

	Carbon deposition (wt. %)		
Catalyst	Reactive	Less active	Total
NiAl	4.52	0.9	5.42
NiMgAl	5.59	0.95	6.54
NiCeAl	5.63	1.21	6.84
NiKAl	5.43	1.16	6.59

5.3. Summary

In the first section of this chapter, the effect of different reaction conditions (*e.g.* CO_2/CH_4 and total feed flow rate) and Al_2O_3 supported metal (Ni, Co, Cu and Mn) catalysts on the plasma-catalytic dry methane reforming has been investigated in a coaxial DBD reactor. In the plasma reforming reaction without catalyst, the CO_2/CH_4 molar ratio significantly affects the conversion of reactants, the selectivity and yield of major products, as well as the ratio of H_2/CO, while the variation of the total reactant flow rate does not change the H_2/CO ratio and the selectivity of syngas. Combining the DBD with the Ni/Al_2O_3 and Mn/Al_2O_3 catalysts significantly enhances the conversion of CH_4 and shows a synergistic effect of plasma-catalysis for CH_4 conversion. The maximum CH_4 conversion of 19.6% was achieved in the plasma-catalytic dry reforming over the Ni/Al_2O_3 catalyst at a discharge power of 7.5 W and a gas flow rate of 50 ml min^{-1}, followed by the Mn/Al_2O_3, Co/Al_2O_3 and Cu/Al_2O_3. However, the presence of these catalysts in the plasma did not enhance the conversion of CO_2. In addition, packing these Al_2O_3 supported catalysts into the discharge gap enhanced the yields of CO and H_2, especially the Ni/Al_2O_3 catalyst. The effect of these catalysts on the carbon balance of the process agreed with the conversions of CH_4 and CO_2 using different catalysts in the plasma system. The maximum energy efficiency of the plasma-catalytic reforming process obtained in this chapter was much higher than that of the plasma reforming process using similar dielectric barrier discharges although it was still relatively low compared to those using gliding arc or thermal plasma. The results show that these catalysts had different effects on the reaction performance of the plasma reforming process, which also suggests that there is still room for the improvement of the overall energy efficiency of the plasma process by combining with highly active and cost-effective catalysts.

In the final section of this chapter, plasma-catalytic biogas reforming over promoted Ni/Al_2O_3 catalysts has been carried out in a coaxial dielectric barrier discharge reactor at 160 ^oC. The combination of the Ni-based catalysts and the DBD plasma exhibited a synergistic effect at low temperature, enhancing the conversion of CH_4, the yield of H_2 and the energy efficiency of the plasma process, compared with the reaction using plasma alone or catalyst alone at the same temperature of 160 ^oC. The promoted catalysts showed a significant improvement on the reforming performance. In the plasma-catalytic biogas reforming, the Ni-based catalyst promoted

by K species showed the best performance, enhanced the conversion of both CO_2 and CH_4, the yield of H_2, CO and C_2 –C_4 alkanes, the total energy efficiency and the fuel production efficiency of the plasma process. While the Mg- promoted catalyst remarkably increased the H_2/CO ratio in the product. In addition, compared with using the NiAl catalyst, although the promoted catalysts increased the amount of carbon deposition on the surface of the spent catalyst due to their significant enhancement on the conversion of feed gas, the total amount of carbon deposition was still remarkably less than the reported values in thermal catalytic DRM reactions. TGA analysis showed that the increased carbonaceous species were mainly a reactive species, suggesting that the promoted catalysts were relatively easy to be regenerated during and after reforming reaction.

Chapter 6. Plasma-catalytic biogas reforming at elevated temperatures

In the previous chapter, Ni/Al_2O_3 was identified the best among the Co, Cu, Mn and Ni catalysts; while K was found the best among the K, Mg and Ce promoters. In this chapter, plasma-catalytic biogas reforming has been carried out in a dielectric barrier discharge (DBD) reactor, with and without a $Ni\text{-}K/Al_2O_3$ catalyst. The effect of the following process parameters on the reforming performance has been investigated: the preparation method of the $Ni\text{-}K/Al_2O_3$ catalyst, the temperature of the reforming process and the K loading of the Ni- catalysts. The performance of biogas reforming has been evaluated under three different operating conditions (plasma-alone, plasma-catalysis and thermal catalysis), in terms of conversion, selectivity, yield and energy efficiency. The carbon deposition on the spent catalyst was also discussed.

6.1. Effect of preparation method on plasma-catalytic biogas reforming using a $Ni\text{-}K/Al_2O_3$ catalyst

6.1.1. Experimental setup

Details of the experimental setup can be found in Chapter 2. In this section, the discharge power was fixed at 16 W. During the reforming reaction, the temperature of the reactor was always lower than 160 ^oC, monitored by a fibre optic thermometer (FOB102). A gas mixture of CH_4 and CO_2 with a CH_4/CO_2 molar ratio of 3: 2 was used as feed gas, and the total gas flow rate was 50 ml min^{-1}.

A catalyst consisting of 8 wt.% Ni and 2 wt.% K was prepared by the impregnation method as follows: The initial step was the calcination of support (Al_2O_3 granular) at 400 ^oC for 5 hrs. Following this, a calculated amount of the support was added to the solution of $Ni(NO_3)_2$ and KNO_3 salts (Alfa Aesar, ACS reagents). The mixture slurry was stirred for 1 hr, left to impregnation for 3 hrs, then dried at 90 °C overnight.

Subsequently, half of the catalyst was calcinated in a tube furnace at 400 °C for 4 hrs. This is known as thermal calcination (TC).. Meanwhile, the other half was calcinated in a DBD plasma at the same temperature and for the same period, this is known as plasma-calcination (PC). Again, the temperature was monitored using the fibre optic thermometer. The plasma-discharge power for calcination was 13 W, and external heating was applied to assure the calcination temperature was 400 ± 10 °C. By doing so, the effect of plasma on the catalyst during calcination, in addition to the effect of temperature, could be identified. After calcination, two samples of catalyst (0.4 g each) was packed into the reactor and sandwiched by quartz wool. One of the samples was reduced (50 ml min^{-1} Ar/H_2 flow, 20 vol.% H_2) at 350 °C for 40 minutes in a tube furnace, known as thermal reduction (TR). The other sample was reduced in an Ar/H_2 discharge at a discharge power of 13 W (50 ml min^{-1}, 20 vol.% H_2) at the same temperature and for the same period as for the thermal reduction. This is known as plasma-reduction (PR).Figure 6.1 shows the photos of the synthesised catalysts.

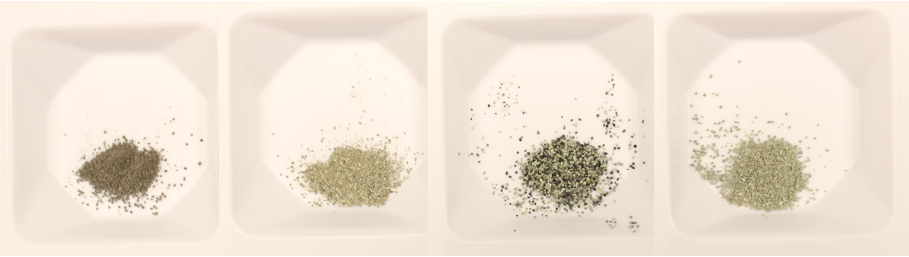

Figure 6.1 Photos of fresh Ni-K/Al_2O_3 catalysts prepared by different methods. (From left to right: HC + HR, HC + PR, PC + HR and PC + PR)

6.1.2. Results and discussion

In this section, results are presented of the experimental conversion of CH_4 and CO_2 to syngas over different catalysts, while the operational parameters such as CH_4/CO_2 molar ratio, feed flow rate and discharge power were held constant. Figure 6.2 shows the effect of preparation method of catalyst on the conversions of CH_4 and CO_2 in the plasma-catalytic biogas reforming. Clearly, the catalysts prepared by thermal calcination (TC) enhanced the CO_2 conversion compared to those prepared by the PC method, regardless of reduction method. One possible explanation for this result is that the plasma might act to collapse the pores on the surface of the catalyst, reducing the

specific surface area of the support and consequently decreasing the conversion of CH_4 and CO_2. For comparison, catalysts prepared by plasma reduction (PR) were found to promote CH_4 conversion, regardless of calcination method. It could be that the conversion of CH_4 is dependent on the oxidation states of the active metal species on the catalysts, and in this work, the non-thermal plasma was better at reducing metal particles supported on the catalysts than the thermal method. Remarkably, the catalyst prepared by thermal calcination and plasma reduction (TC+PR) achieved the best conversion of CH_4 (31.6%) and CO_2 (22.8%). It is also notable that the conversion of CO_2 was always smaller than that of CH_4. This probably results from side-reactions (*e.g.* water-gas shift reaction, CO oxidation by OH radicals and Boudard reaction), which convert the produced CO and H_2O into CO_2 and H_2, thus lowering the apparent conversion of CO_2.

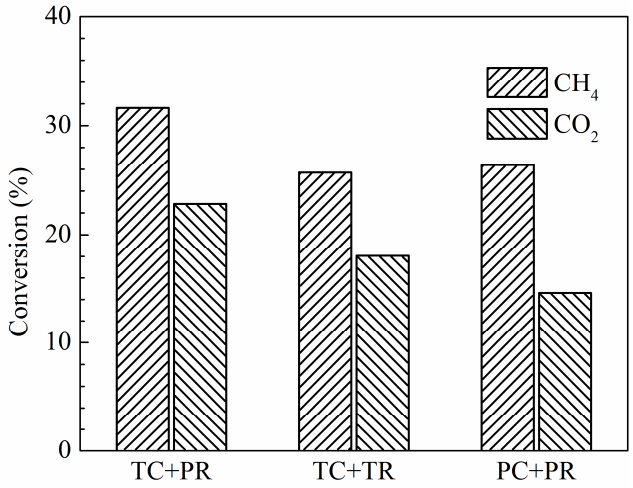

Figure 6.2 Conversions of CH_4 and CO_2 over different catalysts. (CH_4/CO_2 molar ratio 1.5, flow rate 50 ml min^{-1}, and discharge power 16 W)

Figure 6.3 shows the effect of preparation method of the catalyst on the selectivity and yield of H_2 and CO. The catalysts prepared by thermal calcination (TC) improved the selectivity of H_2, regardless of the reduction method. For comparison, the reduction method showed an insignificant influence on the selectivity of H_2. Both the calcination and reduction methods exhibited limited effects on the selectivity of CO. As a result, the catalyst prepared by thermal calcination and plasma reduction (TC+PR) achieved the highest H_2 selectivity of 41.6%. This result implies that by changing the preparation method of the catalyst, the selectivity for different products can be adjusted, even

without changing the composition of the catalyst. The catalyst prepared by thermal calcination and plasma reduction (TC+PR) also had the best yield of H_2 (13.7%) and CO (9.0%), due to the high conversion of CH_4 and CO_2, and high selectivity of H_2 achieved over the same catalyst.

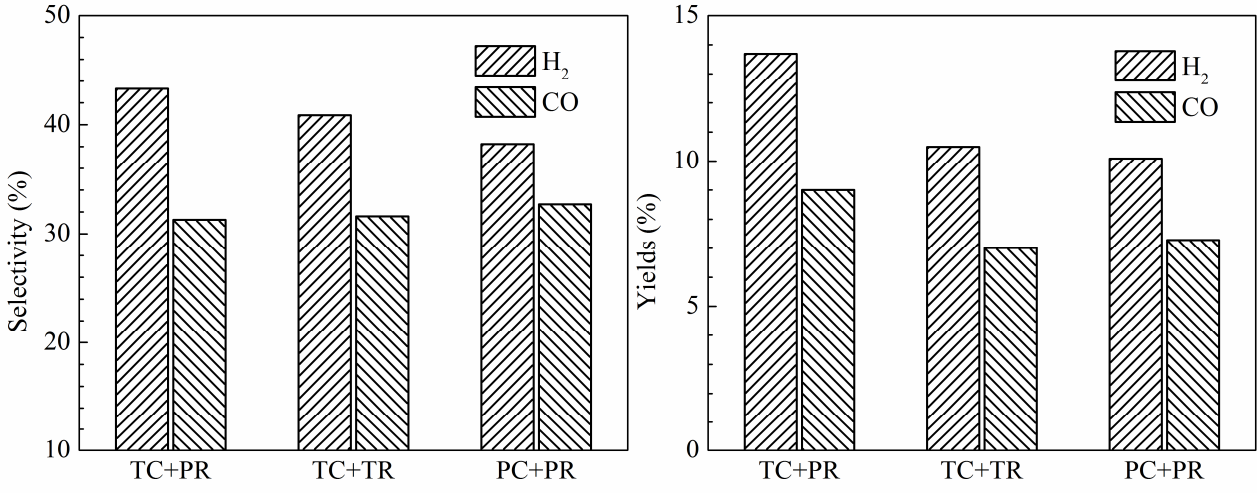

Figure 6.3 (a) Selectivity and (b) yield of H_2 and CO over different catalysts. (CH_4/CO_2 molar ratio 1.5, flow rate 50 ml min^{-1}, and discharge power 16 W)

Figure 6.4 shows the H_2/CO molar ratio in the product and the carbon balance of the reforming process. Notably, the catalyst prepared by the TC+PR method increased the H_2/CO molar ratio compared to other catalysts, due to the significant enhancement of H_2 production. By contrast, the plasma-calcinated and reduced (PC+PR) catalyst exhibited the highest carbon balance (93.3%), which means only 6.7% of the carbon in the feed gas was undetected after reaction. Since the undetected carbon can be used to estimate the amount of by-products that were produced during reforming, such as solid carbon, the result implies that less by-products were produced over the PC+PR catalyst. The PC+PR catalyst would consequently have a longer lifetime than the catalysts prepared by other methods.

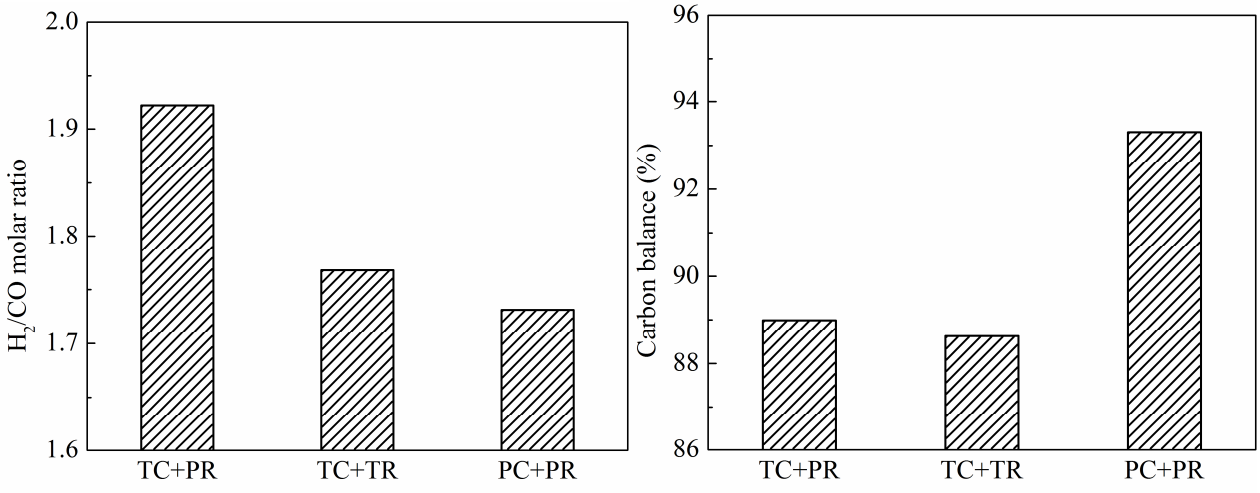

(a) (b)

Figure 6.4 (a) H_2/CO molar ratio in the products and (b) carbon balance of the reforming process. (CH_4/CO_2 molar ratio 1.5, flow rate 50 ml min^{-1}, and discharge power 16 W)

C_2 – C_4 hydrocarbons including ethane, ethylene, acetylene, propane and butane were also detected among the products of the plasma-catalytic biogas reforming process. Figure 6.5 shows the effect of preparation method of the catalyst on the selectivity and yield of these hydrocarbons. The selectivity of ethane, ethylene and acetylene shows a significant dependence on the preparation method of the catalyst. In contrast to selectivity for H_2 and CO seen with the TC+PR catalyst, the highest selectivity for ethane (20.5%), ethylene (4.7%) and acetylene (1.4%) was achieved by the catalyst prepared by plasma-calcination and plasma-reduction (PC+PR). The lowest selectivity for these three hydrocarbons was achieved by the TC+PR catalyst. This result suggests that the plasma-calcination process suppressed the selectivity for syngas, but promoted that for C_2 – C_4 hydrocarbons. The preparation method of catalyst was found to have a limited effect on selectivity for propane and butane. Notably, the selectivity of acetylene was always higher than that of ethylene, regardless of the catalyst used. This might be ascribed to the different formation mechanisms of the hydrocarbons. Remarkably, the highest yields of the mentioned C_2 – C_4 hydrocarbons were simultaneously achieved using the catalyst prepared by thermal calcination and plasma-reduction (TC+PR). The highest yields of ethane, ethylene, acetylene, propane and butane using the TC+PR catalyst were 5.1%, 0.16%, 0.17%, 1.2% and 0.39% respectively. This was due to the high conversion of CH_4 and CO_2 using this catalyst.

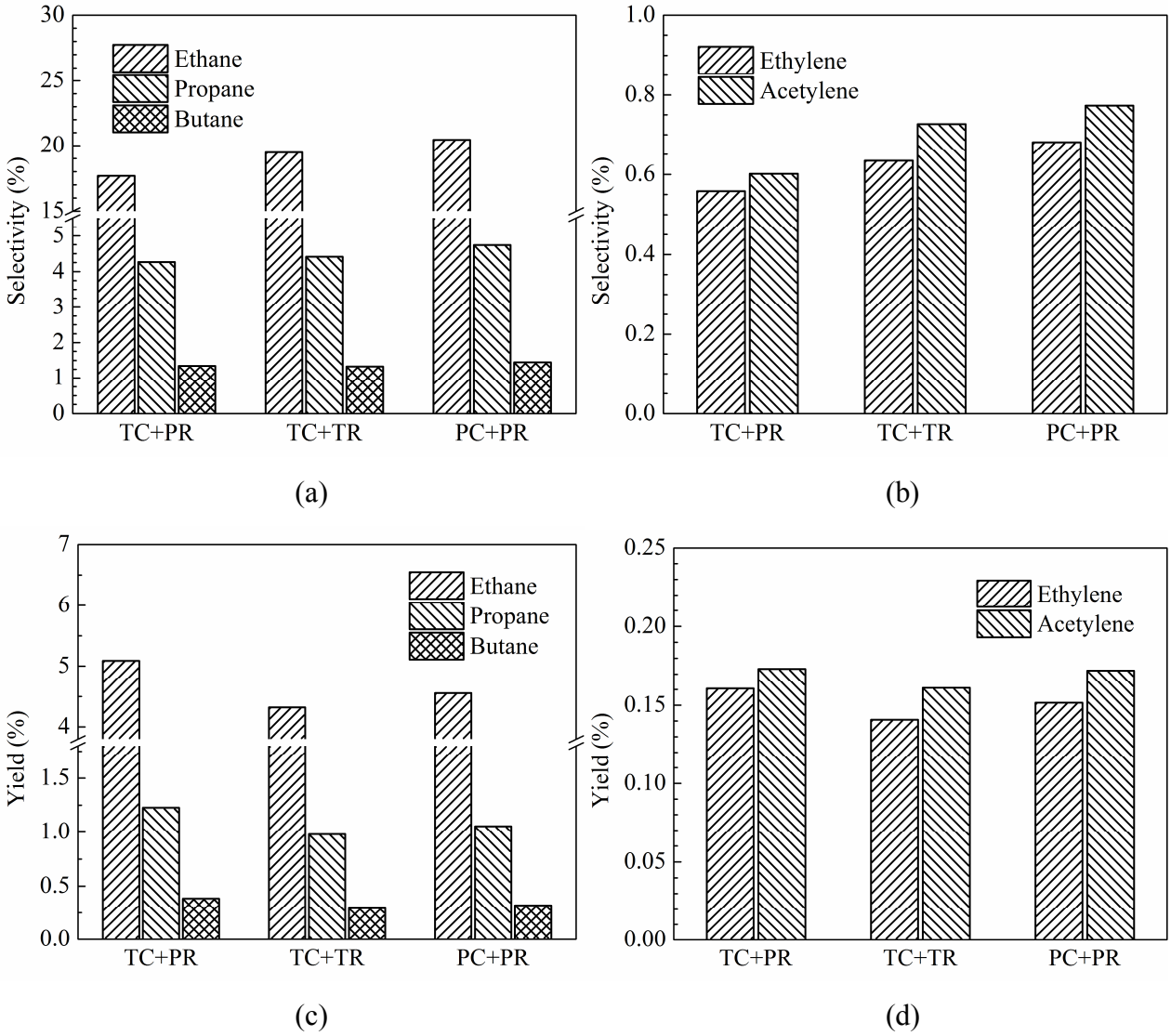

Figure 6.5 Effect of preparation method on the production of $C_2 - C_4$ hydrocarbons. (a) Selectivity of alkanes; (b) Yield of alkanes; (c) Selectivity of ethylene and acetylene; (d) Yield of C_2H_4 and C_2H_2. (CH_4/CO_2 molar ratio 1.5, flow rate 50 ml min^{-1}, and discharge power 16 W)

Figure 6.6 shows the influence of preparation method of catalyst on the total energy efficiency and fuel production efficiency of plasma biogas reforming. Clearly, compared with the plasma reforming of biogas over TC+TR or PC+PR catalysts, the reforming over TC+PR catalyst enhanced the total energy efficiency and fuel production efficiency due to the outstanding improvement of conversion and yield. The highest total energy efficiency (0.669 mmol kJ^{-1}) and fuel production efficiency (14.4%) were achieved using the TC+PR catalyst.

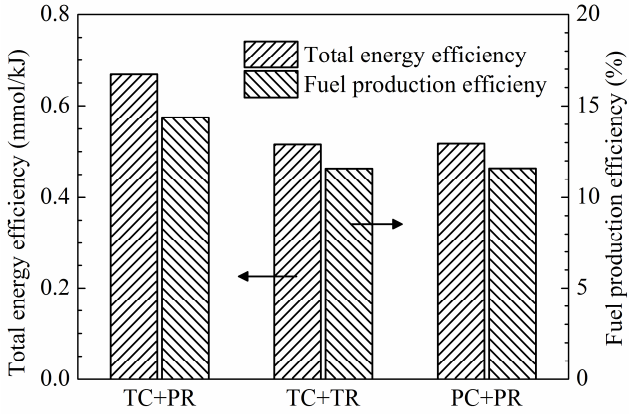

Figure 6.6 Energy efficiency of biogas reforming over different catalysts. (CH_4/CO_2 molar ratio 1.5, flow rate 50 ml min^{-1}, and discharge power 16 W)

6.2. Effect of temperature on biogas reforming using a Ni-K/Al_2O_3 catalyst

This section investigates the reforming of biogas over a Ni-K/Al_2O_3 catalyst in a coaxial DBD reactor at elevated temperatures. The performance of reforming under three different operating conditions (plasma-alone, plasma-catalysis and thermal catalysis) are investigated, in terms of conversion, selectivity, yield, H_2/CO molar ratio in the product, carbon balance and energy efficiency. The synergy of plasma-catalysis, and the carbon deposition on the catalyst are also discussed.

6.2.1. Experimental setup

The experimental setup is explained in Chapter 2. In this section, the discharge power of the DBD plasma in the reforming was 16 W, determined by calculating the area of *Q*-*U* on the Lissajous figures. The DBD reactor was placed in a tube furnace, which enabled biogas reforming to be investigated under three different conditions: plasma-alone, thermal catalysis and plasma-catalysis. Under plasma-alone conditions, no catalyst or quartz wool was placed in the reactor. In thermal catalytic reaction, the Ni-K/Al_2O_3 catalyst and quartz wool were packed in the middle of the reactor and heated in the tube furnace in absence of plasma. In the plasma-catalytic process, the catalyst and quartz wool were placed in the DBD plasma resulting in interaction between the plasma and catalyst. The temperature inside of the reactor was adjusted in

the range between 160 ºC and 400 ºC for all three conditions. When the plasma was on, the heating power was adjusted accordingly so that the plasma-alone, thermal catalytic and plasma-catalytic processes were carried out over the same temperatures.

The 8 wt.% Ni – 2 wt.% K/Al_2O_3 catalyst was prepared by the TC+PR method as described in the previous section. The catalyst was characterised using the same equipment and methods as explained in Chapter 5.

6.2.2. Textural properties of the Ni based catalysts

Figure 6.7 shows the XRD patterns of the Al_2O_3 support and fresh catalysts. Three prominent diffraction peaks located at 2θ = 37.6°, 45.9° and 67.0° respectively can be found on the XRD profile of Al_2O_3 support, corresponding to the cubic structure of alumina crystallite (JCPDS 10–425) [37]. On the XRD profiles of the catalysts, the diffraction peaks corresponding to NiO crystallite (JCPDS 1–75–197) can be clearly identified [98], as labelled by solid diamond marks in the figure. On the XRD pattern of the Ni-K/Al_2O_3 catalyst, the diffraction peaks related to cubic K_2O or KNO_3 crystallites are not observed, suggesting that the KNO_3 precursor has been completely decomposed in the calcination, and the K content has been well dispersed on the surface of the support. The average sizes of NiO crystallite on the Ni/Al_2O_3 and Ni-K/Al_2O_3 catalysts are calculated by the Scherrer's formula and summarised in Table 6.1 [244].

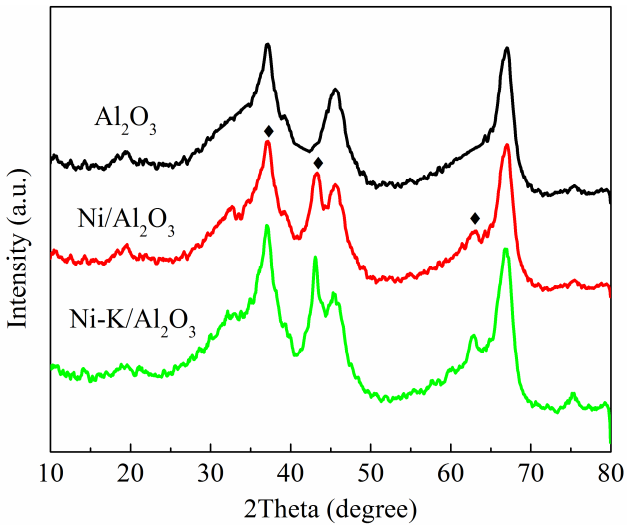

Figure 6.7 XRD results of the alumina support and Ni- based catalysts. (♦ NiO)

Comparing with the Ni/Al_2O_3 catalyst, the addition of K-promoter not only increased the average crystallite size, but also decreased the BET specific surface area

of the promoted catalyst. As shown in Table 6.1, the BET area of the Ni/Al_2O_3 catalyst was 165 m^2 g^{-1}, while that of the $Ni\text{-}K/Al_2O_3$ catalyst decreased to 152 m^2 g^{-1}, due to the enhanced coverage of catalyst's surface by the larger crystallite. This result suggests that the K promoter has changed the surface properties of the Ni/Al_2O_3 catalyst.

Table 6.1 Textural properties of fresh catalyst samples.

Catalyst	Specific surface area (m^2 g^{-1})	Mean pore diameter (nm)	Mean crystallite size (nm)
Ni/Al_2O_3	165	5.9	6.1
$Ni\text{-}K/Al_2O_3$	152	5.6	7.8

6.2.3. Reducibility of the catalysts

H_2-TPR has been used to determine the reducibility of the catalysts, as shown in Figure 6.8.

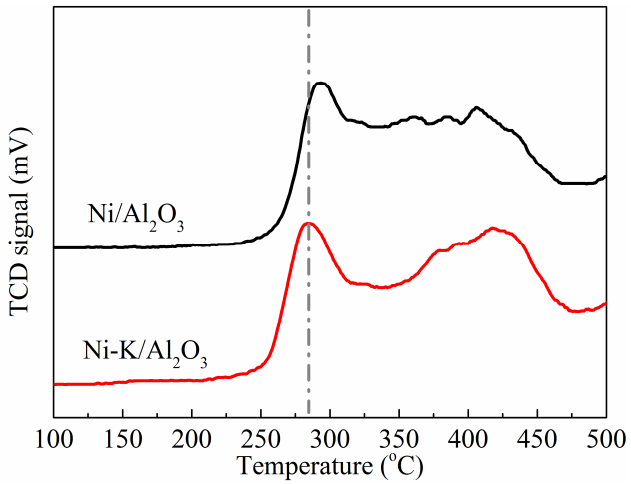

Figure 6.8 TPR profile of the catalysts.

In the biogas reforming, reducibility determines the redox status of active metal species, thus is very important for the reactivity and performance of a catalyst. The TPR result of the Ni/Al_2O_3 catalyst exhibits a very typical dual-peak feature. The first peak centred at 290 °C corresponds to the reduction of bulk NiO, while the overlapping peak located at 420 °C is assigned to the reduction of less-active Ni species. The latter has interacted with the alumina support and comparing with the bulk Ni species, requires higher temperature to be reduced [120]. The $Ni\text{-}K/Al_2O_3$ catalyst shows a pattern very

similar to that of the Ni/Al_2O_3 catalyst. However it is still clear that the reduction temperature of bulk NiO decreased by about 20 °C, indicating an improved reducibility of the $Ni\text{-}K/Al_2O_3$ catalyst. The catalyst with increased reducibility would therefore achieve a better performance at low temperatures.

6.2.4. Biogas reforming over the $Ni\text{-}K/Al_2O_3$ catalyst at elevated temperatures

Figure 6.9 shows the effect of temperature on the conversion of CH_4 and CO_2 in the biogas reforming process. Remarkably, CH_4 and CO_2 were not effectively converted until the DBD plasma was present, regardless of temperature. In the thermal catalytic reforming, when the temperature changed from 160 °C to 400 °C, the CO_2 conversion was always lower than 1%, while that of CH_4 slightly increased with the temperature but still remained lower than 1.5%. This is plausible since the thermal equilibrium conversion of CH_4 and CO_2 is 0 at a temperature lower than 230 °C. When the temperature increases to 390 °C, the equilibrium conversion of CH_4 is 2.3%, while that of CO_2 is 6.5% at the same temperature. This result suggests that the optimal working temperature for the $Ni\text{-}K/Al_2O_3$ catalyst is higher than 400 °C, since the performance of thermal catalytic reforming was strongly dependent on the temperature. During the plasma reforming of biogas without a catalyst, the CH_4 conversion was in the range of 23.8% to 25.1% when the temperature increased from 160 °C to 370 °C, suggesting an insignificant effect of temperature on the CH_4 conversion. However, CO_2 conversion decreased from 18.2% to 12.3% during the same plasma-alone process. It is probable that the discharge-mode of plasma changed in response to the increasing temperature. Atmospheric-pressure DBD plasma can operate in filamentary, patterned or completely diffuse mode, depending on the composition of feed gas and the surface properties of dielectric layer [211]. The temperatures of feed gas and reactor determines the discharge-mode, and consequently affects plasma properties of plasma and the performance of corresponding plasma-driven reactions, such as the discharge voltage and discharge power of plasma, and the conversion of feed gas [212-214]. In this study, the discharge-mode of the DBD plasma is expected to transform when the temperature increased, resulting in decreased conversion of CO_2. In the plasma-catalytic biogas reforming process, where the DBD plasma was combined with external heating, both of the CH_4 and CO_2 conversions were suppressed when the temperature increased. For instance, when the reaction temperature increased from 160 °C to 400 °C, the CH_4

conversion decreased from 31.6% to 22.9%, while that of CO_2 decreased from 22.8% to 10.3%. Notably, when the temperature was higher than 300 °C, the value of both CH_4 and CO_2 conversions in plasma-catalytic reforming became smaller than those obtained in the plasma-alone process, implying that side-reactions of CH_4 conversion into carbon solids or hydrocarbons were more pronounced at high temperatures in the absence of the Ni-K/Al_2O_3 catalyst, and accordingly, the carbon balance of the plasma-catalytic biogas reforming would be expected to be higher than that of the plasma-alone process at high temperatures. Moreover, the value of CH_4 conversion was always higher than that of CO_2 at the same temperature, regardless of reaction conditions, implying the occurrence of side-reactions that consumed CO to produce CO_2. As a consequence, the overall conversion of CO_2 was decreased.

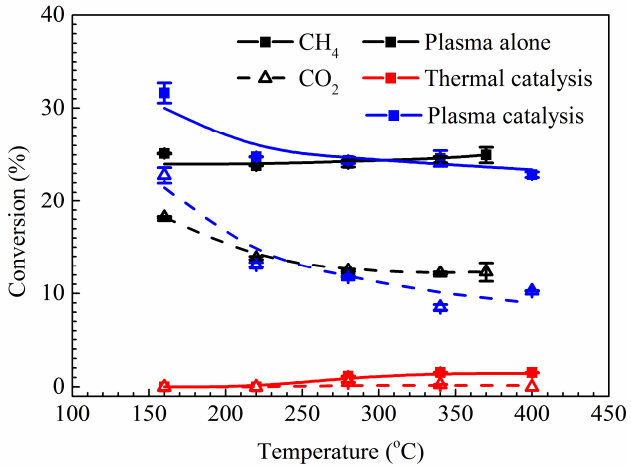

Figure 6.9 The conversion of CH_4 (solid square) and CO_2 (hollow triangle) under different operational conditions. (CH_4/CO_2 = 1.5 and flow rate 50 ml min^{-1})

Figure 6.10 shows the effect of temperature on selectivity and yield of syngas (H_2 and CO) in biogas reforming under different conditions. Interestingly, selectivity for both H_2 and CO decreased at elevated temperatures, regardless of the presence of Ni-K/Al_2O_3 catalyst. In the plasma-alone process, when the temperature increased from 160 °C to 370 °C, the selectivity for H_2 decreased from 41.6% to 38.0%, while that for CO decreased from 32.6% to 29.0%. During the plasma-catalytic process, when the temperature increased from 160 °C to 400 °C, the selectivity for H_2 decreased from 43.3% to 38.5%, while that for CO decreased from 31.3% to 25.6%. This illustrates that reactions such as CH_4 conversion into solid carbon or hydrocarbons were promoted at higher temperatures, thus decreasing the selectivity for CO and H_2. It agrees with the

results of conversions shown in Figure 6.9. Notably, the combination of DBD plasma with the Ni-K/Al_2O_3 catalyst increased the selectivity for H_2 but decreased that for CO as compared with the case using plasma alone, regardless of temperature. This suggests that plasma- catalysis could adjust the selectivity of products. No H_2 or CO was detected during thermal catalytic biogas reforming at any temperature investigated, and so the corresponding selectivity and yield are presented as zero in the figure.

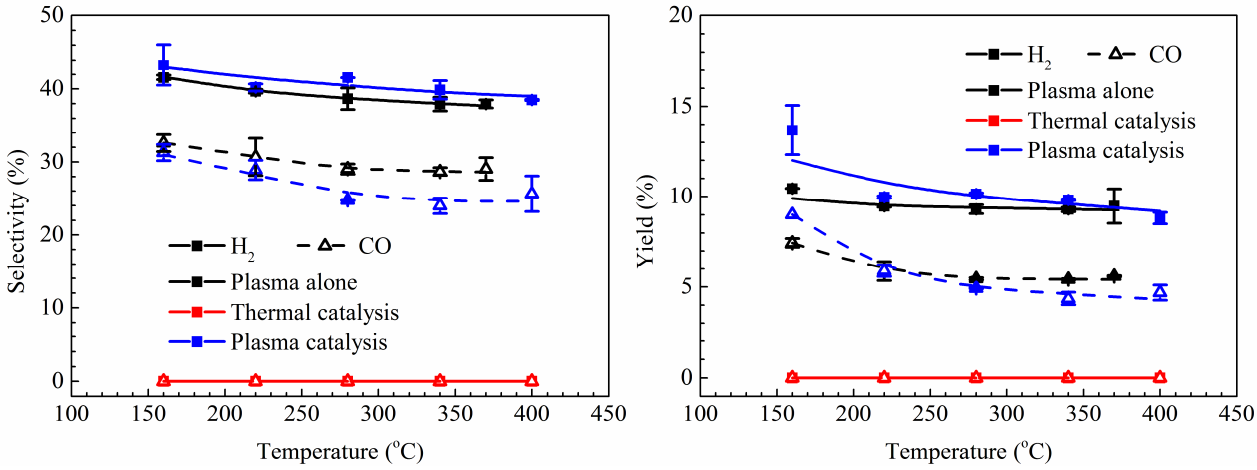

(a) (b)

Figure 6.10 (a) Selectivity and (b) yield of H_2 (solid square) and CO (hollow triangle) under different conditions. (CH_4/CO_2 = 1.5 and flow rate 50 ml min^{-1})

In accordance with the results of conversion and selectivity, the yield of CO during the plasma-alone process, and the yield of H_2 and CO during plasma-catalytic reforming both decreased as the temperature was elevated. However, the temperature exhibited a limited effect on the yield of H_2 (9.5%–10.5%) in the plasma-alone process, since the CH_4 conversion stayed almost the same in this case. More specifically, in the plasma reforming of biogas without a catalyst, the yield of CO decreased from 7.4% to 5.6% when the temperature increased from 160 °C to 370 °C. During the plasma-catalytic biogas reforming, the yield of H_2 changed from 13.7% to 8.8%, and that of CO decreased from 9.0% to 4.7%, when the temperature increased from 160 °C to 400 °C. It can be concluded that the combination of non-thermal plasma with the promoted catalyst improved the production of H_2 and simultaneously suppressed that of CO, as compared with the process using plasma alone.

The H_2/CO molar ratio of the produced syngas is important for further utilisation processes. For instance a H_2/CO ratio of 2 is often required for the synthesis of diesel

fuels, olefins and dimethyl ether (DME). Figure 6.11 shows the effect of temperature on the H_2/CO molar ratio in the product. Clearly, the molar ratio was always larger than 1.7, regardless of reaction conditions. The H_2/CO ratio of syngas from the plasma-catalytic reforming was always larger than that from the plasma-alone process. During plasma reforming in the absence of a catalyst, the H_2/CO molar ratio increased from 1.75 to 1.97 when the temperature increased from 160 °C to 370 °C. For comparison, during the plasma-catalytic reforming process the molar ratio firstly increased along with the temperature until its maximum of 2.71 at 340 °C, then decreased to 2.33 as the temperature further increased to 400 °C. The H_2/CO molar ratio obtained from the thermal-catalytic reforming was excluded, since no H_2 or CO was detected during the process at all. The results suggest that plasma-catalysis facilitated the conversion of CH_4, therefore increasing the production of H_2 and the H_2/CO molar ratio.

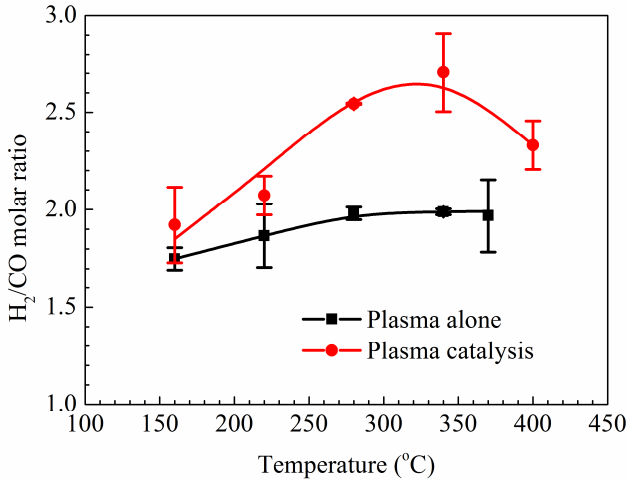

Figure 6.11 The H_2/CO molar ratio of produced syngas under different conditions. (CH_4/CO_2 = 1.5 and flow rate 50 ml min^{-1})

In addition to syngas, the product of biogas reforming also consisted of ethane, propane and a small amount of butane. Figure 6.12 shows the effect of temperature on the selectivity and yield of C_2 –C_4 alkanes in biogas reforming. In the plasma reforming process, with or without the Ni-K/Al_2O_3 catalyst, the selectivity of all alkanes increased with temperature. The selectivity of ethane exhibited the most significant improvement, increasing from 17.7% to 24.1% as temperature increased from 160 °C to 400 °C. By contrast, the temperature had very little influence on the yield of hydrocarbon products. During the plasma-catalytic reforming, the yield of ethane decreased from 5.1% to 4.4%

when the temperature increased from 160 °C to 400 °C. This is explained that CH_4 was the carbon source for the formation of alkanes, with CH_4 conversion significantly decreased in the plasma-catalytic process at elevated temperatures. Even so, the selectivity and yield of ethane achieved via plasma-catalysis were always higher than those achieved in other processes, regardless of temperature, suggesting that the combination of DBD plasma and the Ni-K/Al_2O_3 catalyst promoted the production of ethane. During thermal catalytic reforming, the yield of alkanes was negligible.

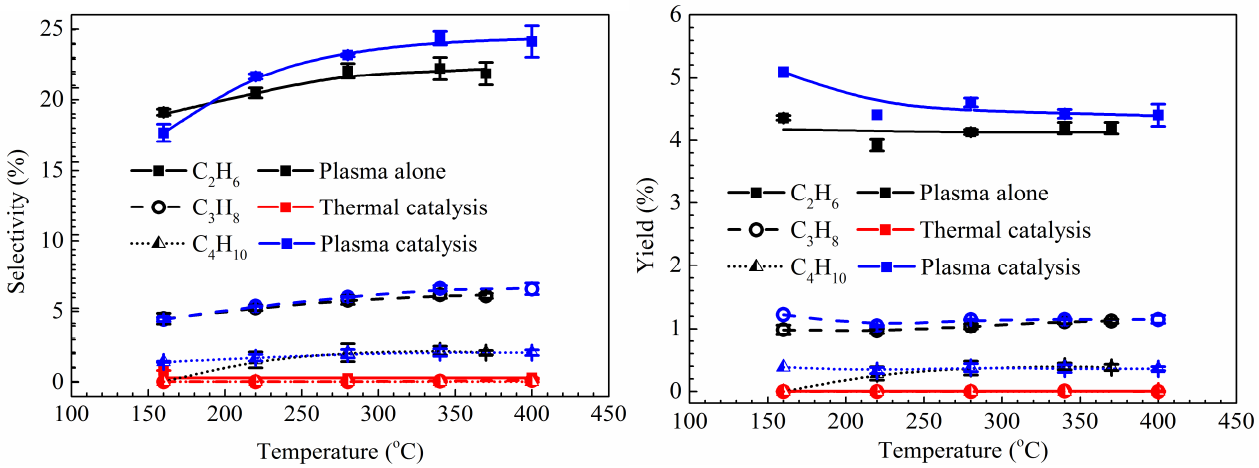

(a) (b)

Figure 6.12 (a) Selectivity and (b) yield of ethane (solid square), propane (hollow circle), and butane (half triangle) under different conditions. (CH_4/CO_2 = 1.5 and flow rate 50 ml min^{-1})

The carbon balance can be used to estimate the amount of products that were undetected in GC, such as solid carbon deposition, C_5 and higher hydrocarbons and oxygenated compounds. Figure 6.13(a) presents the carbon balance of the biogas reforming process under different operational conditions. The carbon balance of thermal catalytic reforming was always higher than 98%, due to the negligible conversion of CH_4 and CO_2 in this process. The carbon balance of the plasma-alone process decreased at elevated temperatures, suggesting the enhanced formation of by-products, most probably carbon and alcohols, at higher temperatures [167]. On the contrary, the carbon balance of the plasma-catalytic reforming increased with temperature. It can be partially explained by a decreasing conversion of CH_4 and CO_2 at high temperatures (as shown in Figure 6.9). It also implies that in plasma-catalysis, the production of carbon might be reduced at higher temperatures, which was confirmed

by TGA analysis as shown in Figure 6.15. Moreover, the carbon balance of plasma-alone and plasma-catalytic reforming were always lower than 95% regardless of temperature, suggesting the occurrence of carbon deposition. In fact, obvious carbon deposition was observed on the inner surface of the quartz reactor after the experiments, as shown in Figure 6.13(b).

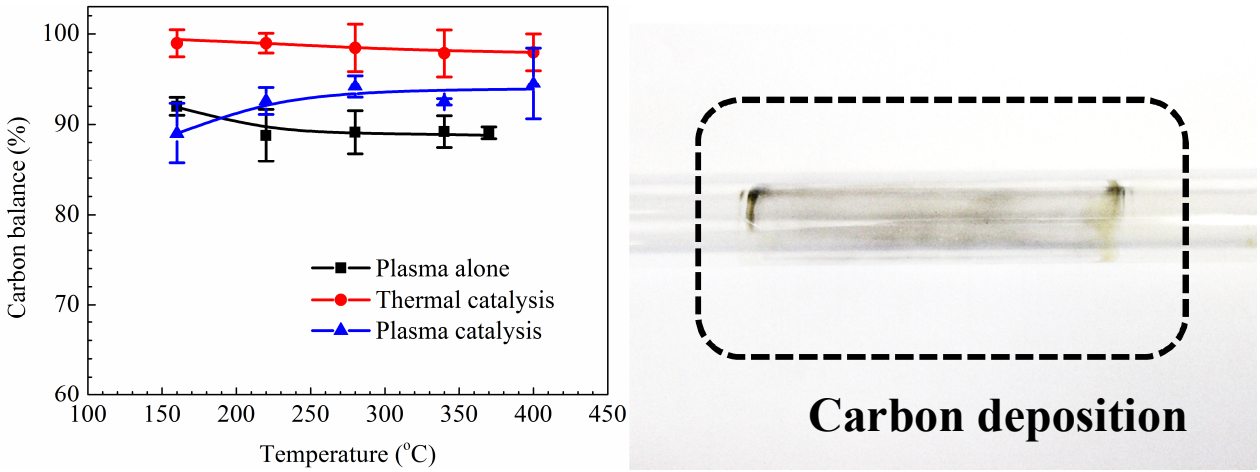

(a) (b)

Figure 6.13 (a) Carbon balance of different processes; (b) carbon deposition in the DBD reactor. (CH_4/CO_2 = 1.5 and flow rate 50 ml min^{-1})

Figure 6.14 shows the influence of temperature on total energy efficiency and fuel production efficiency of biogas reforming. Clearly, comparing with the plasma reforming of biogas in the absence of a catalyst, the combination of DBD plasma with the Ni-K/Al_2O_3 catalyst enhanced both efficiencies at a temperature lower than 250 °C, due to the synergy of plasma-catalysis. The total energy efficiency and fuel production efficiency of the plasma-alone and plasma-catalytic processes both decreased rapidly at higher temperatures. All of these results may be understood that the discharge power of DBD plasma was fixed at 16 W, and the temperature was elevated by increasing the heating power. The elevated temperature changed the discharge-mode of the plasma, and so suppressed the conversion of CH_4 and CO_2, while the increased heating power lowered the overall energy efficiency of the process. The total energy efficiency and fuel production efficiency of the thermal reforming process were almost 0 due to the very low conversion of feed gas and negligible amount of products. In our previous work [98], the total energy efficiency for the conversion of CO_2 and CH_4 during the catalytic dry reforming of methane in DBD reactors (with a CH_4/CO_2 molar ratio of 1)

was summarised. The reported values ranged between 0.033 and 0.72 mmol kJ^{-1}. In this study, the highest total energy efficiency (0.53 mmol kJ^{-1}) was comparable with this previous work, achieved in the plasma-catalytic biogas reforming at 160 °C and with a CH_4/CO_2 molar ratio of 1.5. Tao *et al.* summarised the fuel production efficiency of syngas during the methane dry reforming (DRM) process in DBD reactors in their review [180]. The fuel production efficiency were reported over a range of 3%–4%. For comparison, the highest fuel production efficiency recorded in the present study was 14.4%, achieved at a discharge power of 16 W and with a CH_4/CO_2 molar ratio of 1.5. All of these results suggest that in this present work, the biogas reforming reaction was particularly effective under the investigated conditions.

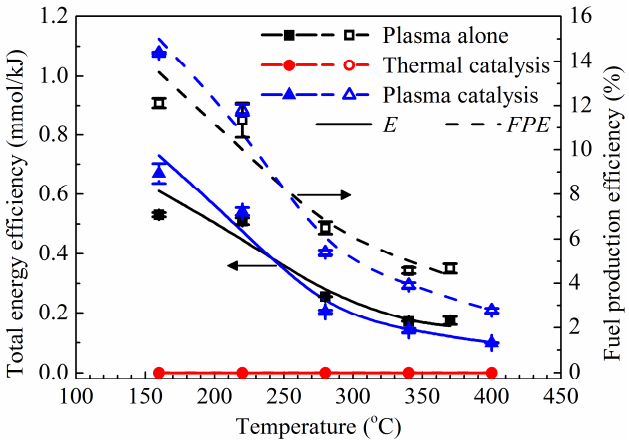

Figure 6.14 Effect of temperature on the total energy efficiency (solid lines) for the conversion of feed gas, and fuel production efficiency (dashed lines) of the reforming processes. (CH_4/CO_2 = 1.5 and flow rate 50 ml min^{-1})

Synergy capacity has been used to quantify the performance of plasma-catalytic biogas reforming, compared with that using plasma alone or catalyst alone at the same temperature (Table 6.2). The positive values of synergy capacity in the table clearly show that the synergy of plasma-catalysis improved the degree of conversion of CH_4 and CO_2, and also the energy efficiency of the process (total energy efficiency and fuel production efficiency). However, this promotional effect only occurred at temperatures lower than 220 °C, and it deteriorated quickly as the temperature increased. At temperatures higher than 220 °C, no positive effect of plasma-catalysis was observed at all, in terms of the conversion of feed gas and energy efficiency of the process. By contrast, the synergistic effect between the plasma and catalyst upon the yield of

hydrocarbons (ethane and acetylene are taken here as examples) only occurred at temperatures higher than 220 °C. The evolution of synergy capacity in response to temperature might be ascribed to the fact that the discharge changed from filamentary mode to diffuse mode as the temperature increased.

Table 6.2 Synergy capacity (unit: %) of plasma catalytic biogas reforming. (CH_4/CO_2 = 1.5 and flow rate 50 ml min^{-1})

Temperature (°C)	SC_{CH4}	SC_{CO2}	SC_{C2H6}	SC_{C2H2}	SC_E	SC_{FPE}
160	22.2	25.3	-11.3	-19.9	26.0	18.7
220	4.0	-5.4	5.8	-21.0	6.4	4.0
280	-3.0	-9.1	3.9	16.1	-20.2	-17.0
340	-5.3	-31.6	9.7	18.8	-17.9	-14.4
>370	-13.6	-16.5	9.0	4.6	-43.0	-40.7

6.2.5. Effect of temperature on carbon deposition

The types of carbon deposition on the spent catalyst can be divided into three categories, as explained in Chapter 5. As shown in Figure 6.15, the peak located at about 310 °C represents the reactive C_α species which usually exist as amorphous carbon and can be easily oxidised to form CO. The peak at about 520 °C was assigned to the less active C_β species which usually exist in the mixed form of amorphous and filamentous carbon [124]. Negligible amounts of C_γ species were observed on the spent catalyst. As the temperature increased from 160 °C to 400 °C, the carbon deposition on the spent catalyst was significantly reduced, reflected by the weight loss corresponding to different carbonaceous species as shown in Table 6.3. This result agrees with the recorded conversion of CH_4 and CO_2, and the carbon balance of the plasma-catalytic reforming, as shown in Figure 6.9 and Figure 6.13. Interestingly, the amount of carbon deposition in this work was remarkably less than the reported value obtained after the thermal catalytic dry reforming of methane over a Ni/Al_2O_3 catalyst [130], even though the CH_4/CO_2 molar ratio in this work was higher than that in a DRM process. This result is a clear evidence that the introduction of plasma reduced the carbon deposition on catalyst during the catalytic biogas reforming at elevated temperatures.

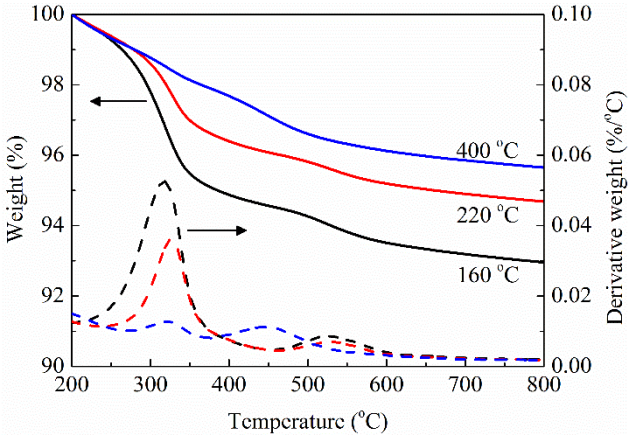

Figure 6.15 TPO and DTA profiles of spent Ni-K/Al_2O_3 catalyst after reforming at different temperatures. (CH_4/CO_2 = 1.5, total feed flow rate 50 ml min^{-1}, and discharge power 16 W).

It is also interesting that the decreased amount of carbon deposition at higher temperatures was ascribed to the reduction of reactive C_α species by the CO_2 and O species on the surface of the catalyst, while the oxidation temperature of the C_α species was very close to the reduction temperature of the Ni species on the Ni-K/Al_2O_3 catalyst (Figure 6.8). For instance the amount of reactive carbonaceous species on the spent catalyst significantly diminished from 5.45 to 2.06 wt.% when the temperature increased from 160 °C to 400 °C, while that of less active C_β species almost remained constant. The reducibility of a catalyst is usually related to the surface oxygen mobility of the catalyst, which is very important for catalytic oxidation reactions [22]. This result therefore implies that the decreased carbon deposition found in plasma-catalytic biogas reforming at high temperatures is not only due to the decreased conversion of CH_4 and CO_2, but might also be due to the removal of deposited carbonaceous species; the reactive species react with CO_2 or O species to form CO, and consequently "regenerate" the catalyst. Moreover, as the temperature increased from 160 °C to 400 °C, the oxidation temperature of C_β species over the Ni-K/Al_2O_3 catalyst decreased by about 80 °C, suggesting the removal of C_β species became easier at 400 °C. Clearly, this catalyst would have a much longer lifetime in the plasma-reforming of biogas.

Table 6.3 The amount of carbon deposition on the spent Ni-K/Al_2O_3 catalyst.

Reaction temperature (°C)	Carbon deposition (wt.%)		
	Reactive	Less active	Total
160	5.45	1.36	6.81
220	3.97	1.26	5.23
400	2.06	1.31	3.37

6.3. Effect of K loading on the plasma-catalytic biogas reforming over a Ni-K/Al_2O_3 catalyst

This section further investigates the effect of K loading on the performance of plasma-catalytic biogas reforming over a Ni-K/Al_2O_3 catalysts at low temperatures, in terms of the textural properties of the catalyst, the conversion of biogas, the production of syngas and hydrocarbons, the energy efficiency of the process, and the carbon deposition on the spent catalyst.

6.3.1. Experimental setup

The experimental setup was the same as explained in the first section of this chapter. More specifically, the discharge power of the DBD plasma was 16 W. The temperature inside of the reactor was about 160 °C, monitored by a fibre optic thermometer (FOB102).

The 8 wt.% Ni– x wt.% K/γ–Al_2O_3 (x = 0, 2, 4, 6 and 8) catalysts were prepared by the method explained in the second section of this chapter. 0.4 g catalyst was packed and sandwiched into the reactor with quartz wool. Prior to the plasma–catalytic reforming reactions, the catalyst was reduced in an Ar/H_2 discharge at a discharge power of 13 W (50 ml min^{-1}, 20 vol. % H_2) for 40 minutes in the same DBD reactor. The Ni-K/Al_2O_3 catalyst with different K loadings are denoted as 8NiAl, 8Ni2KAl, 8Ni4KAl, 8Ni6KAl and 8Ni8KAl respectively in the discussions below. Although 8 wt.% is a relatively large loading for promoter in a catalyst, the corresponding results are still included in order to give a complete view of the effects of promoter- loading on the reforming performance. The characterization of the catalysts, such as XRD, H_2-TPR and TGA, were carried out as described in Chapter 5.

6.3.2. XRD analysis of the catalysts

Figure 6.16 shows the XRD patterns of the K-promoted catalysts. There are three prominent diffraction peaks located at 2θ = 37.6°, 45.9° and 67.0°, corresponding to the cubic structure of alumina crystallite (JCPDS 10–425), as labelled by dash lines on the figure. NiO (JCPDS 1–75–197) signals, labelled by diamond marks, can also be clearly seen on the XRD patterns of all catalysts. The addition of potassium increased the size of metal crystallites on the surface of the catalyst, calculated by Scherrer equation. For instance the average crystallite sizes of the 8NiAl, 8Ni2KAl and 8Ni4KAl catalysts were 6.1 nm, 7.8 nm and 9.9 nm respectively. No obvious reflection of cubic K_2O (JCPDS 23–493) was observed from the samples, with the exception of the 8Ni6KAl catalyst, implying the good dispersion of K content on all of the other catalysts [233].

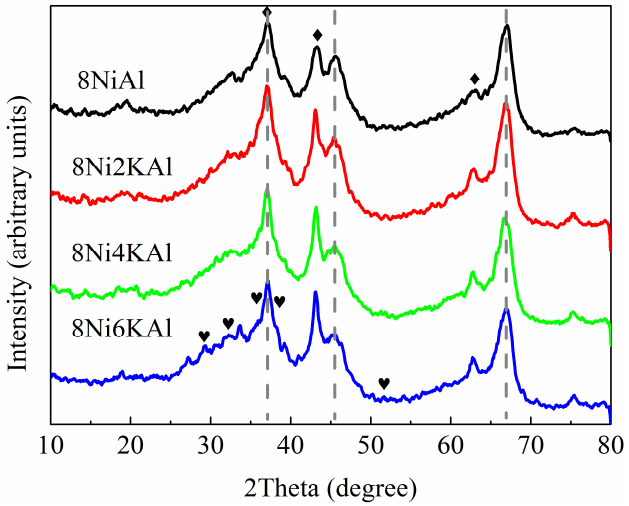

Figure 6.16 XRD patterns of the catalysts. (♦ NiO, ♥ K_2O, dash line γ–Al_2O_3)

6.3.3. Reducibility of the catalysts

Figure 6.17 shows the H_2–TPR results of the promoted catalysts. Al_2O_3 support was excluded because it can only be effectively reduced at temperatures higher than 900 °C [245]. The first reduction peak occurred at about 270 °C on the TPR figure corresponded to the reduction of bulk NiO, while the second one at 400 °C was assigned to the reduction of NiO which had interacted with the Al_2O_3 support. The peaks related to the reduction of bulk K_2O and KNO_3 were not found, suggesting the total decomposition of KNO_3 precursor and good dispersion of K content during calcination.

Interestingly, the reduction temperature of the promoted catalysts decreased slightly as the K loading increased from 0% to 4%; however, when the K loading increased from 4% to 6%, the reduction temperature of bulk NiO species significantly increased from 290 to 380 °C, indicating that the catalyst with a K loading smaller than 4 wt.% would exhibit a better reducibility. The reduction temperature of the catalysts followed the order of 8Ni6KAl > 8NiAl > 8Ni2KAl > 8Ni4KAl.

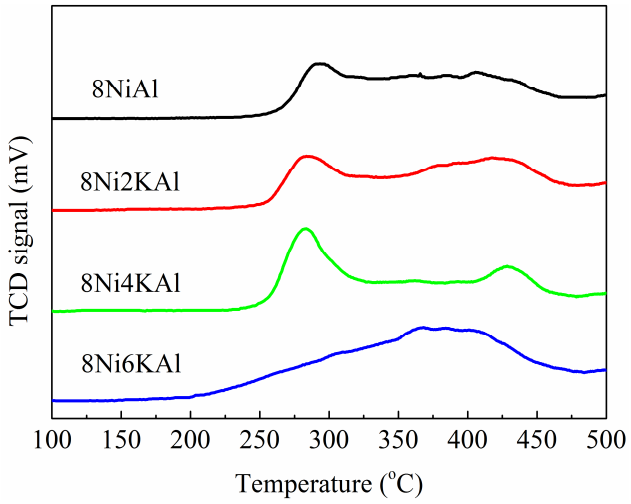

Figure 6.17 H_2–TPR profiles of the fresh catalysts.

6.3.4. Plasma-catalytic biogas reforming over K-promoted catalysts

Figure 6.18 shows the dependence of CH_4 and CO_2 conversion on the K loading of catalysts. The result obtained from plasma-driven biogas reforming without a catalyst is also listed for comparison. Comparing with the 8NiAl catalyst, the catalysts with addition of 2, 4, or 6 wt.% K enhanced the CH_4 conversion, while only the 8Ni2KAl catalyst exhibited higher CO_2 conversion. Amongst all of the investigated catalysts, the highest conversions of CH_4 and CO_2 (31.6% and 22.8% respectively) were achieved over the 8Ni2KAl catalyst. The CH_4 and CO_2 conversions were suppressed when the K loading further increased (> 2 wt.%). This was ascribed to the better dispersion of Ni species on the surface of the 8Ni2KAl catalyst, confirmed by its smaller crystallite size as calculated previously [172]. Interestingly, the conversion of CH_4 was always higher than that of CO_2. Several works on thermal catalytic dry reforming over Ni-based catalysts however reported that the conversion of CO_2 to be always higher than that of CH_4 during the reaction, due to the reverse water–gas shift

reaction [95, 129]. The different behavior implies that the combination of plasma and catalyst can adjust the equilibrium composition of the reforming reaction.

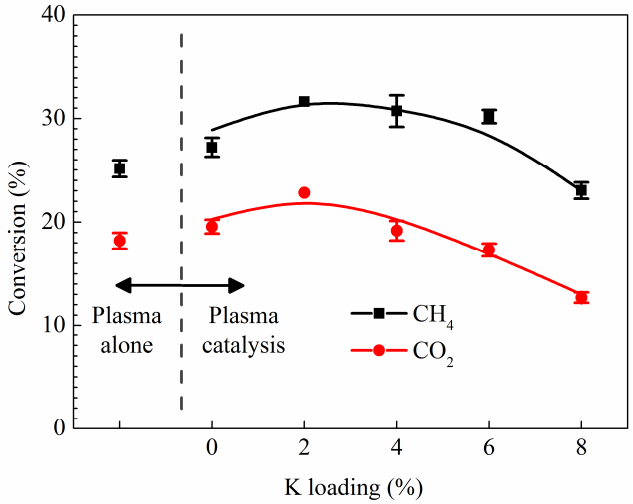

Figure 6.18 Conversions of CH_4 and CO_2 over the catalysts with different K loadings. (CH_4/CO_2 molar ratio 1.5, flow rate 50 ml min^{-1}, and discharge power 16 W)

Figure 6.19 shows the effect of K loading on the selectivity and yield of products in the biogas reforming process. By increasing K loading, selectivity for H_2 was almost constant, while that for CO was decreased. Besides, the K loading showed a limited effect on selectivity for C_2 –C_4 hydrocarbons, such as propane, butane, ethylene and acetylene, except that the lowest selectivity for ethane was achieved over the 8Ni2KAl catalyst. The highest yields of H_2, CO and ethane were achieved over the 8Ni2KAl catalyst, owing to the significant improvement of CH_4 and CO_2 conversion seen with this catalyst. However, the K loading exhibited a limited effect on the yield of other products (C_2H_2, C_2H_4, C_3H_8 and C_4H_{10}).

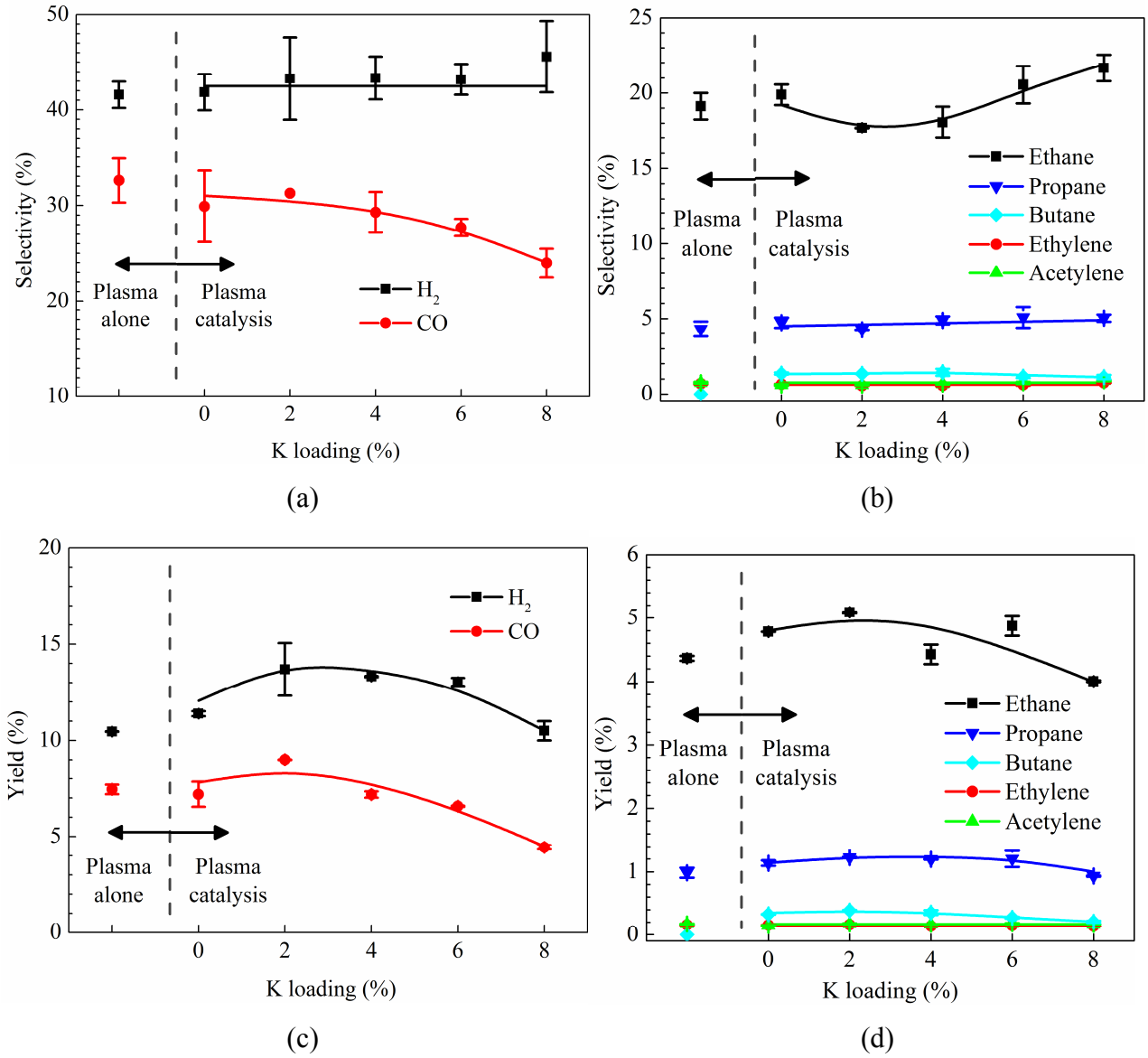

Figure 6.19 Effect of K loading on plasma-catalytic biogas reforming. (a) Selectivity of syngas; (b) Selectivity of C_2 –C_4 hydrocarbons; (c) Yield of syngas; (d) Yield of C_2 –C_4 hydrocarbons. (CH_4/CO_2 molar ratio 1.5, flow rate 50 ml min^{-1}, and discharge power 16 W)

Figure 6.20 shows the influence of K loading on the H_2/CO molar ratio in the product. The H_2/CO ratio was significantly increased from 1.75 to 2.83 when the K loading increased from 0 wt.% to 8 wt.%, being consistent with the evolution of selectivity for H_2 and CO as shown in Figure 6.19. Syngas with a H_2/CO molar ratio of 2 is suitable for further utilization in the Fischer-Tropsch process. However, syngas with a H_2/CO ratio of 3 or larger results in the preferential formation of methane in the F–T process. This is unsatisfactory, because it is generally desirable to utilise the F–T

process for the formation of higher hydrocarbons, which are more valuable. Methane is abundant and cheap, and thus considered an undesirable by-product in this circumstance. This is also true in most coal–to–liquid (CTL) or gas–to–liquid (GTL) applications. In this aspect, the 8NiAl and 8Ni2KAl catalysts were more promising for the potential future application of plasma-catalytic biogas reforming with K–promoted catalysts.

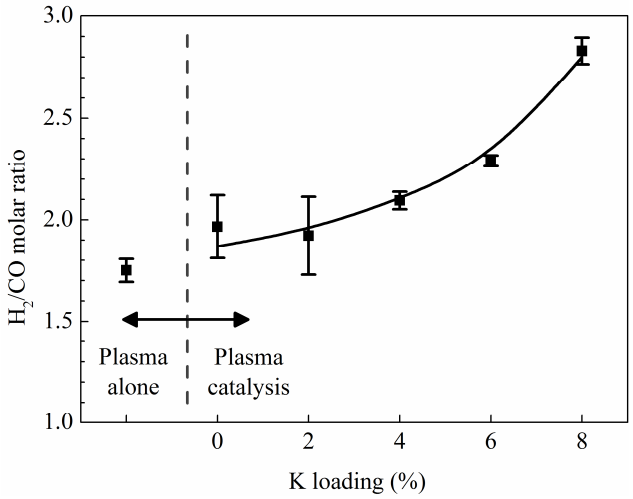

Figure 6.20 H_2/CO molar ratio in the product. (CH_4/CO_2 molar ratio 1.5, flow rate 50 ml min^{-1}, and discharge power 16 W)

Due to the significant improvement in yield of syngas and C_2 –C_4 hydrocarbons, biogas reforming using the 8Ni2KAl catalyst is expected to be energy-efficient. In fact, the highest total energy efficiency for the conversion of CH_4 and CO_2 (0.67 mmol kJ^{-1}) and the highest fuel production efficiency of the reforming process (14.4%) were both achieved using the 8Ni2KAl catalyst, as shown in Figure 6.21. The lowest fuel production efficiency of 10.8% was achieved using the 8Ni8KAl catalyst.

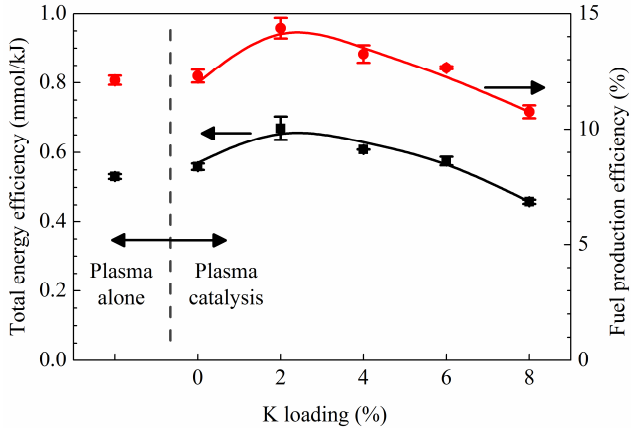

Figure 6.21 Total energy efficiency and fuel production efficiency of biogas reforming over the catalysts with different K loadings. (CH_4/CO_2 molar ratio 1.5, flow rate 50 ml min^{-1}, and discharge power 16 W)

The synergy capacity is used to evaluate the effect of K loading upon the plasma-catalytic synergy (Table 6.4). The synergy capacity obtained over the 8Ni2KAl catalyst was generally an order of magnitude larger than those of other catalysts, highlighting the outstanding synergistic effect of plasma-catalysis over the 8Ni2KAl catalyst for enhancing the conversion of CH_4 and CO_2, and improving the yield of products such as H_2, CO, ethane and propane. The suppressive effect of the 8Ni6KAl and 8Ni8KAl catalysts upon the CO_2 conversion and CO production could also be clearly identified from their distinctly negative synergy capacity. The synergy of plasma-catalysis over the 8NiAl catalyst was limited as compared against the rest of the catalysts.

Table 6.4 Synergy capacity (unit: %) of plasma-catalytic biogas reforming using the Ni-K/Al_2O_3 catalysts. (CH_4/CO_2 molar ratio 1.5, flow rate 50 ml min^{-1}, and discharge power 16 W)

Catalyst	SC_{CH4}	SC_{CO2}	SC_{H2}	SC_{CO}	SC_{C2H6}	SC_{C3H8}	SC_{E}	SC_{FPE}
8NiAl	8	7	9	-3	9	16	5	3
8Ni2KAl	26	25	31	21	17	25	28	24
8Ni4KAl	22	5	27	-4	1	22	16	13
8Ni6KAl	20	-5	25	-12	12	22	11	7
8Ni8KAl	-8	-30	0	-40	-8	-5	-10	-12

6.3.5. Carbon deposition on spent catalysts

As explained previously, the carbon deposits on the spent catalyst can be divided into three categories according to their oxidation temperatures [242, 243], distinguished by the oxidation peaks on the TGA profiles. Figure 6.22 shows the TGA profiles of the spent catalysts, while Table 6.5 summarizes the weight loss corresponding to different carbonaceous species. It can be concluded that carbon deposition was significantly enhanced upon the K-promoted catalysts. The largest amount of deposited carbon was recorded on the 8Ni6KAl catalyst, as compared with that on the others decreasing monotonically with K loading. This is consistent with the improved conversion of feed gas and carbon balance as shown previously.

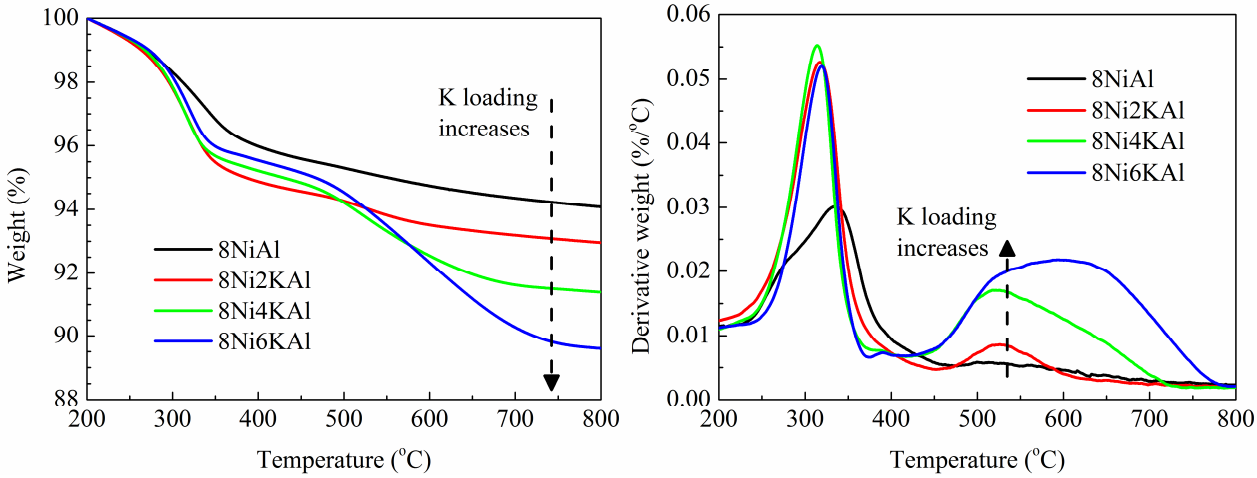

(a) (b)

Figure 6.22 Effect of K loading on the carbon deposition during plasma-catalytic biogas reforming. (a) TPO profiles of spent catalyst; (b) DTA analysis of spent catalyst. (CH_4/CO_2 = 1.5, feed flow rate 50 ml min^{-1}, and discharge power 16 W)

As compared against the 8NiAl catalyst, although the total amount of deposited carbon increased from 5.4 wt.% to 6.6 wt.% seen with the 8Ni2KAl catalyst, 78% of the increased carbonaceous species were reactive species (C_α). Moreover, the oxidation temperature of C_α species on the spent 8Ni2KAl decreased from 340 °C to 320 °C. All of these results suggest that the carbon deposition on the 8Ni2KAl catalyst would be easier to remove. By contrast, comparing with the 8NiAl catalyst, the reactive carbon deposition on the spent 8Ni4KAl and 8Ni6KAl catalysts were almost the same, while the amount of less active species was significantly increased, and the oxidation

temperature of the less active carbonaceous species on the spent 8Ni6KAl catalyst increased from 520 ºC to 600 ºC. The results of TGA analysis implies that by adjusting the K loading, the composition of carbon deposition in the plasma-catalytic biogas reforming process may be controlled. It also confirmed the coke resistance of the 8Ni2KAl catalyst.

Table 6.5 Amount of carbon deposited on the spent catalysts.

	Carbon deposition (wt. %)		
Catalyst	Reactive	Less active	Total
8NiAl	4.52	0.90	5.42
8Ni2KAl	5.43	1.16	6.59
8Ni4KAl	4.90	3.63	8.53
8Ni6KAl	4.54	5.77	10.31

6.4. Summary

The Ni-K/Al_2O_3 catalyst prepared by thermal calcination and plasma reduction (TC+PR) methods exhibited remarkable performance in plasma-catalytic biogas reforming at low temperatures. When compared against the catalysts prepared by TC+TR or PC+PR methods, the TC+PR catalyst achieved the best performance, in terms of the conversion of CH_4 and CO_2, the selectivity of H_2, the yield of products, and the energy efficiency. The Ni-K catalyst prepared by plasma-calcination and plasma-reduction (PC+PR) method showed the highest selectivity of ethane, ethylene and acetylene. It also achieved the highest carbon balance. It can be concluded that the Ni-K/Al_2O_3 catalysts prepared by the thermal calcination (TC) method improved conversion of CO_2 and the selectivity of H_2, while those reduced by plasma (PR) enhanced the conversion of CH_4. However both of the calcination and reduction methods exhibited limited effect on the selectivity of CO, propane and butane under the same conditions.

During the plasma-catalytic biogas reforming over a Ni-K/Al_2O_3 catalyst prepared by TC+PR method, the CO_2 and CH_4 in the feed gas were not effectively converted until the DBD plasma was initiated in the reactor. Higher degree of conversion was found to occur at lower temperatures. Syngas and ethane made up the majority of the products. The combination of plasma with catalyst improved the production of H_2 and

simultaneously suppressed that of CO, as compared with the process using plasma alone. As the temperature increased, production of ethane, propane, butane and carbon solids were enhanced. Moreover, the total energy efficiency and the fuel production efficiency decreased at elevated temperatures, due to suppressed conversion of feed gas and increased power consumption.

The synergy between DBD plasma and Ni-based catalyst in terms of the production of alkanes was observed at a temperature higher than 220 ^{o}C. By contrast, the synergistic effect on the conversion of CO_2 and CH_4 only occurred at a temperature lower than 220 ^{o}C. In the plasma-catalytic reforming, total amount of carbon deposited on the spent catalyst significantly diminished at higher temperatures. On one hand, this result is a clear evidence that the plasma-catalytic synergy is temperature-dependent. On the other hand, it implies that the Ni-K/Al_2O_3 catalyst would have a longer lifetime under this plasma-catalytic condition.

Further studies on the plasma-catalytic biogas reforming have been performed at 160 ^{o}C, using Ni-K/Al_2O_3 catalysts with different K loadings. The results revealed that the best performance was achieved using a catalyst with 2 wt.% K loading. This particular catalyst achieved the highest conversion of CH_4 and CO_2, the largest yield of products (such as H_2, CO, ethane, propane and butane) and the best energy efficiency of reforming process. Moreover, by increasing the K content, the selectivity of H_2 and CO and the corresponding H_2/CO molar ratio in the product were decreased. TGA analysis clearly showed that K loading determined the morphology of the carbon deposition.

Chapter 7. Conclusion and outlook

7.1. Conclusion

This project systematically investigates CO_2 hydrogenation and biogas reforming using plasma-catalysis. The investigations consist of screening of catalysts, comparison of thermal catalytic to plasma-catalytic processes, and evaluation of the synergistic effects between non-thermal plasma and catalyst.

Generally, H_2 was the hydrogen source of CO_2 hydrogenation reactions, while CH_4 served as the hydrogen source in the biogas reforming reactions. In the thermal catalytic processes, CO_2 hydrogenation and biogas reforming require high reaction temperature (> 300 ^oC) to effectively convert CO_2. In this project, high CH_4 selectivity (> 90%) was achieved in the thermal catalytic CO_2 hydrogenation; while syngas was the predominant product of biogas reforming process. In the plasma-driven or plasma-catalytic processes, the reactions can be initiated at relatively low temperatures. In this case, CO was always one of the major products. In CO_2 hydrogenation and biogas reforming, better conversions of feed gas and higher yields of major products were achieved using the Ni and Co based catalysts, compared to using Cu and Mn based catalysts.

In CO_2 hydrogenation, CO and CH_4 were the major products, while a small amount (< 1000 ppm) of alkenes and alkynes were also produced. The thermal catalytic process clearly showed a temperature-dependence, and particularly achieved higher CH_4 selectivity than that of plasma hydrogenation at the optimal temperatures. For instance, in Chapter 4, high CO_2 conversion and energy efficiency were achieved using the Ni/Al_2O_3 catalyst over a temperature range between 320 ^oC and 380 ^oC. The plasma-driven CO_2 hydrogenation was initiated without a catalyst and at low temperatures (from room temperature to 160 ^oC); yet, the CO_2 conversion slightly decreased at elevated temperatures. It is highlighted in the plasma-driven process that the CO selectivity was nearly 100%. In the plasma-catalytic reactions, synergistic effects between the DBD plasma and catalyst were observed at low temperatures. As seen with

the plasma-driven or thermal catalytic processes, the plasma-catalytic CO_2 hydrogenation further increased CO_2 conversion and energy efficiency due to the plasma-catalytic synergy. For instance, the CO_2 conversion was enhanced by 36% in the plasma-catalytic CO_2 hydrogenation using Mn/Al_2O_3 catalyst and at low temperatures; the CO yield was improved by 114%, and the energy efficiency of CO production was increased by 116%, compared to that obtained in the plasma reaction without a catalyst.

As for biogas reforming, syngas was the major product and 0–10 vol.% unsaturated hydrocarbons (such as ethylene and acetylene) were also detected among the products. In thermal catalytic biogas reforming, the conversion of CO_2 and CH_4 were negligible at temperatures lower than 400 ^oC. In the plasma-reforming in absence of a catalyst, the reaction of biogas reforming was initiated at 160 ^oC. However, at elevated temperatures, the conversion of feed gas was suppressed and the energy efficiency rapidly decreased. The combination of plasma and catalysts significantly enhanced the conversion of feed gas, and a plasma-catalytic synergy was observed. In the plasma-catalytic biogas reforming under ambient conditions, compared among the Co, Cu, Mn and Ni based catalysts, the maximum CH_4 conversion (20%) was achieved using the Ni/Al_2O_3 catalyst, at a discharge power of 7.5 W and a gas flow rate of 50 ml min^{-1}. By contrast, the CH_4 conversion was only 14% as seen using plasma alone. However, the presence of these catalysts in the plasma did not enhance the conversion of CO_2. In addition, the yield of syngas was enhanced using the mentioned catalysts. Significant plasma-catalytic synergy was observed under restricted conditions. For instance, during the plasma-catalytic biogas reforming using a $Ni\text{-}K/Al_2O_3$ catalyst, the synergy with the production of alkanes was identified at temperatures higher than 280 ^oC; while the synergy with the conversion of CO_2 and CH_4 was only observed at temperatures lower than 160 ^oC. Moreover, the K, Mg and Ce promoters exhibited promotional effects on the reforming performance, in terms of conversion of reactants, yield of syngas and C_2–C_4 alkanes, and fuel production efficiency.

Under all conditions mentioned above, the CO_2 conversion was also determined by the composition of the reactant gas (H_2/CO_2 and CH_4/CO_2 molar ratio), in addition to temperature, selection of catalyst and presence of plasma. In CO_2 hydrogenation at low temperatures, increasing the H_2 content in the reactant mixture significantly increased the CO_2 conversion. In biogas reforming reactions, the CH_4/CO_2 molar ratio determined various results including conversion of reactants, selectivity and yield of

major products and H_2/CO molar ratio in the effluent gas. However, the total feed flow rate showed limited effect on these results. Moreover, plasma-driven and plasma-catalytic CO_2 hydrogenation were greatly promoted by the addition of Ar in the feed gas. With the addition of Ar in the feed gas, the electrical properties were changed; various results were improved such as the conversion of CO_2, the selectivity of CH_4 and the fuel production efficiency. However, the selectivity of CO was maintained. Plasma-catalytic synergy was also enhanced by the addition of Ar.

7.2. Outlook

The industrial application of thermal catalytic CO_2 conversion has been delayed by two challenges: (1) High power consumption is needed to effectively convert the inert CO_2 molecules; and (2) Catalysts deactivate rapidly due to sintering and carbon deposition. In order to convert CO_2 into fuels or valuable chemicals, hydrogenation of CO_2 under mild conditions is necessary. H_2 and CH_4 can be used as the hydrogen source. In the course of this project, plasma-catalysis successfully initiates CO_2 hydrogenation (either with H_2 or CH_4) at atmospheric pressure and low temperatures, without significant deactivation of catalyst. The combination of non-thermal plasma and transitional metal catalyst is key for the reactions under ambient conditions. As found in this project, the power supply should match with the plasma reactor, and the plasma reactor should match with the type of plasma. This determines the power consumption and energy efficiency of the plasma process. The gas gap and discharge length should be adjusted so that catalysts can be packed into the plasma reactor, while a stable discharge can be obtained. Catalysts are still required to effectively convert CO_2 and adjust the selectivity of products, although non-thermal plasma can initiate CO_2 conversion at low temperatures. Above all, the catalyst should be carefully designed, in terms of active metal species, support, promoter and loading of active species and promoters. These parameters significantly affect the performance of the catalyst. In addition, the resulting catalysts should be active under thermal catalytic and plasma-catalytic conditions. The same catalysts should be also stable at elevated temperatures; they should not be damaged or decomposed in the discharge. Moreover, the configuration of reactor should guarantee that with the catalyst-bed inside of the reactor, the plasma and catalyst are in contact with each other, but maintaining a stable discharge. To fully exploit the plasma-catalytic synergy, reaction conditions such as

temperature and Ar addition should be considered. These parameters change the discharge properties of the working gases in the reactor and subsequently affect the reaction results.

Along with the potential application of plasma-catalytic CO_2 conversion, concerns regarding plasma-catalysis and upgradation of the process have been raised. For instance, the selectivity of target product is to be improved; the separation of products has not been thoroughly investigated yet. Notably, as compared to the thermal catalytic process, although plasma-catalytic reaction requires lower temperature to achieve the same degree of conversion, external heating is still required to further improve the CO_2 conversion and increase the reaction rate coefficient, resulting in extra energy consumption thus decreasing the energy efficiency. Moreover, plasma-catalytic CO_2 conversion into liquid hydrocarbons, aldehydes and alcohols would be also interesting, but it is kinetically difficult. Unfortunately, the mechanism of plasma-catalytic reaction is not yet fully understood. As compared to corona or gliding arc reactors, the volume inside of a DBD reactor is small, thus restricting the mean electron energy of DBD plasma. The configuration of DBD reactor can be upgraded to provide larger gap distance and plasma volume. This would increase the treatment capacity of the reactor and enhance the electric field between the electrodes. In the study on plasma-catalysis, the reactions in the gas-phase should be distinguished from the reactions on the catalysts' surface. The individual effect of plasma and catalyst on the reaction should be identified. It is also important to study the effect of gaseous species (produced by plasma) on the catalyst. More comprehensive study on designing the catalyst is needed for promoting catalytic reactivity, and improving the overall energy efficiency of the plasma-process. These problems have to be solved when the research on plasma-catalytic CO_2 conversion is pushed forward.

Appendix

This section is an overview of the reactions included in the model in Chapter 4, provided by Chao Xu.

Table A7.1 Neutral-neutral reactions in this model, with the corresponding rate constants adopted from NIST database. The group M for the three-body collision is made of the background gas.

No.	Reaction	Rate constant (cm^3s^{-1})
N1	$CH_4 + H \Rightarrow CH_3 + H_2$	8.43×10^{-19}
N2	$CH_4 + CH \Rightarrow C_2H_4 + H$	9.74×10^{-11}
N3	$CH_4 + CH_2 \Rightarrow CH_3 + CH_3$	2.78×10^{-19}
N4	$CH_4 + C_2H \Rightarrow C_2H_2 + CH_3$	1.31×10^{-12}
N5	$CH_4 + C_2H_3 \Rightarrow C_2H_4 + CH_3$	2.28×10^{-18}
N6	$CH_4 + C_2H_5 \Rightarrow C_2H_6 + CH_3$	1.83×10^{-24}
N7	$CH_4 + C_3H_7 \Rightarrow C_3H_8 + CH_3$	4.38×10^{-24}
N8	$CH_3 + CH_3 \Rightarrow C_2H_5 + H$	2.71×10^{-19}
N9	$CH_3 + CH_3 + M \Rightarrow C_2H_6 + M$	1.56×10^{-26} (cm^6s^{-1})
N10	$CH_3 + CH_2 \Rightarrow C_2H_4 + H$	7.01×10^{-11}
N11	$CH_3 + C_2H_5 \Rightarrow C_2H_4 + CH_4$	1.91×10^{-12}
N12	$CH_3 + C_2H_5 + M \Rightarrow C_3H_8 + M$	1.93×10^{-23} (cm^6s^{-1})
N13	$CH_3 + C_2H_6 \Rightarrow C_2H_5 + CH_4$	7.21×10^{-21}
N14	$CH_3 + C_2H_4 \Rightarrow C_2H_3 + CH_4$	1.94×10^{-21}
N15	$CH_3 + C_2H_3 \Rightarrow C_2H_2 + CH_4$	6.51×10^{-13}
N16	$CH_3 + C_2H_3 + M \Rightarrow C_3H_6 + M$	4.91×10^{-30} (cm^6s^{-1})
N17	$CH_3 + C_2H_2 \Rightarrow C_2H + CH_4$	7.65×10^{-26}
N18	$CH_3 + C_3H_8 \Rightarrow C_3H_7 + CH_4$	1.02×10^{-20}
N19	$CH_3 + C_3H_7 \Rightarrow C_3H_6 + CH_4$	3.07×10^{-12}

N20	$CH_3 + H_2 \Rightarrow H + CH_4$	9.90×10^{-21}
N21	$CH_3 + H \Rightarrow CH_2 + H_2$	9.96×10^{-22}
N22	$CH_3 + H + M \Rightarrow CH_4 + M$	2.97×10^{-28} (cm^6s^{-1})
N23	$CH_2 + CH_2 \Rightarrow C_2H_2 + 2H$	5.27×10^{-11}
N24	$CH_2 + C_2H_5 \Rightarrow C_2H_4 + CH_3$	3.01×10^{-11}
N25	$CH_2 + C_2H_3 \Rightarrow C_2H_2 + CH_3$	3.01×10^{-11}
N26	$CH_2 + C_2H \Rightarrow C_2H_2 + CH$	3.01×10^{-11}
N27	$CH_2 + C_3H_8 \Rightarrow C_3H_7 + CH_3$	1.02×10^{-20}
N28	$CH_2 + C_3H_7 \Rightarrow C_2H_4 + C_2H_5$	3.01×10^{-11}
N29	$CH_2 + C_3H_7 \Rightarrow C_3H_6 + CH_3$	3.01×10^{-12}
N30	$CH_2 + H_2 \Rightarrow CH_3 + H$	5.00×10^{-15}
N31	$CH_2 + H \Rightarrow CH + H_2$	2.01×10^{-10}
N32	$CH + C_2H_6 + M \Rightarrow C_3H_7 + M$	1.14×10^{-29} (cm^6s^{-1})
N33	$CH + C_2H_6 \Rightarrow C_3H_6 + H$	3.00×10^{-11}
N34	$CH + H_2 \Rightarrow CH_2 + H$	6.80×10^{-13}
N35	$CH + H \Rightarrow C + H_2$	1.00×10^{-10}
N36	$C + H_2 \Rightarrow CH + H$	1.50×10^{-10}
N37	$C_2H_6 + C_2H_3 \Rightarrow C_2H_5 + C_2H_4$	3.39×10^{-21}
N38	$C_2H_6 + C_2H \Rightarrow C_2H_2 + C_2H_5$	5.99×10^{-12}
N39	$C_2H_6 + C_3H_7 \Rightarrow C_3H_8 + C_2H_5$	3.16×10^{-22}
N40	$C_2H_6 + CH_2 \Rightarrow C_3H_8$	4.80×10^{-12}
N41	$C_2H_6 + H \Rightarrow C_2H_5 + H_2$	4.96×10^{-17}
N42	$C_2H_5 + C_2H_5 \Rightarrow C_2H_6 + C_2H_4$	2.41×10^{-12}
N43	$C_2H_5 + C_2H \Rightarrow C_2H_2 + C_2H_4$	3.01×10^{-12}
N44	$C_2H_5 + C_3H_8 \Rightarrow C_2H_6 + C_3H_7$	3.62×10^{-22}
N45	$C_2H_5 + C_3H_7 \Rightarrow C_2H_4 + C_3H_8$	1.91×10^{-12}
N46	$C_2H_5 + C_3H_7 \Rightarrow C_2H_6 + C_3H_6$	2.41×10^{-12}
N47	$C_2H_5 + H_2 \Rightarrow C_2H_6 + H$	2.91×10^{-21}
N48	$C_2H_5 + H \Rightarrow CH_3 + CH_3$	5.99×10^{-11}
N49	$C_2H_5 + H \Rightarrow C_2H_4 + H_2$	3.01×10^{-12}
N50	$C_2H_5 + H \Rightarrow C_2H_6$	5.99×10^{-11}
N51	$C_2H_5 + C_2H_4 \Rightarrow C_3H_6 + CH_3$	3.82×10^{-17}
N52	$C_2H_4 \Rightarrow C_2H_2 + H_2$	1.40×10^{-27}

N53	$C_2H_4 + C_2H \Rightarrow C_2H_2 + C_2H_3$	1.40×10^{-10}
N54	$C_2H_4 + H \Rightarrow C_2H_3 + H_2$	6.70×10^{-05}
N55	$C_2H_4 + H \Rightarrow C_2H_5$	1.30×10^{-12}
N56	$C_2H_4 + H_2 + M \Rightarrow C_2H_6 + M$	6.86×10^{-36} (cm^6s^{-1})
N57	$C_2H_3 + C_2H_3 \Rightarrow C_2H_4 + H_2$	1.90×10^{-12}
N58	$C_2H_3 + C_2H \Rightarrow C_2H_2 + C_2H_2$	1.90×10^{-12}
N59	$C_2H_3 + C_3H_8 \Rightarrow C_2H_4 + C_3H_7$	3.40×10^{-20}
N60	$C_2H_3 + C_3H_7 \Rightarrow C_3H_8 + C_2H_2$	2.01×10^{-12}
N61	$C_2H_3 + C_3H_7 \Rightarrow C_3H_6 + C_2H_4$	2.01×10^{-12}
N62	$C_2H_3 + H_2 \Rightarrow C_2H_4 + H$	9.78×10^{-20}
N63	$C_2H_3 + H \Rightarrow C_2H_2 + H_2$	2.01×10^{-11}
N64	$C_2H_3 + H + M \Rightarrow C_2H_4 + M$	8.26×10^{-30} (cm^6s^{-1})
N65	$C_2H_2 + H \Rightarrow C_2H + H_2$	6.12×10^{-27}
N66	$C_2H_2 + H + M \Rightarrow C_2H_3 + M$	2.81×10^{-31} (cm^6s^{-1})
N67	$C_2H + C_3H_8 \Rightarrow C_2H_2 + C_3H_7$	5.99×10^{-12}
N68	$C_2H + C_3H_7 \Rightarrow C_3H_6 + C_2H_2$	1.00×10^{-11}
N69	$C_2H + H_2 \Rightarrow C_2H_2 + H$	1.52×10^{-13}
N70	$C_2H + H + M \Rightarrow C_2H_2 + M$	9.44×10^{-30} (cm^6s^{-1})
N71	$C_3H_8 + H \Rightarrow C_3H_7 + H_2$	5.15×10^{-17}
N72	$C_3H_7 + C_3H_7 \Rightarrow C_3H_6 + C_3H_8$	2.81×10^{-12}
N73	$C_3H_7 + H_2 \Rightarrow C_3H_8 + H$	7.12×10^{-21}
N74	$C_3H_7 + H \Rightarrow C_3H_6 + H_2$	3.01×10^{-12}
N75	C3H7 + H => C3H8	9.68×10^{-11}
N76	$C_3H_6 + H + M \Rightarrow C_3H_7 + M$	3.79×10^{-33} (cm^6s^{-1})
N77	$H + H + M \Rightarrow H_2 + M$	6.00×10^{-33} (cm^6s^{-1})
N78	$O + O + M \Rightarrow O_2 + M$	7.19×10^{-33} (cm^6s^{-1})
N79	$CH_4 + O \Rightarrow CH_3 + OH$	5.54×10^{-18}
N80	$CH_3 + O \Rightarrow CH_2O + H$	1.12×10^{-10}
N81	$CH_3 + O \Rightarrow CO + H_2 + H$	2.80×10^{-11}
N82	$CH_2 + O \Rightarrow CO + H_2$	5.53×10^{-11}
N83	$CH_2 + O \Rightarrow CO + 2H$	8.29×10^{-11}
N84	$CH_2 + O_2 \Rightarrow CO_2 + H_2$	1.42×10^{-12}
N85	$CH_2 + O_2 \Rightarrow CO + H_2O$	1.42×10^{-12}

N86	$CH_2 + O_2 \Rightarrow CH_2O + O$	5.39×10^{-13}
N87	$CH + O \Rightarrow CO + H$	6.90×10^{-11}
N88	$CH + O_2 \Rightarrow CO_2 + H$	1.20×10^{-11}
N89	$CH + O_2 \Rightarrow CO + OH$	8.00×10^{-12}
N90	$CH + O_2 \Rightarrow HCO + O$	8.00×10^{-12}
N91	$CH + O_2 \Rightarrow CO + H + O$	1.20×10^{-11}
N92	$C + O_2 \Rightarrow CO + O$	2.45×10^{-13}
N93	$C_2H_6 + O \Rightarrow C_2H_5 + OH$	5.11×10^{-16}
N94	$C_2H_5 + O \Rightarrow CH_3HCO + H$	8.80×10^{-11}
N95	$C_2H_5 + O \Rightarrow CH_2O + CH_3$	6.90×10^{-11}
N96	$C_2H_5 + O \Rightarrow C_2H_4 + OH$	4.40×10^{-11}
N97	$C_2H_5 + O_2 \Rightarrow C_2H_4 + HO_2$	3.80×10^{-15}
N98	$C_2H_4 + O \Rightarrow CH_2HCO + H$	2.63×10^{-13}
N99	$C_2H_4 + O \Rightarrow HCO + CH_3$	4.51×10^{-13}
N100	$C_2H_3 + O \Rightarrow C_2H_2 + OH$	1.25×10^{-11}
N101	$C_2H_3 + O \Rightarrow CO + CH_3$	1.25×10^{-11}
N102	$C_2H_3 + O \Rightarrow HCO + CH_2$	1.25×10^{-11}
N103	$C_2H_3 + O \Rightarrow CH_2CO + H$	1.25×10^{-11}
N104	$C_2H_3 + O_2 \Rightarrow CH_2O + HCO$	9.00×10^{-11}
N105	$C_2H_2 + O \Rightarrow CH_2 + CO$	6.75×10^{-14}
N106	$C_2H_2 + O \Rightarrow C_2HO + H$	6.75×10^{-14}
N107	$C_2H + O \Rightarrow CH + CO$	1.70×10^{-11}
N108	$C_2H + O_2 \Rightarrow HCO + CO$	3.00×10^{-11}
N109	$C_2H + O_2 \Rightarrow C_2HO + O$	1.00×10^{-12}
N110	$C_3H_8 + O \Rightarrow C_3H_7 + OH$	2.73×10^{-15}
N111	$H_2 + O \Rightarrow OH + H$	9.32×10^{-18}
N112	$H + O + CH_4 \Rightarrow OH + CH_4$	4.33×10^{-32} (cm^6s^{-1})
N113	$H + O_2 \Rightarrow OH + O$	1.87×10^{-22}
N114	$H + O_2 + CH_4 \Rightarrow HO_2 + CH_4$	5.40×10^{-32} (cm^6s^{-1})
N115	$CH_4 + OH \Rightarrow CH_3 + H_2O$	6.62×10^{-15}
N116	$CH_4 + HO_2 \Rightarrow CH_3 + H_2O_2$	8.76×10^{-27}
N117	$CH_4 + HCO \Rightarrow CH_3 + CH_2O$	6.07×10^{-30}
N118	$CH_4 + CH_3O \Rightarrow CH_3OH + CH_3$	9.42×10^{-20}

N119	$CH_3 + CO + CH_4 \Rightarrow CH_3CO + CH_4$	4.19×10^{-36} (cm^6s^{-1})
N120	$CH_3 + H_2O \Rightarrow CH_4 + OH$	1.82×10^{-25}
N121	$CH_3 + OH \Rightarrow CH_2 + H_2O$	1.13×10^{-12}
N122	$CH_3 + OH \Rightarrow CH_2OH + H$	1.32×10^{-11}
N123	$CH_3 + OH \Rightarrow CH_3O + H$	1.90×10^{-10}
N124	$CH_3 + OH \Rightarrow CH_3OH$	2.30×10^{-27}
N125	$CH_3 + HO_2 \Rightarrow CH_3O + OH$	3.00×10^{-11}
N126	$CH_3 + HO_2 \Rightarrow CH_4 + O_2$	5.99×10^{-12}
N127	$CH_3 + CH_2O \Rightarrow CH_4 + HCO$	6.14×10^{-18}
N128	$CH_3 + HCO \Rightarrow CH_4 + CO$	2.00×10^{-10}
N129	$CH_3 + CH_3O \Rightarrow CH_4 + CH_2O$	4.00×10^{-11}
N130	$CH_3 + CH_3CHO \Rightarrow CH_4 + CH_3CO$	4.95×10^{-18}
N131	$CH_2 + CO_2 \Rightarrow CH_2O + CO$	3.90×10^{-14}
N132	$CH_2 + H_2O \Rightarrow CH_3 + OH$	1.90×10^{-16}
N133	$CH_2 + OH \Rightarrow CH_2O + H$	3.00×10^{-11}
N134	$CH_2 + HO_2 \Rightarrow CH_2O + OH$	3.00×10^{-11}
N135	$CH_2 + CH_2O \Rightarrow CH_3 + HCO$	1.00×10^{-14}
N136	$CH_2 + HCO \Rightarrow CH_3 + CO$	3.00×10^{-11}
N137	$CH_2 + CH_3O \Rightarrow CH_3 + CH_2O$	3.00×10^{-11}
N138	$CH + CO_2 \Rightarrow 2CO + H$	9.68×10^{-13}
N139	$CH + CO_2 \Rightarrow HCO + CO$	9.68×10^{-13}
N140	$CH + CO \Rightarrow C_2HO$	4.04×10^{-30}
N141	$C_2H_6 + OH \Rightarrow C_2H_5 + H_2O$	2.46×10^{-13}
N142	$C_2H_6 + HO_2 \Rightarrow C_2H_5 + H_2O_2$	6.36×10^{-24}
N143	$C_2H_6 + HCO \Rightarrow C_2H_5 + CH_2O$	2.19×10^{-26}
N144	$C_2H_6 + CH_3O \Rightarrow C_2H_5 + CH_3OH$	2.72×10^{-18}
N145	$C_2H_5 + OH \Rightarrow C_2H_4 + H_2O$	4.00×10^{-11}
N146	$C_2H_5 + HO_2 \Rightarrow C_2H_6 + O_2$	5.00×10^{-13}
N147	$C_2H_5 + HO_2 \Rightarrow C_2H_4 + H_2O_2$	5.00×10^{-13}
N148	$C_2H_5 + CH_2O \Rightarrow C_2H_6 + HCO$	4.47×10^{-18}
N149	$C_2H_5 + HCO \Rightarrow C_2H_6 + CO$	2.00×10^{-10}
N150	$C_2H_5 + CH_3O \Rightarrow C_2H_6 + CH_2O$	4.00×10^{-11}
N151	$C_2H_4 + OH \Rightarrow C_2H_3 + H_2O$	1.54×10^{-16}

N152	$C_2H_4 + HO_2 \Rightarrow CH_3CHO + OH$	1.62×10^{-20}
N153	$C_2H_3 + H_2O \Rightarrow C_2H_4 + OH$	1.82×10^{-25}
N154	$C_2H_3 + OH \Rightarrow C_2H_2 + H_2O$	5.00×10^{-11}
N155	$C_2H_3 + CH_2O \Rightarrow C_2H_4 + HCO$	4.41×10^{-18}
N156	$C_2H_3 + HCO \Rightarrow C_2H_4 + CO$	1.50×10^{-10}
N157	$C_2H_3 + CH_3O \Rightarrow C_2H_4 + CH_2O$	4.00×10^{-11}
N158	$C_2H_2 + OH \Rightarrow C_2H + H_2O$	1.77×10^{-22}
N159	$C_2H_2 + HO_2 \Rightarrow CH_2CO + OH$	1.62×10^{-20}
N160	$C_2H + OH \Rightarrow CH_2 + CO$	3.00×10^{-11}
N161	$C_2H + OH \Rightarrow C_2H_2 + O$	3.00×10^{-11}
N162	$C_2H + HO_2 \Rightarrow C_2H_2 + O_2$	3.00×10^{-11}
N163	$C_2H + HO_2 \Rightarrow C_2HO + OH$	3.00×10^{-11}
N164	$C_2H + HCO \Rightarrow C_2H_2 + CO$	1.00×10^{-10}
N165	$C_2H + CH_3O \Rightarrow C_2H_2 + CH_2O$	4.00×10^{-11}
N166	$C_3H_8 + OH \Rightarrow C_3H_7 + H_2O$	3.76×10^{-15}
N167	$C_3H_8 + CH_3O \Rightarrow C_3H_7 + CH_3OH$	1.42×10^{-17}
N168	$C_3H_7 + CH_2O \Rightarrow C_3H_8 + HCO$	4.10×10^{-18}
N169	$C_3H_7 + HCO \Rightarrow C_3H_8 + CO$	1.00×10^{-10}
N170	$C_3H_7 + CH_3O \Rightarrow C_3H_8 + CH_2O$	4.00×10^{-11}
N171	$H_2 + OH \Rightarrow H + H_2O$	7.02×10^{-15}
N172	$H_2 + HCO \Rightarrow H + CH_2O$	2.78×10^{-26}
N173	$H + CO_2 \Rightarrow CO + OH$	1.40×10^{-29}
N174	$H + CO + M \Rightarrow HCO + M$	1.54×10^{-34}
N175	$H + H_2O \Rightarrow H_2 + OH$	5.86×10^{-26}
N176	$H + OH \Rightarrow H_2 + O$	1.05×10^{-16}
N177	$H + OH + M \Rightarrow H_2O + M$	4.33×10^{-30}
N178	$H + HO_2 \Rightarrow H_2 + O_2$	5.90×10^{-12}
N179	$H + HO_2 \Rightarrow H_2O + O$	2.40×10^{-12}
N180	$H + HO_2 \Rightarrow OH + OH$	7.20×10^{-11}
N181	$H + CH_2O \Rightarrow H_2 + HCO$	5.72×10^{-14}
N182	$H + CH_2O \Rightarrow H_2 + HCO$	3.86×10^{-14}
N183	$H + HCO \Rightarrow H_2 + CO$	1.50×10^{-10}
N184	$H + CH_3O \Rightarrow H_2 + CH_2O$	2.32×10^{-11}

N185	$H + CH_3O => CH_3 + OH$	9.93×10^{-12}
N186	$H + CH_3CHO => H_2 + CH_3CO$	8.98×10^{-14}
N187	$H + CH_2CO => CH_3 + CO$	1.04×10^{-13}
N188	$H + C_2HO => CH_2 + CO$	2.50×10^{-10}
N189	$CO + O + M => CO_2 + M$	1.11×10^{-35}
N190	$O + H_2O => OH + OH$	4.48×10^{-24}
N191	$O + OH => H + O_2$	3.46×10^{-11}
N192	$O + HO_2 => O_2 + OH$	5.70×10^{-11}
N193	$O + CH_2O => OH + HCO$	1.73×10^{-13}
N194	$O + HCO => CO + OH$	5.00×10^{-11}
N195	$O + HCO => H + CO_2$	5.00×10^{-11}
N196	$O + CH_3O => CH_3 + O_2$	2.20×10^{-11}
N197	$O + CH_3O => OH + CH_2O$	3.00×10^{-12}
N198	$O + CH_3CHO => OH + CH_3CO$	4.68×10^{-13}
N199	$O + CH_2CO => CH_2 + CO_2$	2.29×10^{-13}
N200	$O + CH_2CO => CH_2O + CO$	7.88×10^{-14}
N201	$O + CH_2CO => HCO + CO + H$	4.33×10^{-14}
N202	$O + CH_2CO => 2HCO$	4.33×10^{-14}
N203	$O + C_2HO => 2CO + H$	1.90×10^{-10}
N204	$O_2 + HCO => CO + HO_2$	5.10×10^{-12}
N205	$O_2 + CH_3O => CH_2O + HO_2$	1.97×10^{-15}
N206	$O_2 + CH_2CHO => CH_2O + CO + OH$	3.00×10^{-14}
N207	$O_2 + C_2HO => 2CO + OH$	6.46×10^{-13}
N208	$CO + OH => CO_2 + H$	1.25×10^{-13}
N209	$CO + CH_3O => CO_2 + CH_3$	6.56×10^{-20}
N210	$H_2O + CH_3O => CH_3OH + OH$	1.67×10^{-14}
N211	$OH + OH => H_2O + O$	1.47×10^{-12}
N212	$OH + OH + M => H_2O_2 + M$	6.86×10^{-31}
N213	$OH + HO_2 => O_2 + H_2O$	1.10×10^{-10}
N214	$OH + CH_2O => H_2O + HCO$	8.47×10^{-12}
N215	$OH + HCO => CO + H_2O$	1.70×10^{-10}
N216	$OH + CH_3O => CH_2O + H_2O$	3.00×10^{-11}
N217	$OH + CH_3CHO => CH_3CO + H_2O$	1.49×10^{-11}

N218	$OH + CH_2CO \Rightarrow CO + CH_2OH$	1.14×10^{-11}
N219	$2HO_2 \Rightarrow H_2O_2 + O_2$	1.63×10^{-12}
N220	$HO_2 + CH_2O \Rightarrow H_2O_2 + HCO$	1.05×10^{-20}
N221	$HO_2 + HCO \Rightarrow OH + H + CO_2$	5.00×10^{-11}
N222	$HO_2 + CH_3O \Rightarrow CH_2O + H_2O_2$	5.00×10^{-13}
N223	$CH_2O + CH_3O \Rightarrow CH_3OH + HCO$	1.14×10^{-15}
N224	$2HCO \Rightarrow CH_2O + CO$	5.00×10^{-11}
N225	$2CH_3O \Rightarrow CH_2O + CH_3OH$	1.00×10^{-10}
N226	$CH_4 + CH_3CO \Rightarrow CH_3CHO + CH_3$	1.14×10^{-29}
N227	$CH_4 + CH_2OH \Rightarrow CH_3OH + CH_3$	2.55×10^{-27}
N228	$CH_3 + H_2O_2 \Rightarrow CH_4 + HO_2$	5.46×10^{-14}
N229	$CH_3 + CH_3OH \Rightarrow CH_4 + CH_3O$	1.01×10^{-20}
N230	$CH_3 + CH_3OH \Rightarrow CH_4 + CH_2OH$	2.66×10^{-20}
N231	$CH_3 + CH_2OH \Rightarrow CH_4 + CH_2O$	4.00×10^{-12}
N232	$CH_2 + H_2O_2 \Rightarrow CH_3 + HO_2$	1.00×10^{-14}
N233	$CH_2 + CH_3CO \Rightarrow CH_2CO + CH_3$	3.00×10^{-11}
N234	$CH_2 + CH_3OH \Rightarrow CH_3O + CH_3$	1.01×10^{-20}
N235	$CH_2 + CH_3OH \Rightarrow CH_2OH + CH_3$	2.66×10^{-20}
N236	$CH_2 + CH_2OH \Rightarrow CH_2O + CH_3$	2.00×10^{-12}
N237	$CH_2 + CH_2OH \Rightarrow C_2H_4 + OH$	4.00×10^{-11}
N238	$C_2H_5 + H_2O_2 \Rightarrow C_2H_6 + HO_2$	2.83×10^{-15}
N239	$C_2H_5 + CH_3OH \Rightarrow C_2H_6 + CH_3O$	3.50×10^{-22}
N240	$C_2H_5 + CH_3OH \Rightarrow C_2H_6 + CH_2OH$	9.49×10^{-22}
N241	$C_2H_5 + CH_2OH \Rightarrow C_2H_6 + CH_2O$	4.00×10^{-12}
N242	$C_2H_5 + CH_2OH \Rightarrow CH_3OH + C_2H_4$	4.00×10^{-12}
N243	$C_2H_3 + H_2O_2 \Rightarrow C_2H_4 + HO_2$	5.46×10^{-14}
N244	$C_2H_3 + CH_3OH \Rightarrow C_2H_4 + CH_3O$	1.01×10^{-20}
N245	$C_2H_3 + CH_3OH \Rightarrow C_2H_4 + CH_2OH$	2.66×10^{-20}
N246	$C_2H_3 + CH_2OH \Rightarrow C_2H_4 + CH_2O$	5.00×10^{-11}
N247	$C_2H_2 + CH_2OH \Rightarrow C_2H_3 + CH_2O$	3.32×10^{-19}
N248	$C_2H + CH_3OH \Rightarrow C_2H_2 + CH_3O$	2.00×10^{-12}
N249	$C_2H + CH_3OH \Rightarrow C_2H_2 + CH_2OH$	1.00×10^{-11}
N250	$C_2H + CH_2OH \Rightarrow C_2H_2 + CH_2O$	5.99×10^{-11}

N251	$C_3H_7 + OH => C_3H_6 + H_2O$	4.00×10^{-11}
N252	$C_3H_7 + H_2O_2 => C_3H_8 + HO_2$	7.08×10^{-17}
N253	$C_3H_7 + CH_3OH => C_3H_8 + CH_3O$	3.51×10^{-22}
N254	$C_3H_7 + CH_3OH => C_3H_8 + CH_2OH$	8.45×10^{-22}
N255	$C_3H_7 + CH_2OH => C_3H_8 + CH_2O$	1.90×10^{-12}
N256	$C_3H_7 + CH_2OH => C_3H_6 + CH_3OH$	8.00×10^{-13}
N257	$H + H_2O_2 => H_2O + OH$	4.20×10^{-14}
N258	$H + H_2O_2 => H_2 + HO_2$	5.15×10^{-15}
N259	$H + CH_3OH => CH_2OH + H_2$	1.27×10^{-15}
N260	$H + CH_3OH => CH_3O + H_2$	3.18×10^{-16}
N261	$H + CH_2OH => CH_2O + H_2$	1.00×10^{-11}
N262	$H + CH_2OH => CH_3 + OH$	1.90×10^{-10}
N263	$H + CH_2OH + M => CH_3OH + M$	1.18×10^{-29}
N264	$O + H_2O_2 => HO_2 + OH$	8.91×10^{-16}
N265	$O + H_2O_2 => O_2 + H_2O$	8.91×10^{-16}
N266	$O + CH_3CO => OH + CH_2CO$	8.75×10^{-11}
N267	$O + CH_3CO => CO_2 + CH_3$	2.63×10^{-10}
N268	$O + CH_3OH => OH + CH_2OH$	1.12×10^{-14}
N269	$O + CH_3OH => OH + CH_3O$	1.68×10^{-15}
N270	$O + CH_2OH => CH_2O + OH$	7.00×10^{-11}
N271	$O_2 + CH_2OH => CH_2O + HO_2$	9.70×10^{-12}
N272	$OH + H_2O_2 => HO_2 + H_2O$	1.70×10^{-12}
N273	$OH + CH_3CO => CH_2CO + H_2O$	2.00×10^{-11}
N274	$OH + CH_3CO => CH_3 + CO + OH$	5.00×10^{-11}
N275	$OH + CH_3OH => H_2O + CH_2OH$	7.67×10^{-13}
N276	$OH + CH_3OH => H_2O + CH_3O$	1.35×10^{-13}
N277	$OH + CH_2OH => CH_2O + H_2O$	4.00×10^{-11}
N278	$HO_2 + CH_3CO => CH_3 + CO_2 + OH$	5.00×10^{-11}
N279	$HO_2 + CH_3OH => CH_2OH + H_2O_2$	1.10×10^{-22}
N280	$HO_2 + CH_2OH => CH_2O + H_2O_2$	2.00×10^{-11}
N281	$CH_2O + CH_3CO => CH_3CHO + HCO$	1.17×10^{-22}
N282	$CH_2O + CH_2OH => CH_3OH + HCO$	4.22×10^{-18}
N283	$HCO + H_2O_2 => CH_2O + HO_2$	1.50×10^{-18}

N284	$HCO + CH_3CO \Rightarrow CH_3CHO + CO$	1.50×10^{-11}
N285	$HCO + CH_3OH \Rightarrow CH_2O + CH_2OH$	6.85×10^{-23}
N286	$HCO + CH_2OH \Rightarrow 2CH_2O$	3.00×10^{-10}
N287	HCO + CH2OH => CH3OH + CO	2.00×10^{-10}
N288	$CH_3O + CH_3CO \Rightarrow CH_3OH + CH_2CO$	1.00×10^{-11}
N289	$CH_3O + CH_2OH \Rightarrow CH_2O + CH_3OH$	4.00×10^{-11}
N290	$H_2O_2 + CH_3CO \Rightarrow CH_3CHO + HO_2$	3.05×10^{-19}
N291	$H_2O_2 + CH_2OH \Rightarrow CH_3OH + HO_2$	6.56×10^{-17}
N292	$CH_3CO + CH_3OH \Rightarrow CH_3CHO + CH_2OH$	2.22×10^{-22}
N293	$2CH_2OH \Rightarrow CH_2O + CH_3OH$	8.00×10^{-12}
N294	$C_3H_5 + O_2 \Rightarrow CH_3CHO + HCO$	7.21×10^{-12}
N295	$HCO + CH_3CO \Rightarrow CH_3CHO + CO$	1.50×10^{-11}
N296	$CH_3CHOH + O \Rightarrow CH_3CHO + OH$	1.50×10^{-10}
N297	$CH_3CHOH + O_2 \Rightarrow CH_3CHO + HO_2$	1.90×10^{-11}
N298	$CH_3 + HCO \Rightarrow CH_3CHO$	4.42×10^{-11}
N299	$CH + O_2 \Rightarrow HCO + O$	1.45×10^{-10}
N300	$C_2H_3 + O_2 \Rightarrow CH_2O + HCO$	2.62×10^{-12}
N301	$C_2H + O_2 \Rightarrow CO + HCO$	4.00×10^{-12}
N302	$CH_2O + O \Rightarrow HCO + OH$	1.67×10^{-13}
N303	$CH_2O + H \Rightarrow H_2 + HCO$	5.52×10^{-14}
N304	$CH_2O + OH \Rightarrow HCO + H_2O$	9.38×10^{-12}
N305	$CH_2O + HO_2 \Rightarrow HCO + H_2O_2$	2.52×10^{-18}
N306	$CH_2O + CH_3 \Rightarrow HCO + CH_4$	6.14×10^{-18}
N307	$HCO + CH_2 \Rightarrow CO + CH_3$	3.01×10^{-11}
N308	$HCO + O \Rightarrow CO + OH$	5.00×10^{-11}
N309	$HCO + O \Rightarrow CO_2 + H$	5.00×10^{-11}
N310	HCO + H => CO + H2	1.13×10^{-10}
N311	$HCO + O_2 \Rightarrow CO + HO_2$	5.20×10^{-12}
N312	$HCO + OH \Rightarrow CO + H_2O$	1.83×10^{-10}
N313	$HCO \Rightarrow CO + H$	3.35×10^{-22}
N314	$HCO + CH_3 \Rightarrow CO + CH_4$	4.00×10^{-11}
N315	$CH_3 + O_2 \Rightarrow CH_3O_2$	2.21×10^{-12}
N316	$CH_4 + O_2 \Rightarrow CH_3O_2 + H$	3.80×10^{-76}

N317	$CH_3CO + O_2 => CH_3COOO$	5.00×10^{-12}
N318	$C_2H_5 + O_2 => C_2H_5OO$	1.50×10^{-28}
N319	$CH_3CHO + O_2 => CH_3COOOH$	5.16×10^{-23}
N320	$CH_3CHO + CH_3COOO => CH_3COOOH + CH_3CO$	1.34×10^{-17}
N321	$CH_3CHO + OH => CH_3COOH + H$	2.00×10^{-21}
N322	$CH_3O_2 + CH_3COOO => CH_3COOH + CH_2O + O_2$	5.50×10^{-12}
N323	$CH_3COOOH + C_3H_6 => CH_3COOH + C_3H_6O$	3.85×10^{-14}
N324	$CO + OH => COOH$	1.20×10^{-12}
N325	$CH_3 + COOH => CH_3COOH$	5.81×10^{-10}
N326	$CH_3CO + O => CH3COO$	1.99×10^{-10}
N327	$CH_3COO + H => CH_3COOH$	3.79×10^{-11}
N328	$C_2H_5 + OH => C_2H_5OH$	1.28×10^{-10}
N329	$2C_2H_5OO => C_2H_5OH + CH_3CHO + O_2$	2.34×10^{-14}
N330	$CH_3CHOH + H => C_2H_5OH$	8.30×10^{-11}
N331	$CH_2O + OH => HCOOH + H$	2.01×10^{-13}
N332	$CH_3CHO + H => CH_3CHOH$	2.49×10^{-18}
N333	$C_2H_5OH + O => CH_3CHOH + OH$	1.03×10^{-13}
N334	$C_2H_5OH + OH => CH_3CHOH + H_2O$	5.00×10^{-13}
N335	$C_2H_5OH + CH_3 => CH_4 + CH_3CHOH$	2.79×10^{-56}
N336	$CH_3 + CH_3CO => CH_3COCH_3$	6.97×10^{-20}
N337	$CH_3COCH_3 + O => CH_3COCH_2 + OH$	1.13×10^{-15}
N338	$CH_3COCH_3 + OH => CH_3COCH_2 + H_2O$	2.20×10^{-13}
N339	$CH_3COCH_3 + H => CH_3COCH_2 + H_2$	6.70×10^{-16}
N340	$CH_3COCH_3 + HO_2 => CH_3COCH_2 + H_2O_2$	3.49×10^{-16}
N341	$CH_3COCH_3 + CH_3 => CH_3COCH_2 + CH_4$	5.56×10^{-20}
N342	$C_3H_7 + CH_3 => C_4H_{10}$	7.02×10^{-21}
N343	$CH_3OH + C_4H_9 => C_4H_{10} + CH_2OH$	7.98×10^{-22}
N344	$CH_4 + C_4H_9 => C_4H_{10} + CH_3$	8.82×10^{-23}
N345	$CH_2O + C_4H_9 => C_4H_{10} + HCO$	9.23×10^{-18}
N346	$C_2H_4 + C_2H_5 => C_4H_9$	9.58×10^{-19}
N347	$C_2H_5 + C_2H_5 => C_4H_{10}$	1.66×10^{-11}
N348	$C_4H_9 + H => C_4H_{10}$	4.26×10^{-11}

Table A7.2 Electron-impact reactions in the model. All the rate constants for these reactions are determined by the cross section of each particle and instantaneous electron temperature, as the equation (9) defined in reference [195].

No.	Reaction		Rate constant
E1	$e^- + CH_4 \Rightarrow CH_3 + H^-$	Dissociative Attachment	$f(\sigma)$, ε
E2	$e^- + CH_4 \Rightarrow CH_2^- + H_2$	Dissociative Attachment	$f(\sigma)$, ε
E3	$e^- + CH_4 \Rightarrow e^- + CH_4$	Momentum Transfer	$f(\sigma)$, ε
E4	$e^- + CH_4 \Rightarrow e^- + CH_{4(V24)}$	Vibrational Excitation	$f(\sigma)$, ε
E5	$e^- + CH_4 \Rightarrow e^- + CH_{4(V13)}$	Vibrational Excitation	$f(\sigma)$, ε
E6	$e^- + CH_4 \Rightarrow e^- + CH_3 + H$	Dissociative Excitation	$f(\sigma)$, ε
E7	$e^- + CH_4 \Rightarrow e^- + CH_2 + 2H$	Dissociative Excitation	$f(\sigma)$, ε
E8	$e^- + CH_4 \Rightarrow e^- + CH + 3H$	Dissociative Excitation	$f(\sigma)$, ε
E9	$e^- + CH_4 \Rightarrow 2e^- + CH_4^+$	Ionisation	$f(\sigma)$, ε
E10	$e^- + CO_2 \Rightarrow CO + O^-$	Dissociative Attachment	$f(\sigma)$, ε
E11	$e^- + CO_2 \Rightarrow e^- + CO_2^*$	Momentum Transfer	$f(\sigma)$, ε
E12-19	$e^- + CO_2 \Rightarrow e^- + CO_{2(V1-8)}$	Vibrational Excitation	$f(\sigma)$, ε
E20-27	$e^- + CO_2 \Rightarrow e^- + CO_{2(E1-8)}$	Electronic Excitation	$f(\sigma)$, ε
E28	$e^- + CO_2 \Rightarrow 2e^- + CO_2^+$	Ionisation	$f(\sigma)$, ε
E29	$e^- + CO_2 \Rightarrow e^- + CO + O$	Dissociative Excitation	$f(\sigma)$, ε
E30	$e^- + CH_3 \Rightarrow e^- + CH_{3(P)}$	Excitation	$f(\sigma)$, ε
E31	$e^- + CH_3 \Rightarrow e^- + CH_2 + H$	Dissociative Excitation	$f(\sigma)$, ε
E32	$e^- + CH_3 \Rightarrow e^- + CH + H_2$	Dissociative Excitation	$f(\sigma)$, ε
E33	$e^- + CH_3 \Rightarrow e^- + H + C + H_2$	Dissociative Excitation	$f(\sigma)$, ε
E34	$e^- + CH_3 \Rightarrow 2e^- + CH_3^+$	Ionisation	$f(\sigma)$, ε
E35	$e^- + CH_3 \Rightarrow 2e^- + H + CH_2^+$	Dissociative Ionisation	$f(\sigma)$, ε
E36	$e^- + CH_3^+ \Rightarrow 2e^- + H + H^+ + CH^+$	Dissociative Ionisation	$f(\sigma)$, ε
E37	$e^- + CH_3^+ \Rightarrow 2e^- + H_2 + H^+ + C^+$	Dissociative Ionisation	$f(\sigma)$, ε
E38	$e^- + CH_2 \Rightarrow e^- + CH_2^*$	Excitation	$f(\sigma)$, ε
E39	$e^- + CH_2 \Rightarrow e^- + CH + H$	Dissociative Excitation	$f(\sigma)$, ε
E40	$e^- + CH_2 \Rightarrow e^- + C + H_2$	Dissociative Excitation	$f(\sigma)$, ε
E41	$e^- + CH_2 \Rightarrow e^- + C + 2H$	Dissociative Excitation	$f(\sigma)$, ε
E42	$e^- + CH_2 \Rightarrow 2e^- + CH_2^+$	Ionisation	$f(\sigma)$, ε
E43	$e^- + CH_2 \Rightarrow 2e^- + H + CH^+$	Dissociative Ionisation	$f(\sigma)$, ε

E44	$e^- + CH_2^+ \Rightarrow 2e^- + H + H^+ + C^+$	Dissociative Ionisation	$f(\sigma)$, ε
E45	$e^- + C \Rightarrow e^- + C$	Momentum Transfer	$f(\sigma)$, ε
E46	$e^- + C \Rightarrow e^- + C_{(1D)}$	Excitation	$f(\sigma)$, ε
E47	$e^- + C \Rightarrow e^- + C_{(1S)}$	Excitation	$f(\sigma)$, ε
E48	$e^- + C \Rightarrow 2e^- + C^+$	Ionisation	$f(\sigma)$, ε
E49	$e^- + CO \Rightarrow e^- + CO$	Momentum Transfer	$f(\sigma)$, ε
E50-59	$e^- + CO \Rightarrow e^- + CO_{(V1\text{-}10)}$	Vibrational Excitation	$f(\sigma)$, ε
E60-64	$e^- + CO \Rightarrow e^- + CO_{(E1\text{-}5)}$	Electronic Excitation	$f(\sigma)$, ε
E65	$e^- + CO \Rightarrow e^- + C + O$	Dissociative Excitation	$f(\sigma)$, ε
E66	$e^- + CO \Rightarrow 2e^- + CO^+$	Ionisation	$f(\sigma)$, ε
E67	$e^- + H_2 \Rightarrow H + H^-$	Dissociative Attachment	$f(\sigma)$, ε
E68	$e^- + H_2 \Rightarrow e^- + H_{2(j0\text{-}2,\ j1\text{-}3)}$	Rotational Excitation	$f(\sigma)$, ε
E69-71	$e^- + H_2 \Rightarrow e^- + H_{2(V1\text{-}3)}$	Vibrational Excitation	$f(\sigma)$, ε
E72	$e^- + H_2 \Rightarrow e^- + H_2(B^1\Sigma_u^+)$	Electronic Excitation	$f(\sigma)$, ε
E73	$e^- + H_2 \Rightarrow e^- + H_2(c^3\Pi_u)$	Electronic Excitation	$f(\sigma)$, ε
E74	$e^- + H_2 \Rightarrow e^- + H_2(a^3\Sigma_g^+)$	Electronic Excitation	$f(\sigma)$, ε
E75	$e^- + H_2 \Rightarrow e^- + H_2(C^1\Pi_u)$	Electronic Excitation	$f(\sigma)$, ε
E76	$e^- + H_2 \Rightarrow e^- + H_2(^1\Sigma_g^+)$	Electronic Excitation	$f(\sigma)$, ε
E77	$e^- + H_2 \Rightarrow e^- + H_2(D^3\Pi_u)$	Electronic Excitation	$f(\sigma)$, ε
E78	$e^- + H_2 \Rightarrow e^- + H_{2(E1\text{-}2)}$	Electronic Excitation	$f(\sigma)$, ε
E79	$e^- + H_2 \Rightarrow e^- + H_{2(Rydberg)}$	Rydberg Excitation	$f(\sigma)$, ε
E80	$e^- + H_2 \Rightarrow 2e^- + H_2^+$	Ionisation	$f(\sigma)$, ε
E81	$e^- + H \Rightarrow e^- + H$	Momentum Transfer	$f(\sigma)$, ε
E82	$e^- + H \Rightarrow e^- + H_{(2p)}$	Excitation	$f(\sigma)$, ε
E83	$e^- + H \Rightarrow e^- + H_{(2s)}$	Excitation	$f(\sigma)$, ε
E84	$e^- + H \Rightarrow 2e^- + H^+$	Ionisation	$f(\sigma)$, ε
E85	$e^- + O_2 \Rightarrow O_2^-$	Attachment	$f(\sigma)$, ε
E86	$e^- + O_2 \Rightarrow e^- + O_2$	Momentum Transfer	$f(\sigma)$, ε
E87-89	$e^- + O_2 \Rightarrow e^- + O_{2(R1\text{-}3)}$	Rotational Excitation	$f(\sigma)$, ε
E90-93	$e^- + O_2 \Rightarrow e^- + O_{2(V1\text{-}4)}$	Vibrational Excitation	$f(\sigma)$, ε
E94	$e^- + O_2 \Rightarrow e^- + O_2(b^1\Sigma^+)$	Electronic Excitation	$f(\sigma)$, ε
E95	$e^- + O_2 \Rightarrow e^- + O_2(a^1\delta^+)$	Electronic Excitation	$f(\sigma)$, ε
E96-101	$e^- + O_2 \Rightarrow e^- + O + O$	Dissociative Excitation	$f(\sigma)$, ε

E102	$e^- + O_2 \Rightarrow 2e^- + O_2^+$	Ionisation	$f(\sigma)$, ε
E103	$e^- + O \Rightarrow e^- + O$	Momentum Transfer	$f(\sigma)$, ε
E104	$e^- + O \Rightarrow e^- + O_{(1D)}$	Excitation	$f(\sigma)$, ε
E105	$e^- + O \Rightarrow e^- + O_{(1S)}$	Excitation	$f(\sigma)$, ε
E106	$e^- + O \Rightarrow 2e^- + O^+$	Ionisation	$f(\sigma)$, ε
E107	$e^- + H_2O \Rightarrow H_2 + O^-$	Dissociative Attachment	$f(\sigma)$, ε
E108	$e^- + H_2O \Rightarrow OH + H^-$	Dissociative Attachment	$f(\sigma)$, ε
E109	$e^- + H_2O \Rightarrow H + OH^-$	Dissociative Attachment	$f(\sigma)$, ε
E110	$e^- + H_2O \Rightarrow e^- + H_2O$	Momentum Transfer	$f(\sigma)$, ε
E111-113	$e^- + H_2O \Rightarrow e^- + H_2O_{(V1\text{-}3)}$	Vibrational Excitation	$f(\sigma)$, ε
E114	$e^- + H_2O \Rightarrow e^- + H + OH$	Dissociative Excitation	$f(\sigma)$, ε
E115	$e^- + H_2O \Rightarrow e^- + H_2 + O$	Dissociative Excitation	$f(\sigma)$, ε
E116	$e^- + H_2O \Rightarrow 2e^- + H_2O^+$	Ionisation	$f(\sigma)$, ε
E117	$e^- + C_2H_2 \Rightarrow e^- + C_2H_2$	Momentum Transfer	$f(\sigma)$, ε
E118-120	$e^- + C_2H_2 \Rightarrow e^- + C_2H_{2(V2,5\ \&31)}$	Vibrational Excitation	$f(\sigma)$, ε
E121-122	$e^- + C_2H_2 \Rightarrow e^- + C_2H_{2(E1\ \&2)}$	Electronic Excitation	$f(\sigma)$, ε
E123	$e^- + C_2H_2 \Rightarrow e^- + H + C_2H$	Dissociative Excitation	$f(\sigma)$, ε
E124	$e^- + C_2H_2 \Rightarrow e^- + 2H + C_2$	Dissociative Excitation	$f(\sigma)$, ε
E125	$e^- + C_2H_2 \Rightarrow e^- + CH + CH$	Dissociative Excitation	$f(\sigma)$, ε
E126	$e^- + C_2H_2 \Rightarrow e^- + C + CH_2$	Dissociative Excitation	$f(\sigma)$, ε
E127	$e^- + C_2H_2 \Rightarrow 2e^- + C_2H_2^+$	Ionisation	$f(\sigma)$, ε
E128	$e^- + C_2H_2^+ \Rightarrow e^- + C_2H^+ + H$	Dissociation of Ion	$f(\sigma)$, ε
E129	$e^- + C_2H_2^+ \Rightarrow e^- + C_2H + H^+$	Dissociation of Ion	$f(\sigma)$, ε
E130	$e^- + C_2H_2^+ \Rightarrow e^- + H_2 + C_2^+$	Dissociation of Ion	$f(\sigma)$, ε
E131	$e^- + C_2H_2^+ \Rightarrow e^- + CH + CH^+$	Dissociation of Ion	$f(\sigma)$, ε
E132	$e^- + C_2H_2^+ \Rightarrow e^- + C + CH_2^+$	Dissociation of Ion	$f(\sigma)$, ε
E133	$e^- + C_2H_2^+ \Rightarrow e^- + C^+ + CH_2$	Dissociation of Ion	$f(\sigma)$, ε
E134	$e^- + C_2H_2^+ \Rightarrow 2e^- + C_2H^+ + H^+$	Dissociative Ionisation	$f(\sigma)$, ε
E135	$e^- + C_2H_2^+ \Rightarrow 2e^- + C_2^+ + H_2^+$	Dissociative Ionisation	$f(\sigma)$, ε
E136	$e^- + C_2H_2^+ \Rightarrow 2e^- + C_2^+ + H + H^+$	Dissociative Ionisation	$f(\sigma)$, ε
E137	$e^- + C_2H_2^+ \Rightarrow 2e^- + CH^+ + CH^+$	Dissociative Ionisation	$f(\sigma)$, ε
E138	$e^- + C_2H_2^+ \Rightarrow 2e^- + C^+ + H + CH^+$	Dissociative Ionisation	$f(\sigma)$, ε
E139	$e^- + C_2H_2^+ \Rightarrow 2e^- + CH_2^+ + C^+$	Dissociative Ionisation	$f(\sigma)$, ε

E140	$e^- + C_2H_4 \Rightarrow e^- + C_2H_4$	Momentum Transfer	$f(\sigma)$, ε
E141-142	$e^- + C_2H_4 \Rightarrow e^- + C_2H_{4(V1\ \&\ 2)}$	Vibrational Excitation	$f(\sigma)$, ε
E143-144	$e^- + C_2H_4 \Rightarrow e^- + C_2H_{4(E1\ \&\ 2)}$	Electronic Excitation	$f(\sigma)$, ε
E145	$e^- + C_2H_4 \Rightarrow e^- + C_2H_3 + H$	Dissociative Excitation	$f(\sigma)$, ε
E146	$e^- + C_2H_4 \Rightarrow e^- + C_2H_2 + H_2$	Dissociative Excitation	$f(\sigma)$, ε
E147	$e^- + C_2H_4 \Rightarrow e^- + C_2H_2 + 2H$	Dissociative Excitation	$f(\sigma)$, ε
E148	$e^- + C_2H_4 \Rightarrow e^- + C_2H + H_2 + H$	Dissociative Excitation	$f(\sigma)$, ε
E149	$e^- + C_2H_4 \Rightarrow e^- + CH_3 + CH$	Dissociative Excitation	$f(\sigma)$, ε
E150	$e^- + C_2H_4 \Rightarrow e^- + CH_2 + CH_2$	Dissociative Excitation	$f(\sigma)$, ε
E151	$e^- + C_2H_4 \Rightarrow e^- + C + CH_4$	Dissociative Excitation	$f(\sigma)$, ε
E152	$e^- + C_2H_4 \Rightarrow 2e^- + C_2H_4^+$	Ionisation	$f(\sigma)$, ε
E153	$e^- + C_2H_4^+ \Rightarrow e^- + H + C_2H_3^+$	Dissociation of Ion	$f(\sigma)$, ε
E154	$e^- + C_2H_4^+ \Rightarrow e^- + H_2 + C_2H_2^+$	Dissociation of Ion	$f(\sigma)$, ε
E155	$e^- + C_2H_4^+ \Rightarrow e^- + H_2^+ + C_2H_2$	Dissociation of Ion	$f(\sigma)$, ε
E156	$e^- + C_2H_4^+ \Rightarrow e^- + CH_3^+ + CH$	Dissociation of Ion	$f(\sigma)$, ε
E157	$e^- + C_2H_4^+ \Rightarrow e^- + CH_3 + CH^+$	Dissociation of Ion	$f(\sigma)$, ε
E158	$e^- + C_2H_4^+ \Rightarrow e^- + CH_2 + CH_2^+$	Dissociation of Ion	$f(\sigma)$, ε
E159	$e^- + C_2H_4^+ \Rightarrow e^- + CH_4 + C^+$	Dissociation of Ion	$f(\sigma)$, ε
E160	$e^- + C_2H_4^+ \Rightarrow 2e^- + C_2H_3^+ + H^+$	Dissociative Ionisation	$f(\sigma)$, ε
E161	$e^- + C_2H_4^+ \Rightarrow 2e^- + C_2H_2^+ + H_2^+$	Dissociative Ionisation	$f(\sigma)$, ε
E162	$e^- + C_2H_4^+ \Rightarrow 2e^- + C_2H_2^+ + H + H^+$	Dissociative Ionisation	$f(\sigma)$, ε
E163	$e^- + C_2H_4^+ \Rightarrow 2e^- + CH_3^+ + CH^+$	Dissociative Ionisation	$f(\sigma)$, ε
E164	$e^- + C_2H_4^+ \Rightarrow 2e^- + CH_2^+ + CH_2^+$	Dissociative Ionisation	$f(\sigma)$, ε
E165	$e^- + C_2H_4^+ \Rightarrow 2e^- + CH_4^+ + C^+$	Dissociative Ionisation	$f(\sigma)$, ε
E166	$e^- + C_2H_6 \Rightarrow C_2H_6^-$	Attachment	$f(\sigma)$, ε
E167	$e^- + C_2H_6 \Rightarrow e^- + C_2H_6$	Momentum Transfer	$f(\sigma)$, ε
E168-169	$e^- + C_2H_6 \Rightarrow e^- + C_2H_{6(V13\ \&\ 24)}$	Vibrational Excitation	$f(\sigma)$, ε
E170	$e^- + C_2H_6 \Rightarrow e^- + C_2H_5 + H$	Dissociative Excitation	$f(\sigma)$, ε
E171	$e^- + C_2H_6 \Rightarrow e^- + C_2H_4 + H_2$	Dissociative Excitation	$f(\sigma)$, ε
E172	$e^- + C_2H_6 \Rightarrow e^- + C_2H_3 + H + H_2$	Dissociative Excitation	$f(\sigma)$, ε
E173	$e^- + C_2H_6 \Rightarrow e^- + C_2H_2 + 2H_2$	Dissociative Excitation	$f(\sigma)$, ε
E174	$e^- + C_2H_6 \Rightarrow e^- + CH_4 + CH_2$	Dissociative Excitation	$f(\sigma)$, ε
E175	$e^- + C_2H_6 \Rightarrow e^- + CH_3 + CH_3$	Dissociative Excitation	$f(\sigma)$, ε

E176	$e^- + C_2H_6 \Rightarrow 2e^- + C_2H_6^+$	Ionisation	$f(\sigma)$, ε
E177	$e^- + C_2H_6^+ \Rightarrow e^- + C_2H_5^+ + H$	Dissociation of Ion	$f(\sigma)$, ε
E178	$e^- + C_2H_6^+ \Rightarrow e^- + C_2H_4^+ + H_2$	Dissociation of Ion	$f(\sigma)$, ε
E179	$e^- + C_2H_6^+ \Rightarrow e^- + CH_3^+ + CH_3$	Dissociation of Ion	$f(\sigma)$, ε
E180	$e^- + C_2H_6^+ \Rightarrow 2e^- + C_2H_5^+ + H^+$	Dissociative Ionisation	$f(\sigma)$, ε
E181	$e^- + C_2H_6^+ \Rightarrow 2e^- + C_2H_4^+ + H_2^+$	Dissociative Ionisation	$f(\sigma)$, ε
E182	$e^- + C_2H_6^+ \Rightarrow 2e^- + C_2H_4^+ + H + H^+$	Dissociative Ionisation	$f(\sigma)$, ε
E183	$e^- + C_2H_6^+ \Rightarrow 2e^- + C_2H_3^+ + H_2 + H^+$	Dissociative Ionisation	$f(\sigma)$, ε
E184	$e^- + C_2H_6^+ \Rightarrow 2e^- + C_2H_2^+ + H_2 + H_2^+$	Dissociative Ionisation	$f(\sigma)$, ε
E185	$e^- + C_2H_6^+ \Rightarrow 2e^- + CH_4^+ + CH_2^+$	Dissociative Ionisation	$f(\sigma)$, ε
E186	$e^- + C_2H_6^+ \Rightarrow 2e^- + CH_3^+ + CH_3^+$	Dissociative Ionisation	$f(\sigma)$, ε
E187	$e^- + C_3H_6 \Rightarrow C_3H_6^-$	Attachment	$f(\sigma)$, ε
E188	$e^- + C_3H_6 \Rightarrow e^- + C_3H_6$	Momentum Transfer	$f(\sigma)$, ε
E189	$e^- + C_3H_6 \Rightarrow e^- + C_3H_{6(V)}$	Vibrational Excitation	$f(\sigma)$, ε
E190	$e^- + C_3H_6 \Rightarrow e^- + C_3H_5 + H$	Dissociative Excitation	$f(\sigma)$, ε
E191	$e^- + C_3H_6 \Rightarrow e^- + C_3H_4 + H_2$	Dissociative Excitation	$f(\sigma)$, ε
E192	$e^- + C_3H_6 \Rightarrow e^- + C_3H_3 + H + H_2$	Dissociative Excitation	$f(\sigma)$, ε
E193	$e^- + C_3H_6 \Rightarrow e^- + C_3H_2 + 2H_2$	Dissociative Excitation	$f(\sigma)$, ε
E194	$e^- + C_3H_6 \Rightarrow e^- + C_2H_4 + CH_2$	Dissociative Excitation	$f(\sigma)$, ε
E195	$e^- + C_3H_6 \Rightarrow e^- + C_2H_3 + CH_3$	Dissociative Excitation	$f(\sigma)$, ε
E196	$e^- + C_3H_6 \Rightarrow e^- + C_2H_2 + CH_4$	Dissociative Excitation	$f(\sigma)$, ε
E197	$e^- + C_3H_6 \Rightarrow 2e^- + C_3H_6^+$	Ionisation	$f(\sigma)$, ε
E198	$e^- + C_3H_6^+ \Rightarrow e^- + C_2H_5^+ + CH$	Dissociation of Ion	$f(\sigma)$, ε
E199	$e^- + C_3H_6^+ \Rightarrow e^- + C_2H_4^+ + CH_2$	Dissociation of Ion	$f(\sigma)$, ε
E200	$e^- + C_3H_6^+ \Rightarrow e^- + C_2H_3^+ + CH_3$	Dissociation of Ion	$f(\sigma)$, ε
E201	$e^- + C_3H_6^+ \Rightarrow e^- + C_2H_2^+ + CH_4$	Dissociation of Ion	$f(\sigma)$, ε
E202	$e^- + C_3H_6^+ \Rightarrow e^- + CH_4^+ + C_2H_2$	Dissociation of Ion	$f(\sigma)$, ε
E203	$e^- + C_3H_6^+ \Rightarrow e^- + CH_3^+ + C_2H_3$	Dissociation of Ion	$f(\sigma)$, ε
E204	$e^- + C_3H_6^+ \Rightarrow e^- + CH_2^+ + C_2H_4$	Dissociation of Ion	$f(\sigma)$, ε
E205	$e^- + C_3H_6^+ \Rightarrow 2e^- + C_2H_6^+ + C^+$	Dissociative Ionisation	$f(\sigma)$, ε
E206	$e^- + C_3H_6^+ \Rightarrow 2e^- + C_2H_5^+ + CH^+$	Dissociative Ionisation	$f(\sigma)$, ε
E207	$e^- + C_3H_6^+ \Rightarrow 2e^- + C_2H_4^+ + CH_2^+$	Dissociative Ionisation	$f(\sigma)$, ε
E208	$e^- + C_3H_6^+ \Rightarrow 2e^- + C_2H_3^+ + CH_3^+$	Dissociative Ionisation	$f(\sigma)$, ε

E209	$e^- + C_3H_6^+ \Rightarrow 2e^- + C_2H_2^+ + CH_4^+$	Dissociative Ionisation	*f(σ), ε*
E210	$e^- + C_3H_6^+ \Rightarrow 2e^- + C_2H^+ + H + CH_4^+$	Dissociative Ionisation	*f(σ), ε*
E211	$e^- + C_3H_6^+ \Rightarrow 2e^- + C_2H^+ + H^+ + CH_4$	Dissociative Ionisation	*f(σ), ε*
E212	$e^- + C_3H_6^+ \Rightarrow 2e^- + C_2^+ + CH_4^+ + H_2$	Dissociative Ionisation	*f(σ), ε*
E213	$e^- + C_3H_8 \Rightarrow C_3H_8^-$	Attachment	*f(σ), ε*
E214	$e^- + C_3H_8 \Rightarrow e^- + C_3H_8$	Momentum Transfer	*f(σ), ε*
E215-216	$e^- + C_3H_8 \Rightarrow e^- + C_3H_{8(V1\ \&\ 2)}$	Vibrational Excitation	*f(σ), ε*
E217	$e^- + C_3H_8 \Rightarrow e^- + C_3H_{8(E)}$	Electronic Excitation	*f(σ), ε*
E218	$e^- + C_3H_8 \Rightarrow e^- + C_3H_7 + H$	Dissociative Excitation	*f(σ), ε*
E219	$e^- + C_3H_8 \Rightarrow e^- + C_3H_6 + H_2$	Dissociative Excitation	*f(σ), ε*
E220	$e^- + C_3H_8 \Rightarrow e^- + C_3H_4 + 2H_2$	Dissociative Excitation	*f(σ), ε*
E221	$e^- + C_3H_8 \Rightarrow e^- + C_2H_6 + CH_2$	Dissociative Excitation	*f(σ), ε*
E222	$e^- + C_3H_8 \Rightarrow e^- + C_2H_5 + CH_3$	Dissociative Excitation	*f(σ), ε*
E223	$e^- + C_3H_8 \Rightarrow e^- + C_2H_4 + CH_4$	Dissociative Excitation	*f(σ), ε*
E224	$e^- + C_3H_8 \Rightarrow 2e^- + C_3H_8^+$	Ionisation	*f(σ), ε*
E225	$e^- + C_3H_8^+ \Rightarrow e^- + C_2H_5^+ + CH_3$	Dissociation of Ion	*f(σ), ε*
E226	$e^- + C_3H_8^+ \Rightarrow e^- + C_2H_4^+ + CH_4$	Dissociation of Ion	*f(σ), ε*
E227	$e^- + C_3H_8^+ \Rightarrow 2e^- + C_2H_6^+ + CH_2^+$	Dissociative Ionisation	*f(σ), ε*
E228	$e^- + C_3H_8^+ \Rightarrow 2e^- + C_2H_5^+ + CH_3^+$	Dissociative Ionisation	*f(σ), ε*
E229	$e^- + C_3H_8^+ \Rightarrow 2e^- + C_2H_4^+ + CH_4^+$	Dissociative Ionisation	*f(σ), ε*
E230	$e^- + C_3H_8^+ \Rightarrow 2e^- + C_2H_3^+ + CH_4 + H^+$	Dissociative Ionisation	*f(σ), ε*
E231	$e^- + C_3H_8^+ \Rightarrow 2e^- + C_2H_3^+ + H + CH_4^+$	Dissociative Ionisation	*f(σ), ε*
E232	$e^- + C_3H_8^+ \Rightarrow 2e^- + C_2H_3^+ + H_2 + CH_3^+$	Dissociative Ionisation	*f(σ), ε*
E233	$e^- + C_3H_8^+ \Rightarrow 2e^- + C_2H_3^+ + H_2^+ + CH_3$	Dissociative Ionisation	*f(σ), ε*
E234	$e^- + C_3H_8^+ \Rightarrow 2e^- + C_2H_2^+ + CH_4^+ + H_2$	Dissociative Ionisation	*f(σ), ε*
E235	$e^- + C_3H_8^+ \Rightarrow 2e^- + C_2H_2^+ + CH_4 + H_2^+$	Dissociative Ionisation	*f(σ), ε*
E236	$e^- + CH_4^+ \Rightarrow CH_3 + H$	Recombination	[174]
E237	$e^- + CH_4^+ \Rightarrow CH_2 + 2H$	Recombination	[174]
E238	$e^- + CH_4^+ \Rightarrow CH + H_2 + H$	Recombination	[174]
E239	$e^- + CH_3^+ \Rightarrow CH_2 + H$	Recombination	[174]
E240	$e^- + CH_3^+ \Rightarrow CH + H_2$	Recombination	[174]
E241	$e^- + CH_3^+ \Rightarrow CH + 2H$	Recombination	[174]
E242	$e^- + CH_3^+ \Rightarrow C + H + H_2$	Recombination	[174]

E243	$e^- + CH_2^+ \Rightarrow CH + H$	Recombination	[174]
E244	$e^- + CH_2^+ \Rightarrow C + H_2$	Recombination	[174]
E245	$e^- + CH_2^+ \Rightarrow C + 2H$	Recombination	[174]
E246	$e^- + CH^+ \Rightarrow C + H$	Recombination	[174]
E247	$e^- + C_2H_6^+ \Rightarrow C_2H_5 + H$	Recombination	[174]
E248	$e^- + C_2H_6^+ \Rightarrow C_2H_4 + 2H$	Recombination	[174]
E249	$e^- + C_2H_5^+ \Rightarrow C_2H_4 + H$	Recombination	[174]
E250	$e^- + C_2H_5^+ \Rightarrow C_2H_3 + 2H$	Recombination	[174]
E251	$e^- + C_2H_5^+ \Rightarrow C_2H_2 + H + H_2$	Recombination	[174]
E252	$e^- + C_2H_5^+ \Rightarrow C_2H_2 + 3H$	Recombination	[174]
E253	$e^- + C_2H_5^+ \Rightarrow CH_3 + CH_2$	Recombination	[174]
E254	$e^- + C_2H_4^+ \Rightarrow C_2H_3 + H$	Recombination	[174]
E255	$e^- + C_2H_4^+ \Rightarrow C_2H_2 + 2H$	Recombination	[174]
E256	$e^- + C_2H_4^+ \Rightarrow C_2H + H_2 + H$	Recombination	[174]
E257	$e^- + C_2H_3^+ \Rightarrow C_2H_2 + H$	Recombination	[174]
E258	$e^- + C_2H_3^+ \Rightarrow C_2H + 2H$	Recombination	[174]
E259	$e^- + C_2H_2^+ \Rightarrow C_2H + H$	Recombination	[174]
E260	$e^- + C_2H_2^+ \Rightarrow CH + CH$	Recombination	[174]
E261	$e^- + O_2^+ + O_2 \Rightarrow O_2 + O_2$	Recombination	[174]
E262	$e^- + O_2^+ \Rightarrow O + O$	Recombination	[174]
E263	$e^- + CO_2^+ \Rightarrow CO + O$	Recombination	[174]

Table A7.3 Ion-neutral/ions reactions involved in this model, and the corresponding reaction rate constant are adopted from the literature [174].

No.	Reaction	Rate constant (cm^3s^{-1})
I1	$CH_4^+ + C_2H_6 \Rightarrow C_2H_4^+ + CH_4 + H_2$	1.91×10^{-9}
I2	$CH_4^+ + C_2H_4 \Rightarrow C_2H_5^+ + CH_3$	4.23×10^{-10}
I3	$CH_4^+ + C_2H_4 \Rightarrow C_2H_4^+ + CH_4$	1.38×10^{-9}
I4	$CH_4^+ + C_2H_2 \Rightarrow C_2H_3^+ + CH_3$	1.23×10^{-9}
I5	$CH_4^+ + C_2H_2 \Rightarrow C_2H_2^+ + CH_4$	1.13×10^{-9}
I6	$CH_4^+ + H \Rightarrow CH_3^+ + H_2$	1.00×10^{-11}
I7	$CH_4^+ + O \Rightarrow CH_3^+ + OH$	1.00×10^{-9}
I8	$CH_4^+ + O_2 \Rightarrow CH_4 + O_2^+$	3.90×10^{-10}
I9	$CH_3^+ + CH_4 \Rightarrow CH_4^+ + CH_3$	1.36×10^{-10}
I10	$CH_3^+ + CH_4 \Rightarrow C_2H_5^+ + H_2$	1.20×10^{-9}
I11	$CH_3^+ + CH_2 \Rightarrow C_2H_3^+ + H_2$	9.90×10^{-10}
I12	$CH_3^+ + CH \Rightarrow C_2H_2^+ + H_2$	7.10×10^{-10}
I13	$CH_3^+ + C_2H_6 \Rightarrow C_2H_5^+ + CH_4$	1.48×10^{-9}
I14	$CH_3^+ + C_2H_4 \Rightarrow C_2H_3^+ + CH_4$	3.50×10^{-10}
I15	$CH_3^+ + C_2H_3 \Rightarrow C_2H_3^+ + CH_3$	3.00×10^{-10}
I16	$CH_2^+ + CH_4 \Rightarrow CH_3^+ + CH_3$	1.38×10^{-10}
I17	$CH_2^+ + CH_4 \Rightarrow C_2H_5^+ + H$	3.90×10^{-10}
I18	$CH_2^+ + CH_4 \Rightarrow C_2H_4^+ + H_2$	8.40×10^{-10}
I19	$CH_2^+ + CH_4 \Rightarrow C_2H_3^+ + H_2 + H$	2.31×10^{-10}
I20	$CH_2^+ + CH_4 \Rightarrow C_2H_3^+ + 2H_2$	3.97×10^{-10}
I21	$CH^+ + CH_4 \Rightarrow C_2H_4^+ + H$	6.50×10^{-11}
I22	$CH^+ + CH_4 \Rightarrow C_2H_3^+ + H_2$	1.09×10^{-9}
I23	$CH^+ + CH_4 \Rightarrow C_2H_2^+ + H + H_2$	1.43×10^{-10}
I24	$CH^+ + H_2 \Rightarrow CH_2^+ + H$	1.20×10^{-9}
I25	$C_2H_6^+ + C_2H_4 \Rightarrow C_2H_4^+ + C_2H_6$	1.15×10^{-9}
I26	$C_2H_6^+ + C_2H_2 \Rightarrow C_2H_5^+ + C_2H_3$	2.47×10^{-10}
I27	$C_2H_6^+ + H \Rightarrow C_2H_5^+ + H_2$	1.00×10^{-10}
I28	$C_2H_5^+ + H \Rightarrow C_2H_4^+ + H_2$	1.00×10^{-11}
I29	$C_2H_4^+ + C_2H_3 \Rightarrow C_2H_5^+ + C_2H_2$	5.00×10^{-10}

I30	$C_2H_4^+ + C_2H_3 \Rightarrow C_2H_3^+ + C_2H_4$	5.00×10^{-10}
I31	$C_2H_4^+ + H \Rightarrow C_2H_3^+ + H_2$	3.00×10^{-10}
I32	$C_2H_4^+ + O \Rightarrow C_2H_3^+ + HCO$	1.08×10^{-10}
I33	$C_2H_3^+ + C_2H_6 \Rightarrow C_2H_5^+ + C_2H_4$	2.91×10^{-10}
I34	$C_2H_3^+ + C_2H_4 \Rightarrow C_2H_5^+ + C_2H_2$	8.90×10^{-10}
I35	$C_2H_3^+ + C_2H_3 \Rightarrow C_2H_5^+ + C_2H$	5.00×10^{-10}
I36	$C_2H_3^+ + C_2H \Rightarrow C_2H_2^+ + C_2H_2$	3.30×10^{-10}
I37	$C_2H_3^+ + H \Rightarrow C_2H_2^+ + H_2$	6.80×10^{-11}
I38	$C_2H_2^+ + CH_4 \Rightarrow C_2H_3^+ + CH_3$	4.10×10^{-9}
I39	$C_2H_2^+ + C_2H_6 \Rightarrow C_2H_5^+ + C_2H_3$	1.31×10^{-10}
I40	$C_2H_2^+ + C_2H_6 \Rightarrow C_2H_4^+ + C_2H_4$	2.48×10^{-10}
I41	$C_2H_2^+ + C_2H_4 \Rightarrow C_2H_4^+ + C_2H_2$	4.14×10^{-10}
I42	$C_2H_2^+ + C_2H_3 \Rightarrow C_2H_3^+ + C_2H_2$	3.30×10^{-10}
I43	$C_2H_2^+ + H_2 \Rightarrow C_2H_3^+ + H$	1.00×10^{-11}
I44	$O_2^+ + CH_2 \Rightarrow CH_2^+ + O_2$	4.30×10^{-10}
I45	$O_2^+ + CH \Rightarrow CH^+ + O_2$	3.10×10^{-10}
I46	$O_2^+ + C_2H_4 \Rightarrow C_2H_4^+ + O_2$	6.80×10^{-10}
I47	$O_2^+ + C_2H_2 \Rightarrow C_2H_2^+ + O_2$	1.11×10^{-9}
I48	$O_2^+ + O^- \Rightarrow O + O_2$	2.90×10^{-8}
I49	$O_2^+ + O^- \Rightarrow 3O$	2.90×10^{-8}
I50	$O^- + CH_4 \Rightarrow OH^- + CH_3$	1.00×10^{-10}
I51	$O^- + C \Rightarrow e^- + CO$	5.00×10^{-10}
I52	$O^- + H_2 \Rightarrow e^- + H_2O$	7.00×10^{-10}
I53	$O^- + H_2 \Rightarrow OH^- + H$	3.00×10^{-11}
I54	$O^- + H \Rightarrow e^- + OH$	5.00×10^{-10}
I55	$O^- + O \Rightarrow e^- + O_2$	2.30×10^{-11}
I56	$O^- + CO \Rightarrow e^- + CO_2$	6.50×10^{-10}
I57	$CO_2^+ + CH_4 \Rightarrow CH_4^+ + CO_2$	5.50×10^{-10}
I58	$CO_2^+ + C_2H_4 \Rightarrow C_2H_4^+ + CO_2$	1.50×10^{-10}
I59	$CO_2^+ + C_2H_2 \Rightarrow C_2H_2^+ + CO_2$	7.30×10^{-10}
I60	$CO_2^+ + O_2 \Rightarrow O_2^+ + CO_2$	5.30×10^{-11}
I61	$CO_2^+ + O \Rightarrow O_2^+ + CO$	1.64×10^{-10}
I62	$OH^- + CH_3 \Rightarrow e^- + CH_3OH$	1.00×10^{-9}

I63	$OH^- + CH \Rightarrow e^- + CH_2O$	5.00×10^{-10}
I64	$OH^- + C \Rightarrow e^- + HCO$	5.00×10^{-10}
I65	$OH^- + H \Rightarrow e^- + H_2O$	1.40×10^{-9}

Bibliography

[1] R.M. Cuéllar-Franca, A. Azapagic, Carbon capture, storage and utilisation technologies: A critical analysis and comparison of their life cycle environmental impacts, *Journal of CO_2 Utilization*, 9 (2015) 82-102.

[2] A. Bogaerts, T. Kozak, K. van Laer, R. Snoeckx, Plasma-based conversion of CO_2: Current status and future challenges, *Farad. Discuss.*, 183 (2015) 217-232.

[3] M.S. Fan, A.Z. Abdullah, S. Bhatia, Utilization of greenhouse gases through carbon dioxide reforming of methane over Ni–Co/MgO–ZrO_2: Preparation, characterization and activity studies, *Appl. Catal., B: Environ.*, 100 (2010) 365-377.

[4] C.J. Liu, J.Y. Ye, J.J. Jiang, Y.X. Pan, Progresses in the preparation of coke resistant Ni-based catalyst for steam and CO_2 reforming of methane, *ChemCatChem*, 3 (2011) 529-541.

[5] P. Markewitz, W. Kuckshinrichs, W. Leitner, J. Linssen, P. Zapp, R. Bongartz, A. Schreiber, T.E. Müller, Worldwide innovations in the development of carbon capture technologies and the utilization of CO_2, *Energy Environ. Sci.*, 5 (2012) 7281.

[6] D. Li, Y. Nakagawa, K. Tomishige, Methane reforming to synthesis gas over Ni catalysts modified with noble metals, *Applied Catalysis A: General*, 408 (2011) 1-24.

[7] Global temperatures. Available: http://earthobservatory.nasa.gov/Features/WorldOfChange/decadaltemp.php, accessed Feb 23, 2017.

[8] DECC, 2014 UK greenhouse gas emissions, final figures, 2016.

[9] Energy Act 2004. Available: http://www.legislation.gov.uk/ukpga/2004/20/contents, accessed 2017.

[10] Climate Change Act 2008. Available: http://www.legislation.gov.uk/ukpga/2008/27/contents, accessed Dec 17, 2015.

[11] Adoption of the Paris Agreement. Available: http://unfccc.int/resource/docs/2015/cop21/eng/l09r01.pdf, accessed May 17, 2017.

[12] Y. Yan, Y. Dai, H. He, Y. Yu, Y. Yang, A novel W-doped Ni-Mg mixed oxide catalyst for CO_2 methanation, *Appl. Catal., B: Environ.*, 196 (2016) 108-116.

[13] T. Avanesian, G.S. Gusmão, P. Christopher, Mechanism of CO_2 reduction by H_2 on Ru (0001) and general selectivity descriptors for late-transition metal catalysts, *J. Catal.*, 343 (2016) 86-96.

[14] C. Heine, B.A. Lechner, H. Bluhm, M. Salmeron, Recycling of CO_2: Probing the chemical state of the Ni (111) surface during the methanation reaction with ambient-pressure X-Ray photoelectron spectroscopy, *J. Am. Chem. Soc.*, 138 (2016) 13246-13252.

[15] G. Zhou, H. Liu, K. Cui, A. Jia, G. Hu, Z. Jiao, Y. Liu, X. Zhang, Role of surface Ni and Ce species of Ni/CeO_2 catalyst in CO_2 methanation, *Applied Surf. Sci.*, 383 (2016) 248-252.

[16] J. Gao, Y. Wu, C. Jia, Z. Zhong, F. Gao, Y. Yang, B. Liu, Controllable synthesis of α-MoC_{1-x} and β-Mo_2C nanowires for highly selective CO_2 reduction to CO, *Catal. Commun.*, 84 (2016) 147-150.

[17] A.V. Puga, Light-promoted hydrogenation of carbon dioxide—An overview, *Top. Catal.*, 59 (2016) 1268-1278.

[18] Y. Yan, M. Han, A. Konkin, T. Koppe, D. Wang, T. Andreu, G. Chen, U. Vetter, J.R. Morante, P. Schaaf, Slightly hydrogenated TiO_2 with enhanced photocatalytic performance, *J. Mater. Chem.*, 2 (2014) 12708-12716.

[19] I. Kalaitzidou, M. Makri, D. Theleritis, A. Katsaounis, C. Vayenas, Comparative study of the electrochemical promotion of CO_2 hydrogenation on Ru using Na+, K+, H+ and O2− conducting solid electrolytes, *Surf. Sci.*, 646 (2016) 194-203.

[20] V. Jiménez, C. Jiménez-Borja, P. Sánchez, A. Romero, E.I. Papaioannou, D. Theleritis, S. Souentie, S. Brosda, J.L. Valverde, Electrochemical promotion of the CO_2 hydrogenation reaction on composite Ni or Ru impregnated carbon nanofiber catalyst-electrodes deposited on YSZ, *Appl. Catal., B: Environ.*, 107 (2011) 210-220.

[21] M.J. Druyvesteyn, F.M. Penning, The mechanism of electrical discharges in gases of low pressure, *Reviews of Modern Physics*, 12 (1940) 87-174.

[22] X. Zhu, X. Gao, R. Qin, Y. Zeng, R. Qu, C. Zheng, X. Tu, Plasma-catalytic removal of formaldehyde over Cu–Ce catalysts in a dielectric barrier discharge reactor, *Appl. Catal., B: Environ.*, 170 (2015) 293-300.

[23] M. Scapinello, L. Martini, G. Dilecce, P. Tosi, Conversion of CH_4/CO_2 by a nanosecond repetitively pulsed discharge, *J. Phys. D: Appl. Phys.*, 49 (2016) 075602.

[24] Y. Zeng, X. Tu, Plasma-catalytic CO_2 hydrogenation at low temperatures, *IEEE Trans. Plasma Sci.*, 44 (2016) 405-411.

[25] R. Benrabbah, C. Cavaniol, H. Liu, S. Ognier, S. Cavadias, M.E. Gálvez, P. Da Costa, Plasma DBD activated ceria-zirconia-promoted Ni-catalysts for plasma catalytic CO_2 hydrogenation at low temperature, *Catal. Commun.*, 89 (2017) 73-76.

[26] U. Kogelschatz, Dielectric-barrier discharges: Their history, discharge physics, and industrial applications, *Plasma Chemistry and Plasma Processing*, 23 (2003) 1-46.

[27] S. Yao, Plasma reactors for diesel particulate matter removal, *Recent Patents on Chemical Engineering*, 2 (2009) 67-75.

[28] F. Massines, N. Gherardi, N. Naude, P. Ségur, Glow and Townsend dielectric barrier discharge in various atmosphere, *Plasma Physics and Controlled Fusion*, 47 (2005) B577-B588.

[29] H.J. Gallon, H.-H. Kim, X. Tu, J.C. Whitehead, Microscope-ICCD imaging of an atmospheric pressure CH_4 and CO_2 dielectric barrier discharge, *IEEE Trans. Plasma Sci.*, 39 (2011) 2176-2177.

[30] T. Butterworth, R. Elder, R. Allen, Effects of particle size on CO_2 reduction and discharge characteristics in a packed bed plasma reactor, *Chem. Eng. J.*, 293 (2016) 55-67.

[31] W.-C. Chung, M.-B. Chang, Review of catalysis and plasma performance on dry reforming of CH_4 and possible synergistic effects, *Renew. Sustainable Energy Rev.*, 62 (2016) 13-31.

[32] B. Ashford, X. Tu, Non-thermal plasma technology for the conversion of CO_2, *Current Opinion in Green and Sustainable Chemistry*, 3 (2017) 45-49.

[33] E.C. Neyts, Plasma-surface interactions in plasma catalysis, *Plasma Chemistry and Plasma Processing*, 36 (2015) 185-212.

[34] E.C. Neyts, A. Bogaerts, Understanding plasma catalysis through modelling and simulation—a review, *J. Phys. D: Appl. Phys.*, 47 (2014) 224010.

[35] W. Wang, S. Wang, X. Ma, J. Gong, Recent advances in catalytic hydrogenation of carbon dioxide, *Chem. Soc. Rev.*, 40 (2011) 3703-3727.

[36] H.L. Chen, H.M. Lee, S.H. Chen, M.B. Chang, S.J. Yu, S.N. Li, Removal of volatile organic compounds by single-stage and two-stage plasma catalysis systems: A review of the performance enhancement mechanisms, current status, and suitable applications, *Environmental Science & Technology*, 43 (2009) 2216-2227.

[37] X. Tu, J.C. Whitehead, Plasma-catalytic dry reforming of methane in an atmospheric dielectric barrier discharge: Understanding the synergistic effect at low temperature, *Appl. Catal., B: Environ.*, 125 (2012) 439-448.

[38] S. Samukawa, M. Hori, S. Rauf, K. Tachibana, P. Bruggeman, G. Kroesen, J.C. Whitehead, A.B. Murphy, A.F. Gutsol, S. Starikovskaia, U. Kortshagen, J.-P. Boeuf, T.J. Sommerer, M.J. Kushner, U. Czarnetzki, N. Mason, The 2012 plasma roadmap, *J. Phys. D: Appl. Phys.*, 45 (2012) 253001.

[39] J.C. Whitehead, Plasma–catalysis: The known knowns, the known unknowns and the unknown unknowns, *J. Phys. D: Appl. Phys.*, 49 (2016) 243001.

[40] C. Song, Global challenges and strategies for control, conversion and utilization of CO_2 for sustainable development involving energy, catalysis, adsorption and chemical processing, *Catal. Today*, 115 (2006) 2-32.

[41] Q. Schiermeier, Germany's energy gamble, *Nature*, 496 (2013) 156-158.

[42] M.D. Porosoff, X. Yang, J.A. Boscoboinik, J.G. Chen, Molybdenum carbide as alternative catalysts to precious metals for highly selective reduction of CO_2 to CO, *Angew. Chem. Int. Ed.*, 53 (2014) 6705-6709.

[43] G. Centi, E.A. Quadrelli, S. Perathoner, Catalysis for CO_2 conversion: a key technology for rapid introduction of renewable energy in the value chain of chemical industries, *Energy Environ. Sci.*, 6 (2013) 1711.

[44] D.J. Pettigrew, D.L. Trimm, N.W. Cant, The effects of rare earth oxides on the reverse water-gas shift reaction on palladium/alumina, *Catal. Lett.*, (1994) 313-319.

[45] E.J. Jwa, Y.S. Moks, S.B. Lee, Conversion of carbon oxides into methane in a nonthermal plasma-catalytic reactor, *The European Physical Journal Applied Physics*, 56 (2011) 24025.

[46] M. Kano, G. Satoh, S. Iizuka, Reforming of carbon dioxide to methane and methanol by electric impulse low-pressure discharge with hydrogen, *Plasma Chemistry and Plasma Processing*, 32 (2012) 177-185.

[47] H. Liu, X. Zou, X. Wang, X. Lu, W. Ding, Effect of CeO_2 addition on Ni/Al_2O_3 catalysts for methanation of carbon dioxide with hydrogen, *Journal of Natural Gas Chemistry*, 21 (2012) 703-707.

[48] S. Rahmani, M. Rezaei, F. Meshkani, Preparation of promoted nickel catalysts supported on mesoporous nanocrystalline gamma alumina for carbon dioxide methanation reaction, *Journal of Industrial and Engineering Chemistry*, 20 (2014) 4176-4182.

[49] R. Büchel, A. Baiker, S.E. Pratsinis, Effect of Ba and K addition and controlled spatial deposition of Rh in Rh/Al_2O_3 catalysts for CO_2 hydrogenation, *Applied Catalysis A: General*, 477 (2014) 93-101.

[50] H. Lu, X. Yang, G. Gao, K. Wang, Q. Shi, J. Wang, C. Han, J. Liu, M. Tong, X. Liang, C. Li, Mesoporous zirconia-modified clays supported nickel catalysts for CO and CO_2 methanation, *International Journal of Hydrogen Energy*, 39 (2014) 18894-18907.

[51] M. Guo, G. Lu, The regulating effects of cobalt addition on the catalytic properties of silica-supported Ni–Co bimetallic catalysts for CO_2 methanation, *Reaction Kinetics, Mechanisms and Catalysis*, 113 (2014) 101-113.

[52] S. Tada, O.J. Ochieng, R. Kikuchi, T. Haneda, H. Kameyama, Promotion of CO_2 methanation activity and CH_4 selectivity at low temperatures over $Ru/CeO_2/Al_2O_3$ catalysts, *International Journal of Hydrogen Energy*, 39 (2014) 10090-10100.

[53] G. Garbarino, P. Riani, L. Magistri, G. Busca, A study of the methanation of carbon dioxide on Ni/Al_2O_3 catalysts at atmospheric pressure, *International Journal of Hydrogen Energy*, 39 (2014) 11557-11565.

[54] C. Janke, M.S. Duyar, M. Hoskins, R. Farrauto, Catalytic and adsorption studies for the hydrogenation of CO_2 to methane, *Appl. Catal., B: Environ.*, 152-153 (2014) 184-191.

[55] R. Aerts, W. Somers, A. Bogaerts, Carbon dioxide splitting in a dielectric barrier discharge plasma: a combined experimental and computational study, *ChemSusChem*, 8 (2015) 702-716.

[56] F. Brehmer, S. Welzel, M.C.M. van de Sanden, R. Engeln, CO and byproduct formation during CO_2 reduction in dielectric barrier discharges, *J. Appl. Phys.*, 116 (2014) 123303.

[57] G. Chen, T. Silva, V. Georgieva, T. Godfroid, N. Britun, R. Snyders, M.P. Delplancke-Ogletree, Simultaneous dissociation of CO_2 and H_2O to syngas in a surface-wave microwave discharge, *International Journal of Hydrogen Energy*, 40 (2015) 3789-3796.

[58] L.M. Martini, G. Dilecce, G. Guella, A. Maranzana, G. Tonachini, P. Tosi, Oxidation of CH_4 by CO_2 in a dielectric barrier discharge, *Chem. Phys. Lett.*, 593 (2014) 55-60.

[59] R. Aerts, X. Tu, C. De Bie, J.C. Whitehead, A. Bogaerts, An investigation into the dominant reactions for ethylene destruction in non-thermal atmospheric plasmas, *Plasma Process. Polym.*, 9 (2012) 994-1000.

[60] X. Tu, B. Verheyde, S. Corthals, S. Paulussen, B.F. Sels, Effect of packing solid material on characteristics of helium dielectric barrier discharge at atmospheric pressure, *Physics of Plasmas*, 18 (2011) 080702.

[61] A. Bogaerts, W. Wang, A. Berthelot, V. Guerra, Modeling plasma-based CO_2 conversion: Crucial role of the dissociation cross section, *Plasma Sources Sci. Technol.*, 25 (2016) 055016.

[62] W. Wang, A. Berthelot, S. Kolev, X. Tu, A. Bogaerts, CO_2 conversion in a gliding arc plasma: 1D cylindrical discharge model, *Plasma Sources Sci. Technol.*, 25 (2016) 065012.

[63] A. Lebouvier, S.A. Iwarere, P. d'Argenlieu, D. Ramjugernath, L. Fulcheri, Assessment of carbon dioxide dissociation as a new route for syngas production: A comparative review and potential of plasma-based technologies, *Energy Fuels*, 27 (2013) 2712-2722.

[64] D. Mei, X. Zhu, Y.-L. He, J.D. Yan, X. Tu, Plasma-assisted conversion of CO_2 in a dielectric barrier discharge reactor: Understanding the effect of packing materials, *Plasma Sources Sci. Technol.*, 24 (2015) 015011.

[65] D. Mei, X. Zhu, C. Wu, B. Ashford, P.T. Williams, X. Tu, Plasma-photocatalytic conversion of CO_2 at low temperatures: Understanding the synergistic effect of plasma-catalysis, *Appl. Catal., B: Environ.*, 182 (2016) 525-532.

[66] W.C. Chueh, C. Falter, M. Abbott, D. Scipio, P. Furler, S.M. Haile, A. Steinfeld, High-flux solar-driven thermochemical dissociation of CO_2 and H_2O using nonstoichiometric ceria, *Science*, 330 (2010) 1797-1801.

[67] G. Centi, S. Perathoner, Towards solar fuels from water and CO_2, *ChemSusChem*, 3 (2010) 195-208.

[68] H. Arakawa, M. Aresta, J.N. Armor, M.A. Barteau, E.J. Beckman, e. al., Catalysis research of relevance to carbon management: Progress, challenges, and oppotunities, *Chemical reviews*, (2001) 953-996.

[69] K. Oshima, T. Shinagawa, Y. Nogami, R. Manabe, S. Ogo, Y. Sekine, Low temperature catalytic reverse water gas shift reaction assisted by an electric field, *Catal. Today*, 232 (2014) 27-32.

[70] D. Cheng, F.R. Negreiros, E. Apra, A. Fortunelli, Computational approaches to the chemical conversion of carbon dioxide, *ChemSusChem*, 6 (2013) 944-965.

[71] Y. Tanaka, T. Takeguchi, R. Kikuchi, K. Eguchi, Influence of preparation method and additive for Cu–Mn spinel oxide catalyst on water gas shift reaction of reformed fuels, *Applied Catalysis A: General*, 279 (2005) 59-66.

[72] C. Liu, T.R. Cundari, A.K. Wilson, Reaction mechanism of the reverse water-gas shift reaction using first-row middle transition metal catalysts L'M (M = Fe, Mn, Co): a computational study, *Inorganic Chemistry*, 50 (2011) 8782-8789.

[73] M. Usman, W.W. Daud, H.F. Abbas, Dry reforming of methane: Influence of process parameters—A review, *Renew. Sustainable Energy Rev.*, 45 (2015) 710-744.

[74] E.C. Lovell, A. Fuller, J. Scott, R. Amal, Enhancing Ni-SiO_2 catalysts for the carbon dioxide reforming of methane: Reduction-oxidation-reduction pre-treatment, *Appl. Catal., B: Environ.*, 199 (2016) 155-165.

[75] L.L. Xu, F.G. Wang, M.D. Chen, J. Zhang, K.D. Yuan, L.J. Wang, K. Wu, G.Q. Xu, W. Chen, Carbon dioxide reforming of methane over cobalt‐nickel bimetal‐doped ordered mesoporous alumina catalysts with advanced catalytic performances, *ChemCatChem*, 8 (2016) 2536-2548.

[76] S.K. Kundu, E.M. Kennedy, V.V. Gaikwad, T.S. Molloy, B.Z. Dlugogorski, Experimental investigation of alumina and quartz as dielectrics for a cylindrical double dielectric barrier discharge reactor in argon diluted methane plasma, *Chem. Eng. J.*, 180 (2012) 178-189.

[77] N. Abatzoglou, S. Boivin, A review of biogas purification processes, *Biofuels, Bioproducts and Biorefining*, 3 (2009) 42-71.

[78] DECC, UK greenhouse gas and air quality pollutant inventory improvement programme: Analysis of volumes of landfill gas flared in the UK between 1990 and 2013, 2013.

[79] E. Schwab, A. Milanov, S.A. Schunk, A. Behrens, N. Schödel, Dry reforming and reverse water gas shift: Alternatives for syngas production?, *Chemie Ingenieur Technik*, 87 (2015) 347-353.

[80] D. Pakhare, J. Spivey, A review of dry (CO_2) reforming of methane over noble metal catalysts, *Chem. Soc. Rev.*, 43 (2014) 7813-7837.

[81] C. Song, W. Pan, Tri-reforming of methane: a novel concept for catalytic production of industrially useful synthesis gas with desired H_2/CO ratios, *Catal. Today*, 98 (2004) 463-484.

[82] X. Verykios, Catalytic dry reforming of natural gas for the production of chemicals and hydrogen, *International Journal of Hydrogen Energy*, 28 (2003) 1045-1063.

[83] Istadi, N. Amin, Co-generation of synthesis gas and C2+ hydrocarbons from methane and carbon dioxide in a hybrid catalytic-plasma reactor: A review, *Fuel*, 85 (2006) 577-592.

[84] C. Perego, R. Bortolo, R. Zennaro, Gas to liquids technologies for natural gas reserves valorization: The Eni experience, *Catal. Today*, 142 (2009) 9-16.

[85] J.A. Velasco, L. Lopez, M. Velásquez, M. Boutonnet, S. Cabrera, S. Järås, Gas to liquids: A technology for natural gas industrialization in Bolivia, *Journal of Natural Gas Science and Engineering*, 2 (2010) 222-228.

[86] A.W. Budiman, S.-H. Song, T.-S. Chang, C.-H. Shin, M.-J. Choi, Dry reforming of methane over cobalt catalysts: A literature review of catalyst development, *Catalysis Surveys from Asia*, 16 (2012) 183-197.

[87] J. Xu, W. Zhou, Z. Li, J. Wang, J. Ma, Biogas reforming for hydrogen production over nickel and cobalt bimetallic catalysts, *International Journal of Hydrogen Energy*, 34 (2009) 6646-6654.

[88] L. Yuliati, H. Itoh, H. Yoshida, Photocatalytic conversion of methane and carbon dioxide over Gallium oxide, *Chem. Phys. Lett.*, 452 (2008) 178-182.

[89] A. Lanzini, P. Leone, Experimental investigation of direct internal reforming of biogas in solid oxide fuel cells, *International Journal of Hydrogen Energy*, 35 (2010) 2463-2476.

[90] Y. Shiratori, T. Oshima, K. Sasaki, Feasibility of direct-biogas SOFC, *International Journal of Hydrogen Energy*, 33 (2008) 6316-6321.

[91] Y. Hirata, T. Shimonosono, K. Ueda, S. Sameshima, K. Yamaji, Hydrogen formation from a real biogas using electrochemical cell with gadolinium-doped ceria porous electrolyte, *Ceram Int*, 43 (2017) 3639-3646.

[92] Y.H. Hu, E. Ruckenstein, Catalytic conversion of methane to synthesis gas by partial oxidation and CO_2 reforming, *Advances in Catalysis*, 48 (2004) 297-345.

[93] S. Kawi, Y. Kathiraser, J. Ni, U. Oemar, Z. Li, E.T. Saw, Progress in synthesis of highly active and stable nickel‐based catalysts for carbon dioxide reforming of methane, *ChemSusChem*, 8 (2015) 3556-3575.

[94] S. Sengupta, G. Deo, Modifying alumina with CaO or MgO in supported Ni and Ni–Co catalysts and its effect on dry reforming of CH_4, *Journal of CO_2 Utilization*, 10 (2015) 67-77.

[95] Z. Alipour, M. Rezaei, F. Meshkani, Effect of alkaline earth promoters (MgO, CaO, and BaO) on the activity and coke formation of Ni catalysts supported on nanocrystalline Al_2O_3 in dry reforming of methane, *Journal of Industrial and Engineering Chemistry*, 20 (2014) 2858-2863.

[96] X. Tu, H.J. Gallon, M.V. Twigg, P.A. Gorry, J.C. Whitehead, Dry reforming of methane over a Ni/Al_2O_3 catalyst in a coaxial dielectric barrier discharge reactor, *J. Phys. D: Appl. Phys.*, 44 (2011) 274007.

[97] D. Mei, B. Ashford, Y.-L. He, X. Tu, Plasma-catalytic reforming of biogas over supported Ni catalysts in a dielectric barrier discharge reactor: Effect of catalyst supports, *Plasma Process. Polym.*, (2016).

[98] Y. Zeng, X. Zhu, D. Mei, B. Ashford, X. Tu, Plasma-catalytic dry reforming of methane over γ-Al_2O_3 supported metal catalysts, *Catal. Today*, 256 (2015) 80-87.

[99] K. Li, J.-L. Liu, X.-S. Li, X. Zhu, A.-M. Zhu, Warm plasma catalytic reforming of biogas in a heat-insulated reactor: Dramatic energy efficiency and catalyst auto-reduction, *Chem. Eng. J.*, 288 (2016) 671-679.

[100] J.-L. Liu, H.-W. Park, W.-J. Chung, W.-S. Ahn, D.-W. Park, Simulated biogas oxidative reforming in AC-pulsed gliding arc discharge, *Chem. Eng. J.*, 285 (2016) 243-251.

[101] X. Zhu, K. Li, J.-L. Liu, X.-S. Li, A.-M. Zhu, Effect of CO_2/CH_4 ratio on biogas reforming with added O_2 through an unique spark-shade plasma, *International Journal of Hydrogen Energy*, 39 (2014) 13902-13908.

[102] N. Rueangjitt, C. Akarawitoo, S. Chavadej, Production of hydrogen-rich syngas from biogas reforming with partial oxidation using a multi-stage AC gliding arc system, *Plasma Chemistry and Plasma Processing*, 32 (2012) 583-596.

[103] Y.N. Chun, Y.C. Yang, K. Yoshikawa, Hydrogen generation from biogas reforming using a gliding arc plasma-catalyst reformer, *Catal. Today*, 148 (2009) 283-289.

[104] X. Tu, J.C. Whitehead, Plasma dry reforming of methane in an atmospheric pressure AC gliding arc discharge: Co-generation of syngas and carbon nanomaterials, *International Journal of Hydrogen Energy*, 39 (2014) 9658-9669.

[105] B. Zhu, X.-S. Li, C. Shi, J.-L. Liu, T.-L. Zhao, A.-M. Zhu, Pressurization effect on dry reforming of biogas in kilohertz spark-discharge plasma, *International Journal of Hydrogen Energy*, 37 (2012) 4945-4954.

[106] A. Domínguez, Y. Fernández, B. Fidalgo, J. Pis, J. Menéndez, Biogas to syngas by microwave-assisted dry reforming in the presence of char, *Energy Fuels*, 21 (2007) 2066-2071.

[107] Y. Xu, Q. Wei, H. Long, X. Zhang, S. Shang, X. Dai, Y. Yin, CO_2 reforming of CH_4 by synergies of binode thermal plasma and catalysts, *International Journal of Hydrogen Energy*, 38 (2013) 1384-1390.

[108] S. Yao, M. Okumoto, A. Nakayama, E. Suzuki, Plasma reforming and coupling of methane with carbon dioxide, *Energy Fuels*, 15 (2001) 1295-1299.

[109] X. Zhang, M.S. Cha, Electron-induced dry reforming of methane in a temperature-controlled dielectric barrier discharge reactor, *J. Phys. D: Appl. Phys.*, 46 (2013) 415205.

[110] V.J. Rico, J.L. Hueso, J. Cotrino, A.R. González-Elipe, Evaluation of different dielectric barrier discharge plasma configurations as an alternative technology for green C_1 chemistry in the carbon dioxide reforming of methane and the direct decomposition of methanol, *J. Phys. Chem. A*, 114 (2010) 4009-4016.

[111] Q. Wang, B.H. Yan, Y. Jin, Y. Cheng, Dry reforming of methane in a dielectric barrier discharge reactor with Ni/Al_2O_3 catalyst: Interaction of catalyst and plasma, *Energy Fuels*, 23 (2009) 4196 - 4201.

[112] V. Goujard, J.-M. Tatibouët, C. Batiot-Dupeyrat, Use of a non-thermal plasma for the production of synthesis gas from biogas, *Applied Catalysis A: General*, 353 (2009) 228-235.

[113] Y.P. Zhang, Y. Li, Y. Wang, C.J. Liu, B. Eliasson, Plasma methane conversion in the presence of carbon dioxide using dielectric-barrier discharges, *Fuel Processing Technology*, 83 (2003) 101-109.

[114] A.J. Zhang, A.M. Zhu, J. Guo, Y. Xu, C. Shi, Conversion of greenhouse gases into syngas via combined effects of discharge activation and catalysis, *Chem. Eng. J.*, 156 (2010) 601-606.

[115] M. Li, G. Xu, Y. Tian, L. Chen, H. Fu, Carbon dioxide reforming of methane using DC corona discharge plasma reaction, *Journal of Physics Chemistry: A*, 108 (2004) 1687-1693.

[116] D. Li, X. Li, M. Bai, X. Tao, S. Shang, X. Dai, Y. Yin, CO_2 reforming of CH_4 by atmospheric pressure glow discharge plasma: A high conversion ability, *International Journal of Hydrogen Energy*, 34 (2009) 308-313.

[117] G. Scarduelli, G. Guella, D. Ascenzi, P. Tosi, Synthesis of liquid organic compounds from CH_4 and CO_2 in a dielectric barrier discharge operating at atmospheric pressure, *Plasma Process. Polym.*, 8 (2011) 25-31.

[118] J. Sentek, K. Krawczyk, M. Młotek, M. Kalczewska, T. Kroker, T. Kolb, A. Schenk, K.H. Gericke, K. Schmidt Szałowski, Plasma-catalytic methane conversion with carbon dioxide in dielectric barrier discharges, *Appl. Catal., B: Environ.*, 94 (2010) 19-26.

[119] K. Zhang, B. Eliasson, U. Kogelschatz, Direct conversion of greenhouse gases to synthesis gas and C4 hydrocarbons over Zeolite HY promoted by a dielectric-barrier discharge, *Industrial & Engineering Chemistry Research*, 41 (2002) 1462 - 1468.

[120] X. Zhu, P. Huo, Y.P. Zhang, D.G. Cheng, C.J. Liu, Structure and reactivity of plasma treated Ni/Al_2O_3 catalyst for CO_2 reforming of methane, *Appl. Catal., B: Environ.*, 81 (2008) 132-140.

[121] S. Corthals, T. Witvrouwen, P. Jacobs, B. Sels, Development of dry reforming catalysts at elevated pressure: D-optimal vs. full factorial design, *Catal. Today*, 159 (2011) 12-24.

[122] M.H. Pham, V. Goujard, J.M. Tatibouët, C. Batiot-Dupeyrat, Activation of methane and carbon dioxide in a dielectric-barrier discharge-plasma reactor to produce hydrocarbons—Influence of La_2O_3/γ-Al_2O_3 catalyst, *Catal. Today*, 171 (2011) 67-71.

[123] H.J. Gallon, X. Tu, J.C. Whitehead, Effects of reactor packing materials on H_2 production by CO_2 reforming of CH_4 in a dielectric barrier discharge, *Plasma Process. Polym.*, 9 (2012) 90-97.

[124] A. Nandini, K.K. Pant, S.C. Dhingra, K-, CeO_2-, and Mn-promoted Ni/Al_2O_3 catalysts for stable CO_2 reforming of methane, *Applied Catalysis A: General*, 290 (2005) 166-174.

[125] J. Juan-Juan, M.C. Román-Martínez, M.J. Illán-Gómez, Effect of potassium content in the activity of K-promoted Ni/Al_2O_3 catalysts for the dry reforming of methane, *Applied Catalysis A: General*, 301 (2006) 9-15.

[126] Ş. Özkara-Aydınoğlu, A.E. Aksoylu, Carbon dioxide reforming of methane over Co-X/ZrO_2 catalysts (X=La, Ce, Mn, Mg, K), *Catal. Commun.*, 11 (2010) 1165-1170.

[127] L. Xu, H. Song, L. Chou, Carbon dioxide reforming of methane over ordered mesoporous NiO–MgO–Al_2O_3 composite oxides, *Appl. Catal., B: Environ.*, 108 (2011) 177-190.

[128] N. Wang, K. Shen, L. Huang, X. Yu, W. Qian, W. Chu, Facile route for synthesizing ordered mesoporous Ni–Ce–Al oxide materials and their catalytic performance for methane dry reforming to hydrogen and syngas, *ACS Catal.*, 3 (2013) 1638-1651.

[129] R. Dębek, M. Radlik, M. Motak, M.E. Galvez, W. Turek, P. Da Costa, T. Grzybek, Ni-containing Ce-promoted hydrotalcite derived materials as catalysts for methane reforming with carbon dioxide at low temperature – On the effect of basicity, *Catal. Today*, 257 (2015) 59-65.

[130] N. Charisiou, G. Siakavelas, K. Papageridis, A. Baklavaridis, L. Tzounis, D. Avraam, M. Goula, Syngas production via the biogas dry reforming reaction over nickel supported on modified with CeO_2 and/or La_2O_3 alumina catalysts, *Journal of Natural Gas Science and Engineering*, 31 (2016) 164-183.

[131] A.D. Ballarini, S.R. de Miguel, E.L. Jablonski, O.A. Scelza, A.A. Castro, Reforming of CH_4 with CO_2 on Pt-supported catalysts, *Catal. Today*, 107-108 (2005) 481-486.

[132] A. Rousseau, A.V. Meshchanov, J. Roepcke, Evidence of plasma-catalyst synergy in a low-pressure discharge, *Applied Physics Letters*, 88 (2006) 021503.

[133] A. Gil, A. Diaz, L. Gandia, M. Montes, Influence of the preparation method and the nature of the support on the stability of nickel catalysts, *Applied Catalysis A: General*, 109 (1994) 167-179.

[134] M.A. Goula, N.D. Charisiou, K.N. Papageridis, A. Delimitis, E. Pachatouridou, E.F. Iliopoulou, Nickel on alumina catalysts for the production of hydrogen rich mixtures via the biogas dry reforming reaction: Influence of the synthesis method, *International Journal of Hydrogen Energy*, 40 (2015) 9183-9200.

[135] S. Corthals, J. Van Nederkassel, H. De Winne, J. Geboers, P. Jacobs, B. Sels, Design of active and stable $NiCeO_2ZrO_2MgAl_2O_4$ dry reforming catalysts, *Appl. Catal., B: Environ.*, 105 (2011) 263-275.

[136] S. Damyanova, B. Pawelec, K. Arishtirova, J.L.G. Fierro, Ni-based catalysts for reforming of methane with CO_2, *International Journal of Hydrogen Energy*, 37 (2012) 15966-15975.

[137] P.A. Nandini, K.K. Pant, S.C. Dhingra, R. Bhalla, Characterization and activity of K, CeO_2, and Mn promoted Ni/Al_2O_3 catalysts for carbon dioxide reforming of methane, *Industrial & Engineering Chemistry Research*, (2006) 7435-7443.

[138] J. Zhang, H. Wang, A. Dalai, Development of stable bimetallic catalysts for carbon dioxide reforming of methane, *J. Catal.*, 249 (2007) 300-310.

[139] H. Sun, J. Huang, H. Wang, J. Zhang, CO_2 Reforming of CH_4 over Xerogel Ni−Ti and Ni−Ti−Al Catalysts, *Industrial & Engineering Chemistry Research*, 46 (2007) 4444-4450.

[140] X. Tao, F. Qi, Y. Yin, X. Dai, CO_2 reforming of CH_4 by combination of thermal plasma and catalyst, *International Journal of Hydrogen Energy*, 33 (2008) 1262-1265.

[141] M.M. Barroso-Quiroga, A.E. Castro-Luna, Catalytic activity and effect of modifiers on Ni-based catalysts for the dry reforming of methane, *International Journal of Hydrogen Energy*, 35 (2010) 6052-6056.

[142] M. García-Diéguez, E. Finocchio, M.Á. Larrubia, L.J. Alemany, G. Busca, Characterization of alumina-supported Pt, Ni and PtNi alloy catalysts for the dry reforming of methane, *J. Catal.*, 274 (2010) 11-20.

[143] S.A. Chattanathan, S. Adhikari, M. McVey, O. Fasina, Hydrogen production from biogas reforming and the effect of H_2S on CH_4 conversion, *International Journal of Hydrogen Energy*, 39 (2014) 19905-19911.

[144] M. Jafarbegloo, A. Tarlani, A.W. Mesbah, S. Sahebdelfar, Thermodynamic analysis of carbon dioxide reforming of methane and its practical relevance, *International Journal of Hydrogen Energy*, 40 (2015) 2445-2451.

[145] L.T. Hsieh, W.J. Lee, C.T. Li, C.Y. Chen, Y.F. Wang, M.B. Chang, Decomposition of carbon dioxide in the RF plasma environment, *Journal of Chemical Technology and Biotechnology*, 73 (1998) 432-442.

[146] B. Eliasson, C.-j. Liu, U. Kogelschatz, Direct conversion of methane and carbon dioxide to higher hydrocarbons using catalytic dielectric-barrier discharges with zeolites, *Industrial & Engineering Chemistry Research*, 39 (2000) 1221-1227.

[147] K. Zhang, U. Kogelschatz, B. Eliasson, Conversion of greenhouse gases to synthesis gas and higher hydrocarbons, *Energy Fuels*, 15 (2001) 395-402.

[148] A. Montoro-Damas, J.J. Brey, M.A. Rodríguez, A.R. González-Elipe, J. Cotrino, Plasma reforming of methane in a tunable ferroelectric packed-bed dielectric barrier discharge reactor, *Journal of Power Sources*, 296 (2015) 268-275.

[149] S. Chavadej, K. Supat, L.L. Lobban, R.G. Mallinson, Partial oxidation of methane and carbon dioxide reforming with methane in corona discharge with/without Pt/KL catalyst, *Journal of Chemical Engineering of Japan*, 38 (2005) 163-170.

[150] M.-W. Li, C.-P. Liu, Y.-L. Tian, G.-H. Xu, F.-C. Zhang, Y.-Q. Wang, Effects of catalysts in carbon dioxide reforming of methane via corona plasma reactions, *Energy Fuels*, 20 (2006) 1033 - 1038.

[151] Z. Bo, J. Yan, X. Li, Y. Chi, K. Cen, Plasma assisted dry methane reforming using gliding arc gas discharge: Effect of feed gases proportion, *International Journal of Hydrogen Energy*, 33 (2008) 5545-5553.

[152] H. Long, S. Shang, X. Tao, Y. Yin, X. Dai, CO_2 reforming of CH_4 by combination of cold plasma jet and Ni/γ-Al_2O_3 catalyst, *International Journal of Hydrogen Energy*, 33 (2008) 5510-5515.

[153] A. Ghorbanzadeh, R. Lotfalipour, S. Rezaei, Carbon dioxide reforming of methane at near room temperature in low energy pulsed plasma, *International Journal of Hydrogen Energy*, 34 (2009) 293-298.

[154] J.-L. Liu, X.-S. Li, X. Zhu, K. Li, C. Shi, A.-M. Zhu, Renewable and high-concentration syngas production from oxidative reforming of simulated biogas with low energy cost in a plasma shade, *Chem. Eng. J.*, 234 (2013) 240-246.

[155] B. Zhu, X.-S. Li, J.-L. Liu, X. Zhu, A.-M. Zhu, Kinetics study on carbon dioxide reforming of methane in kilohertz spark-discharge plasma, *Chem. Eng. J.*, 264 (2015) 445-452.

[156] J. Pacheco, G. Soria, M. Pacheco, R. Valdivia, F. Ramos, H. Frías, M. Durán, M. Hidalgo, Greenhouse gas treatment and H_2 production, by warm plasma reforming, *International Journal of Hydrogen Energy*, 40 (2015) 17165-17171.

[157] Z.A. Allah, J.C. Whitehead, Plasma-catalytic dry reforming of methane in an atmospheric pressure AC gliding arc discharge, *Catal. Today*, 256 (2015) 76-79.

[158] H.H. Nguyen, K.-S. Kim, Combination of plasmas and catalytic reactions for CO_2 reforming of CH_4 by dielectric barrier discharge process, *Catal. Today*, 256 (2015) 88-95.

[159] K. Li, J.-L. Liu, X.-S. Li, X.-B. Zhu, A.-M. Zhu, Post-plasma catalytic oxidative CO_2 reforming of methane over Ni-based catalysts, *Catal. Today*, 256 (2015) 96-101.

[160] X.-G. Zheng, S.-Y. Tan, L.-C. Dong, S.-B. Li, H.-M. Chen, S.-A. Wei, Experimental and kinetic investigation of the plasma catalytic dry reforming of methane over perovskite $LaNiO_3$ nanoparticles, *Fuel Processing Technology*, 137 (2015) 250-258.

[161] V. Shapoval, E. Marotta, Investigation on plasma‐driven methane dry reforming in a self‐triggered spark reactor, *Plasma Process. Polym.*, 12 (2015) 808-816.

[162] S. Kameshima, K. Tamura, Y. Ishibashi, T. Nozaki, Pulsed dry methane reforming in plasma-enhanced catalytic reaction, *Catal. Today*, 256 (2015) 67-75.

[163] D. Czylkowski, B. Hrycak, M. Jasiński, M. Dors, J. Mizeraczyk, Microwave plasma-based method of hydrogen production via combined steam reforming of methane, *Energy*, 113 (2016) 653-661.

[164] M.S. Lim, Y.N. Chun, Carbon dioxide destruction with methane reforming by a novel plasma-catalytic converter, *Plasma Chemistry and Plasma Processing*, 36 (2016) 1211-1228.

[165] S. Albertazzi, P. Arpentinier, F. Basile, P. Del Gallo, G. Fornasari, D. Gary, A. Vaccari, Deactivation of a Pt/γ-Al_2O_3 catalyst in the partial oxidation of methane to synthesis gas, *Applied Catalysis A: General*, 247 (2003) 1-7.

[166] H. Tian, X. Li, L. Zeng, J. Gong, Recent Advances on the Design of Group VIII Base-Metal Catalysts with Encapsulated Structures, *ACS Catal.*, 5 (2015) 4959-4977.

[167] K. Zhang, T. Mukhriza, X. Liu, P.P. Greco, E. Chiremba, A study on CO_2 and CH_4 conversion to synthesis gas and higher hydrocarbons by the combination of catalysts and dielectric-barrier discharges, *Applied Catalysis A: General*, 502 (2015) 138-149.

[168] G. Zhang, L. Hao, Y. Jia, Y. Du, Y. Zhang, CO_2 reforming of CH_4 over efficient bimetallic Co–Zr/AC catalyst for H_2 production, *International Journal of Hydrogen Energy*, 40 (2015) 12868-12879.

[169] J.L. Ewbank, L. Kovarik, F.Z. Diallo, C. Sievers, Effect of metal–support interactions in Ni/Al_2O_3 catalysts with low metal loading for methane dry reforming, *Applied Catalysis A: General*, 494 (2015) 57-67.

[170] V. Dal Santo, A. Gallo, A. Naldoni, M. Guidotti, R. Psaro, Bimetallic heterogeneous catalysts for hydrogen production, *Catal. Today*, 197 (2012) 190-205.

[171] P. Djinović, I.G.O. Črnivec, B. Erjavec, A. Pintar, Influence of active metal loading and oxygen mobility on coke-free dry reforming of Ni–Co bimetallic catalysts, *Appl. Catal., B: Environ.*, 125 (2012) 259-270.

[172] M.H. Amin, K. Mantri, J. Newnham, J. Tardio, S.K. Bhargava, Highly stable Ytterbium promoted Ni/γ-Al_2O_3 catalysts for carbon dioxide reforming of methane, *Appl. Catal., B: Environ.*, 119-120 (2012) 217-226.

[173] H. Cheng, S. Feng, W. Tao, X. Lu, W. Yao, G. Li, Z. Zhou, Effects of noble metal-doping on Ni/La_2O_3–ZrO_2 catalysts for dry reforming of coke oven gas, *International Journal of Hydrogen Energy*, 39 (2014) 12604-12612.

[174] R. Snoeckx, R. Aerts, X. Tu, A. Bogaerts, Plasma-based dry reforming: A computational study ranging from the nanoseconds to seconds time scale, *The Journal of Physical Chemistry C*, 117 (2013) 4957-4970.

[175] V.M. Gonzalez-delaCruz, R. Pereñiguez, F. Ternero, J.P. Holgado, A. Caballero, In Situ XAS Study of Synergic Effects on Ni–Co/ZrO_2 Methane Reforming Catalysts, *The Journal of Physical Chemistry C*, 116 (2012) 2919-2926.

[176] A. Ballarini, F. Basile, P. Benito, I. Bersani, G. Fornasari, S. de Miguel, S.C.P. Maina, J. Vilella, A. Vaccari, O.A. Scelza, Platinum supported on alkaline and alkaline earth

metal-doped alumina as catalysts for dry reforming and partial oxidation of methane, *Applied Catalysis A: General*, 433-434 (2012) 1-11.

[177] M. Radlik, M. Adamowska-Teyssier, A. Krztoń, K. Kozieł, W. Krajewski, W. Turek, P. Da Costa, Dry reforming of methane over $Ni/Ce_{0.62}Zr_{0.38}O_2$ catalysts: Effect of Ni loading on the catalytic activity and on H_2/CO production, *Comptes Rendus Chimie*, 18 (2015) 1242-1249.

[178] T. Manley, The electric characteristics of the ozonator discharge, *Transactions of the Electrochemical Society*, 84 (1943) 83-96.

[179] L. Wang, Y.H. Yi, Y. Zhao, R. Zhang, J.L. Zhang, H.C. Guo, NH_3 decomposition for H_2 generation: Effects of cheap metals and supports on plasma–Catalyst synergy, *ACS Catal.*, 5 (2015) 4167-4174.

[180] X. Tao, M. Bai, X. Li, H. Long, S. Shang, Y. Yin, X. Dai, CH_4–CO_2 reforming by plasma – challenges and opportunities, *Progress in Energy and Combustion Science*, 37 (2011) 113-124.

[181] X. Tu, H.J. Gallon, J.C. Whitehead, Transition behavior of packed-bed dielectric barrier discharge in argon, *IEEE Trans. Plasma Sci.*, 39 (2011) 2172.

[182] G. Centi, S. Perathoner, Opportunities and prospects in the chemical recycling of carbon dioxide to fuels, *Catal. Today*, 148 (2009) 191-205.

[183] D. Mei, Y.L. He, S. Liu, J. Yan, X. Tu, Optimization of CO_2 conversion in a cylindrical dielectric barrier discharge reactor using design of experiments, *Plasma Process. Polym.*, 13 (2015) 544-556.

[184] M.A.A. Aziz, A.A. Jalil, S. Triwahyono, S.M. Sidik, Methanation of carbon dioxide on metal-promoted mesostructured silica nanoparticles, *Applied Catalysis A: General*, 486 (2014) 115-122.

[185] B. Lu, K. Kawamoto, Preparation of mesoporous CeO_2 and monodispersed NiO particles in CeO_2, and enhanced selectivity of NiO/CeO_2 for reverse water gas shift reaction, *Materials Research Bulletin*, 53 (2014) 70-78.

[186] H.D.A.L. Viana, J.T.S. Irvine, Catalytic properties of the proton conductor materials: $Sr_3CaZr_{0.5}Ta_{1.5}O_{8.75}$, $BaCe_{0.9}Y_{0.1}O_{2.95}$ and $Ba_3Ca_{1.18}Nb_{1.82}O_{8.73}$ for reverse water gas shift, *Solid State Ionics*, 178 (2007) 717-722.

[187] A.A. Upadhye, I. Ro, X. Zeng, H.J. Kim, I. Tejedor, M.A. Anderson, J.A. Dumesic, G.W. Huber, Plasmon-enhanced reverse water gas shift reaction over oxide supported Au catalysts, *Catalysis Science & Technology*, 5 (2015) 2590-2601.

[188] T.C. Hales, Historical overview of the Kepler conjecture, The Kepler Conjecture, *Springer*, , 2011, pp. 65-82.

[189] Z. Falkenstein, J.J. Coogan, Microdischarge behaviour in the silent discharge of nitrogen-oxygen and water-air mixtures, *J. Phys. D: Appl. Phys.*, (1997) 817-825.

[190] D.J. Griffiths, Introduction to Electrodynamics, 3rd Edition, *Prentice-Hall*, Upper Saddle River, 2007.

[191] M.R. Stuart, Dielectric constant of quartz as a function of frequency and temperature, *J. Appl. Phys.*, 26 (1955) 1399.

[192] A. Van Itterbeek, K. De Clippeleir, Measurements on the dielectric constant of carbon dioxide as a function of pressure and temperature, *Physica*, 13 (1947) 459-464.

[193] A. Michels, P. Sanders, S. A., The dielectric constant of hydrogen at pressure up to 1425 atm, and at temperatures of 25 ^{o}C and 100 ^{o}C, *Physica*, 2 (1935) 753-756.

[194] A.B. Bryan, The dielectric constants of Argon and Neon, *Phys. Rev.*, 34 (1929) 615-617.

[195] Y. Yi, C. Xu, L. Wang, J. Yu, Q. Zhu, S. Sun, X. Tu, C. Meng, J. Zhang, H. Guo, Selectivity control of H_2/O_2 plasma reaction for direct synthesis of high purity H_2O_2 with desired concentration, *Chem. Eng. J.*, 313 (2017) 37-46.

[196] M. Ramakers, I. Michielsen, R. Aerts, V. Meynen, A. Bogaerts, Effect of Argon or Helium on the CO_2 conversion in a dielectric barrier discharge, *Plasma Process. Polym.*, 12 (2015) 755-763.

[197] N. Sadeghi, D.W. Setser, M. Touzeau, Reactions of metastable argon atoms with molecular hydrogen at 300 and 80 K: origin of the ultraviolet chemiluminescence, *J. Phys. Chem. A*, 106 (2002) 8399-8405.

[198] G.W. Taylor, D.W. Setser, Chemical applications of metastable argon atoms. Generation, identification and characterization of CO (a3Π), *Chem. Phys. Lett.*, 8 (1971) 51-54.

[199] A. Bogaerts, R. Gijbels, Effects of adding hydrogen to an argon glow discharge: overview of relevant processes and some qualitative explanations, *J. Anal. At. Spectrom.*, 15 (2000) 441-449.

[200] C. De Bie, J. van Dijk, A. Bogaerts, The dominant pathways for the conversion of methane into oxygenates and syngas in an atmospheric pressure dielectric barrier discharge, *The Journal of Physical Chemistry C*, 119 (2015) 22331-22350.

[201] L. Wang, S. Liu, C. Xu, X. Tu, Direct conversion of methanol to n-C_4H_{10} and H_2 in a dielectric barrier discharge reactor, *Green Chemistry*, 18 (2016) 5658-5666.

[202] S.Y. Lin, H. Guo, Case study of a prototypical elementary insertion reaction: C(1D)+H_2 →CH+H, *J. Phys. Chem. A*, 108 (2004) 10066-10071.

[203] L.B. Harding, R. Guadagnini, G.C. Schatz, Theoretical studies of the reactions H+CH →C+H_2 and C+H_2→CH_2 using an ab initio global ground-state potential surface for CH_2, *Journal of Physical Chemistry*, 97 (1993) 5472-5481.

[204] H. Arai, S. Nagai, M. Hatada, Radiolysis of methane containing small amounts of carbon monoxide-formation of organic acids, *Radiation Physics and Chemistry (1977)*, 17 (1981) 211-216.

[205] G. Friedrichs, J.T. Herbon, D.F. Davidson, R.K. Hanson, Quantitative detection of HCO behind shock waves: The thermal decomposition of HCO, *Physical Chemistry Chemical Physics*, 4 (2002) 5778-5788.

[206] S.-J. Choe, H.-J. Kang, S.-J. Kim, S.-B. Park, D.-H. Park, D.-S. Huh, Adsorbed carbon formation and carbon hydrogenation for CO_2 methanation on the Ni (111) surface: ASED-MO study, *Bulletin of the Korean Chemical Society*, 26 (2005) 1682-1688.

[207] G.A. Mills, F.W. Steffgen, Catalytic methanation, *Catalysis Reviews*, 8 (1974) 159-210.

[208] K. Li, C. Yin, Y. Zheng, F. He, Y. Wang, M. Jiao, H. Tang, Z. Wu, DFT study on the methane synthesis from syngas on a cerium-doped Ni (111) surface, *The Journal of Physical Chemistry C*, 120 (2016) 23030-23043.

[209] G. Auriemma, D. Fidanza, G. Pirozzi, C. Satriano, Experimental determination of the Townsend coefficient for Argon-CO_2 gas mixtures at high fields, *Nucl. Instrum. Methods Phys. Res., Sect. A*, (2003) 484-489.

[210] K.P. Brand, Dielectric strength, boiling point and toxicity of gases - different aspects of the same basic molecular properties, *IEEE Trans. Electr. Insul.*, EI-17 (1982) 451-456.

[211] U. Kogelschatz, Filamentary, patterned, and diffuse barrier discharges, *IEEE Trans. Plasma Sci.*, 30 (2002) 1400-1408.

[212] J.H. Choi, Y. Noma, T. Tomai, K. Terashima, Temperature-dependent transition of discharge pattern of He/air cryoplasma, *Applied Physics Letters*, 93 (2008) 081504.

[213] Y. Shuiliang, W. Shan, J. Qi, H. Jingyi, J. Boqiong, W. Zuliang, Equation of energy injection to a dielectric barrier discharge reactor, *Plasma Science and Technology*, 18 (2016) 804.

[214] M. Abdel-Salam, Calculating the effect of high temperatures on the onset voltages of negative discharges, *J. Phys. D: Appl. Phys.*, 9 (1976) L149.

[215] X. Tu, H.J. Gallon, J.C. Whitehead, Plasma-assisted reduction of a NiO/Al_2O_3 catalyst in atmospheric pressure H_2/Ar dielectric barrier discharge, *Catal. Today*, 211 (2013) 120-125.

[216] E. van Steen, G.S. Sewell, R.A. Makhothe, C. Micklethwaite, H. Manstein, M. de Lange, C.T. O'Connor, TPR study on the preparation of impregnated Co/SiO_2 catalysts, *J. Catal.*, 162 (1996) 220-229.

[217] C.L. Bianchi, TPR and XPS investigations of Co/Al_2O_3 catalysts promoted with Ru, Ir and Pt, *Catal. Lett.*, 76 (2001) 155-159.

[218] B. Sexton, A. Hughes, T. Turney, An XPS and TPR study of the reduction of promoted cobalt-kieselguhr Fischer-Tropsch catalysts, *J. Catal.*, 97 (1986) 390-406.

[219] G. Wen, Y. Xu, Z. Xu, Z. Tian, Characterization and catalytic properties of the Ni/Al_2O_3 catalysts for aqueous-phase reforming of glucose, *Catal. Lett.*, 129 (2009) 250-257.

[220] T.K. Das, G. Jacobs, P.M. Patterson, W.A. Conner, J. Li, B.H. Davis, Fischer – Tropsch synthesis: Characterization and catalytic properties of rhenium promoted cobalt alumina catalysts☆, *Fuel*, 82 (2003) 805-815.

[221] A.Y. Khodakov, Fischer-Tropsch synthesis: Relations between structure of cobalt catalysts and their catalytic performance, *Catal. Today*, 144 (2009) 251-257.

[222] G. Jacobs, Y. Ji, B.H. Davis, D. Cronauer, A.J. Kropf, C.L. Marshall, Fischer–Tropsch synthesis: Temperature programmed EXAFS/XANES investigation of the influence of support type, cobalt loading, and noble metal promoter addition to the reduction behavior of cobalt oxide particles, *Applied Catalysis A: General*, 333 (2007) 177-191.

[223] D.G. Cheng, Plasma decomposition and reduction in supported metal catalyst preparation, *Catalysis Surveys from Asia*, 12 (2008) 145-151.

[224] T. Nozaki, K. Okazaki, Non-thermal plasma catalysis of methane: Principles, energy efficiency, and applications, *Catal. Today*, 211 (2013) 29-38.

[225] J. Karuppiah, Y.S. Mok, Plasma-reduced $Ni/\gamma–Al_2O_3$ and $CeO_2–Ni/\gamma–Al_2O_3$ catalysts for improving dry reforming of propane, *International Journal of Hydrogen Energy*, 39 (2014) 16329-16338.

[226] H.J. Gallon, X. Tu, M.V. Twigg, J.C. Whitehead, Plasma-assisted methane reduction of a NiO catalyst—Low temperature activation of methane and formation of carbon nanofibres, *Appl. Catal., B: Environ.*, 106 (2011) 616-620.

[227] S. Mahammadunnisa, P. Manoj Kumar Reddy, B. Ramaraju, C. Subrahmanyam, Catalytic nonthermal plasma reactor for dry reforming of methane, *Energy Fuels*, 27 (2013) 4441-4447.

[228] B.H. Yan, Q. Wang, Y. Jin, Y. Cheng, Dry reforming of methane with carbon dioxide using pulsed DC arc plasma at atmospheric pressure, *Plasma Chemistry and Plasma Processing*, 30 (2010) 257-266.

[229] Y. Sun, Y. Nie, A. Wu, D. Ji, F. Yu, J. Ji, Carbon dioxide reforming of methane to syngas by thermal plasma, *Plasma Science and Technology*, 14 (2012) 252-256.

[230] X. Zhu, X. Gao, X. Yu, C. Zheng, X. Tu, Catalyst screening for acetone removal in a single-stage plasma-catalysis system, *Catal. Today*, 256 (2015) 108-114.

[231] K.J. Jeon, H.R. Moon, A.M. Ruminski, B. Jiang, C. Kisielowski, R. Bardhan, J.J. Urban, Air-stable magnesium nanocomposites provide rapid and high-capacity hydrogen storage without using heavy-metal catalysts, *Nature Materials*, 10 (2011) 286-290.

[232] M.E. Gálvez, S. Ascaso, P. Stelmachowski, P. Legutko, A. Kotarba, R. Moliner, M.J. Lázaro, Influence of the surface potassium species in Fe–K/Al_2O_3 catalysts on the soot oxidation activity in the presence of NOx, *Appl. Catal., B: Environ.*, 152-153 (2014) 88-98.

[233] G. Avgouropoulos, T. Ioannides, H. Matralis, Influence of the preparation method on the performance of CuO–CeO_2 catalysts for the selective oxidation of CO, *Appl. Catal., B: Environ.*, 56 (2005) 87-93.

[234] L. Ji, S. Tang, H. Zeng, J. Lin, K. Tan, CO_2 reforming of methane to synthesis gas over sol–gel-made Co/γ-Al_2O_3 catalysts from organometallic precursors, *Applied Catalysis A: General*, 207 (2001) 247-255.

[235] S. Tauster, S. Fung, R.L. Garten, Strong metal-support interactions. Group 8 noble metals supported on titanium dioxide, *J. Am. Chem. Soc.*, 100 (1978) 170-175.

[236] A. Erdőhelyi, J. Cserényi, F. Solymosi, Activation of CH_4 and its reaction with CO_2 over supported Rh catalysts, *J. Catal.*, 141 (1993) 287-299.

[237] D. San José-Alonso, M. Illán-Gómez, M. Román-Martínez, K and Sr promoted Co alumina supported catalysts for the CO_2 reforming of methane, *Catal. Today*, 176 (2011) 187-190.

[238] A.D. Mazzoni, M.A. Sainz, A. Caballero, E.F. Aglietti, Formation and sintering of spinels ($MgAl_2O_4$) in reducing atmospheres, *Materials Chemistry and Physics*, (2002) 30-37.

[239] N. Wang, Z. Xu, J. Deng, K. Shen, X. Yu, W. Qian, W. Chu, F. Wei, One‐pot synthesis of ordered mesoporous NiCeAl oxide catalysts and a study of their performance in methane dry reforming, *ChemCatChem*, 6 (2014) 1470-1480.

[240] Q. Wang, B.-H. Yan, Y. Jin, Y. Cheng, Investigation of dry reforming of methane in a dielectric barrier discharge reactor, *Plasma Chemistry and Plasma Processing*, 29 (2009) 217-228.

[241] H.K. Song, J.-W. Choi, S.H. Yue, H. Lee, B.-K. Na, Synthesis gas production via dielectric barrier discharge over Ni/γ-Al_2O_3 catalyst, *Catal. Today*, 89 (2004) 27-33.

[242] Z. Zhang, X. Verykios, Carbon dioxide reforming of methane to synthesis gas over supported Ni catalysts, *Catal. Today*, 21 (1994) 589-595.

[243] L. Zhang, L. Li, Y. Zhang, Y. Zhao, J. Li, Nickel catalysts supported on MgO with different specific surface area for carbon dioxide reforming of methane, *Journal of Energy Chemistry*, 23 (2014) 66-72.

[244] A.L. Patterson, The Scherrer formula for X-ray particle size determination, *Phys. Rev.*, 56 (1939) 978.

[245] Y.F. Han, Z.Y. Zhong, K. Ramesh, F.X. Chen, L.W. Chen, Effects of different types of γ-Al_2O_3 on the activity of gold nanoparticles for CO oxidation at low-temperatures, *Journal of Physical Chemistry C*, (2007) 3163-3170.